Alma Mater Studiorum – Università di Bologna
in cotutela con Macquarie University

DOTTORATO DI RICERCA IN

ASTRONOMIA

Ciclo **XXIX**

Settore Concorsuale di afferenza:
02/C1 - Astronomia, Astrofisica, Fisica della Terra e dei Pianeti

Settore Scientifico disciplinare:
FIS/05 - Astronomia e Astrofisica

Modelling the faint radio sky: the pathway to SKA

Presentata da: Alessandro Maini

Coordinatore Dottorato
Francesco R. Ferraro

Relatore
Gabriele Giovannini

Co-Relatori
Isabella Prandoni
Ray P. Norris
Lee R. Spitler

Esame finale anno 2016

Ai miei genitori,
ai miei amici,
e alla persona che più di tutte ha sofferto
la lontananza durante questo pogetto,
la mia cara nonna Melania.

To my parents,
to my friends,
and to the person who suffered the most
the separation during this project,
my beloved grandmother Melania.

Except where acknowledged in the customary manner, the material presented in this thesis is, to the best of my knowledge, original.

This thesis has not been submitted in whole or part for a degree in any other university or institution than Macquarie University and Università di Bologna.

Alessandro Maini 24th October 2016

Acknowledgements

A PhD Thesis is a very long travel, which leads you in contact with several people, Institutions, and, in my case, Countries.

As cotutelle PhD student, I had the opportunity to work with four different Institutions (Università di Bologna, Macquarie University, Istituto di Radioastronomia, and CSIRO Astronomy & Space Science), and I had the pleasure to meet and work with several people. All the people I met contributed to this final product. I am very grateful to each of them for their help, their patience, and their support.

First of all, a huge thanks to my Supervisors:

Gabriele Giovannini, for having proposed me this beautiful and interesting project.

Isabella Prandoni, for all the work she did with me all along the period of the project, giving me suggestions and help to understand how to start and carry out such a task like a PhD.

Ray Norris, for its support and suggestions that helped me during the most challenging period of the project.

Lee Spitler, for being always attentive, supportive, and (even more important!) friendly.

Cormac Reynolds and Chris Phillips deserve for sure a lot of thanks. They always helped me during my data reductions, showing patience and a lot of wisdom.

A big thanks also to my priceless friends:

Roberto Iaconi, who bore with me for almost two years now, sharing with me a lot of experiences in the land of Australia.

Marco Bertolotti, Paolo Bolzoni, Simone Bolzoni, Massimiliano Dall'Argine, and Dario Faccini, the core of my Italian friends, who bore with my absence for the amount of time I spent in Australia.

Valentina Baccetti, Stefania Barsanti, Tiffany Day, Dimitri Douchin, Daniel MacDonald, and Andrea Tabacchini, the core of my Australian friends, met by good fortune in the gorgeous land of Australia!

Andreas Herzog, Glen Rees, Noelia Herrera Ruiz, and Michael Cowley, fellows in this travel.

Last but not least, a big thanks to my parents and relatives, who waited almost two years to see my face in person again.

Many, many thanks to you all!

Institutional-wise, I am very grateful to all the structures I worked with, for their help and support. In particular I would like to thanks the Istituto di Radio Astronomia (IRA) at Consiglio Nazionale delle Ricerche, and the Higher Degree Research (HDR) at Macquarie University. I acknowledge funding support from Cotutelle International Macquarie University Research Excellence Scholarship (iMQRES).

List of Publications

- Herrera Ruiz N., Middelberg E., Norris R. P., and **Maini A.**
  Unveiling the origin of the radio emission in Radio Quiet Quasars
  Astronomy and Astrophysics **589**,
  L2 (2016).

- **Maini A.**, Prandoni I., Norris R. P., Giovannini G., and Spitler L. R.
  Compact radio cores in radio-quiet active galactic nuclei
  Astronomy and Astrophysics **589**,
  L3 (2016).

- **Maini A.**, Prandoni I., Norris R. P., Spitler L. R., Mignano A., Lacy M., and Morganti R.
  Infrared-Faint Radio Sources in the SERVS deep fields:
  Pinpointing active galactic nuclei at high redshift.
  Accepted for publication on 23th August 2016 by Astronomy and Astrophysics,
  http://dx.doi.org/10.1051/0004-6361/201629391

List of Acronyms

AGN	Active Galactic Nuclei
ACS	Advanced Camera for Surveys
ADAF	Advection-Dominated Accretion Flows
ADIOS	Advection-dominated Inflow/Outflows Solution
AIPS	Astronomical Image Processing System
ALMA	Atacama Large Millimeter/submillimeter Array
ASKAP	Australian Square Kilometre Array Pathfinder
ASKAP-BETA	ASKAP - Boolardy Engineering Test Array
ATCA	Australia Telescope Compact Array
ATLAS	Australia Telescope Large Area Survey
ATNF	Australia Telescope National Facility
BH	Black hole
BLR	Broad-Line Region
(E)CDFS	(Extended) *Chandra* Deep Field South
CDSCC	Canberra Deep Space Communication Complex
CANDELS	Cosmic Assembly Near-infrared Deep Extragalactic Legacy Survey
CHILES Con Pol	COSMOS H I Large Extragalactic Survey Continuum Polarization
COSMOS	Cosmological Evolution Survey
CSIRO	Commonwealth Scientific and Industrial Research Organisation
CSS	Compact Steep-Spectrum
DR	Data Release
D.R.	Dynamic Range
DRAO	Dominion Radio Astrophysical Observatory
ELAIS-N1	European Large Area ISO Survey-North 1 (-South 1)
EMU	Evolutionary Map of Universe
FIR	Far infrared ($25\,\mu\mathrm{m} \lesssim \lambda \lesssim 350\,\mu\mathrm{m}$)
FLITECAM	First Light Infrared TEst CAMera
FR I (II)	Fanaroff-Riley I (II)
FIRST	Faint Images of the Radio Sky at Twenty centimeters
FORCAST	Faint Object infraRed CAmera for the SOFIA Telescope
GEMS	Galaxy Evolution from Morphologies and SEDs
GMOS	*Gemini* Multi-Object Spectrographs
GMRT	Giant Microwave Radio Telescope
GOODS-S	Great Observatories Origins Deep Survey-South
GPS	GigaHertz-Peaked Spectrum
GRASIL	GRAphite and SILicate

HDF-N	*Hubble* Deep Field North
HerMES	*Herschel* Multi-tiered Extragalactic Survey
HFF	*Hubble* Flanking Fields
HP	High-Power
HPBW	Half-Power BeamWidth
HzRG	High-redshift Radio Galaxy
IFRS	Infrared-faint radio source
IGM	Inter-Galactic Medium
ISM	Inter-Stellar Medium
IMF	Initial Mass Function
IR	Infra-red ($0.7\,\mu\mathrm{m} \lesssim \lambda \lesssim 350\,\mu\mathrm{m}$)
IRAC	InfraRed Array Camera
IRAF	Image Reduction and Analysis Facility
JVLA	(Karl G.) Jansky Very Large Array
JWST	James Webb Space Telescope
LBA	(Australian) Long Baseline Array
ULIRG	(Ultra-) Luminous InfraRed Galaxy
LH	Lockman Hole
LINER	Low-Ionization Nuclear Emission-Line Region galaxy
LOFAR	LOw-Frequency ARray
LP	Low-Power
MeerKAT	"More of" Karoo Array Telescope
MERLIN	Multi-Element Radio-Linked Interferometer Network
MIGHTEE	MeerKAT International GigaHertz Tiered Extragalactic Exploration
MIPS	Multiband Imaging Photometer for *Spitzer*
MIR	Mid infrared ($5\,\mu\mathrm{m} \lesssim \lambda \lesssim 25\,\mu\mathrm{m}$)
MIRI	Mid-InfraRed Instrument
MOST	Molonglo Observatory Synthesis Telescope
MRO	Murchison Radio-astronomy Observatory
MUSYC	Multiwavelength Survey by Yale-Chile
MWA	Murchison Widefield Array
NASA	National Aeronautics and Space Administration
NDWFS	NOAO Deep Wide-Field Survey
NICMOS	Near Infrared Camera and Multi-Object Spectrometer
NIR	Near infrared ($0.7\,\mu\mathrm{m} \lesssim \lambda \lesssim 5\,\mu\mathrm{m}$; or from I- to M-band)
NIRCam	Near Infrared Camera
NIRI	Near InfraRed Imager and spectrometer
NLR	Narrow-Line Region
NT	Non-Thermal
NVSS	NRAO VLA Sky Survey
OIRS	Optically Invisible Radio Source
PACS	Photodetector Array Camera and Spectrometer
PEP	PACS Evolutionary Probe
PLE	Pure Luminosity Evolution
PSF	Point Spread Function
QSG	Quasi-stellar Galaxy
QSO	Quasi-stellar Object

QSS	Quasi-stellar Radio Source
RFI	Radio Frequency Interference
RIAF	Radiatively Inefficient Accretion Flows
RL	Radio-Loud
RLG	Radio-Loud Galaxy
RLF	Radio Luminosity Function
RQ	Radio-Quiet
RQQ	Radio-Quiet Quasar
RSN	Radio SuperNova
SBG	Star-Burst Galaxy
SDSS	Sloan Digital Sky Survey
SED	Spectral Energy Distribution
SEIP	*Spitzer* Enhanced Imaging Products
SERVS	*Spitzer* Extragalactic Representative Volume Survey
SF(G)	Star-Forming (Galaxy)
SFR	Star-Formation Rate
SKA	Square Kilometre Array
SMBH	Super-Massive Black Hole
SN(R)	SuperNova (Remnant)
SOFIA	Stratospheric Observatory For Infrared Astronomy
SPIRE	Spectral and Photometric Imaging REceiver
(s)SFR	(specific) Star-Formation Rate
SUMSS	Sydney University Molonglo Sky Survey
SWIRE	*Spitzer* Wide-area IR Extragalactic Survey
UKIRT	United Kingdom Infra-red Telescope
URC	Unified Radio Catalog
USS	Ultra-Steep Spectrum
UV	Ultra-Violet ($0.01\,\mu\mathrm{m} \lesssim \lambda \lesssim 0.35\,\mu\mathrm{m}$)
(e)VLA	(expanded) Very Large Array
VLBA	Very Long Baseline Array
VLBI	Very Long Baseline Interferometry
VLSS	VLA Low-Frequency Sky Survey
VLT	Very Large Telescope
WENSS	Westerbork Northern Sky Survey
WFC3	Wide Field Camera 3
WISE	Wide-Field Infrared Survey Explorer
WODAN	Westerbork Observations of the Deep Apertif Northern Sky radio survey
WSRT	Westerbork Synthesis Radio Telescope
xFLS	(*Spitzer*) extragalactic First Look Survey
XMM-LSS	X-ray Multi-mirror Mission–Large Scale Structure
YSN	Young SuperNova

Abstract

In the last decade our understanding of the faint radio sky has undergone a significant change. Our perception of weak radio sources has been deeply changed due to the discovery that the so-called radio-quiet active galactic nuclei are not, in fact, radio silent, but simply faint as they finally started to be detected. Moreover, a new, unexpected class of radio-loud active galactic nuclei has been recently discovered, the so-called infrared-faint radio sources. This class of rare objects discovered in deep radio surveys, is emerging as a potentially promising class of sources to pre-select high-redshift powerful radio-loud active galactic nuclei.

In this Thesis, I present my contribution to the ongoing efforts to understand the nature of both these types of active galactic nuclei.

On the topic of radio-quiet active galactic nuclei, I searched for compact radio cores within a number of these sources, selected from deep radio samples. The search for these cores is particularly useful to shed light on the nature of the radio emission in high-redshift radio-quiet active galactic nuclei, which origin is currently hotly debated (star formation in the host galaxy or active nucleus). In particular, I searched for compact radio emission through long baseline radio interferometric observations of a selected sample of these sources. I also conducted a literature review, searching for such compact emissions in deep radio samples with high resolution (parsec-scale) observations already available, where radio-quiet active galactic nuclei were not recognised as such, by applying new classification criteria. In my experiment, I detected compact and bright radio cores in two active galactic nuclei classified as radio quiet, and I helped to classify other three detected objects in another experiment. Reviewing the literature, I found other five of these sources provided of a compact radio core. Therefore, I here report on a first direct evidence of radio cores in radio-quiet active galactic nuclei at cosmological redshifts. My preliminary analysis also indicates that star formation and active-galactic-nuclei-related radio emission likely coexist in these objects.

On the topic of infrared-faint radio sources, I searched for the infrared counterparts of the radio faintest tail (sub-mJy/mJy) of the distribution of these objects. Moreover, I compared the radio/IR properties of the IR-detected infrared-faint radio sources with those expected for a number of known classes of objects. I found that these sources are mostly consistent with a mixture of powerful, high-redshift ($z \gtrsim 3$) radio-loud active galactic nuclei, as their radio brighter ($\gg 1$ mJy) counterparts. Their faintness is likely to be ascribed to higher redshifts ($z > 3$–4). Some contamination by lower redshift ($z \sim 2$) heavily dust-enshrouded star forming galaxies can be present at the lowest end of their radio flux distribution ($S_{1.4\,\mathrm{GHz}} \leq 0.1$ mJy). This research was not only useful to better understand the nature of these sources, but provided further evidence that they may potentially be a useful resource to pre-select very high redshift ($z > 4$) active galactic nuclei candidates and, if confirmed, to explore the onset of the radio-loud active galactic nuclei phenomenon in the distant Universe.

The future, planned sub-mJy radio surveys (the ones expected to be delivered by the new facilities like ASKAP and SKA) will sample active galactic nuclei in the million, and the

above mentioned classes will constitute a relevant fraction of the future radio catalogues. Developing methods to recognise them, and to correctly address their nature, is fundamental to fully exploiting these surveys.

Contents

List of Figures

List of Tables

1 Introduction

For most of its history radio astronomy has been somewhat isolated as a separated branch of Astrophysics (Heckman & Best, 2014; Padovani et al., 2015b; Padovani, 2016). The study of active galactic nuclei (AGN; see Section 1.2), discovered during the 1950s, has been since then one of the most active research field within radio astronomy, but also suffered isolation and evolved relatively independent of observational investigations of AGN at other wavelengths as well as studies of their hosts: galaxies.

The astrophysics communities of galaxy scientists and AGN scientists researched independently primarily because the very idea that AGN were very peculiar objects prevented any attempt to synthesise in one single big picture galaxy and AGN evolution and interplay. Indeed, AGN were initially thought to be rare objects, harboured by few, peculiar galaxies and therefore studied primarily for two reasons that did not relate to their host galaxies. First, it was immediately clear that AGN were highly redshifted objects and could help astronomers to understand how the Universe within which we live was in the far past, and how it is structured on large-scales. Second, these bright radio sources provided a powerful laboratory of basic physics, by far more powerful than any terrestrial laboratory. For instance, AGN help to probe high-energy processes and test the physics in extreme environments.

This separation of the radio and galaxy communities, was not helped by the strong differences in flux detection limits typical of radio and optical surveys during the 1950–2000s. For instance, μJy-level sensitivity regimes were reached by optical instruments (like the *Hubble* Space Telescope) already in the 1990s, while in the radio domain they have been reached only recently (see Figures 1.1 and 1.2). Moreover, the sources of emission in these two classes of objects trace very different underlying physical mechanisms: galaxy scientists worked mainly at optical and infrared (IR) wavelengths, where stars and inter-stellar medium generate the vast majority of their energy output through thermal processes, while AGN scientists worked mainly at radio frequencies, where the dominant emission mechanism is non-thermal synchrotron radiation, originated by electrons spiralling in magnetic fields, and accelerated in the vicinity of the active nucleus.

Nowadays things have changed, and understanding the galaxy-AGN connection has become one of the most compelling and intriguing topics in contemporary Astrophysics.

Several are the reasons for this change. Firstly, it became clear that AGN are by far more

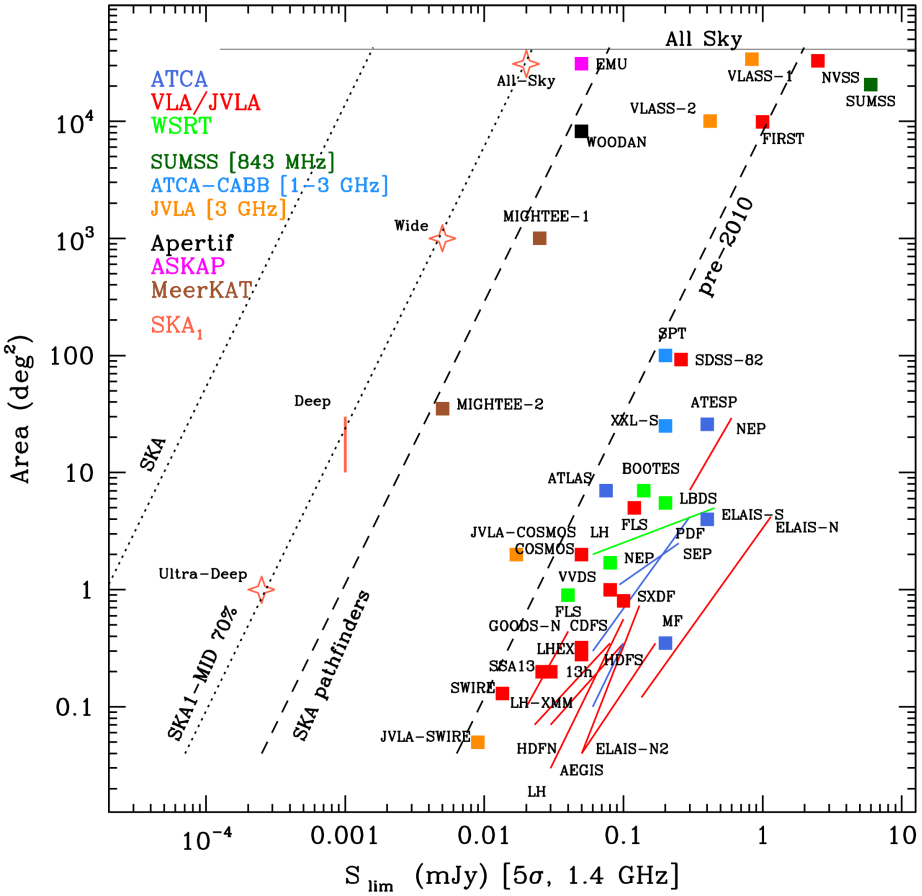

Figure 1.1: Comparison of flux density limits (5σ sensitivity, in mJy) and sky coverage (deg^2) for several existing and planned continuum radio surveys, with observing frequencies in the range 0.8–3.0 GHz. The diagonal black lines show the approximate limits for surveys: the dashed line on the right is based on available telescope time on pre-2010 radio facilities; the dashed and dotted lines on the left are based on several implementation stages of the future Square Kilometre Array (SKA; Dewdney et al. 1999) radio telescope. Coloured diagonal lines on bottom-right represent completed surveys based on several follow-ups, from wide and shallow to smaller and deep ones. Focusing on all-sky/very wide area surveys, the Sydney University Molonglo Sky Survey (SUMSS; Bock et al. 1999), performed between 1999 and 2007, delivered a catalogue with a 5σ sensitivity around 6 mJy. The NRAO VLA Sky Survey (NVSS; Condon et al. 1998), carried out between 1993 and 1996, delivered a catalogue with 5σ sensitivity around 2.5 mJy. The Faint Images of the Radio Sky at Twenty centimetres survey (FIRST; White et al. 1997), carried out between 1995 and 1996, provided a catalogue with 5σ sensitivity around 1 mJy. The VLA Sky Survey (VLASS[a]), recently re-designed into a single-element (corresponding to VLASS-1 in the Figure) and now started, will cover 80% of the sky to a target depth of 70 μJy in the 2–4 GHz S-band of the Karl G. Jansky Very Large Array (JVLA), with a resolution of 2.5 arcsec^2 (Lacy et al., 2016). The Evolutionary Map of Universe (EMU; Norris et al. 2011b), to be carried out with the Australian SKA Pathfinder (ASKAP), and the Westerbork Observations of the Deep Apertif Northern Sky radio survey (WODAN; Röttgering et al. 2011; Norris et al. 2013) are starting in these years, and should reach a 5σ sensitivity around 50 μJy. The MeerKAT International Giga-Hertz Tiered Extragalactic Exploration (MIGHTEE; Jarvis 2012), now under revision, will also start in the next future, and should cover about 30 deg^2 down to a theoretical rms sensitivity of 1 μJy (see MIGHTEE-2 in Figure). The MIGHTEE-1 is under discussion. The planned, full operational SKA radio surveys are planned to reach the verge of the nano-Jansky regime. Image from Prandoni & Seymour (2015).

[a] https://science.nrao.edu/science/surveys/vlass/vlass-white-papers

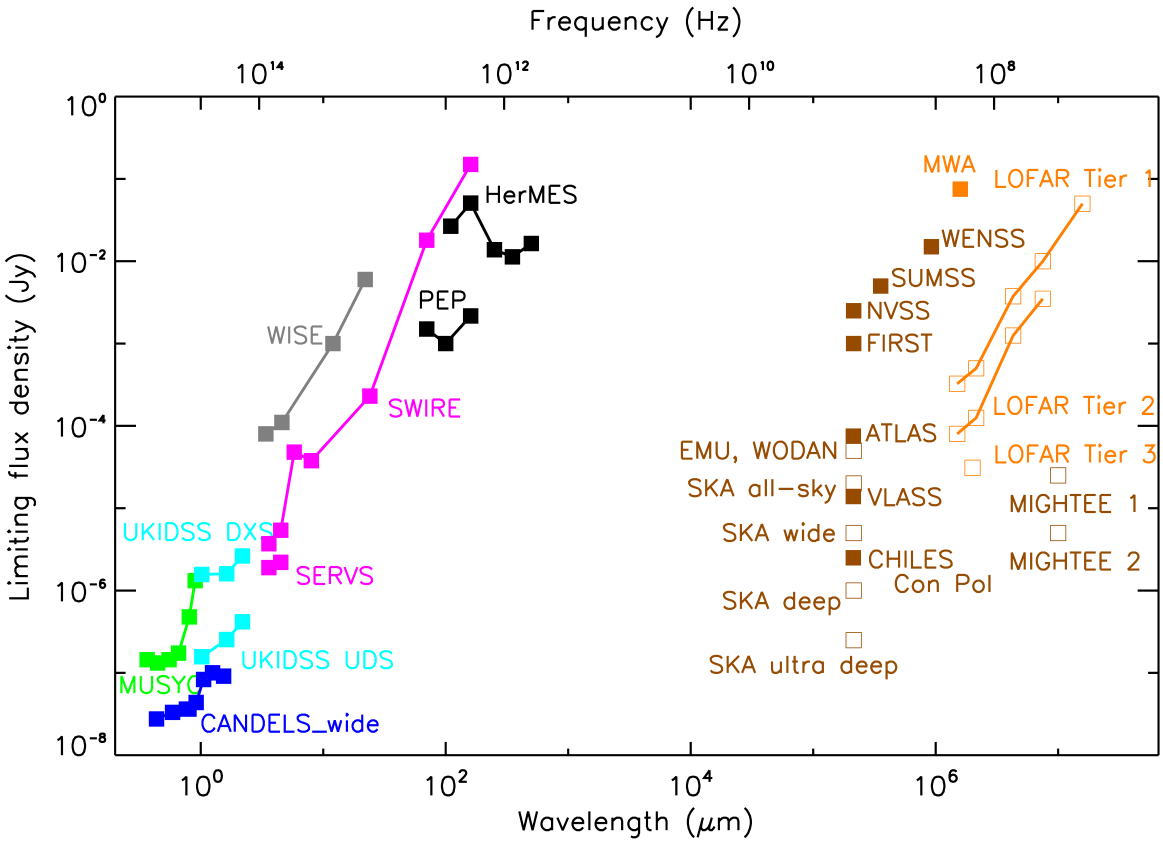

Figure 1.2: Point-source 5σ detection limit for several existing and planned astronomical surveys. From left to right: green points refer to Multiwavelength Survey by Yale-Chile (MUSYC; Gawiser et al. 2006); blue points refer to *Hubble* Cosmic Assembly Near-infrared Deep Extragalactic Legacy Survey wide (CANDLES; Grogin et al. 2011); cyan points refer to United Kingdom Infra-red Telescope (UKIRT) Infrared Deep Sky Survey (UKIDSS; Lawrence et al. 2007), in particular the Deep Extragalactic Survey (DXS[a]) and the Ultra-Deep Survey (UDS[b]); magenta points refer to *Spitzer*-based surveys, in particular the *Spitzer* Wide-area IR Extragalactic Survey (SWIRE[c]; Lonsdale et al. 2003) and the *Spitzer* Extragalactic Representative Volume Survey (SERVS; Mauduit et al. 2012); grey points refer to Wide-field Infrared Survey Explorer (WISE; Wright et al. 2010); black points refer to *Herschel*-based surveys, in particular the Photodetector Array Camera and Spectrometer (PACS) Evolutionary Probe (PEP; Magnelli et al. 2013) and the *Herschel* Multi-tiered Extragalactic Survey (HerMES; Oliver et al. 2012). Brown squares refer to completed and on-going (filled squares and name on the right) or planned (empty squares and name on the left) radio surveys, in the frequency range 0.1–3.0 GHz. From top to bottom: Westerbork Northern Sky Survey (WENSS; Rengelink et al. 1997); SUMSS (Bock et al., 1999); NVSS (Condon et al., 1998); FIRST (White et al., 1997); Australia Telescope Large Area radio Survey (ATLAS; Norris et al. 2006); EMU (Norris et al., 2011b); WODAN (Röttgering et al., 2011; Norris et al., 2013); SKA1 all-sky continuum survey (Prandoni & Seymour, 2015); VLASS (Lacy et al., 2016); SKA Wide survey (Prandoni & Seymour, 2015); Cosmological Evolution Survey (COSMOS) H I Large Extragalactic Survey Continuum Polarization (CHILES Con Pol; PI: Hales C. A.); and SKA Deep and Ultra-Deep surveys (Prandoni & Seymour, 2015). On the right, shifted for clarity but actually planned at 1.4 GHz, are reported in brown the 5σ detection limits for the MeerKAT International GigaHertz Tiered Extragalactic Exploration Tier 1 and 2 surveys (MIGHTEE; Jarvis 2012). Orange squares refer to completed and on-going (filled squares) or planned (empty squares) radio surveys, with frequencies < 0.3 GHz. From top to bottom: Murchison Widefield Array survey (MWA; Bernardi et al. 2013); low-frequency array large area (LOFAR) Tier 1, LOFAR Tier 2, and LOFAR Tier 3 surveys (Röttgering et al., 2010).

[a] http://www.ukidss.org/surveys/dxs/dxs.html
[b] http://www.ukidss.org/surveys/uds/uds.html
[c] http://swire.ipac.caltech.edu/swire/astronomers/program.html

common than previously thought (see e.g. Magorrian et al. 1998), and that the first AGN discovered were only the tip of the iceberg, i.e. the most powerful of a substantial population (see Ho 2008 for a comprehensive review on the topic). Furthermore, the extensive use of multiwavelength surveys (from radio to X-ray) allowed to discover a local and faint counterpart population of the far and powerful AGN discovered in the first decades of radio astronomy. Therefore AGN are now viewed as a common phase in the lifecycle of typical galaxies (Magorrian et al., 1998; Gruppioni et al., 2011).

Moreover, in the last decades it became widely recognised that a super-massive black hole (SMBH, $M_{BH} > 10^5\,M_\odot$) lies in the centre of virtually all galaxies with a hot spheroidal component (commonly called 'bulge'; e.g., Kormendy & Richstone 1995; Magorrian et al. 1998), and it is also widely accepted that SMBHs are the primary engine of AGN (see Sect. 1.2). Indeed, thanks to deep *Hubble*-based studies of star and gas dynamics within the bulge of galaxies, evidence were find about a tight correlation between the SMBH masses and the velocity dispersion of their host bulges (see, e.g., Ferrarese & Merritt 2000; Gebhardt et al. 2000). Besides confirming that AGN were widespread in the past, this findings highlighted how the properties of the SMBH population are linked to those of the harbouring bulge by a history of reciprocal-regulated growth feedbacks (see Kormendy & Ho 2013 for a comprehensive review on the topic).

Finally, it has been found that the history of SMBH growth (traced by the average intensity of the AGN emission) and the history of stellar mass growth within the galaxies (traced by the average star-forming activity) are so similar that some type of interplay has to be at work during the history of the Universe. This has been observed up to intermediate redshifts (e.g., Canalizo & Stockton 2001; Netzer et al. 2007; Silverman et al. 2009). A rise in both the star-formation rates and AGN accretion rates is observed or inferred since redshift $z \sim 10$ down to a redshift of $z \sim 3$ (e.g., Mannucci 2007; Silverman et al. 2008; Aird et al. 2010). Both rates peak in at redshifts $z = 3$–2 and then they decline smoothly by a factor of 10 to the present times (Shankar et al., 2009; Behroozi et al., 2013).

The separation between the communities of galaxy scientists and AGN scientists has finally started to be recomposed, and the connection between galaxies and AGN evolution exposed. However, a lot of work is still needed to reach for a comprehensive understanding about the evolution of these objects. In the last decades, indeed, a lot of new details have emerged that demand that astronomers bridge the AGN and galaxy fields. A review of relevant findings is presented below.

1.1 Galaxy bimodality

Galaxy-wise, one of the most relevant results in the past decade has been the discovery of a bimodality in the way they populate the parameter space of the stellar mass galaxy content versus the specific star-formation rate (sSFR; i.e. the star-formation rate per unit of stellar mass within the galaxy). This bimodality, discovered thanks to the Sloan Digital Sky Survey (SDSS; York et al. 2000) in the local Universe (Kauffmann et al., 2003; Baldry et al., 2004), seems to be in place at least up to redshift ~ 2.5 (Whitaker et al., 2012), where the peak of both AGN and star-forming activity took place.

As shown in Figure 1.3, there are two main galaxy populations. One population is characterised by a rough relationship between its stellar mass content and its specific star-formation rate (e.g., Brinchmann et al. 2004; Schiminovich et al. 2007; Leslie et al. 2016), and belongs to the so-called '(blue) star-forming galaxy main sequence'. In general, galaxies belonging

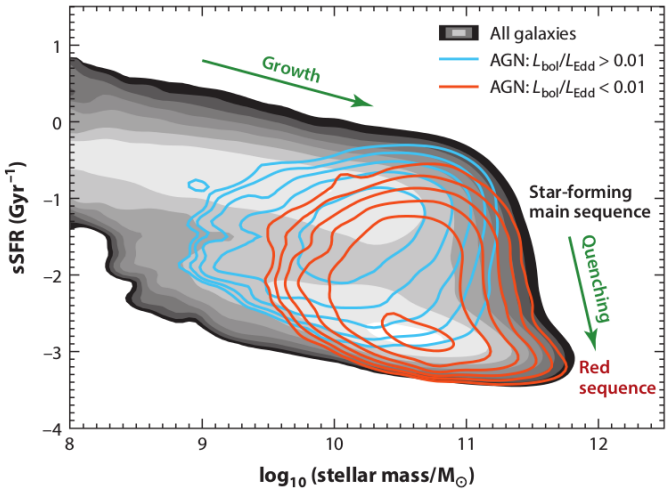

Figure 1.3: The distribution of galaxies into the plane of stellar mass content versus specific star-formation rate, for the SDSS main galaxy sample (the grey scale indicates the frequency of the galaxies, with each lighter colour shade marking a factor two increase). Galaxies gather around a main sequence of SFGs and a secondary sequence of quenched galaxies. Blue and red contours show the frequencies of AGN in high-accretion mode (Eddington ratio $\lambda = L_{Bolometric}/L_{Eddington} > 0.01$) and low-accretion mode ($\lambda < 0.01$), with contours spaced by a factor of two (see Sect. 1.2 for details). From Heckman & Best (2014).

to this sequence are characterised by specific low-to-moderate ongoing star-forming activity (Log sSFR $\gtrsim -1.5\,\mathrm{Gyr}^{-1}$; which results also in a blue colour dominance for this population), comparatively small stellar masses ($M_\star \sim 10^8$–$10^{10}\,M_\odot$), low surface stellar mass densities ($\mu_\star = 0.5\,M_\star/(\pi\,R_{50}^2) \lesssim 10^8\,M_\odot\,\mathrm{kpc}^{-2}$, where R_{50} is the radius enclosing 50% of the Petrosian flux of the galaxy), and small concentrations of their light ($ci = R_{90}/R_{50} \lesssim 3$; Deng 2013).

In contrast, the other population consists of galaxies with little ongoing specific star-forming activity (sSFR $\sim -2/-3\,\mathrm{Gyr}^{-1}$; which results in a more aged stellar population, then with redder colours), large stellar masses ($M_\star \sim 10^{10}$–$10^{12}\,M_\odot$), high surface mass densities ($\mu_\star \gtrsim 10^9\,M_\odot\,\mathrm{kpc}^{-2}$), and large concentration of light ($ci \gtrsim 2$). This second population belongs to the so-called 'red sequence'.

The discovery of this bimodality led to a new picture about the evolution of galaxies (e.g., Lilly et al. 2013; Heckman & Best 2014). Nowadays, the widespread interpretation is that the typical galaxy evolves along the blue star-forming sequence, increasing strongly in mass (through accretion of cold gas from the cosmic web and, potentially, through mergers with other galaxies) and progressively decreasing in specific star-forming activity. At some point the star-forming activity is strongly quenched and the galaxy shifts into the red sequence, where mass accretion can proceed mainly through mergers with other galaxies.

The physical processes that cause a galaxy to shift from the blue (star-forming) sequence to the red (passively evolving) sequence is unknown. A proposed scenario is that a galaxy's environment impacts the accreting flow of cold gas from the surrounding extra-galactic environment. From the dynamic point of view, this may happen as the regime of rapid accretion of cold gas from the galactic web eventually transitions into a regime of slow accretion of hot gas in hydrostatic equilibrium (Dekel et al., 2009).

However, what heats up the gas content of the galactic surroundings is still debated. One of the most popular scenario is the the so-called 'AGN negative feedback', in which the AGN-driven outflows heat up, or even disperse, the surrounding gas. This can prevent further cold accretion onto the galaxy and hence quench future star-forming activity (see, e.g., Croton et al. 2006; McNamara & Nulsen 2007; Cattaneo et al. 2009). On the other hand, the situation is not clear as examples have been found where AGN enhance star-forming activity ('AGN positive feedback'; see, e.g., Klamer et al. 2004; Gaibler et al. 2012; Zinn et al. 2013;

Karouzos et al. 2014) due to the jets emerging from the central SMBH. These jets generate shocks in the interstellar medium of the galaxy and are thought to trigger gravitational collapse of the gas clouds and induce star formation.

The idea that AGN can affect the star-formation history within the galaxy was one of the main driver that made the galaxy-AGN interplay a fundamental topic of the contemporary Astrophysics. A comprehensive understanding of the underlying mechanisms, however, is still lacking, and the main ongoing challenge in this field is disentangling AGN and star-forming activity within galaxies. Only once separated, the co-evolution of these two major components of typical galaxies can be fully analysed.

1.2 Active galactic nuclei typology

AGN-wise, the situation is at least as complex as for galaxies. The category of 'AGN' encompasses several type of objects, not all of which show the AGN-driven outflows above mentioned. What joins all these objects together is the presence of an active SMBH within the galaxy centre, which reveals itself through some type of activity that is not related to the stellar activity within the galaxy.

As always when a summary is attempted, it is useful to state beforehand that the characteristics that define AGN types are too fluid to be easily categorised, which in turn reflect the difficulty to draw firm conclusion about their nature. In Figure 1.4 is reported a schematic representation of the internal components of the AGN phenomenon, and below is reported a summarised description of the main features that define the two most-extensively studied classes of AGN.

1.2.1 Radiative-mode AGN

When the SMBH is experiencing rapid accretion (with dynamically cold accretion flows and high Eddington ratio, i.e. $\lambda = L_{Bol.}/L_{Edd.} = 0.01–1$), the AGN is called 'radiative-mode', 'cold-mode', or 'quasar-mode' AGN (see Figure 1.4, left). In these objects the energetic output is mainly in the form of electromagnetic radiation, produced by an efficient conversion of the potential energy of the gas accreted by the SMBH. Radiative-mode AGN are mostly radio-quiet (RQ), i.e. their radio emission is faint and difficult to detect (see Sect. 1.3 for details). When radio-loud (RL), they are typically associated to RL quasi-stellar objects (QSO) or Fanaroff-Riley II radio galaxies[1]. These are the AGN that fit well into the original AGN Unification Scheme (Antonucci 1993; see also Netzer 2015 and references therein).

Theoretical models show that in radiative-mode AGN (both RL and RQ), the central SMBH is surrounded by an accretion disk through which the inflow of material takes place. This accretion disk is geometrically thin, optically thick, and reaches into the radius of the innermost stable orbit (i.e. the closest orbit in which a particle can stably rotate the central BH under the general relativity regime). The total thermal continuum emission of the disk spans from the extreme UV down through the visible portion of the electromagnetic spectrum

[1]The Fanaroff and Riley (FR) classification, divides radio galaxies in two groups on the base of their large-scale radio morphology. Fanaroff-Riley type I (FR I) sources are characterised by a core-dominated radio emission (i.e., nucleus and inner jets appear brightest than their outer features). Fanaroff-Riley type II (FR II) sources, on the contrary, are characterised by edge-dominated radio emission (i.e., their radio lobes appear brightest than the inner features), and present strong emission in compact regions of the lobes, called 'hot-spots'. In general, FR II radio galaxies are more radio-luminous and more extended than their type I counterpart (see Fanaroff & Riley 1974 for details).

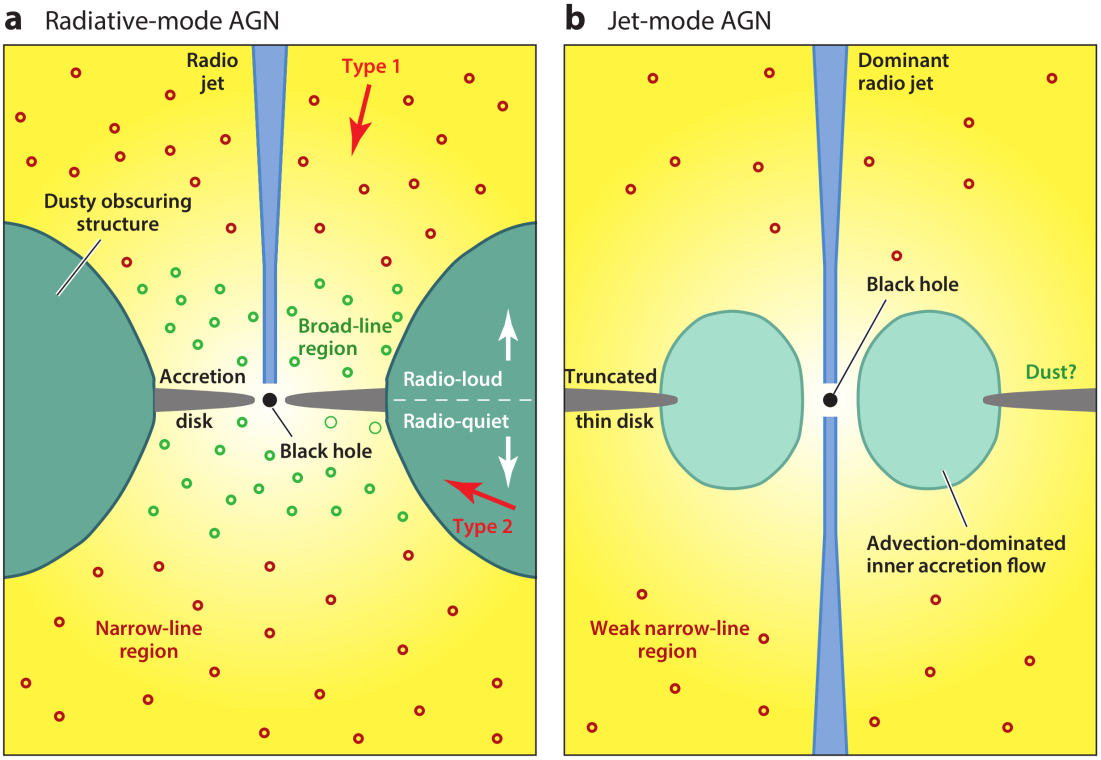

Figure 1.4: Schematic representation of the internal components of the AGN phenomenon, both for 'radiative-mode' ('cold-mode', 'quasar-mode') AGN (on the left), and for the 'jet-mode' ('hot-mode', 'radio-mode') AGN (on the right). See text for details. From Heckman & Best (2014).

due to its well-ordered temperature gradient as a function of radius of the disk. The resulting SED is a rising power-law (see Figure 1.6 and Sect. 1.4 for details).

The accretion disk is immersed in a hot corona, which scatters photons from the disk up into the X-ray regime (inverse Compton) and diffuse them in every directions. The X-ray photons which scatter back to the accretion disk are modified through fluorescence and reflection (Pounds et al., 1990; Fabian, 1999). A population of dense gas clouds orbit the central SMBH at distance scales of light-days to light-years. Radiation from the disk and corona heat and photoionise these clouds. This leads to the production of a large number of UV-, optical-, and near-IR-permitted emission lines. The velocity dispersion of the population of clouds is typically several thousand kilometres per second, leading to its designation as 'broad-line region' (BLR).

On the equatorial plane and on larger scales, the SMBH and accretion disk are encircled by a region of dusty molecular gas known as the 'dusty torus'. The inner radius of the torus is set by the sublimation temperature of the most refractory dust grains. In this region some of the incident UV/visible photons from the accretion disk and the soft X-rays from the hot corona are absorbed by the dust, and re-emitted as thermal IR emission. The characteristic rising power law in the NIR and MIR bands indicates a well ordered dependence between the dust components at different temperatures. Indeed, it is this feature that defines the so-called AGN wedge colour-colour diagram ($\mathrm{Log}(S_{5.8\,\mu\mathrm{m}}/S_{3.6\,\mu\mathrm{m}})$ vs. $\mathrm{Log}(S_{8.0\,\mu\mathrm{m}}/S_{4.5\,\mu\mathrm{m}})$; see, e.g., Lacy et al. 2001; Donley et al. 2012; and Sect. 3.6 for more details). The power-law SED supports the idea that the dust is primarily heated up by the central AGN (and not by sources which have an extended irregular spatial distribution, like numerous star-forming regions), resulting in a smooth temperature gradient from inside to outside of the dusty torus (Haas et al., 2003).

Radiation from accretion disk and BLR can escape freely along the polar axis of the obscuring structure, were more quiescent and lower-density population of clouds lies on scales of few hundred to few thousand parsecs away from the SMBH. This radiation photoionises the gas within these clouds, producing a wealth of UV-, optical-, and IR-forbidden and -permitted emission lines. The velocity dispersion of this population of clouds is of several hundred kilometres per second, and is hence called 'narrow-line region' (NLR).

The observation of a radiative-mode AGN through a line of sight close to the polar axis of the obscuring structures results in a direct view of the SMBH, of the disk/corona, and of the BLR. These objects are usually called Type 1 (or unobscured) AGN. When the observation takes place from a line of sight close to the equatorial plane of the obscuring structure, the central region is hidden, and these objects are called Type 2 (or obscured) AGN.

1.2.2 Jet-mode AGN

The second relevant class of AGN consists of objects where the SMBH is experiencing slow accretion (with gas accreted at about the galaxy virial temperature of $\sim 10^6$ K, and with low Eddington ratio, i.e. $\lambda < 0.01$). The primary energetic output from these AGN is not in the form of electromagnetic radiation[2], but in the form of kinetic energy, transported in two-sided collimated outflows (jets). These AGN are called 'jet-mode', 'hot-mode', or 'radio-mode' AGN (see Figure 1.4, right). They are mostly RL, and typically associated to FR I and II radio galaxies. When RQ, they are associated to the so-called low-ionization nuclear emission-line region galaxies (LINER), and can display small-scale radio jets (see, e.g., Heckman 1980; Laing et al. 1994).

In these objects the structure surroundings the central SMBH is simpler than what predicated by the Unification Model. The accretion disk is absent (or truncated) in the inner region, and is replaced by a geometrically thick structure in which the inflow timescale is shorter than the radiative cooling time (see, e.g., Narayan & Yi 1994; Ho 2008). These structures are called advection-dominated or radiatively inefficient accretion flows (ADAF/RIAF). In addition, they do not have the BLR and there are several indications that they do not have a dusty torus (if present, dust must be distributed in patches; see, e.g., Gonzalez-Martin et al. 2015). In jet-mode AGN no dichotomy between unobscured vs. obscured (or Type 1 vs. 2) is seen (see, e.g., Maoz et al. 2005), and there is not sign of AGN in their SED (aside for few and weak low excitation lines; see Heckman & Best 2014 for more details).

The jets are the most conspicuous feature of these class of objects, and are most easily detected at radio wavelengths due to the synchrotron emission they produce thanks to their nature of flow of plasma of particles. They can extend from parsec scales (when the emission is synchrotron self-absorbed) all the way out to scales far beyond the galaxy itself (reaching megaparsec scales in extreme cases). From the detailed study of local jets, it has been found that they travel at relativistic velocities when launched, but rapidly decelerate and destabilize through interaction with the gaseous halo surrounding the galaxy.

What it is really relevant to notice, is that radiation and matter interact differently with the surrounding medium in the two cases. 'Radiative-mode' AGN are expected to interact mainly through thermal heating of gas or radiation pressure on dust encircling the SMBH. The effect is the acceleration of this matter in a high-velocity wind, which could quench the star formation sweeping away the inter-stellar medium (ISM) within the host galaxy (see, e.g., Sturm et al. 2011; Zubovas & King 2012; Maiolino et al. 2012). In this scenario, the

[2] indeed these objects are also known as 'radiative inefficient' AGN

interaction is therefore mainly with the intra-galaxy medium, which is heated up and swept outside the galaxy.

'Jet-mode' AGN, on the other hand, are expected to interact mainly through the jets and the matter accelerated within the jets, therefore mainly with the inter-galactic medium (IGM). Observations have been presented about the presence of bubbles and cavities within the diffuse X-rays halos of clusters, groups and individual galaxies (see, e.g., Scheuer 1974b; McNamara et al. 2000; Gastaldello et al. 2009; Croston et al. 2011). In this scenario, the interaction is therefore mainly with the extra-galactic medium, which is shocked and heated up, and can result in the disruption of the galactic web feeding the galaxy.

Ongoing and future optical and IR surveys, reaching the sub-μJy regime (see Figure 1.2), are now sampling the intermediate/high-redshift ($1 \lesssim z \lesssim 4$) regime, where the peak of both AGN and star-forming activity can be analysed. The forthcoming and future deep radio surveys, like the EMU- and SKA-based ones, will keep on pace with these surveys, and will probe the majority of radio-AGN in the same interval range. The synergy between these surveys will finally disclose the interplay between galaxies and AGN, hopefully providing a full understanding of the processes that shaped the current population of objects within the Universe.

1.3 Radio-loud and radio-quiet AGN dichotomy

As mentioned in Sect. 1.2, radiative-mode and jet-mode AGN are characterised by very different energy output. This difference reflect itself also in the magnitude of the radio emission, to the point that most radiative-mode AGN are faint in radio and difficult to detect, whereas most jet-mode AGN are powerful in radio and easy to detect also at high redshift.

In the radio regime ($\lambda \gtrsim 1$ mm; $\nu \lesssim 300$ GHz), only a small fraction (10%–20%) of AGN show a powerful radio emission, 2–4 orders of magnitude greater than the radio emission from the large majority of AGN. Those AGN which radio emission is powerful are called RL AGN, while those AGN which radio emission is faint, or (especially in the past) undetected at all, are called RQ AGN. While there must be a link between radio loudness/quietness and the inner AGN structure (see Figure 1.4), RL and RQ AGN do not show a 1:1 map with it. Therefore, some additional ingredients are required to fully understand the AGN phenomenon.

The 'RL/RQ dichotomy' is an outstanding and long-lasting open question in Astrophysics research. In the following this issue is discussed following its historical evolution, up to the most recent findings. From its discovery during the first all-sky radio surveys that cross-matched to optical observations (see, e.g., Sandage 1965; Burbidge 1967), many attempts have been made to search for an underlying cause for the two types of AGN, but any attempt to disentangle it faced opposing interpretations, and recurrent re-interpretations of older analyses.

During the 1950s the first wide-sky radio surveys were published (see, for instance, the famous series of Cambridge catalogues: Ryle et al. 1950; Shakeshaft et al. 1955; Edge et al. 1959; Pilkington & Scott 1965, and following). Many of these included searches for counterparts at wavelengths other than radio to better understand the nature of those sources. Early work found that the counterparts, when found, appeared star-like in the optical and were therefore named quasi-stellar radio sources (QSS), or 'quasar' (Chiu, 1964).

The apparent physical link between star-like appearance and radio emission was a short-lived one, as in the same years Sandage (1965) discovered a large population of objects

with optical characteristics very similar to QSSs, but with no radio counterpart. Sandage named these sources quasi-stellar galaxies (QSG). A new definition was coined to encompass both these populations (while also disregarding their radio luminosity): quasi-stellar objects (QSO; Burbidge 1967).

With time, as the angular resolution of the telescopes improved, the galaxy nature of most of these quasi-stellar sources was confirmed. This made their name, QSO, which has still lasted, a mere relic of the past. Indeed, the very name 'quasar' became synonymous with QSO. The observational dichotomy in the radio emission, however, endured and more than 20 years later Kellermann introduced the definitions 'radio-loud' and 'radio-quiet' (Kellermann et al., 1989).

In his classical work, Kellermann pointed out how, despite an extensive search for radio emission in QSGs, the years among the 1960s and the 1990s saw only a marginal improvement in the detection rate of the radio counterparts of these sources. The most relevant finding of those years was the fact that only ∼10–15% of all QSOs in optically selected samples have radio counterpart down to a radio flux density limit of ∼10 mJy (Kellermann et al., 1989; Urry & Padovani, 1995). Despite sensitivity improvements, the RQ population remained largely undetected in radio surveys. Undeterred, astronomers kept searching for a still undetected substantial population sources at increasingly fainter radio fluxes.

This findings led to two different hypotheses about the RL/RQ dichotomy. The first proposal is that two distinct physical processes are at work in RL and RQ objects: one process being 10^2–10^4 times more powerful and ten times less common than the other (e.g., Kellermann et al. 1989; Baloković et al. 2012). The second proposal is that RL and RQ objects come from a common population that experiences intermittent radio emission with active periods ten time shorter than quiescent ones (e.g., Kellermann et al. 1989; Cirasuolo et al. 2003).

To test the existence of two distinct physical processes within QSOs, astronomers searched for a bimodal distribution in their radio luminosity distribution. Kellermann et al. (1989) observed with the Very Large Array (VLA) an optically complete and bright (and therefore low-redshift, $z < 0.5$) sample of QSOs, and built the first and still most widespread definitions of radio-loudness and radio-faintness based on optically-selected samples. They defined RL those sources which rest-framed ratio $R^{r.f.}_{Kel} = \mathrm{Log}(L_{5\,\mathrm{GHz}}/L_{B-\mathrm{band}}) > 1$ (see also Wilkes & Elvis 1987), and RQ those with $R^{r.f.}_{Kel} = \mathrm{Log}(L_{5\,\mathrm{GHz}}/L_{B-\mathrm{band}}) < 0$.

With time, the RL/RQ dichotomy issue was addressed from other points of view and using other selection bands, which led to several definitions for the RL/RQ classification. Most of them are based on a ratio between two luminosities, similarly to the criterion proposed by Kellermann. For instance, Terashima & Wilson (2003) proposed the criterion $R_X = \mathrm{Log}\,(\nu\, L_{5,\mathrm{GHz}}/L_{2-10\,\mathrm{keV}}) > -4.5$ to define radio-loudness, which makes use of the hard X-ray band and is then less affected by gas obscuration than the Kellermann one.

Another criterion often adopted is based on the observed infrared-to-radio ratio ($q_{24\,obs} = \mathrm{Log}(S_{24\,\mu\mathrm{m}}/S_{1.4\,\mathrm{GHz}})$), which takes into account the correlation between these two emissions in star-forming galaxies (see, e.g., Appleton et al. 2004; Sargent et al. 2010). Following this last criterion, a source is classified as radio-loud when $q_{24\,obs}$ show a radio excess, i.e. when it is smaller than the expected correlation value derived from star-forming galaxy samples or from prototypical star-forming galaxies like M82 (see e.g. Bonzini et al. 2013; and Sects. 2.2.1 and 1.5.1 for details). As discussed later in this Thesis, a recently proposed criterion, originally introduced to pinpoint IFRSs, turns out to be efficient in identifying powerful RL AGN. This criterion makes use of the observed radio-to-infrared ratio at 1.4 GHz and 3.6 μm, $R_{3.6} = S_{1.4\,\mathrm{GHz}}/S_{3.6\,\mu\mathrm{m}} > 500$ (see Zinn et al. 2011; and Sects. 1.5.3 and 4.8 for details).

Other more complex combined indices, based on more than two bands, have been proposed. Padovani et al. (2011), for instance, define RQ sources whose $R_V = \mathrm{Log}(S_{1.4\,\mathrm{GHz}}/S_{V-\mathrm{band}}) < 1.4$ and, at the same time, $L_{2-10\,\mathrm{keV}} > 10^{42}\,\mathrm{erg\,s^{-1}}$. Lacy et al. (2001) proposed a criterion fully based on the *Spitzer* infrared array camera (IRAC) bands (i.e. the infrared 3.6, 4.5, 5.8, and 8.0 μm bands). This criterion, recently revisited by Donley et al. (2012), is useful to pinpoint radiative-mode AGN (both RL and RQ) through the signature of the dusty torus surroundings the central SMBH in the infrared band (see Sect. 3.6 for more details).

Finally, other classifications rest on the radio power only. To this last category belongs the criterion proposed by Miller et al. (1990), who define a source RL when $L_{5\,\mathrm{GHz}} = \mathrm{Log}(L_{5\,\mathrm{GHz}}(\mathrm{W\,Hz^{-1}\,sr^{-1}})) > 25$ and RQ when $L_{5\,\mathrm{GHz}} < 24$ (see also Goldschmidt et al. 1999); or the criterion proposed by Hooper et al. (1995), for which a source is RL when $L_{8.4\,\mathrm{GHz}} = \mathrm{Log}(L_{8.4\,\mathrm{GHz}}(\mathrm{W\,Hz^{-1}})) > 25$ and RQ when $L_{8.4\,\mathrm{GHz}} < 25$ (see also Hooper et al. 1996); or the criterion proposed by Kellermann et al. 2016, for which a source is RL when $L_{6\,\mathrm{GHz}} = \mathrm{Log}(L_{6\,\mathrm{GHz}}(\mathrm{W\,Hz^{-1}})) > 24$ and RQ when $L_{6\,\mathrm{GHz}} < 23$. An extensive review on the topic can be found in Hao et al. (2014).

Even if Kellermann et al. (1989) claimed to have found bimodality in the QSO radio luminosity distribution, the controversy continued during the 1990s and 2000s, with some claiming it (e.g., Strittmatter et al. 1980; Ivezić et al. 2002, 2004; Zamfir et al. 2008), and other claiming only a smooth transition region between the two regimes (e.g., White et al. 2000; Lacy et al. 2001; Cirasuolo et al. 2003).

The issue of RL/RQ dichotomy is complicated by the fact that RL and RQ AGN SEDs have only subtle differences in their features from X-ray to mid-infrared (see, e.g., Sanders et al. 1989; Antonucci 1993; Elvis et al. 1994; Shang et al. 2011; and Sect. 1.4), and only show a marked difference in the measured radio excess.

Most of the RL radio emission is non-thermal, and it is linked to the presence of bipolar outflows, in the shape of powerful and extended relativistic jets (Urry & Padovani, 1995; Dunlop et al., 2003; Padovani et al., 2015a; Orienti et al., 2015). Such jets span scales up to hundred of kiloparsecs or even megaparsecs. The non-thermal emission mechanism has been recognised as synchrotron radiation, produced by a population of electrons transported in a relativistic outflows from the vicinity of the central SMBH, and is associated with the jets themselves and lobes resulting from jet interaction with the surrounding medium. Jets and lobes are therefore the most evident features in these type of objects (see, e.g., Harris & Krawczynski 2006; Kapinska et al. 2015).

While the emission mechanism in RL AGN is now well established as synchrotron radiation from energetic particles in jets and lobes, in RQ AGN the mechanism of radio emission is by far less clear (Giroletti & Panessa, 2009; Padovani et al., 2015a). RQ AGN, as stated by their name, have negligible emission in the radio part of the spectrum, and seem not to form powerful and extended relativistic jets. From the macroscopic point of view, the RL/RQ dichotomy debate is therefore associated to the existence (or not) of the jets themselves (Dunlop et al., 2003). However, while for long time it was assumed that RQ AGN were radio-silent, recent findings have shown that they are only radio-faint, and can be characterised by radio luminosity as high as $L_{1.4\,\mathrm{GHz}} \sim 10^{25}\,\mathrm{W\,Hz^{-1}}$ (e.g. Bonzini et al. 2013).

Supporters of the bimodal interpretation propose that radio emission in RQ AGN originates from star formation activity in the host galaxy (e.g., Kimball et al. 2011; Padovani et al. 2011; Bonzini et al. 2013), rather than from an AGN. This would imply radio flux levels impossible to detect with past radio surveys, and only detectable with the current ones (Bonzini et al., 2013, 2015), therefore justifying the long-lasting lack of radio counterparts for the great majority of objects. People claiming no real RL/RQ dichotomy between these two

populations argue that RQ AGN may be simply a scaled down version of RL AGN both in brightness and extension, displaying then faint and mini (i.e. galactic- or sub-galactic-scale) radio jets (e.g., Giroletti & Panessa 2009; Prandoni et al. 2010; Jarvis & Rawlings 2004).

Others propose that AGN and SF activity both contribute to the total radio emission, reassessing the key role of the AGN/galaxy interplay from the radio point of view. Seyfert 2 galaxies are a well-established example of such composite systems in the local Universe (e.g., Roy et al. 1998), and recent studies indicate that composite AGN/SF systems may constitute a significant fraction of the galaxy population at high redshifts (e.g., Gruppioni et al. 2011; Del Moro et al. 2013). Some RL AGN, moreover, are already known to harbour a strong star-forming activity (see, e.g., Rees et al. 2016).

Indeed, a significant fraction of the unresolved radio emission in RQ AGN comes from processes related to the stellar evolution, like synchrotron-emitting cosmic rays accelerated by supernovae, and thermal free-free bremsstrahlung emission from the ionized gas in star-forming H II regions. In local galaxies ($z \lesssim 0.03$), where angular resolution and sensitivity are high enough, the radio emission appears to be spread across the galaxy. Circumnuclear starburst rings (composed by several star forming regions) have been observed within Circinus Galaxy (e.g. Elmouttie et al. 1998), and within NGC 7469 and NGC 7586 (Orienti & Prieto, 2010). Even more clear is the case of the Seyfert galaxy NGC 1097, where the arcsecond scale radio emission appears to trace the profile of the host galaxy and its spiral arms (e.g., Condon 1987; Hummel et al. 1987).

The fact that the tight radio/FIR correlation found for SFGs holds also for RQ AGN, supports a scenario where a relevant part of the radio emission in RQ AGN is related to stellar processes, while the agreement is poor in RL AGN due to the contamination by the important emission of relativistic jets. The origin of the radio emission from the nucleus of RQ AGN, on the other hand, is matter of debate. In local samples, the FIR flux density has been found to better correlate with the low-resolution kpc-scale radio flux density, rather than with the high-resolution pc-scale emission from complexes of supernova remnants (Kewley et al., 2000). Therefore a dominant stellar origin for the nuclear emission has been disfavoured (see e.g. Panessa et al. 2007 and Sect. 3.4 for some details).

While the main mechanism proposed so far is synchrotron radiation from mildly relativistic mini-jets (Orienti & Prieto, 2010), a range of other hypotheses has been proposed to explain the nuclear radio emission. It has been proposed that radio emission is due to thermal free-free emission from the X-ray heated corona, or wind arising from the molecular disk (e.g. Gallimore et al. 2004); other people claim that the basic mechanism is due to a thermal cyclo-synchrotron emission by low-efficient accretion flow (like Advection-Dominated Accretion Flows –ADAF–, see e.g. Narayan & Yi 1994; or Advection-Dominated Inflow/Outflows Solution –ADIOS–, see e.g. Blandford & Begelman 1999), or, of course, a combination of the above mechanisms (Ghisellini et al., 2004).

The inconvenient truth is that, while it would be relevant to compare the properties of the two AGN classes in the radio band (where they differ the most), this is still difficult due to the gap in sensitivity between radio and optical-/IR-based surveys (Padovani et al. 2015a; Figure 1.2), which are usually used to select samples of RQ AGN. In addition, separating star-formation and accretion components is difficult at radio wavelengths for objects without obvious large-scale jets. Therefore, multiwavelength data is often used to help disentangling these two processes (White et al., 2015).

Nowadays, the nuclear radio emission of RQ AGN has been investigated mainly in nearby objects, and the RL/RQ dichotomy has been addressed mainly through multi-band

analyses. For instance, an empirical correlation has been found between radio and X-ray nuclear luminosities, suggesting a strong coupling between accretion flow and radio emission, the same type of correlation that has been found for RL AGN which radio emission is well known to be related with BH accretion-driven relativistic jets (see e.g. Panessa et al. 2007).

In low-redshift RQ AGN ($0.025 \lesssim z \lesssim 0.3$), high-resolution imaging (Very Long Baseline Interferometry –VLBI– based, parsec scales) obtained for some objects revealed the presence of non-thermal emission from jet-like structures (e.g. Nagar et al. 2002), and in several objects double or triple radio structures have been resolved on scales of a few kilo-parsecs (see, e.g., Blundell & Beasley 1998; Kukula et al. 1998; Ulvestad et al. 2005). On the other hand, in most low-redshift RQ and radio-intermediate (i.e., with radio excess in between RQ and RL ones) AGN, the radio sources remain unresolved or (at best) marginally resolved, even at VLBI resolution scales. Therefore, the resolved samples are too sparse to be of any significant statistical value. In these samples the brightness temperatures (or their lower limits) are $T_B \gtrsim 10^6$ K, suggesting that the radio emission cannot be produced by a starburst (Wang et al., 2006; Cirasuolo et al., 2003).

On the other hand, the study of non-local RQ AGN is difficult due to the weakness of these objects. Poor resolution and insufficient surface brightness sensitivity in the radio band prevented comprehensive studies of RQ AGN, and disentangling the AGN-related emission from the stellar contribution is a hard task to perform. If resolution and sensitivity are not adequate, indeed, the nuclear component may be washed out by the star-formation related emission, and the radio properties may be polluted by the contribution from different components. So it is not surprising that several authors have concluded that radio emission in these sources is due to starburst phenomena, i.e. the mechanism involved would be thermal emission from SNRs in very dense environment (Terlevich et al., 1992; Cirasuolo et al., 2003).

At the moment, VLBI observations are the most effective in detecting compact components with high brightness temperatures (above 10^6 K) and with high core dominance (i.e., with high ratio between milliarcsecond and arcsecond flux densities). However, no complete radio-selected sample of RQ AGN has been investigated so far with such high resolution, and extensive VLBI-based surveys are still in their early days (see, e.g., Middelberg et al. 2011a; Herrera-Ruiz et al. in prep.; Herrera-Ruiz PhD Thesis).

Only future, high-sensitivity deep radio surveys (like EMU and those proposed for the SKA) will be able to probe RQ AGN in samples of statistical significance (see, e.g., Jarvis & Rawlings 2004). Even more interesting, these future surveys will produce radio-selected samples, which will not be affected by obscuration by dust and neutral Hydrogen, contrasting dramatically with optical- and X–ray-selected samples, based on which the great majority of studies undertaken so far are. SKA will also provide sub-arcsec resolution at frequencies $\gtrsim 1$ GHz, allowing to trace sub-kpc and kpc-scale radio emission in RQ AGN. This together with VLBI follow-ups should help in getting a complete view of RQ AGN from a radio perspective.

1.4 Spectral energy distribution

A powerful way to classify galaxies from the point of view of the energy output is through their so-called spectral energy distribution (SED), i.e. the way the flux density from the objects spreads with respect to the frequency (or wavelength) of the radiation spectrum. As described below, low-redshift galaxies are classified into three main categories, depending on the dominant activity within them, which in turn affects the SED of the galaxy.

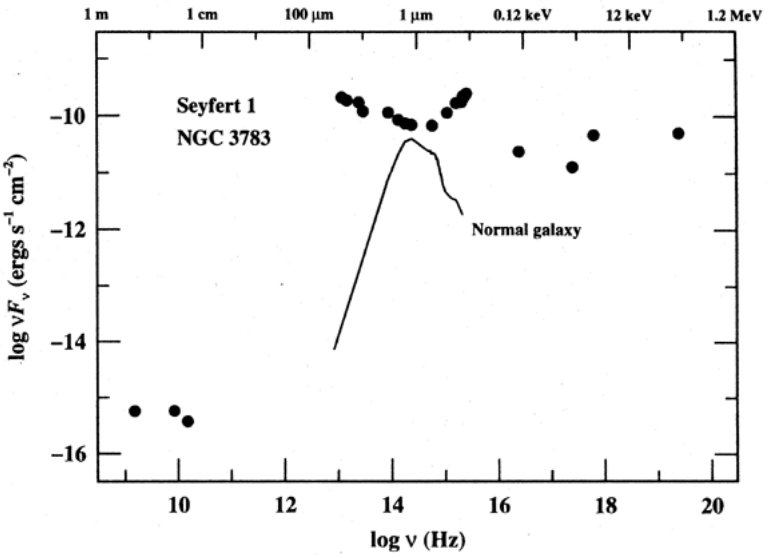

Figure 1.5: Comparison (from radio to γ-ray energies) between the SED of the Seyfert 1 galaxy NGC 3783 (a radio-quiet AGN) and the template spectrum of a normal spiral galaxy. From Peterson (1997).

When the SED of an object is dominated by thermal emission mechanisms, notably stellar light (with a single prominent peak in the near-infrared –NIR–), the object is classified as 'normal galaxy' (see Figure 1.5). The radio emission in normal galaxies is very weak and it is mainly due to relativistic cosmic-ray electrons accelerated by shocks from supernovae in sparse supernova remnants (SNR), and to free-free bremsstrahlung emission from rare H II regions. The great majority of galaxies are classified as normal, and the very galaxy within which we live belongs to this category.

When the SED is again dominated by thermal emission mechanisms, but with two notable peaks produced by the stellar light (in the NIR) and by the dust (which produces an even more prominent peak in the far-infrared –FIR–), the object is classified as 'star-forming galaxy' or 'star-burst galaxy' (SFG or SBG, depending on the intensity of this ongoing activity; see Figure 1.6, light-grey track). The radio emission in these objects is due to relativistic cosmic-ray electrons accelerated by shocks from supernovae in copious SNRs, and to free-free bremsstrahlung emission from massive and widespread H II regions. These objects were typically more frequent in the past ages of the Universe.

The rest of galaxies belongs to the class of 'active galaxies', and their SED is dominated by non-stellar emission mechanisms. The SED of active galaxies is wider than the one of non-active galaxies, with contributions that may be very relevant at radio and high-energies bands, and it overcomes the SED of non-active galaxies over most of the electromagnetic spectrum (see Figures 1.5 and 1.6).

After decades of study, it has been concluded that the SED of active galaxies is dominated by the activity of the central SMBH and of its immediate surroundings. SMBHs can be active or quiescent. When active, their energy emission overcomes the thermal emission from the rest of the galaxy within which they lie from the IR to the highest energies, from which the name of 'active' galaxy. Given that the ultimate engine of energy emission in active galaxies is the activity within their nuclei, they can be called by extension 'active galactic nuclei' (AGN). When SMBHs are inactive (or quiescent), like the SMBH at the centre of our own galaxy, the Milky Way (Genzel et al., 1997), they are retained as relic of past and extincted AGN which built them up (e.g., Yu & Tremaine 2002; Aller & Richstone 2002; Gruppioni et al. 2011), and the thermal emission from the stellar population or from the ongoing star-forming activity dominate the galaxy. The galaxy is hence named as 'normal' or 'star-forming'.

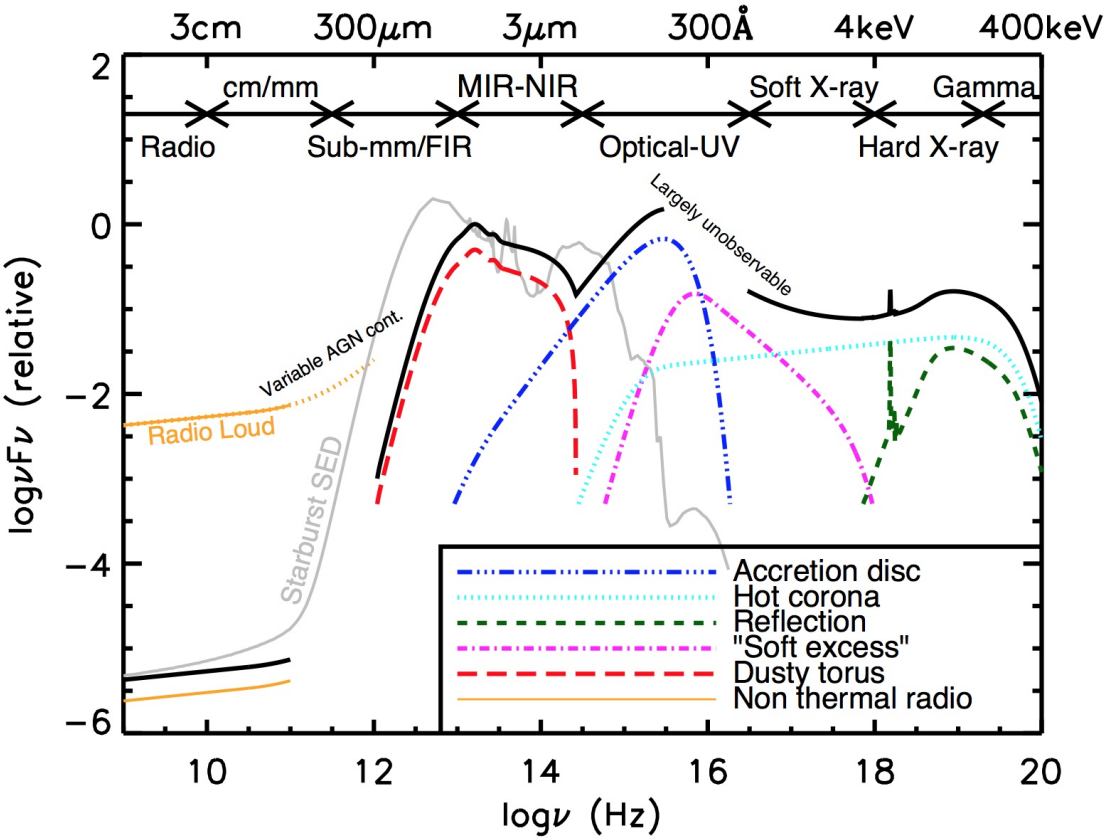

Figure 1.6: Schematic representation of the SED of radio-loud and radio-quiet AGN, loosely based on the observed SEDs from Elvis et al. (1994); Richards et al. (2006) and other. The black solid curve represents the total SED, while the various coloured curves (arbitrarily offset) represent the individual components. In the mm-FIR regime the SED is uncertain due to the various potential sources (AGN and star-forming activity), but it is commonly believed that the AGN contribution to the overall SED of a galaxy is minimal when compared to SF contribution, except for the most intrinsically luminous quasars and powerful RL AGN. RL AGN have radio emission that can be several orders of magnitude higher than RQ AGN (both shown with orange lines). The grey curve shows the SED of M82, from radio to ultra-violet (UV), taken from the Graphite and Silicate (GRASIL) library Silva et al. (1998), as an example of prototypical SBG. From Harrison (official web page).

The energy source of AGN is gravitational in nature, and is basically triggered by accretion of matter onto the central SMBH (see, e.g., Lynden-Bell 1969; Urry & Padovani 1995; Canalizo & Stockton 2001; Richards et al. 2006). Following the well-known Unification Model (Antonucci, 1993), all the matter pulled toward the BH arranges itself in an accretion disk, within which it loses angular momentum through viscous and/or turbulent processes before to be swallowed up by the central object. The (still not well understood) interplay between infalling matter, emerging radiation, BH spin and magnetic phenomena affects the final accretion rate of the BH, and the duty cycle of the AGN (i.e., the relative times spent by the SMBH into active and quiescent phases).

This simplified model explains fairly well the main features of the radiative-mode AGN spectra from X-ray to sub-millimetre wavelengths, and the continuum in each spectral region can be ascribed to distinct energy generation mechanisms. At least four are the distinct mechanisms thought to be at work within this type of AGN (Urry & Padovani 1995; see Figure 1.6).

In the gamma/hard X-ray regime ($E_\gamma \gtrsim 2\,\mathrm{keV}$; $\lambda \lesssim 0.6\,\mathrm{nm}$; $\nu \gtrsim 4.8 \times 10^{17}\,\mathrm{Hz}$) the AGN

spectrum is typically a more or less flat power-law (Kawaguchi et al., 2001; Mainieri et al., 2007), and the emission mechanism is ascribed to inverse Compton on photons emerging from the disk, by a hot and optically thin corona mainly composed by a plasma of electrons (Urry & Padovani, 1995) which surrounds the central BH (see, e.g., Haardt & Maraschi 1991; Haardt et al. 1994).

Moving from the soft X-ray regime ($E_\gamma \sim 0.1$–$2\,\mathrm{keV}$; $\lambda \sim 10.0$–$0.1\,\mathrm{nm}$; $\nu \sim 3 \times 10^{16}$–$3 \times 10^{18}\,\mathrm{Hz}$) towards the UV-optical regime ($\lambda \sim 0.7$–$0.01\,\mu\mathrm{m}$; $\nu \sim 4 \times 10^{14} - 3 \times 10^{16}\,\mathrm{Hz}$), the thermal emission from the Compton thin plasma composing the hot corona is replaced by the so called 'big blue bump'. Towards its extreme UV end ($\lesssim 0.1\,\mu\mathrm{m}$) a spectral break marks its edge (Zheng et al., 1997; Shang et al., 2005), while at the other end (at $\sim 1\,\mu\mathrm{m}$) it is limited by the 'near-infrared inflection' (Elvis et al., 1994; Richards et al., 2006). This feature, where the AGN emission reaches its peak, is ascribed to thermal emission from the accretion disc immediately surroundings the central SMBH (Shields, 1978), and is rich in emission lines (Vanden Berk et al., 2001; Telfer et al., 2002).

In the IR regime ($\lambda \sim 350$–$0.7\,\mu\mathrm{m}$; $\nu \sim 8.6 \times 10^{12}$–$4 \times 10^{14}\,\mathrm{Hz}$) there is a 'mid-infrared bump', limited by the 'near-infrared inflection' (at $\sim 1\,\mu\mathrm{m}$; Elvis et al. 1994) and by the so called 'mm-break' at its millimetre edge (Elvis et al., 1994). This ubiquitous feature is ascribed to the dusty torus surroundings the central SMBH, heated up by the nuclear radiation to temperatures in the range $T \sim 50$–$10^3\,\mathrm{K}$ (Neugebauer et al., 1979; McAlary & Rieke, 1988; Sanders et al., 1989). Its orientation with respect to the Earth line of sight is thought to be the cause of the distinction between Type 1 and Type 2 quasars (i.e., unobscured or obscured objects).

In fact, the SED of AGN are all pretty similar from X-ray to sub-millimetre wavelengths, which is interpreted as clear sign of a common central engine. However, the reported SED-based classification has been mainly built on radiative-mode AGN (e.g., Richards et al. 2006), and jet-mode AGN population tends to escape this simplified scheme. Indeed, in radiatively inefficient AGN, dusty torus and BLR are missing while the accretion disk is geometrically thick (see Sect. 1.2.2 for more details), and its emission is dominated by non-thermal dynamics (see, e.g., Blandford & Begelman 1999; Begelman 2012).

Therefore the Unification Model (Antonucci, 1993), which provides a very good schematic description of radiatively efficient AGN, fails to describe radiatively inefficient AGN. The SED of jet-mode AGN is usually dominated by the SED of the hosting galaxy (typically a quiescent early type galaxy), and can be very difficult to separate these two components. Usually, the main AGN feature within these objects is the presence of an excess of radio emission, which classifies them as radio-loud.

1.5 Infrared-faint radio sources: a new class of high-redshift RL AGN?

Deep radio surveys, like the ones expected to be delivered by ASKAP and SKA, are promising not only to analyse RQ AGN and the low-luminosity tail end of the RL AGN distribution, but also to discover high-redshift ($z \gtrsim 2$–3) powerful RL AGN. Indeed, it is expected that these sources have flux densities in the mJy or sub-mJy regime. On the other hand, these objects are rare and sparse, and high sensitivity has to be coupled with wide-field observations (like the one of the EMU survey; Norris et al. 2011b) to discover these objects in statistically meaningful samples. However, this also rise the problem to effectively recognise these sources among the millions that these surveys are expected to deliver.

During the years, several criteria have been developed to pinpoint RL AGN at high redshift. One of the most used relies on the steepness of the radio spectra ($\alpha < -1$, see Sect. 1.7 about the convention adopted; see e.g. Afonso et al. 2011). Recently, a new class of RL AGN has emerged from deep radio surveys, the one of the infrared-faint radio sources, which is exposed in the follow.

1.5.1 Discovery and first hypotheses

Infrared-Faint Radio Sources (IFRS) are a relatively new class of rare objects first identified by Norris et al. (2006) and Middelberg et al. (2008a) in the *Chandra* Deep Field-South (CDFS) and in the European Large Area ISO Survey-South 1 (ELAIS-S1) fields, respectively. They were serendipitously discovered during the cross-matching of the deep ($S_{1.4\,\mathrm{GHz}} \gtrsim 50$–$100\,\mu$Jy) radio Australia Telescope Large Area Survey (ATLAS; Norris et al. 2006; Middelberg et al. 2008a), with the *Spitzer* Wide-area IR Extragalactic Survey (SWIRE[3]; Lonsdale et al. 2003). The main scientific aim of cross-matching multiwavelength surveys such as ATLAS and SWIRE is to understand the formation and evolution of galaxies in the early universe, and radio and IR observations are complementary in recognising when a source is a SFG or an AGN.

It is well know that in SFGs the radio emission is strongly correlated with the FIR through the relations:

$$q^{\mathrm{SFG}}_{24\,\mu\mathrm{m}} = \log \frac{S_{24\,\mu\mathrm{m}}}{S_{1.4\,\mathrm{GHz}}} = 0.84 \pm 0.28$$

$$q^{\mathrm{SFG}}_{70\,\mu\mathrm{m}} = \log \frac{S_{70\,\mu\mathrm{m}}}{S_{1.4\,\mathrm{GHz}}} = 2.15 \pm 0.16$$

(see Appleton et al. 2004; Boyle et al. 2007; Mao et al. 2011), where S is the flux density of the source.

SFGs are therefore expected to have 1.4 GHz flux densities slightly greater or about equal to the 24 μm flux densities, and more than hundred times lower than the 70 μm flux densities. Radio galaxies and RL AGN in general, on the other hand, depart very strongly from these relations, with 1.4 GHz flux densities that can be tens or hundreds of times the 24 and the 70 μm IR flux densities ($q^{\mathrm{RL\,AGN}}_{24\,\mu\mathrm{m}} \ll 1$ and $q^{\mathrm{RL\,AGN}}_{70\,\mu\mathrm{m}} \ll 1$; see, e.g., Bonzini et al. 2013, Seymour et al. 2009). This behaviour is a direct consequence of the contribution of the AGN in the radio band, which strongly dominates over the star formation activity. RQ AGN have similar $q_{24\,\mu\mathrm{m}}$ values to SFGs, as they are characterised by no or very small radio excesses (see Chapters 2 and 3).

All the ATLAS sources (1σ sensitivity limits of about 40 μJy) were expected to have a counterpart in the sensitive SWIRE survey (1σ sensitivities of 0.74, 1.08, 9.6 and 7.56 μJy in the four IRAC bands, respectively; and of 46 μJy in the 24 μm multiband imaging photometer for *Spitzer* –MIPS– band). More specifically this was expected for all extragalactic radio sources with $z \lesssim 2$ belonging to any known class of objects, regardless the radio power triggering mechanism (AGN or SF), and for any reasonable dust-obscuration value and evolutionary model (Norris et al. 2006, 2011a).

However, 22 radio sources in CDFS (representing ~3% of the sample; Norris et al. 2006) and 29 radio sources in ELAIS-S1 (~2% of the sample; Middelberg et al. 2008a) were found

[3] http://swire.ipac.caltech.edu/swire/swire.html

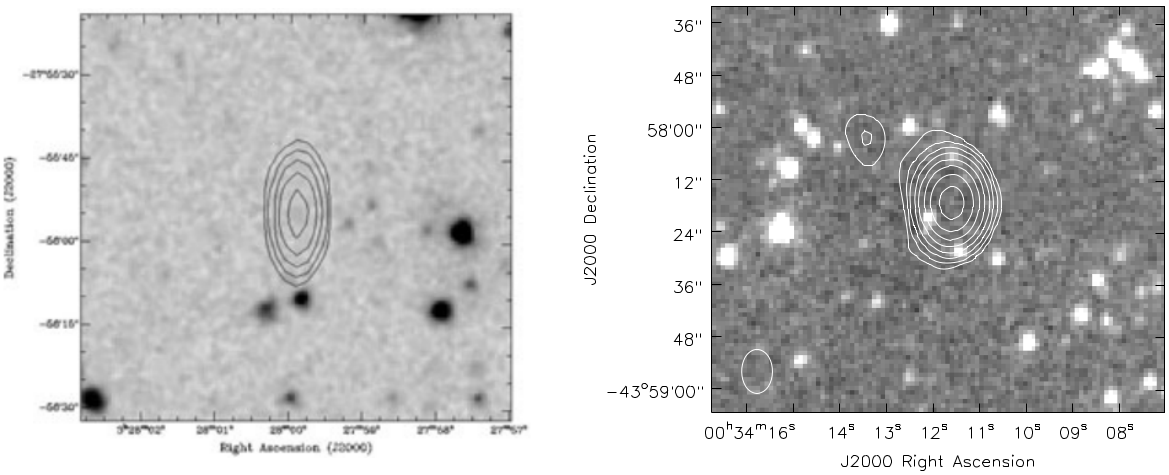

Figure 1.7: Three IFRSs from the original catalogues by Norris et al. (2006) and Middelberg et al. (2008a). (*Left*) CS0114 in the CDFS; radio contours at 0.5, 1.0, 2.0, 3.0 and 4.0 mJy from ATLAS survey are superimposed to a SWIRE 3.6 μm image in grey-scale (Norris et al., 2007b). (*Right*) ES0427 (central source) and ES0433 (two-contour object north-east of ES0427) in ELAIS-S1; radio contours at 0.1, 0.2, 0.4, ... mJy are superimposed to a SWIRE 3.6 μm image; in the bottom-left corner of the image is the synthesised beam (Middelberg et al., 2008b).

to have no counterpart down to the SWIRE detection limit at any band (see Fig. 1.7 for three examples). The unmatched ATLAS radio sources span a wide range of 1.4 GHz flux densities (from some tenths mJy to more than 20 mJy). Statistically unusual noise peaks or imaging artifacts could explain the weakest objects, but the reality of the detections stronger than 1 mJy was hardly questionable and a SWIRE counterpart was expected.

These sources showed a radio-to-IR flux density ratio (computed based on the average detection limit of SWIRE) of the order of 100 or above, sign of radio sources particularly bright with respect to the host galaxy. These unexpected objects were called 'infrared-faint radio sources' according to this prominent feature, and their first characterisation was simply related to the utter lack of IR counterparts in the SWIRE survey (Norris et al., 2006; Middelberg et al., 2008a).

A first attempt to quantify the average IR flux of these sources was performed by Norris et al. (2006). They stacked the SWIRE images for the 22 IFRSs (and for the subsample of the 8 radio-brightest among them, to avoid any possible contamination from artifacts) in the CDFS field, in all the IRAC bands (3.6, 4.5, 5.8 and 8.0 μm) and in the 24 μm MIPS band, but no signal was detected, implying a mean IR flux density for these objects well below the SWIRE sensitivities (e.g., $\overline{S}_{3.6\,\mu\mathrm{m}} \lesssim 0.5\,\mu$Jy[4], and $\overline{S}_{24\,\mu\mathrm{m}} \lesssim 30\,\mu$Jy for the whole sample of 22 sources; $\overline{S}_{3.6\,\mu\mathrm{m}} \lesssim 0.8\,\mu$Jy, and $\overline{S}_{24\,\mu\mathrm{m}} \lesssim 50\,\mu$Jy for the subsample). Such low IR upper limits excluded that these sources could simply belong to the dim tail of the distribution of usual classes of objects, at the same time implying that they have unusual IR properties.

Garn & Alexander (2008) found another sample of 14 IFRSs cross-matching the 610 MHz Giant Microwave Radio Telescope (GMRT; Garn et al. 2007) and the 1.4 GHz VLA (Condon et al., 2003) surveys with the *Spitzer* extragalactic First Look Survey (xFLS; Lacy et al. 2005). Besides confirming the existence of such type of sources in an independent field, they derived two-point spectral indices and found a uniform distribution between 0.0 and −1.4 (from flat to ultra steep spectrum), possibly a hint of a population of composite nature.

[4]The symbol $\overline{\ }$ is used to represent the statistical operation of mean, as the symbol $\tilde{\ }$ of median.

Garn & Alexander (2008) also stacked the IRAC xFLS images at 3.6, 4.5, 5.8 and 8.0 μm, and found a slight increase in the stacked flux density at 3.6 and 4.5 μm, but no emission at all at 5.8 and 8.0 μm. Constraining the SEDs of known objects with these IR upper limits and radio measures, they concluded that IFRSs are probably at high and very high redshifts ($z \gtrsim 2$–4). Garn & Alexander (2008) took also into account the MIPS sensitivity limits in the xFLS survey (0.21 mJy at 24 μm, and 10 mJy at 70 μm), and computed $\widetilde{q}_{24\,\mu\mathrm{m}} < -0.7$ and $\widetilde{q}_{70\,\mu\mathrm{m}} < 1$, well below the typical values derived for SFGs by Appleton et al. (2004).

The nature of such sources was hard to determine because nearly all information about them was obtained at radio wavelengths. No IR detections nor optical counterparts were found, so local ($z \lesssim 2$) SFGs and AGN could be excluded. Those sparse constraints led inevitably to a very extended first set of hypotheses:

- High-redshift RL galaxies (Norris et al., 2006);
- SFGs or AGN in a transient phase in which electrons are producing radio emission, but there is insufficient dust to produce detectable IR emission (Norris et al., 2006);
- SFGs or AGN at extremely high redshift, or with extreme dust extinction, or a combination of distance and obscuration, so that all their IR emission is radiated beyond 24 μm, making these sources undetectable by *Spitzer* (Norris et al., 2006);
- Radio lobes or hotspots of nearby radio sources unrecognised as such (Norris et al. 2006, 2011a);
- A population of high latitude Galactic Pulsars (Cameron et al., 2011);
- A new class of exotic Galactic or extragalactic objects, like e.g. dust-poor dwarf galaxies hosting a RL AGN at moderate redshift.

The results found by Norris et al. (2006) and Garn & Alexander (2008) at 24 μm ($q_{24\,\mu\mathrm{m}} \lesssim -0.4$) highlight how strongly IFRSs depart from the classical MIR-radio correlation for SFGs. This suggested from the very beginning a possible AGN-driven radio emission (Norris et al., 2006; Garn & Alexander, 2008; Zinn et al., 2011). Moreover, the extreme $R_{3.6} = S_{1.4\,\mathrm{GHz}}/S_{3.6\,\mu\mathrm{m}}$ ratios (typically $\gtrsim 10^2$) put them in the upper tail of the AGN regime ($R_{3.6} \sim 10^{-1} - 10^{+3}$; Middelberg et al. 2011a).

IFRS searches were later extended to the SWIRE ELAIS-N1 field by Banfield et al. (2011), which made use of the Dominion Radio Astrophysical Observatory (DRAO) 1.4 GHz survey (Taylor et al., 2007; Grant et al., 2010; Banfield et al., 2011). As for the previous samples, the classification in this field was done searching for radio sources without any SWIRE counterpart. The final ELAIS-N1 sample consists of 18 sources, with radio flux densities covering the range between ~ 1 and ~ 360 mJy. The total number of catalogued IFRSs at that time reached therefore the amount of 83.

1.5.2 Early follow-up studies

A first attempt to get more insights on the nature of these objects was carried out by Norris et al. (2007b) and Middelberg et al. (2008b) through the VLBI technique. They both made use of the Australian LBA to investigate 6 IFRSs, at 1.4 and/or 1.6 GHz.

Norris et al. (2007b) targeted the ATLAS sources CS0114 (ATCDFS J032759.89-275554.7) and CS0194 (ATCDFS J032928.59-283618.8) in the CDFS, at 1.6 GHz. CS0194 was undetected, implying that the ATLAS arcsec-scale detection was dominated by an emission

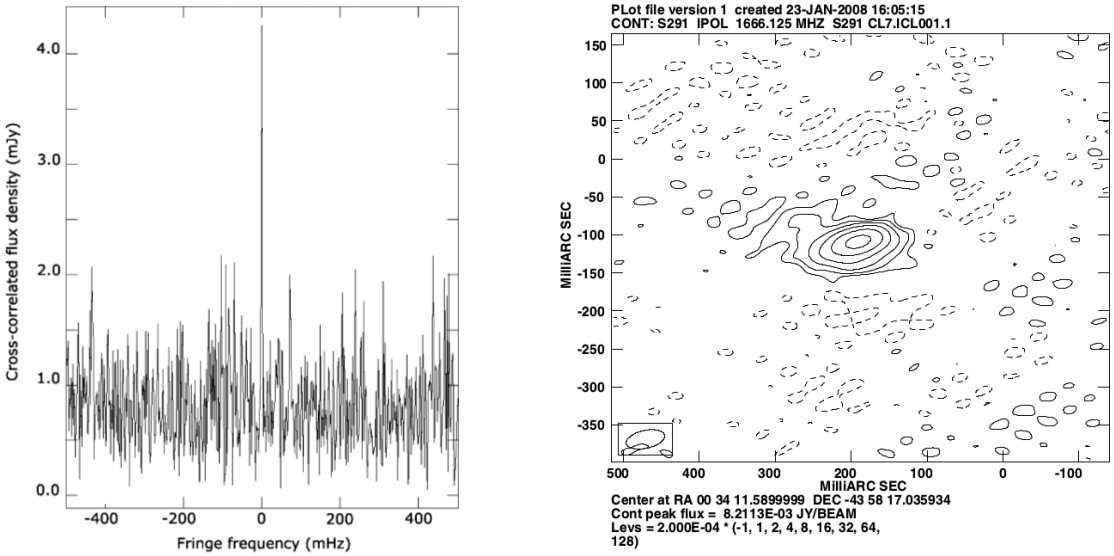

Figure 1.8: LBA detections of IFRSs. (*Left*) Fringe rate spectrum on the Parkes–Narrabri baseline of CS0114 in the CDFS; the source was too weak to be imaged but the correlated flux density was clearly detected on several baselines (Norris et al., 2007b). (*Right*) Contour plot for ES0427 in ELAIS-S1; radio contours are drawn at $(-1, 1, 2, 4, ...) \times 0.2$ mJy, and the restoring beam is 51.7×23.6 mas^2 (Middelberg et al., 2008b).

coming from an extended region, whereas any compact core was below the VLBI sensitivity. On the contrary, CS0114 was detected on several baselines, with the same flux density on all of them (~ 5 mJy, about the 70% of the ATLAS arcesc-scale flux density of 7.17 ± 1.43 mJy; see Fig. 1.8, left). At the baselines involved in the detection, this result implies a core emission with size smaller than 0.03 arcsec, corresponding to a linear size ≤ 260 pc at any redshift.

Middelberg et al. (2008b) observed four IFRSs in the ELAIS-S1 field, at 1.4 and 1.6 GHz: ES0427 (ATELAIS J003411.59-435817.0), ES0509 (ATELAIS J003138.63-435220.8), ES0433 (ATELAIS J003413.43-435802.4) and ES0775 (ATELAIS J003216.05-433329.6). ES0427 was detected with a good Signal-to-Noise ratio (S/N ~ 60), while the remaining sources were undetected. ES0427 has an ATLAS arcsec-scale flux density of 21.36 ± 1.07 mJy, and the LBA observation recovered 58% of it from a linear size smaller than 0.41 arcsec, and 33% of it from a linear scale smaller than 0.032 arcsec (see Fig. 1.8, right), corresponding to a linear size $\lesssim 270$ pc at any redshift.

Such results both imply a brightness temperature $T_B > 10^6$ K. The high brightness temperature reasonably dismisses any thermal mechanism and strongly supports an AGN mechanism for the radio emission.

More interestingly, Middelberg et al. (2008b) collected information for ES0427 at five different frequencies: 843 GHz from SUMSS (Mauch et al., 2003), 1.4 and 2.4 GHz from ATLAS and its follow-up (Zinn et al., 2012), and 4.8 and 8.6 GHz from dedicated ATCA observations (Middelberg et al., 2008b). They fitted these five spectral points with a power-law function with exponent -1.31 ± 0.07. Such steepness over a magnitude in frequency rules out star formation as major contributor to the radio emission (which is expected to produce a spectral index of about -0.7 – -0.8), and strengthened the hypothesis of an AGN harboured by ES0427.

In the range $z = 1$–7, $S_{1.4\,\mathrm{GHz}} \sim 21.36$ mJy implies a radio power of $L_{1.4\,\mathrm{GHz}} \sim 10^{26}$–$10^{28}$ W Hz^{-1}. Such radio powers are typical of powerful radio galaxies, of type FR II, but

the linear size ($\lesssim 24$ kpc as derived by the ATLAS data) is a few times smaller than the typical FR I size, typically smaller than the FR II. Moreover, a high concentrated emission (~ 7 mJy within ~ 270 pc) is quite unusual for a FR tout-court, objects typically dominated by extended radio emission. On the other hand, the very steep spectrum rules out BL-Lacs and Blazars sources, characterised by flatter spectra. Middelberg et al. (2008b) concluded that ES0427 could be a compact steep-spectrum (CSS) source. These sources typically have spectral indices steeper than -0.5 in the GHz range, are smaller than 20 kpc, and have $L_{1.4\,\mathrm{GHz}} \gtrsim 10^{25}$ W Hz^{-1} (O'Dea, 1998)[5].

Huynh et al. (2010) also tried to constrain the SEDs of IFRSs in the Extended *Chandra* Deep Field-South (ECDFS). They searched for optical/NIR counterparts in several surveys: Great Observatories Origins Deep Survey-South (GOODS-S; Giavalisco et al. 2004), Galaxy Evolution from Morphologies and SEDs (GEMS; Rix et al. 2004), and MUSYC (Gawiser et al., 2006). Moreover, they searched for X-ray counterparts on *Chandra* data (Luo et al., 2008). Their IFRS SED modelling can be accounted by a 3C 273-like object lying at redshift $\gtrsim 2$–4. The constraints they found are in good agreement with a scenario of IFRS population mainly composed by RL AGN at high redshift ($z \gtrsim 2$).

Middelberg et al. (2011b) imaged a sample of 18 IFRSs in CDFS and ELAIS-S1 fields using ATCA, at 4.8 and 8.6 GHz. They also searched for counterparts in the 843 MHz SUMSS catalogue (9 counterparts) and in the VLA Low-Frequency Sky Survey data (VLSS, only upper limits available; Cohen et al. 2007). Finally, they joined these data with ATCA 1.4 GHz (Norris et al., 2006; Middelberg et al., 2008a) and 2.3 GHz data (Zinn et al., 2012) to increase the number of spectral points. They extended their previous work (Middelberg et al., 2008b) computing four/five points spectral indices.

Middelberg et al. (2011b) found values in the range $\alpha = -0.76 - -2.38$, with a median value of -1.08. Computing spectral indices between pairs of frequencies they also found a steepening, with median value shifting from $\widetilde{\alpha}^{2.3}_{1.4} = -1.40$ to $\widetilde{\alpha}^{8.6}_{4.8} = -1.53$. They interpreted this steepening as an effect of synchrotron losses, due to a recent shut down or weakening of the central AGN engine in some sources. This interpretation strengthen the IFRSs identification as CSSs, because this class of objects can show a change in spectral slope at frequencies of 1 to 10 GHz (Readhead et al., 1996).

Middelberg et al. (2011b) also compared the spectral indices $\alpha^{2.3}_{1.4}$ of several populations of objects in ELAIS-S1 field (see Fig. 1.9, left). For the whole population they found a median $\widetilde{\alpha}^{2.3}_{1.4} = -0.86$, and for the sub-sample of AGN a median $\widetilde{\alpha}^{2.3}_{1.4} = -0.82$. The difference with respect to the IFRS population ($\widetilde{\alpha}^{2.3}_{1.4} = -1.45$) suggests some peculiar properties of this class of objects, possibly related with its IR faintness.

Banfield et al. (2011) also searched for the spectral indices of the ELAIS-N1 sample, cross-matching the DRAO catalogue with the 325 MHz WENSS survey (Rengelink et al., 1997). They found a counterpart for 7 sources, with a median $\widetilde{\alpha}^{1.4}_{0.325} = -1.29$. For the other 11 sources they found only lower limits, typically with $\alpha^{1.4}_{0.325} > -1.50$.

The extreme characteristics of IFRSs led to link this population with two other exotic classes of objects. Norris et al. (2006) and Garn & Alexander (2008) highlighted a possible relation with the so-called optically-invisible radio sources (OIRS), likely a class of high redshift AGN, even if the IFRS class must have more extreme IR flux density damping. OIRSs were highlighted by Higdon et al. (2005), which defined these sources as compact radio objects revealed in a VLA survey on the Boötes area with no apparent counterpart in

[5] From the evolutionary point of view, CSSs are interpreted as radio galaxies in an early phase of evolution, still compact enough to show self-absorbed synchrotron radio emission at the sub-GHz frequencies, and often associated with dusty environments.

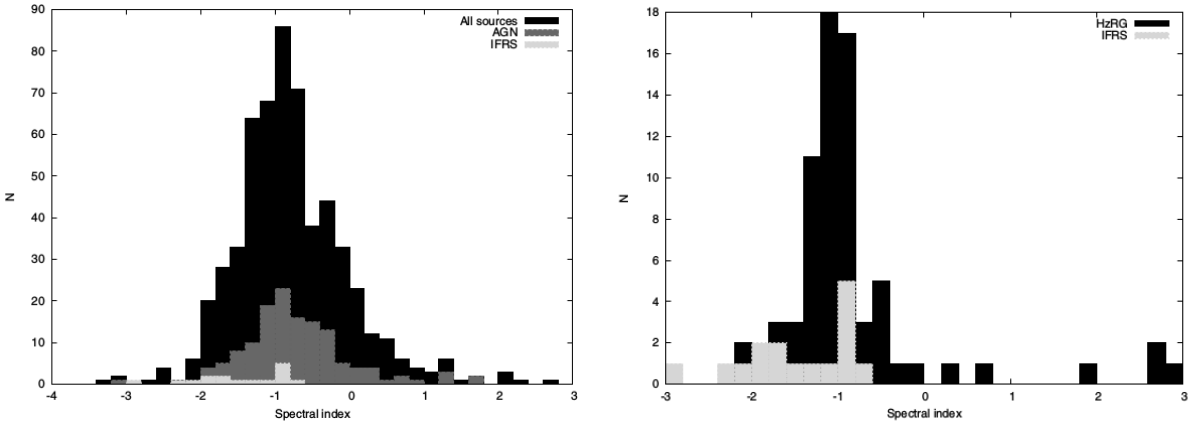

Figure 1.9: (*Left*) Comparison of the spectral indices for several population of objects, within ELAIS-S1 field. (*Right*) Comparison of the spectral indices of the IFRS population within ELAIS-S1 field with the HzRG population studied by Seymour et al. (2007). Both images from Middelberg et al. (2011b).

the multi band optical NOAO deep wide-field survey (NDWFS; Jannuzi & Dey 1999), and with quite few detections in the 24 μm MIPS band of *Spitzer*. With a VLA 1σ sensitivity of $\sim$ 15–40 μJy, and a MIPS 24 μm 1σ sensitivity of $\sim$ 60 μJy, these surveys are comparable with the ATLAS and the SWIRE ones.

Higdon et al. (2008) analysed 35 of such sources, searching for *Spitzer* IRAC and MIPS counterpart. Only 6 of these sources have 24 μm counterpart, with $q_{24\,\mu\mathrm{m}} = -0.24$–$+0.40$, while the 29 sources without MIPS counterpart have $q_{24\,\mu\mathrm{m}} < 0$. These values have been interpreted as due to a population of AGN-powered galaxies lying at high redshift ($z > 1$), possibly related with the fainter end of the high-redshift quasar luminosity function.

The OIRS population shows a clear radio excess relative to the infrared emission (compared to a system powered by star formation), with values similar to the ones reported for the IFRS population. Moreover, the surface densities of these two classes are similar ($\sigma_{IFRS} \sim 10^1$–10^2 deg^{-2}, Zinn et al. 2011; $\sigma_{OIRS} \lesssim 10^1$–$10^2$ deg^{-2}, Higdon et al. 2005) and probably IFRSs and OIRSs overlap to some extent.

Huynh et al. (2010) and Middelberg et al. (2011b), on the other hand, were the first to devise a link between IFRSs and HzRGs. Such class of very rare objects is composed by sources selected from all-sky surveys on the basis of their extreme $R_{3.6}$ ratios (≥ 200) and spectrum steepness ($\alpha \lesssim -1.0$), identified as radio galaxies harbouring very powerful and obscured AGN with redshift $z > 1$ (e.g. Seymour et al. 2007).

Spectral indices are in very good agreement between the two classes (see Fig. 1.9, right), and the $R_{3.6}$ ratios span the same range (see Fig. 1.10 and Fig. 1.11). The two classes of objects are probably related in some way, but their surface densities are very different ($\sigma_{IFRS} \sim 10^1$–10^2 deg^{-2}, Zinn et al. 2011; $\sigma_{HzRG} \sim 10^{-3}$ deg^{-2}, Middelberg et al. 2011b), which makes a straightforward link problematic.

Even if the evidences that IFRSs are extragalactic objects harbouring AGN engines are growing, the hypotesis that some IFRSs could be high-galactic-latitude pulsars can not be ruled out. At observing frequencies close to 1.4 GHz, these objects have flux densities tipically $\gtrsim 10\,\mu$Jy and up to $10^6\,\mu$Jy, and spectral indices spanning the range between -3.5 and $+0.9$, with a median of -1.7 (Manchester et al., 2005). Unfortunately, it is currently impossible to make a reasonable estimate of the number of pulsars presents and detectable per square degree at high galactic latitude, therefore it is impossible to predict what fraction of

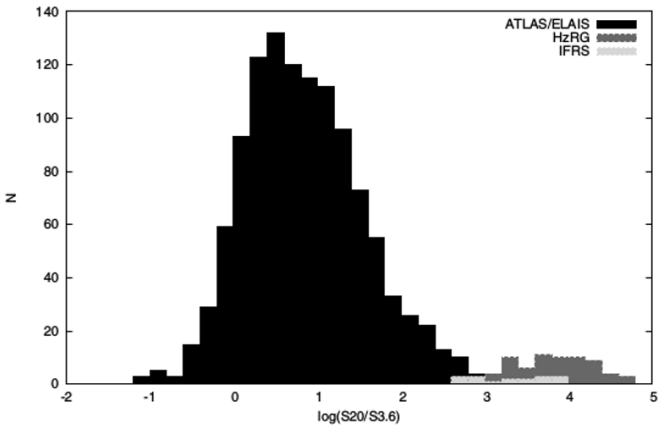

Figure 1.10: Comparison of the $R_{3.6}$ ratios for the whole population of sources within ELAIS-S1 detected by Middelberg et al. (2008a), for the sub-sample of the IFRS population, and for the population of HzRG reported by Seymour et al. (2007). Adapted from Middelberg et al. (2011b).

IFRSs could be a pulsar.

To test the pulsar hypothesis, Cameron et al. (2011) observed 16 IFRSs with the Parkes 64-m radio telescope searching for intrinsic periodic signals. They found that pulse profiles and pulse periods of each candidate were clearly caused by radio frequency interference (RFI) or processing artifact, and concluded that none of the IFRSs in their sample has an emission consistent with being a radio pulsar.

In addition X-ray emissions from the neutron star surface or from the pulsar wind nebula should be detectable if the IFRSs are pulsars. To date, only the IFRS CS0415 has an upper limit constraint (Huynh et al., 2010), which implies an X-ray luminosity 100 times lower than the faintest X-ray emitting pulsars known. Even if such paucity of data do not constitute a conclusive evidence, there is however consistency with the idea that CS0415 is an extragalactic source.

1.5.3 Recent developments

The aforementioned IFRSs lacking of *Spitzer* counterparts, cover a wide range of 1.4 GHz radio fluxes (from tenths to tens of mJy, with a preference around 1–2 mJy), and are collectively known as 'first-generation IFRSs' (Collier et al., 2014).

Despite the several attempts described in the previous Section, a comprehensive analysis of the nature of these IFRSs was challenging due to the fact that they were identified through survey-specific criteria. The request of utter lack of any IR counterpart in the *Spitzer*-based IR surveys implies IFRS samples strongly dependent on the sensitivity of the IR survey, while fainter radio sources lacking of IR counterparts have necessarily smaller $R_{3.6}$ lower limit than the stronger ones. This resulted in a very heterogeneous class of objects.

To overcome this limitation Zinn et al. (2011) developed a set of survey-independent criteria:

- $R_{3.6} = S_{1.4\,\mathrm{GHz}}/S_{3.6\,\mu\mathrm{m}} > 500$;
- $S_{3.6\,\mu\mathrm{m}} < 30\,\mu\mathrm{Jy}$.

The ratio criterion quantifies in a robust value the enormous radio excesses of the sources with respect to the 3.6 μm emission, while the flux criterion enhances the probability that these objects are at cosmological distance. Applying these criteria Zinn et al. (2011) published a list of 55 IFRSs from four fields (xFLS, CDFS, ELAIS-S1 and COSMOS). These sources, with flux densities $S_{1.4\,\mathrm{GHz}} > 1.4$ mJy and often (71% of cases) provided of a 3.6 μm counterpart, represent the first sample of so-called 'second-generation IFRSs'.

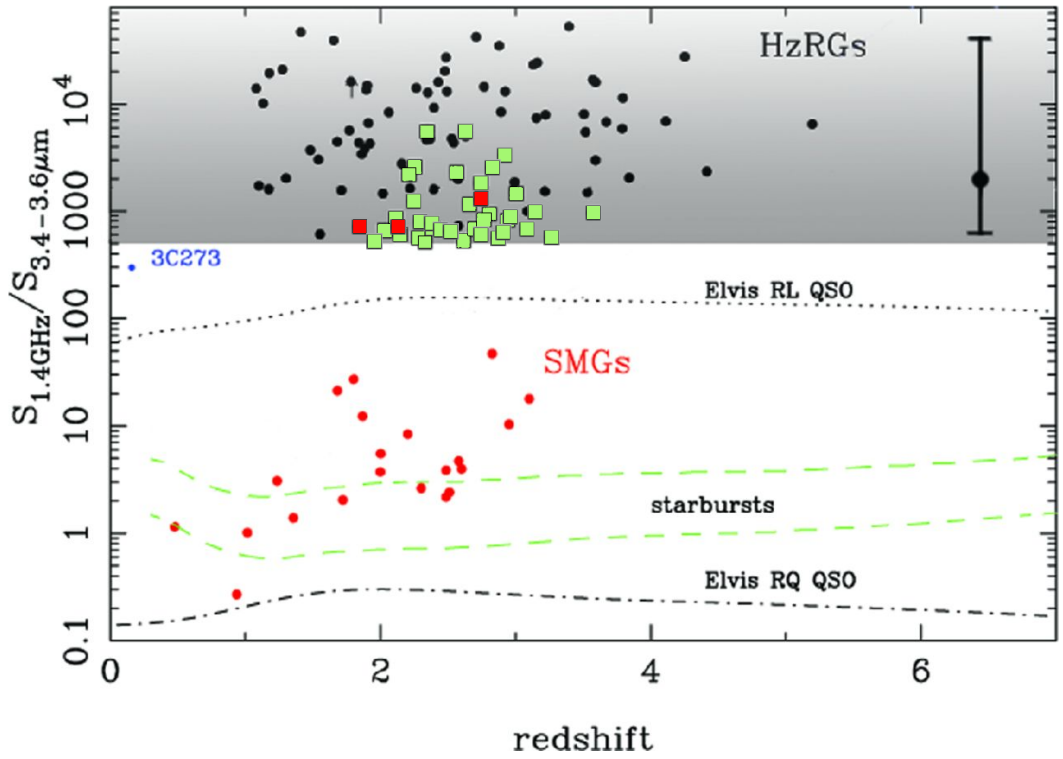

Figure 1.11: $R_{3.6}$ ratio as a function of redshift, for several models. The grey-shaded area represents the ratio range defined by the first Zinn criterion (see Sect. 1.5.3 for more details). The area within the dashed green lines, labelled with 'starbursts', represents the loci of luminous and ultra-luminous infrared galaxies (LIRG and ULIRG; based on the SED template from Rieke et al. 2009), while the dotted and dot–dashed black lines indicate the loci of classical RL and RQ QSOs, respectively (from Elvis et al. 1994). The small black dots within the grey area are the HzRGs studied by Seymour et al. (2007), the red dots show the locations of classical submillimetre galaxies. The large black dot with error bar in the upper-right corner of the plot was obtained by Norris et al. (2011a) as median radio flux density divided by the median 3.6 μm stacked flux density for the CDFS and ELAIS-S1 samples only, while the error bar marks the likely range of the stacked image (obtained by dividing the range of radio flux densities of the IFRSs by the flux density of the marginal detection). The 35 green and 3 red squares represent the approximate positions of IFRSs provided of redshifts from Collier et al. (2014) and Herzog et al. (2014), respectively (see Table 1.1 for details). Adapted from Collier et al. (2014).

Herzog et al. (2014) targeted with the Very Large Telescope (VLT) 4 IFRSs selected from the list by Zinn et al. (2011), and with the explicit request to have a R-band counterpart. For 3 of them they successfully measured spectroscopic redshifts in the range $1.8 \lesssim z \lesssim 2.8$, and due to the presence of broad emission lines of a few thousand km s^{-1} they classified them as Type 1 AGN (see example in Fig. 1.12, left).

Collier et al. (2014), following the criteria by Zinn et al. (2011) and explicitly requiring an IR counterpart, compiled a new list of 1317 IFRSs extracted cross-matching the Wide-Field Infrared Survey Explorer (WISE; Wright et al. 2010) catalogue with the Unified Radio Catalog (URC; Kimball & Ivezić 2008). Among these sources they found a sub-sample of 19 objects with SDSS spectroscopic redshift, and identified as broad-line Type 1 quasars in the range $2 \lesssim z \lesssim 3$ (see example in Fig. 1.12, right).

Collier et al. (2014) interpreted these IFRSs, which have been selected as provided of IR counterpart, as a lower redshift tail of the IFRS population. Moreover, they computed

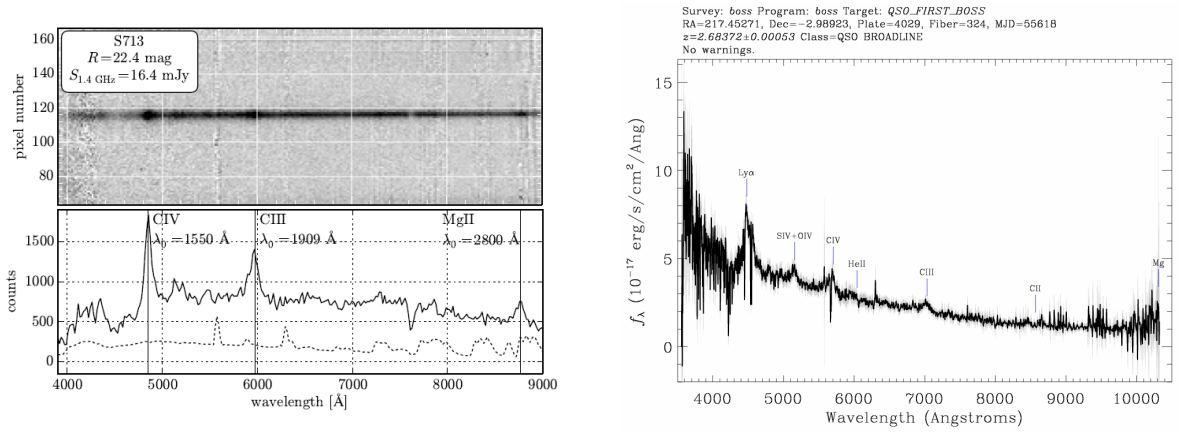

Figure 1.12: (*Left*) Two dimensional spectrum (upper panel) and extracted one dimensional spectrum (lower panel) for IFRS CS0713. Clearly visible are the lines of CIV, [CIII], and MgII redshifted at $z = 2.13 \pm 0.03$; these lines have line widths around $5000\,\mathrm{km\,s^{-1}}$, suggesting the presence of an AGN. From Herzog et al. (2014). (*Right*) One dimensional spectrum of broadline quasar FIRST J142948.6-025921 (IFRS 501 of the Collier catalogue). The redshifted lines of Lyα, CIV, [CIII], and MgII correspond to $z = 2.68 \pm 0.01$. From Collier et al. (2014).

spectral indices for a number of sources. For 208 sources they found a steep two-point spectral index ($\alpha < -0.8$), while for 32 sources they found a peak in the interval between 326 and 4850 MHz, typical of gigaHertz-peaked spectrum (GPS) sources[6]. Collier et al. (2014) interpreted this findings suggesting that a substantial fraction of their sample of IFRSs is composed by CSS and GPS sources, i.e. by young and evolving RL AGN, with small jets extending not far from the galaxy.

Redshift from SDSS Data Release 9 (DR9; Ahn et al. 2012) and Data Release 10 (DR10; Ahn et al. 2014) are available for 35 IFRSs of the Collier et al. (2014) sample, while Herzog et al. (2014) directly measured the redshift of other 3 sources. This helped to discard other hypotheses about the nature of IFRSs. The redshift distribution they found for such IFRSs is in the range $\sim$ 2–3 (see Table 1.1), well beyond the peak distribution of FR II galaxies (which peak at $z \sim 1$) and SFGs (which peak at $z \sim$ 0–0.5). The first case rules out the hypothesis that IFRSs are mostly associated to radio lobes or hot-spots unrecognised as such, in FR II galaxies. The second case rules out that IFRSs are associated to SFGs.

For these sources, it is also possible to compute the intrinsic radio luminosity of these sources. The median radio luminosity for these sources is $\widetilde{L}_{1.4\,\mathrm{GHz}} \sim 3 \times 10^{26}\,\mathrm{W\,Hz^{-1}}$, and all of them is classified as RL.

Herzog et al. (2015b) searched for the first time for FIR counterparts of a sample of 6 IFRSs, using the *Herschel* Space Observatory, at the wavelengths of 100 and 160 μm (PACS instrument; Poglitsch et al. 2010), and 250, 350, and 500 (spectral and photometric imaging receiver –SPIRE– instrument; Griffin et al. 2010). 5 of these objects are from the Zinn et al. (2011) IFRS sample, while 1 is from the original Norris et al. (2006) list of IFRSs. All of these targets has been selected to be bright in the radio (flux densities in the range $\sim$ 7–26 mJy).

No source was detected (not even after the stacking of the sources), but Herzog et al.

[6]GPS sources are very compact radio sources, extended up to some kpc, characterised by a radio emission peaking in the range 1–10 GHz. From the evolutionary point of view, GPS sources are interpreted as radio galaxies in a very early phase of evolution, preceding the CSS phase, still compact enough to show strong self-absorbed synchrotron radio emission at the GHz frequencies.

Table 1.1: Overview of the redshift-provided IFRSs from Collier et al. (2014) and Herzog et al. (2014).

Collier sample

IFRS ID	Radio coordinates (J2000)		$S_{1.4\,\mathrm{GHz}}$	$S_{3.4\,\mu\mathrm{m}}$	$S_{4.6\,\mu\mathrm{m}}$	$R_{3.4}^{(a)}$	$R_{4.6}^{(b)}$	$R_{IR}^{(c)}$	Spectral index	Redshift	K-corr.$^{(d)}$ $L_{1.4\,\mathrm{GHz}}$ ($\times 10^{26}\,\mathrm{W\,Hz^{-1}}$)
	(hh:mm:ss)	(dd:mm:ss)	(mJy)	(μJy)	(μJy)						
(1)	(2)	(3)	(4)	(5)	(6)	(7)	(8)	(9)	(10)	(11)	(12)
23	2:06:22.456	−00:43:20.57	19.93 ± 0.73	28.33 ± 5.27	50.55 ± 10.85	703 ± 133	394 ± 86	1.78 ± 0.51	…	2.38	2.59 ± 0.09
150	11:35:41.053	+45:40:42.34	17.28 ± 0.66	29.10 ± 5.01	60.55 ± 10.15	594 ± 105	285 ± 49	2.08 ± 0.50	0.03	2.14	1.81 ± 0.07
151	11:36:35.014	+61:06:19.31	18.29 ± 0.67	27.28 ± 4.98	33.25 ± 9.98	670 ± 125	550 ± 166	1.22 ± 0.43	−0.01	2.03	1.82 ± 0.07
197	12:27:43.502	+36:42:55.83	24.09 ± 0.83	28.81 ± 5.65	33.68 ± 11.23	836 ± 166	715 ± 240	1.17 ± 0.45	−0.23	2.11	3.31 ± 0.11
275	13:29:22.200	+05:20:14.20	44.45 ± 1.39	29.89 ± 5.78	42.12 ± 11.17	1487 ± 291	1055 ± 282	1.41 ± 0.46	−0.73	2.99	23.48 ± 0.73
345	13:55:04.592	+36:38:02.14	15.95 ± 0.62	28.75 ± 5.08	42.16 ± 9.98	555 ± 100	378 ± 91	1.47 ± 0.43	0.33	2.28	1.31 ± 0.05
398	14:08:54.995	+55:52:17.62	62.86 ± 1.93	26.42 ± 4.57	43.59 ± 8.83	2379 ± 418	1442 ± 295	1.65 ± 0.44	−0.65	2.55	21.06 ± 0.65
418	14:11:57.570	+44:28:03.93	20.08 ± 0.72	25.30 ± 4.82	31.63 ± 9.29	794 ± 154	635 ± 188	1.25 ± 0.44	−0.09	2.26	2.67 ± 0.10
426	14:13:09.245	+24:07:00.57	20.56 ± 0.74	26.18 ± 4.39	43.75 ± 9.23	785 ± 135	470 ± 101	1.67 ± 0.45	−0.11	2.35	2.99 ± 0.11
501	14:29:48.640	−02:59:21.37	18.70 ± 0.69	27.43 ± 5.28	43.07 ± 10.79	682 ± 134	434 ± 110	1.57 ± 0.50	…	2.68	2.99 ± 0.11
514	14:31:30.847	+23:34:22.12	23.62 ± 0.81	22.46 ± 4.26	25.57 ± 8.48	1052 ± 203	924 ± 308	1.14 ± 0.43	0.05	3.59	5.66 ± 0.19
519	14:32:43.181	+23:20:09.85	14.66 ± 0.60	25.07 ± 4.27	<24.15	585 ± 102	>607	<0.96	0.17	2.89	2.10 ± 0.09
545	14:38:21.829	+34:40:01.06	10.70 ± 0.50	20.36 ± 3.90	46.62 ± 8.16	526 ± 104	230 ± 42	2.29 ± 0.59	0.42	2.34	0.82 ± 0.04
564	14:40:48.574	+36:35:35.56	30.75 ± 1.00	26.64 ± 4.12	58.04 ± 8.23	1154 ± 182	530 ± 77	2.18 ± 0.46	−0.43	3.14	11.83 ± 0.38
575	14:42:26.690	+13:29:56.08	20.58 ± 1.05	26.76 ± 5.18	<32.37	769 ± 154	>636	<1.21	−0.11	3.08	4.83 ± 0.25
630	14:52:51.704	+52:39:55.97	126.07 ± 3.80	22.71 ± 4.27	56.25 ± 8.45	5551 ± 1057	2241 ± 343	2.48 ± 0.60	−0.43	2.34	26.74 ± 0.81
642	14:55:06.536	+06:40:18.84	51.47 ± 1.60	23.01 ± 4.56	38.24 ± 9.58	2237 ± 449	1346 ± 340	1.66 ± 0.53	0.24	2.22	4.48 ± 0.14
643	14:55:06.634	+13:59:26.46	16.70 ± 0.65	23.31 ± 4.53	34.88 ± 9.09	716 ± 142	479 ± 126	1.50 ± 0.49	0.06	2.40	2.05 ± 0.08
653	14:56:27.577	+43:55:00.17	27.21 ± 0.91	26.22 ± 3.70	22.56 ± 6.90	1038 ± 150	1206 ± 371	0.86 ± 0.29	−0.33	2.95	8.02 ± 0.27
671	14:59:31.156	+14:56:50.19	133.35 ± 4.02	23.22 ± 4.38	46.57 ± 9.09	5743 ± 1097	2863 ± 566	2.01 ± 0.54	−0.99	2.62	73.20 ± 2.21
682	15:00:48.663	+45:28:06.33	17.42 ± 0.67	28.10 ± 3.86	46.32 ± 7.47	620 ± 88	376 ± 62	1.65 ± 0.35	0.03	2.73	2.77 ± 0.11
792	15:16:09.843	+22:25:07.81	20.08 ± 0.72	23.05 ± 4.10	33.18 ± 8.28	871 ± 158	605 ± 153	1.44 ± 0.44	−0.09	2.78	3.83 ± 0.14
799	15:17:03.800	+24:01:27.25	18.09 ± 0.68	29.18 ± 4.09	54.07 ± 8.47	620 ± 90	335 ± 54	1.85 ± 0.39	−0.00	2.93	3.35 ± 0.13
820	15:20:44.354	+27:06:36.53	46.77 ± 1.46	25.94 ± 4.32	39.60 ± 8.75	1803 ± 305	1181 ± 264	1.53 ± 0.42	−0.26	2.73	10.96 ± 0.34
885	15:33:17.296	+12:18:00.64	23.27 ± 0.80	24.97 ± 3.93	44.44 ± 9.00	932 ± 150	524 ± 108	1.78 ± 0.46	−0.21	2.80	5.29 ± 0.18
912	15:38:26.812	+14:55:05.91	15.13 ± 0.60	27.13 ± 4.77	35.89 ± 10.87	558 ± 101	422 ± 129	1.32 ± 0.46	0.14	2.62	1.94 ± 0.08
943	15:43:14.771	+32:51:37.86	50.28 ± 1.56	20.15 ± 3.84	53.72 ± 7.47	2495 ± 482	936 ± 133	2.67 ± 0.63	−0.83	2.27	16.06 ± 0.50
952	15:45:21.488	+41:30:25.46	67.28 ± 2.05	19.55 ± 3.60	<60.18	3441 ± 642	>1118	<3.08	−0.22	2.88	16.29 ± 0.50
956	15:46:04.404	+44:49:10.52	61.15 ± 1.87	23.70 ± 3.40	22.81 ± 6.68	2580 ± 378	2681 ± 789	0.96 ± 0.31	−0.32	2.79	15.99 ± 0.49
957	15:46:25.297	+36:53:12.78	10.36 ± 0.50	18.23 ± 3.59	48.72 ± 7.54	568 ± 115	213 ± 34	2.67 ± 0.67	0.44	1.94	0.59 ± 0.03
1061	16:09:05.993	+42:53:23.53	11.72 ± 0.54	17.09 ± 3.26	36.89 ± 6.32	686 ± 135	318 ± 56	2.16 ± 0.55	0.35	2.48	1.06 ± 0.05
1086	16:15:20.311	+43:47:25.24	12.48 ± 0.54	17.73 ± 3.22	42.79 ± 6.42	704 ± 131	292 ± 46	2.41 ± 0.57	0.29	2.90	1.53 ± 0.07
1168	16:38:17.398	+41:27:29.71	32.33 ± 1.05	26.93 ± 5.18	43.38 ± 11.34	1200 ± 234	745 ± 196	1.61 ± 0.52	…	2.23	3.76 ± 0.12
1224	17:04:08.588	+44:08:39.48	16.39 ± 0.64	28.52 ± 4.70	<28.54	575 ± 97	>574	<1.00	0.08	3.26	3.23 ± 0.13
1278	17:26:16.517	+32:16:19.84	28.42 ± 0.94	24.18 ± 4.16	31.29 ± 8.36	1175 ± 206	908 ± 245	1.29 ± 0.41	−0.37	2.64	7.14 ± 0.24

Herzog sample

IFRS ID	Radio coordinates (J2000)		$S_{1.4\,\mathrm{GHz}}$	$S_{3.6\,\mu\mathrm{m}}$	$S_{4.5\,\mu\mathrm{m}}$	$R_{3.6}^{(e)}$	$R_{4.5}^{(f)}$	$R_{IR}^{(g)}$	Spectral index$^{(h)}$	Redshift	K-corr.$^{(d)}$ $L_{1.4\,\mathrm{GHz}}$ ($\times 10^{26}\,\mathrm{W\,Hz^{-1}}$)
	(hh:mm:ss)	(dd:mm:ss)	(mJy)	(μJy)	(μJy)						
(1)	(2)	(3)	(4)	(5)	(6)	(7)	(8)	(9)	(10)	(11)	(12)
CS0212	03:29:48.942	−27:31:48.98	18.90 ± 2.61	17.53 ± 0.52	23.44 ± 0.72	1078 ± 152	806 ± 114	1.34 ± 0.06	−0.84	2.76	9.65 ± 1.33
CS0265	03:30:34.661	−28:27:06.51	18.61 ± 3.72	29.32 ± 0.88	38.89 ± 1.18	635 ± 128	479 ± 97	1.33 ± 0.06	−0.75	1.84	3.37 ± 0.67
CS0713	03:35:37.525	−27:50:57.88	16.43 ± 3.29	25.54 ± 0.82	30.63 ± 1.12	643 ± 130	536 ± 109	1.20 ± 0.06	…	2.13	1.76 ± 0.35

$^{(a)}$ $R_{3.4} = S_{1.4\,\mathrm{GHz}}/S_{3.4\,\mu\mathrm{m}}$; $^{(b)}$ $R_{4.6} = S_{1.4\,\mathrm{GHz}}/S_{4.6\,\mu\mathrm{m}}$; $^{(c)}$ $R_{IR} = S_{4.6\,\mu\mathrm{m}}/S_{3.4\,\mu\mathrm{m}}$; $^{(d)}$ 1.4 GHz luminosities are K-corrected using their own spectral index when available. Otherwise, a flat spectral index has been assumed; $^{(e)}$ $R_{3.6} = S_{1.4\,\mathrm{GHz}}/S_{3.6\,\mu\mathrm{m}}$; $^{(f)}$ $R_{4.5} = S_{1.4\,\mathrm{GHz}}/S_{4.5\,\mu\mathrm{m}}$; $^{(g)}$ $R_{IR} = S_{4.5\,\mu\mathrm{m}}/S_{3.6\,\mu\mathrm{m}}$; $^{(h)}$ computed between 1.4 and 20 GHz, from data reported by Franzen et al. (2014).

(2015b) used the upper limits to constraints the SED of IFRSs. Using templates from known objects they applied a redshift fainting, a luminosity scaling, an extinction factor, and a combination of these three contributions to search for the most suitable SED for the IFRSs data. They found that HzRG SED is the one providing the best fitting for their radio-bright IFRS sample, but also CSS source and RL AGN SEDs could be viable under some assumptions.

To confirm on a statistical basis the presence of AGN inside IFRSs, Herzog et al. (2015a) targeted 57 IFRSs belonging to the Collier et al. list with the VLBA. These targets were selected based on their proximity to a VLBA calibrator (distance < 1 deg), and on their visibility during available filler time of the VLBA array. They span a large radio flux density range ($\sim 11 \rightarrow 183$ mJy), which can be considered as representative of the full Collier et al.

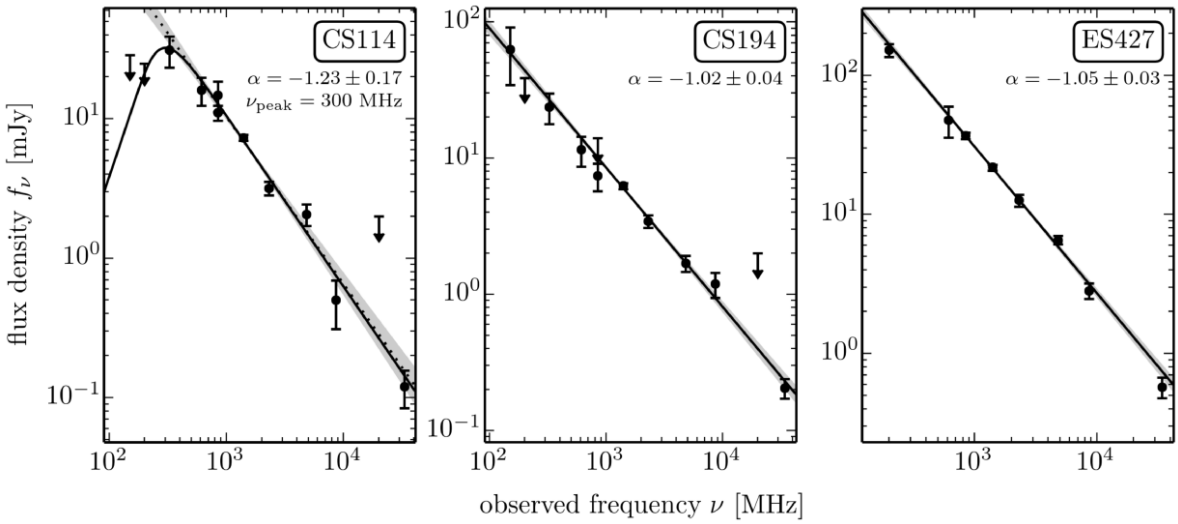

Figure 1.13: Radio SED of some IFRSs. (*Left*) IFRS CS0114 in CDFS; (*Centre*) IFRS CS0194 in CDFS; (*Right*) IFRS ES0427 in ELAIS-S1. All these sources are good candidate ultra-steep spectrum (USS) radio sources (i.e., sources characterised by a very steep spectral index, typically $\alpha < -1.0$; see Sect. 1.7 for the adopted convention). The SED of CS0114 shows a turnover around 200 MHz, while CS0194 and ES0427 are very well described by single power law SEDs. All images from Herzog et al. 2016 and Herzog 2015.

sample ($\sim 8 \rightarrow 793$ mJy). They successfully detected compact cores in 35 of them, confirming that AGN lie in the majority (if not all) of 2nd-generation IFRSs, and establishing them as a new class of AGN. They concluded that IFRSs tend to harbour young AGN in an early stage of evolution, which jets are not yet formed or expanded significantly, resulting in very compact sources. They also found that two sources show double components separated by some hundreds of milliarcsec, possible hint of the ongoing process of jet expansion.

In a more recent work, Herzog et al. (2016) (see also Herzog 2015) performed a comprehensive analysis of the radio SED of 34 out of 55 sources belonging to the original Zinn et al. (2011) list, 19 from CDFS field (Norris et al., 2006) and 15 from ELAIS-S1 field (Middelberg et al., 2008a). They gathered data from 15 radio frequencies, in the range from 150 MHz to 34 GHz, using surveys from several radio telescopes (GMRT, MWA, Molonglo Observatory Synthesis Telescope –MOST; Mills 1981; Robertson 1991–, ASKAP - Boolardy engineering test array –ASKAP-BETA; Hotan et al. 2014–, ATCA).

They highlighted how the vast majority (85%) of their subsample shows a steep radio SED ($\alpha < -0.8$), and a significant percentage (12%) an ultra steep SED ($\alpha < -1.3$), which typically are associated to high-z radio galaxies (see e.g. Miller et al. 2008). Moreover, they found that some of these sources have a SED consistent with GPS and CSS sources (see Fig. 1.13), strengthening the idea that at least some IFRSs are AGN in the earliest stages of their evolution to FR I/FR II radio galaxies.

1.6 Thesis projects

1.6.1 Nuclear activity in radio-quiet AGN

A lot of work has been done in the field of RQ AGN, but still fundamental pieces of the puzzle are missing. One of the main reasons is the difficulty to distinguish among star-forming galaxies, radio-loud AGN and radio-quiet AGN, and this problem will be even more pressing with the future, planned deep large-scale radio surveys. In their seminal work, Bonzini et al. (2013) proposed a set of prescriptions to distinguish among these classes of objects in a powerful and statistically useful way. These prescriptions provide results which are consistent with other proxies, and, given the availability of information at the involved bands, are easy to apply.

With the future, deep radio surveys expected to be delivered by ASKAP and by SKA, these prescriptions will help to provide a quick and reliable classification for millions of objects. This is a fundamental pre-requisite to finally understand on a statistically meaningful base the physical and evolutionary properties of low/intermediate power AGN. In recent years, findings are piling up about the existence of relevant AGN-related activity within sources classified as radio-quiet and lying at low redshift ($z \lesssim 1$). The discovery of analogous activity in sources lying at intermediate and high redshift ($z \gtrsim 1$) will help to answer cosmological key questions (Prandoni et al., 2010). Among the others, of particular relevance is the understanding of the triggering mechanism of AGN radio activity and its duty cycle along the ages, the determination of the BH accretion history of the Universe, and a better understanding of the feedback in RQ AGN. Above all, moreover, is the possibility to derive radio luminosity functions for RL and RQ AGN (as well as for SFGs) from a single radio-based selection function.

In Chapter 2, I present one of the first searches ever of radio cores in RQ AGN at cosmological distance. This work is based on novel VLBI observations of a sub-sample of sub-mJy RQ AGN extracted from the ECDFS radio field (Bonzini et al., 2012, 2013). In Chapter 3 I extend the analysis to other deep radio samples for which VLBI observations were already available. In particular, I used the new Bonzini et al. (2013) criteria to pinpoint RQ AGN and searched for VLBI-sized radio cores. This allowed us to increase the number of radio cores detected in high-redshift RQ AGN, and to perform a first statistical analysis of their properties.

1.6.2 Infrared-faint radio sources

In recent times, a new population of extreme AGN has been discovered in deep radio surveys. These objects have been called infrared-faint radio sources (IFRS) due to their extreme radio-to-IR ratios, and have been found to lie at high and very high redshift ($z \gtrsim 2$). The results obtained so far from statistical samples of bright IFRSs (Collier et al., 2014) show that they are preferentially associated with high-redshift broad-line RL AGN. In addition IFRSs seem to be related in some way with the class of high-redshift radio galaxies (HzRG), which are known to harbour both AGN and SF activity, and are interpreted as the progenitors of the most massive galaxies in the local Universe (Seymour et al., 2008; De Breuck et al., 2010).

Therefore, IFRSs are not a mere curiosity in the skies, and their study is relevant for several topics of the contemporary Astrophysics (Norris et al., 2007b). Understanding their nature can help to understand the spatial distribution and clustering of evolved galaxies in the key redshift range $0.5 < z < 3$; they can help to deepen the formation and evolution history

of galaxies and AGN, their evolutionary relationships and the characterization of their main phases. They can help to better understand formation and evolution of SMBH, and can perhaps be used as background sources to analyse the interposed intergalactic medium. This would help to understand the post-re-ionization epoch, and help to understand whether the main agent of re-ionization are the first stars ever appeared or the generation of first (maybe primordial) BHs.

In Chapter 4, I present a new study of the radio/IR properties of the faint tail of IFRS, based on deeper IR observations, recently made available from Spitzer. In addition I present a new sample of IFRS extracted from the LH region, never explored before in this respect. From a comparison with evolutionary models of known classes of objects, I then provide a comprehensive interpretation of both bright and faint IFRSs, in terms of redshift distribution, and source classification.

1.7 Conventions

When referring to spectral indices and power laws, I will adopt the usual radio convention: $S_\nu = S_0\, \nu^\alpha$. So the steeper the spectral indices the more negative the value of α.

Throughout this Thesis, I adopt a standard flat ΛCDM cosmology with $H_0 = 70\,\mathrm{km\,s^{-1}\,Mpc^{-1}}$ and $\Omega_M = 0.30$ (Komatsu et al., 2011). Luminosity distances, angular scale distances, and linear scales have been computed using the Cosmology Calculator by Wright (2006).

2

Radio-quiet active galactic nuclei

In this Chapter of the Thesis I present the work done in the context of radio-quiet active galactic nuclei (RQ AGN). After a short introduction (Sect. 2.1), I report my personal contribution to the understanding of the origin of the radio emission in high redshift ($z \gtrsim 1$) RQ AGN, based on novel VLBI observations (Sects. 2.2 and 2.3). A short conclusion summarises the current view about the RL/RQ dichotomy (Sect. 2.4).

2.1 Scientific background

In the local and near Universe ($z \lesssim 1$), a huge amount of work has been carried out to better understand the RL/RQ dichotomy. For instance, thanks to multiwavelength surveys and extensive analyses it is now clear that local radio-quiet quasars (RQQ) contain both AGN and star-forming activity, in variable proportions (see, e.g., Condon et al. 1991; Alexander et al. 2005a). At intermediate and high redshifts ($z \gtrsim 1$) the dichotomy is more difficult to address, biased both by the selection function of the samples (often optical- or X–ray-selected), and by unresolved detections and limited sensitivity of the radio follow ups, and no conclusive result has been found.

However, in the last years, radio surveys sampling deeper and deeper the sub-mJy regime surprisingly detected the radio counterparts of RQ sources even at intermediate and high redshifts. This revolutionaised the common idea that only two populations would dominate the radio regime in the interval between 0.01–1 mJy: SFGs and RL AGN. On the contrary, RQ sources are so numerous that their relative importance around 0.1 mJy grows up to 30% of the total population (Bonzini et al., 2013; Smolčić et al., 2015). Together with SFGs they are responsible for the flattening of the normalised radio source counts below 1 mJy (see Fig. 2.1).

The detection of large number of RQ AGN in the sub-mJy radio regime opened new exciting perspectives in the study of deep radio fields, allowing to study the entire AGN population (RL and RQ) at radio wavelengths for the first time. At the same time, however, re-opened the discussion about the main radio emission mechanism in these sources, with renewed discussions on the long-standing problem of properly disentangling the origin of the

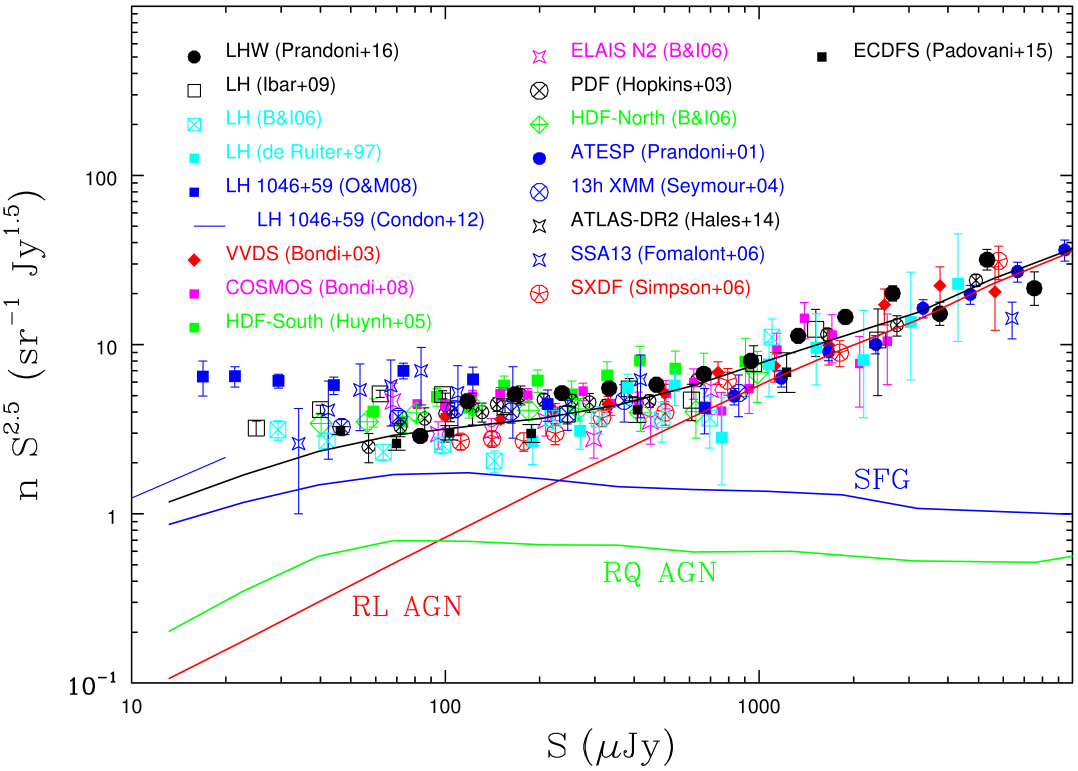

Figure 2.1: A compilation of the observed 1.4 GHz differential radio source counts (normalised to those expected in an Euclidean Universe). The simulated counts (lines) are taken from SKA design study model (Wilman et al., 2008a) and show the contribution of the various source classes: RL AGN (red), RQ AGN (green), and SFG (blue). The sum of all classes is shown in black. Adapted from Prandoni et al. (2016, submitted).

radio emission in RQ AGN, and more in general understanding and quantifying the relevance of the AGN phenomenon in intermediate- and high-redshift population of galaxies, and its connection with the SF activity. This is crucial for the future radio facilities, which surveys will discover RQ AGN in the millions, especially in the redshift range where both AGN and SF activity peak ($z \sim 2$).

2.2 Radio-quiet AGN in the ECDFS field

In this Section I report the original work I did in the field of RQ AGN. This Section is an extended version of the refereed Letter Compact radio cores in Radio-Quiet AGNs *(Maini et al., 2016a). Overall, my contribution to the published Letter is 95%.*

Multi-wavelength studies of deep radio fields show that the sub-mJy population has a composite nature. While RL AGN are the dominant component of the bright ($S \gtrsim 1$ mJy) radio sky (see e.g. Mignano et al. 2008), at fainter flux densities ($\lesssim 0.5$–1 mJy) the contribution from SFGs becomes increasingly important (e.g., Prandoni et al. 2001a; Seymour et al. 2008; Smolčić et al. 2008). Until recently, it was expected that only SFGs and RL AGN

would populate the extragalactic radio sky.

This view has started to change based upon the latest results from new deep, sub-mJy regime radio surveys. In fact, a large number of RQ AGN have been detected at flux densities $\lesssim 500\,\mu$Jy (Padovani et al., 2009; Bonzini et al., 2012). RQ AGN are now thought to partly account for the flattening of the normalised 1.4 GHz differential radio source counts at flux densities $< 500\,\mu$Jy (see Fig. 2.1), and their relative importance grows up to 30% of the total population below 100 μJy (see, e.g., Bonzini et al. 2013; Smolčić et al. 2015; and Figure 5.2). The detection of large numbers of RQ AGN at radio wavelengths interesting allows to study the entire AGN population (RL and RQ) at radio wavelengths for the first time.

Based upon recent works, the properties of RQ AGN and their hosts are starting to emerge. Most RQ AGN are unresolved or barely resolved at few arcsec scale in radio images, indicating that their radio emission is confined in regions that are more or less comparable to the size of the host galaxy. RQ AGN also show similar radio luminosities (10^{21}–10^{25} W Hz^{-1}) and similar optical- and infrared-to-radio flux ratios to SFGs. Furthermore, the radio luminosity functions of RQ AGN and SFGs show similar evolutionary trends (Padovani et al., 2011), and their host galaxies have similar colours, optical morphologies, and stellar masses (Bonzini et al., 2013). Based upon these properties it has been suggested that the radio emission in RQ AGN is mainly triggered by star formation (Padovani et al., 2011; Bonzini et al., 2013; Smolčić et al., 2015).

A key piece of evidence to support this idea was provided by Bonzini et al. (2015), who found that in RQ AGN the radio-derived star formation rates (SFR_{radio}) are consistent with FIR *Herschel*-derived SFR (SFR_{FIR}), even though with a larger dispersion than for SFGs (see also Rees et al. 2016). However, RQ AGN do show the presence of an AGN in one or more bands of the electromagnetic spectrum (e.g., optical, mid-infrared, X-ray), and it is important to assess whether such activity contributes to the radio emission as well.

In fact, it is well known that in the local Universe ($z \lesssim 0.5$) both AGN and SF processes can contribute to the total radio emission in RQ AGN (e.g. Seyfert 2 galaxies; Roy et al. 1998), and there is growing evidence that composite SF/AGN systems can be rather common at medium to high redshift ($z \gtrsim 1$–2; e.g., Daddi et al. 2007a; Del Moro et al. 2013; Rees et al. 2016).

The most reliable way to separate radio structures on several linear scales (from AGN core/inner jets, size $\ll 1$ kpc; to nuclear/disk starbursts, size $\gtrsim 1$ kpc) in intermediate redshift ($z \sim 1$) galaxies is through deep (μJy-level) imaging at milli-arcsec (mas) resolution, using the VLBI technique. VLBI observations are sensitive to very high brightness temperatures ($\gtrsim 10^5$ K), which are an almost unambiguous mark of AGN-driven radio emission.

The ECDFS field is arguably one of the regions within which the multi-wavelength properties of sub-mJy RQ AGN have been most extensively studied. We used the Australian Long Baseline Array (LBA), to search for VLBI-sized components embedded in ECDFS sources classified as RQ AGN. This allowed us to set constraints on the AGN contribution to the total radio emission in these systems.

2.2.1 Strategy, observations and data reduction

Our targets were selected from a catalogue of 883 radio sources already detected at 1.4 GHz from VLA observations (Miller et al., 2008, 2013). The original catalogue, centred at $3^{\mathrm{h}}\,32^{\mathrm{m}}\,28.0^{\mathrm{s}}$, $-27^{\circ}\,48'\,30.0''$ (J2000), has a typical 1σ sensitivity of $\sim 7.4\,\mu$Jy and an angular resolution of 2.8×1.6 arcsec^2, and is complete down to an average flux limit of $37\,\mu$Jy.

The same sources are also provided with extensive and deep multi-wavelength coverage.

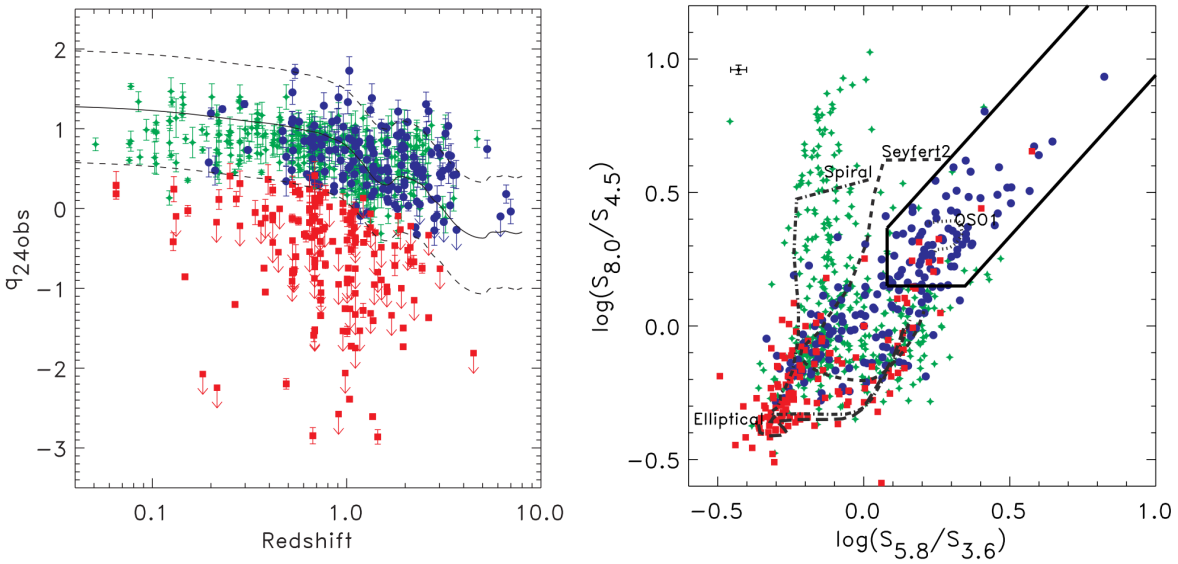

Figure 2.2: The two diagrams used by Bonzini et al. (2013) to classify sources from the Miller et al. (2013) catalogue. Red squares refer to RL AGN, blue circles to RQ AGN, and green crosses to SFGs. (*Left*) $q_{24\,obs}$ vs. redshift. The solid black line shows the evolution of $q_{24\,obs}$ for the prototypical star-forming galaxy M82 as a function of redshift; dashed lines represent the 2σ dispersion around the template, while down-pointing arrows are 3σ upper limits. (*Right*) AGN wedge colour-colour diagram. The black solid line encloses the so-called 'Donley wedge' (Donley et al., 2012), within which lie sources whose AGN emission dominates the IR (see Sect. 1.2.1 for details). Colour-colour tracks of a 13 Gyr old elliptical galaxy (long dashed line), a spiral galaxy (dot-dashed line), a Type 2 Seyfert galaxy (dashed line) and a Type 1 QSO (dotted line; all from Polletta et al. 2007) are also plotted, for redshift range 0.1–3. The black cross on the top left of the diagram shows the typical uncertainty. From Bonzini et al. (2013).

The ATLAS surveys at 5.5 GHz (Huynh et al., 2012) and 1.4 GHz (Hales et al., 2014) allowed to derive 1.4–5 GHz spectral indexes; *Spitzer* (Lonsdale et al., 2003; Surace et al., 2005) and *Herschel* (Lutz et al., 2011) survey programs provided deep multi-wavelength information in the IR band; optical surveys (space based –Swinbank, HST Project ID 12866; Rix, HST Project ID 9500– and ground based –Gawiser et al. 2006; Taylor et al. 2009; Damen et al. 2011–) provided optical/UV high-resolution images; finally, *Chandra* surveys (Lehmer et al., 2005; Xue et al., 2011) provided X-ray counterparts for a number of objects.

This allowed a secure classification of all the sources from the Miller et al. catalogue into three classes: RL AGN, RQ AGN, and SFGs (Bonzini et al., 2013). The classification of Bonzini et al. (2013) is primarily based on the observed infrared-to-radio ratio ($q_{24\,obs} = \mathrm{Log}(S_{24\,\mu\mathrm{m}}/S_{1.4\,\mathrm{GHz}})$). Any source that shows a significant radio excess with respect to a SFG template (M82, redshifted up to $z = 10$) is classified as RL (see Figure 2.2, left). Sources with no significant radio excess are classified as RQ AGN if they show a clear evidence for AGN in the hard X-ray band ($L_{2-8\,\mathrm{keV}} > 10^{42}$ erg s^{-1})[7] and/or in the NIR and MIR bands (i.e., the source lies inside the AGN wedge of the IRAC colour-colour diagram, see Figure 2.2, right); Donley et al. 2012). Otherwise, a SFG classification is adopted.

[7] Bonzini et al. 2013 take this criterion from Szokoly et al. 2004, which define the hard X-ray band between 2 and 10 keV. Bonzini et al. 2013 use the interval between 2 and 8 keV due to the fact that the *Chandra* data (Lehmer et al., 2005; Xue et al., 2011) refer to the interval 2–8 keV.

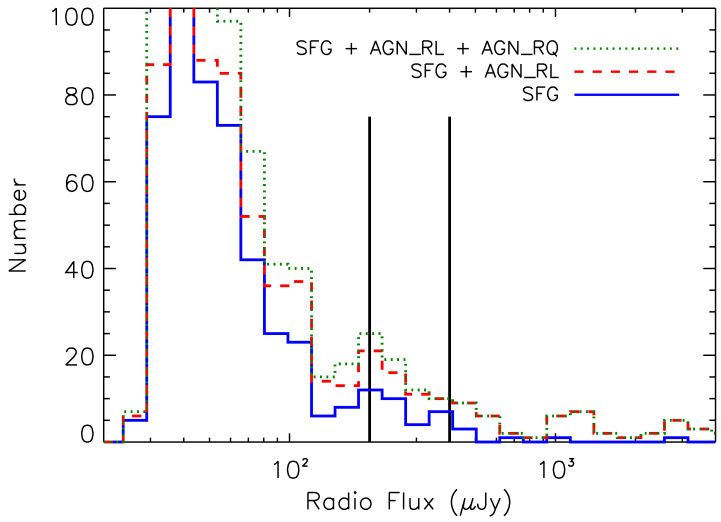

Figure 2.3: Stacked histogram of the radio flux density distributions of the Bonzini et al. (2013) sources. The solid blue curve refers to SFGs, the red dashed curve adds to it the RL AGN, the green dotted curve adds to them the secure (QF = 3) RQ AGN. The two black vertical lines delimit the flux range of the sample we targeted (200–400 μJy).

Following this scheme, Bonzini et al. (2013) defined also a quality flag (QF) which expresses the reliability of the classification. Sources for which all the criteria agree (or are not in contradiction) have been classified as secure (QF = 3); sources showing a small radio excess ($q_{24\,obs,\,M82} - 2\sigma < q_{24\,obs} < q_{24\,obs,\,M82} - 1\sigma$, where σ is defined as the spread of the $q_{24\,obs}$ distribution for local SFGs; Sargent et al. 2010) or with a clear signature of AGN but lacking of redshift, have been classified as reasonable (QF = 2); all the other sources have been classified as tentative (QF = 1).

The ECDFS field has been also observed with the Very Long Baseline Array (VLBA) by Middelberg et al. (2011a) (see Sect. 3.1 for further details). However, the position of the field (Dec $\sim -28°$) is not well suited for the VLBA, and the average elevation of the field during the experiment was only $\sim 20°$. This limited the sensitivity of the observations: only sources brighter than 400–1000 μJy (depending on the position in the field) could be detected. The VLBA detected one RQ AGN with a flux density $> 400\,\mu$Jy, but the source is flagged only as reasonable (QF = 2 in the catalogue of Bonzini et al. 2013).

Sources securely classified as RQ AGN (QF = 3) are all fainter than 400 μJy (see Fig. 2.3). Deeper VLBI observations are therefore needed to probe the RQ AGN population in the ECDFS field, and to assess whether or not AGN cores are present in such sources. As part of my Thesis project, I pushed VLBI observations to deeper fluxes using the Australian Long Baseline Array (LBA), which is better suited to observe of this southern field.

VLBI observations at μJy level are challenging. In order to increase the effectiveness of our experiment and our detection chances, we focused on four RQ AGN with secure classification (QF = 3), selected among the brightest (flux densities $200\,\mu\text{Jy} < S_{1.4\,\text{GHz}} < 400\,\mu\text{Jy}$) and unresolved (on arcsec-scale) sources. We added a control sample of four RL AGN that satisfy the same criteria, selected to match as close as possible flux density and redshift distributions of the RQ AGN. This control sample not only allows us to check our data analysis procedure, but also measures the fraction of RL AGN detected in LBA observations.

The VLBI observations took place in five different runs, between March 2014 and March 2015, for a total of 51.5 hours. Seven radio telescopes were asked for this experiment, with actual availability depending on the run. In Table 2.1 is reported the synopsis of the runs.

Four of the requested telescopes are part of the Australia Telescope National Facility (ATNF), and are operated by the Commonwealth Scientific and Industrial Research Organisation (CSIRO): the 12-m diametre antenna 1 of the ASKAP facility, located at the Murchison Radio-astronomy Observatory (MRO); the phased array Australia Telescope Compact

Table 2.1: Observation runs of the project.

Run	Start Date	UT range	Target(s)	Antennas						
(1)	(2)	(3)	(4)	(5)						
A	09/03/2014	0/02:30:00 – 0/12:00:00	RQ26, RL106, RL728	AK	AT	Cd	Ho	Mp	Pa	
B	04/06/2014	0/18:00:00 – 1/05:00:00	RQ174, RQ851		AT	Cd		Mp	Pa	Ti
C	26/11/2014	0/07:00:00 – 0/19:00:00	RL183, RL287	AK	AT	Cd	Ho		Pa	Ti
D	30/03/2015	0/00:00:00 – 0/10:00:00	RQ851		AT	Cd	Ho	Mp	Pa	
E	31/03/2015	0/22:00:00 – 1/07:00:00	RQ76		AT	Cd	Ho	Mp	Pa	

Run	t_{Obs}	ν_{Obs}	IFs	CHANs	BW per IF	Total BW	ϑ_{MAX}
	(hrs)	(GHz)		per IF	(MHz)	(MHz)	(arcsec)
(1)	(6)	(7)	(8)	(9)	(10)	(11)	(12)
A	9.5	1.666	8	16	8.0	64.0	0.326
B	11	1.650	2	32	16.0	32.0	0.329
C	12	1.410	1	128	64.0	64.0	0.160
D	10	1.410	1	128	64.0	64.0	0.385
E	9	1.410	1	128	64.0	64.0	0.385
Total	51.5						

UT = Universal Time; AK = ASKAP; AT = ATCA; Cd = Ceduna; Ho = Hobart; Mp = Mopra; Pa = Parkes; Ti = Tidbinbilla; t_{Obs} = Observation time; ν_{Obs} = Average frequency of observation; IFs = Intermediate Frequencies; CHANs = Channels; BW = Bandwidth; ϑ_{MAX} = Maximum angular size of sensitivity.

Array (ATCA), located in the Paul Wild Observatory near Narrabri; the Mopra 22-m antenna near Coonabarabran; and the 64-m antenna of the Parkes Radio Telescope, located near the town of Parkes. The Narrabri phased array consisted of five antennas of 22-m diametre each; it observed in tied array mode (i.e., the voltages of each antenna are added together directly) arranged in ultra compact configurations (EW367 for runs A and C; EW352 for run B; H214 for runs D and E)[8].

Two of the requested antennas are operated by the University of Tasmania: the 30-m antenna of the Ceduna Radio Observatory, located near Ceduna; and the 26-m antenna of the Mount Pleasant Observatory, located near Hobart.

Lastly, we asked for the 70-m diametre antenna located in the Canberra Deep Space Communication Complex (CDSCC), operated by the United States government agency National Aeronautics and Space Administration (NASA). In Table 2.2 is reported an overview of the main characteristics of the involved antennas.

The bandwidth of each run was 64 MHz (except for run B, 32 MHz), with a spectral resolution of 500 kHz. The average observing frequencies were 1.666 GHz (run A), 1.650 GHz (run B), and 1410 GHz (runs C, D, and E). The data were correlated at the Pawsey Centre for Supercomputing, with an integration time of 2 seconds to prevent time smearing.

The observing strategy was designed to cope with the faintness of the targets. We observed in cycles of six minutes by switching between target and phase calibrator (respectively, 70% and 30% of the time of each cycle). Every 1–1.5 hours, at least 5 minutes have been devoted to point the fringe finder. When more than one target was present (runs A, B, and C), the six-minutes cycles have been shared among the targets, with dedicated time

[8]EW367 and EW352 are East-West linear configurations, with a maximum baseline of 367 and 352 m, respectively; H214 is a 'T'-shaped configuration, with three antennas on the East-West branch of the array, and two antennas on the North-South spur, with a maximum baseline of 247 m.

Table 2.2: Overview of the antenna characteristics.

Antenna		Diametre	Effective Area	SEFD (Jy)	SEFD (Jy)	T_{sys} (K)	T_{sys} (K)
		(m)	(m^2)	(1.4 GHz)	(1.6 GHz)	(1.4 GHz)	(1.6 GHz)
(1)	(2)	(3)	(4)	(5)	(6)	(7)	(8)
ASKAP	AK	12	18.85	6000	6000	41.0	41.0
ATCA	AT	22 (× 5)	34.56 (× 5)	66	66	4.1	4.1
Ceduna	Cd	30	47.12	900	800	15.4	13.7
Hobart	Ho	26	40.84	470	420	7.0	6.2
Mopra	Mp	22	34.56	340	340	4.3	4.3
Parkes	Pa	64	100.53	40	42	1.5	1.5
Tidbinbilla	Ti	70	109.96	$23^{(a)}$	23	$0.9^{(a)}$	0.9

SEFD = System Equivalent Flux Density, as reported by the official CSIRO web page[a]. Cols. 5 and 7 values (1.4 GHz) have been used for the runs C, D and E; Cols. 6 and 8 values (1.6 GHz) have been used for the runs A and B. The values of the system temperature (Cols. 7 and 8) have been computed following the formula: $T_{sys} = (SEFD \times A_{eff})/(2\,k_B)$, where A_{eff} is the effective area of the telescope (Col. 4), and $k_B = 1.38 \times 10^3$ Jy m^2 K^{-1} is the Boltzmann's constant. $^{(a)}$ The SEFD for Tidbinbilla at 1.4 GHz is only presumed; at the epoch of observations and data reduction none information was provided for this value.

[a] http://www.atnf.csiro.au/vlbi/dokuwiki/doku.php/lbaops/lbacalibrationnotes/nominalsefd.

inversely proportional to their brightness. This allowed to optimise the (u,v)-plane coverage for each target. Overall, in each run ~68% of the time was devoted to the target(s), ~25% to the phase calibrator, and ~7% to the fringe finder.

As fringe finder we used QSO B0208-512 (also: J0210-5101, 0208-512), located about 28 degrees away from the targets (RA: 02^h 10^m 46.200427^s; Dec: -51° 01' 01.89178"). As phase calibrator we used QSO J0348-2749 (also: 0346-279), about 3.85 degrees away from the targets (RA: 03^h 48^m 38.144578^s; Dec: -27° 49' 13.56570"). Both these sources were already targeted by Middelberg et al. (2011a) in their study of the field with VLBA (see Sect. 3.1).

Data calibration and imaging were carried out with the *Astronomical Image Processing System* (AIPS)[9] software package. As a first step we applied onsource flagging (provided by ATNF) and manual flagging using the task `UVFLG`. Ionospheric Faraday rotation and dispersive delay were corrected for using `VLBATECR`, and cross-correlation amplitude spectra were calibrated from auto-correlation data using `ACCOR`. We used `CLCOR` to correct the nominal gain for each antenna (see Table 2.2, Cols. 5 and 6), and corrected for parallactic angle using the task `VLBAPANG`. We then corrected the instrumental phases and delays using the fringe finder and `VLBAMPCL`. Finally, we referred the phases of our targets to the phase of the phase calibrator through the task `VLBAFRGP`. When needed, a band-pass calibration was applied with the task `BPASS`.

The a priori calibration was followed by a series of phase-only and amplitude+phase self-calibrations runs on the phase calibrator. As first step, we manually removed the phase calibration data affected by interferences using the task `IBLED`, then we `SPLIT`ted the phase calibrator from the multi-data file, and we applied the tasks `IMAGR` and `CALIB` in the loops

[9] http://www.aips.nrao.edu/index.shtml

of self-calibration. After each loop, we checked for the improvement in the dynamic range (D.R.) of the resultant image. The solution was used to calibrate the multi-data file, and then the targets were SPLITted.

We imaged the UV data with the task IMAGR into 2048×2048 pixel maps, with a pixel size of 1×1 mas^2 and natural weighting, and combining all the channels at this stage to increase sensitivity and UV coverage. The images were cleaned with the Cotton-Schwab algorithm in a circle of 512 pixels radius centred on the detections. Typical restoring beams are $\sim 65 \times 42$ mas^2.

2.2.2 Results

Run C (RL183 and RL287) was affected by severe problems that prevented a good outcome. AK and Ti observed only for fractions of the planned time (6 discontinuous and 3 hours, respectively), Cd suffered a disk failure resulted in total data loss, and AT and Pa were on source with 1 and 2 (respectively) hours delay. Ho was therefore the only full-operational antenna. Of the remaining six sources successfully observed (two RL and four RQ AGN), three were detected: one RL AGN (RL106) and two RQ AGN (RQ851 and RQ76). For the others 3σ upper limits were set.

2.2.2.1 Detected Sources

RL106

Source 106 of the Miller et al. (2013) catalogue (RA: $03^h\,31^m\,30.75^s$; Dec: -27° 57' 35.1") is classified as a RL AGN by Bonzini et al. (2013) because of its high radio excess ($q_{24\,obs} = -0.99 \pm 0.08$; Lutz et al. 2011) and its location inside the IRAC colour-colour diagram, where it lies well within the region occupied by elliptical galaxies ($\mathrm{Log}(S_{5.8\,\mu\mathrm{m}}/S_{3.6\,\mu\mathrm{m}}) = -0.48 \pm 0.04$; $\mathrm{Log}(S_{8.0\,\mu\mathrm{m}}/S_{4.5\,\mu\mathrm{m}}) = -0.52 \pm 0.05$; Lonsdale et al. 2003; Surace et al. 2005).

The optical counterpart, located ~ 1.3" away from the Miller et al. source (see Fig. 2.4, top-left and -right), has AB-magnitudes 18.72, 16.94, 16.09, 15.19, and 13.44 in the U, B, V, R, and I-bands, respectively (Damen et al., 2011).

We detected a VLBI counterpart at the same position of the Miller et al. coordinates (RA: $03^h\,31^m\,30.75^s$; Dec: -27° 57' 35.1"; see Fig. 2.4, bottom-left), with a peak flux density of 155 μJy (S/N ratio ~ 9.1) out of the 360 μJy of the VLA detection (Miller et al., 2013). The AGN radio emission at VLBI scales accounts for (at least) $\sim 43\%$ of the total radio emission. Being a RL AGN, the undetected radio flux (see Table 2.3, Cols. 14 and 15), is probably due to resolved AGN structures (e.g. jets), that could not be detected due to the limited (u,v)-plane coverage (see Table 2.3, Col. 13; and Sect. 2.3).

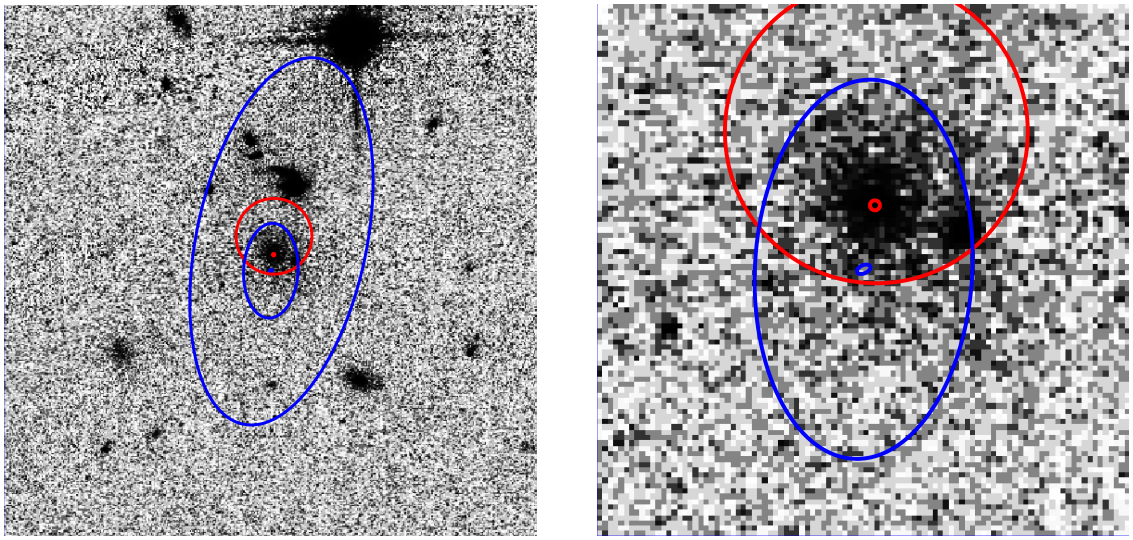

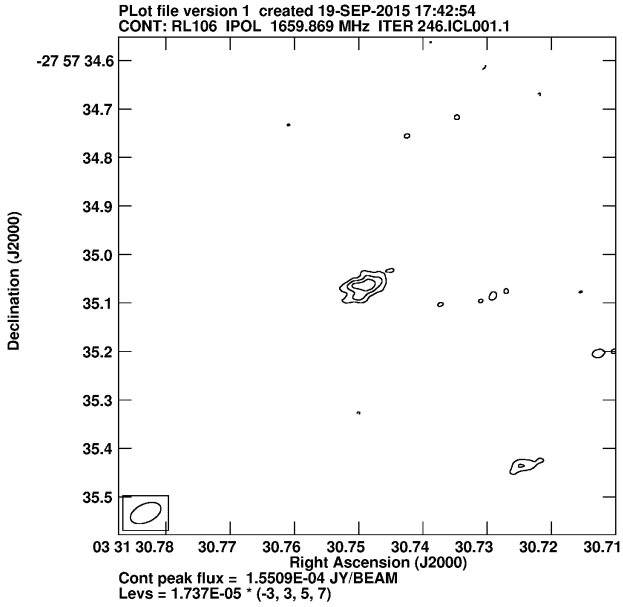

Figure 2.4: Images of RL 106:
(*Top*) HST images centred on the radio source 106 from the catalogue of Miller et al. (2008), with inverted colour maps. Both images have a resolution of 0.05×0.05 arcsec^2/pxl and are $\sim 20 \times 20$ (*Left*) and $\sim 5 \times 5$ (*Right*) arcsec^2 wide. The images come from the 'Total image'[a], and are part of the HST program GO-12866 (PI: Swinbank). The bigger blue ellipse refers to ATLAS source C374 by Norris et al. (2006); the intermediate blue ellipse is MBF 106 by Miller et al. (2013); the smaller blue ellipse is our LBA detection. The big red circle is the position of the optical and infrared counterpart, as reported by Damen et al. (2011), while the small red circle is the position of the HST counterpart as reported by Swinbank. The axes of the ellipses have been computed as 3σ of the PSF ($1.274 \times$ PSF) of each catalogue.
(*Bottom*) LBA detection. The isophotes are drawn at -3, 3, 5 and 7 times the image 1σ noise ($17.4\,\mu$Jy). The image is $\sim 1 \times 1$ arcsec^2 wide. From Maini et al. (2016a).

[a] i.e., the image obtained combining all the different wavelength filters available within the area; see http://hla.stsci.edu/hla_faq.html for more details

RQ76

Source 76 of the Miller et al. (2013) catalogue (RA: $03^{h}\,31^{m}\,25.30^{s}$; Dec: -27° 59' 59.0") is classified as a RQ AGN by Bonzini et al. (2013) because it does not have a radio excess ($q_{24\,obs}$ = 0.54±0.03; Lonsdale et al. 2003; Surace et al. 2005), has a powerful X-ray emission ($L_{2-8\,\mathrm{keV}} = (4.2 \pm 0.3) \times 10^{44}\,\mathrm{erg\,s^{-1}}$; Lehmer et al. 2005), and is located in the IRAC colour-colour diagram within the AGN wedge ($\mathrm{Log}(S_{5.8\,\mu\mathrm{m}}/S_{3.6\,\mu\mathrm{m}})$ = 0.50±0.03; $\mathrm{Log}(S_{8.0\,\mu\mathrm{m}}/S_{4.5\,\mu\mathrm{m}})$ = 0.60±0.02; Lonsdale et al. 2003; Surace et al. 2005).

The optical counterpart, located ~ 0.67" away from the Miller source (see Fig. 2.5, top-left and -right), has AB-magnitudes 16.87, 16.33, 16.14, 15.69, and 15.02 in the *U*, *B*, *V*, *R*, and *I*-bands, respectively (Damen et al., 2011).

We detected a VLBI counterpart ~ 1.2" away from the VLA coordinates (RA: $03^{h}\,31^{m}\,25.23^{s}$; Dec -27° 59' 58.3"; see Fig. 2.5, bottom-left), with a peak flux density of 186 μJy (S/N ratio ~ 8.1) out of the 269 μJy of the VLA flux density (Miller et al., 2013). The AGN radio emission at VLBI scales accounts for (at least) ~ 69% of the total radio emission. The offset between the two radio positions is significant, but our detection lies inside the (large) positional error ellipse of the radio source ($2.9 \times 1.6\,\mathrm{arcsec}^2$) reported by Miller et al. (2013), is only 0.77" far from the HST counterpart (Rix et al., 2004), and there is no other radio emission detected by the VLA which is consistent with the measured VLBI detection. We therefore conclude that the VLBI detection is unambiguously the same source as the VLA detection, and the offset may be explained in terms of extended structures, with the emission perhaps associated with a knot in the jet.

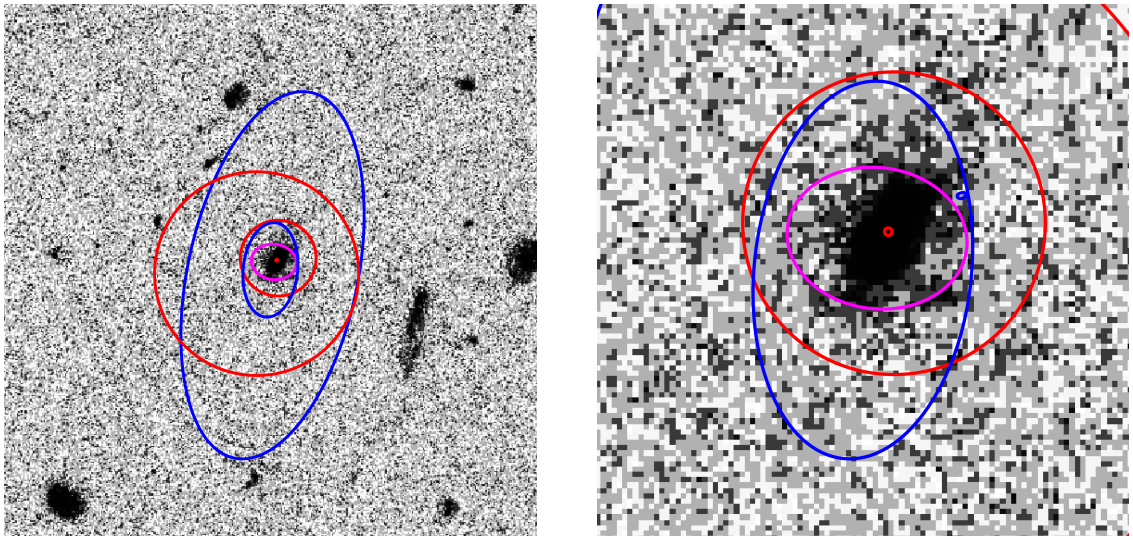

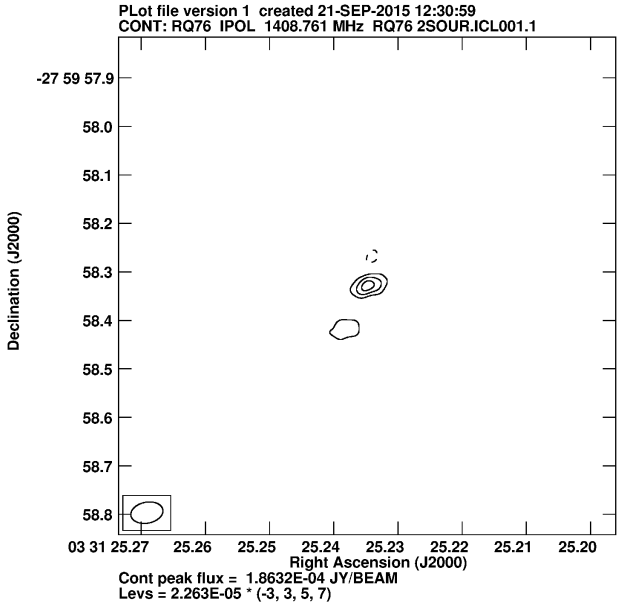

Figure 2.5: Images of RQ 76:
(*Top*) HST images centred on the radio source 76 from the Miller et al. (2008) catalogue, with inverted colour maps. Both images have a resolution of 0.05×0.05 arcsec^2/pxl and are $\sim 20 \times 20$ (*Left*) and $\sim 5 \times 5$ (*Right*) arcsec^2 wide. The images come from the 'Total image'[a], and are part of the HST program GO-9500 (PI: Rix). The bigger blue ellipse refers to ATLAS source C358 by Norris et al. (2006); the intermediate blue ellipse is MBF 76 by Miller et al. (2013); the smallest blue ellipse is our LBA detection. The bigger red circle is the position of the 24 μm detection by MIPS (Lonsdale et al., 2003; Surace et al., 2005), the intermediate red circle is the position of the optical and infrared counterpart as reported by Damen et al. (2011), while the small red circle is the position of the HST counterpart as reported by Rix. In magenta, the position of the X-ray counterpart LBA 47 by Lehmer et al. (2005). The axes of the ellipses have been computed as 3σ of the PSF ($1.274 \times$ PSF) of each catalogue.
(*Bottom*) LBA detection. The isophotes are drawn at -3, 3, 5 and 7 times the image 1σ noise (22.6 μJy). The image is $\sim 1 \times 1$ arcsec^2 wide. From Maini et al. (2016a).

[a] see caption of Figure 2.4 for details

RQ851

Source 851 of the Miller et al. (2013) catalogue (RA: $03^h\,33^m\,36.44^s$; Dec: -27° 43' 55.6") is classified as a RQ AGN by Bonzini et al. (2013) because it has no radio excess ($q_{24\,obs}$ = 0.34±0.03; Lonsdale et al. 2003; Surace et al. 2005) and is located in the the AGN wedge of the IRAC colour-colour diagram ($\mathrm{Log}(S_{5.8\,\mu\mathrm{m}}/S_{3.6\,\mu\mathrm{m}})$ = 0.26±0.03; $\mathrm{Log}(S_{8.0\,\mu\mathrm{m}}/S_{4.5\,\mu\mathrm{m}})$ = 0.14±0.02; Lonsdale et al. 2003; Surace et al. 2005).

The optical counterpart, located ∼0.93" away from the Miller source (see Fig. 2.6, top-left and -right), has AB-magnitudes 17.83, 17.44, 17.22, 16.66, and 15.45 in the *U*, *B*, *V*, *R*, and *I*-bands, respectively (Damen et al., 2011).

We detected a VLBI counterpart ∼0.1" away from the Miller et al. coordinates (RA: $03^h\,33^m\,36.44^s$; Dec: -27° 43' 55.7"; see Fig. 2.6, bottom-left), with a peak flux density of 110 μJy out of the 222 μJy of the VLA detection (Miller et al., 2013). The AGN radio emission at VLBI scales accounts for at least ∼ 50% of the total radio emission. Our VLBI detection has a S/N ratio ∼5.5, and we therefore consider this detection as tentative.

This source is located within the area observed by Middelberg et al. (2011a) in their VLBA experiment (see Sect. 3.1 for further details), but was not detected by them. As reported in Sect. 2.2.1, the sensitivity of the observations was severely limited by the low elevation of the field (∼20°), and RQ851 lies beyond the half-power beamwidth (HPBW) of the VLBA primary beam. Both these factors contributed to the non-detection.

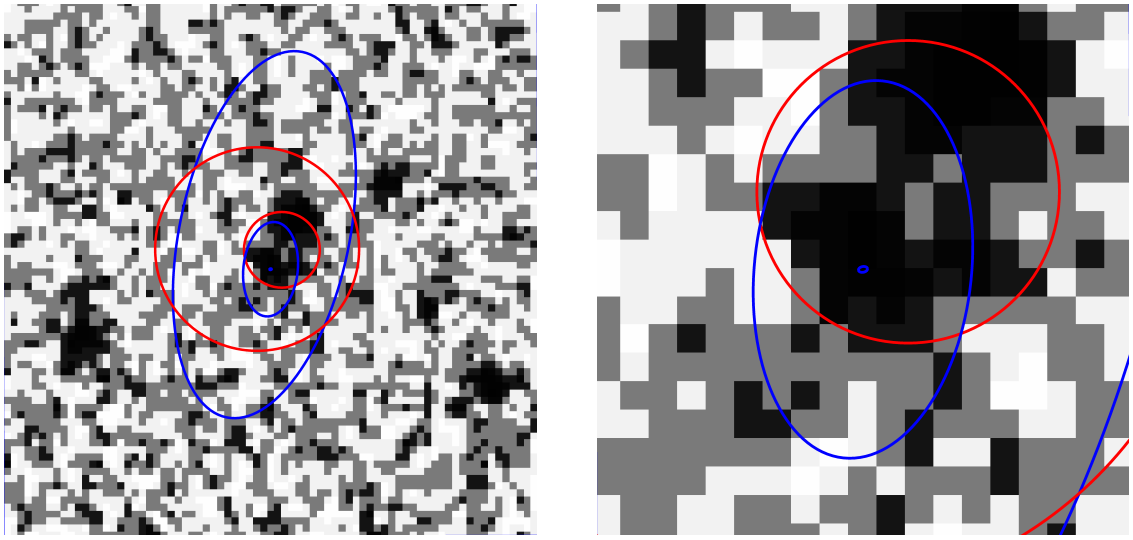

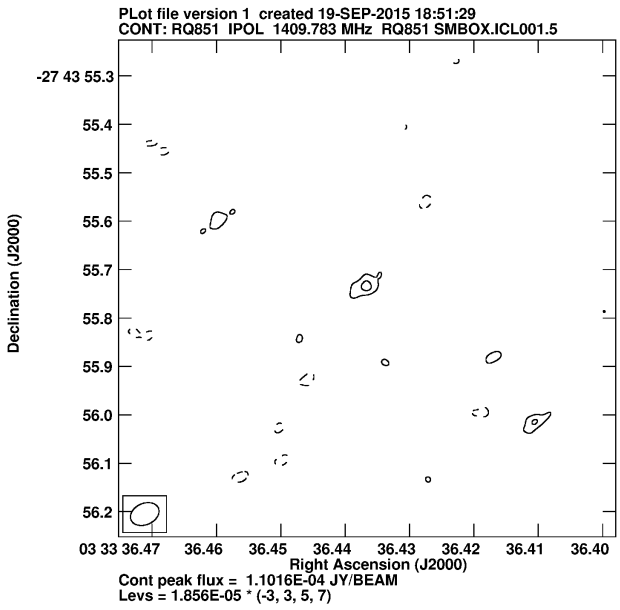

Figure 2.6: Images of RQ 851:
(*Top*) MUSYK images centred on the radio source 851 from the catalogue of Miller et al. (2008), with inverted colour maps. Both images have a resolution of 0.267×0.267 arcsec^2/pxl and are $\sim 20 \times 20$ (*Left*) and $\sim 5 \times 5$ (*Right*) arcsec^2 wide. The images are in the K-band, and are part of the MUSYC project (Cardamone et al., 2010). The bigger blue ellipse refers to ATLAS source C592 by Norris et al. (2006); the intermediate blue ellipse is MBF 851 by Miller et al. (2013); the smallest blue ellipse is our LBA detection. The bigger red circle is the position of the 24 μm detection by MIPS (Lonsdale et al., 2003; Surace et al., 2005), while the small red circle is the position of the optical and infrared counterpart, as reported by Damen et al. (2011). The axes of the ellipses have been computed as 3σ of the PSF ($1.274 \times$ PSF) of each catalogue.
(*Bottom*) LBA detection. The isophotes are drawn at -3, 3, 5 and 7 times the image 1σ noise (18.6 μJy). The image is $\sim 1 \times 1$ arcsec^2 wide. From Maini et al. (2016a).

2.2.2.2 Undetected Sources

RQ26

Source 26 of the Miller et al. (2013) catalogue (RA: $03^h\,31^m\,14.46^s$; Dec: -27° 55' 46.59") is classified as a RQ AGN by Bonzini et al. (2013) because of its robust IR excess ($q_{24\,obs}$ = 1.05±0.02; Lonsdale et al. 2003; Surace et al. 2005) and location in the AGN wedge of the IRAC colour-colour diagram ($\mathrm{Log}(S_{5.8\,\mu\mathrm{m}}/S_{3.6\,\mu\mathrm{m}})$ = 0.84±0.03; $\mathrm{Log}(S_{8.0\,\mu\mathrm{m}}/S_{4.5\,\mu\mathrm{m}})$ = 0.97±0.03; Lonsdale et al. 2003; Surace et al. 2005).

We found no VLBI counterpart down to a 3σ flux density level of ~ 157 μJy, or ~ 50% of the VLA flux density of 318 μJy (Miller et al., 2013).

RQ174

Source 174 of the Miller et al. (2013) catalogue (RA: $03^h\,31^m\,44.01^s$; Dec: -27° 38' 35.12") is classified as a RQ AGN by Bonzini et al. (2013) because of a significant IR excess ($q_{24\,obs}$ = 0.13±0.03; Lonsdale et al. 2003; Surace et al. 2005) and powerful X-ray emission ($L_{2-8\,\mathrm{keV}}$ = (6.6 ± 3.2) × 10^{43} erg s^{-1}; Lehmer et al. 2005).

We found no VLBI counterpart down to a 3σ flux density level of ~ 125 μJy, or ~ 42% of the VLA flux density of ~ 300 μJy (Miller et al., 2013).

RL728

Source 728 of the Miller et al. (2013) catalogue (RA: $03^h\,33^m\,11.79^s$; Dec: -27° 41' 38.26") is classified as a RL AGN by Bonzini et al. (2013) because of a slight radio excess ($q_{24\,obs}$ = −0.15±0.02; Lutz et al. 2011) and strong X-ray emission ($L_{2-8\,\mathrm{keV}}$ = (4.2±2.5) × 10^{42} erg s^{-1}; Lehmer et al. 2005). It is located far from the AGN wedge in the IRAC colour-colour diagram ($\mathrm{Log}(S_{5.8\,\mu\mathrm{m}}/S_{3.6\,\mu\mathrm{m}})$ = −0.19±0.01; $\mathrm{Log}(S_{8.0\,\mu\mathrm{m}}/S_{4.5\,\mu\mathrm{m}})$ = −0.06±0.002; Damen et al. 2011).

We found no VLBI counterpart down to a 3σ flux density level of ~ 109 μJy, or ~ 30% of the VLA flux density of ~ 326 μJy (Miller et al., 2013).

It is interesting to note that, based on the new FIR SFR estimation reported by Bonzini et al. (2015), this source is associated with a SB galaxy (see Table 2.3). We can therefore argue that this is most likely a misclassified source.

2.3 Nature of VLBI detections

For a long time, VLBI detections have been regarded as unambiguous evidence of AGN-driven radio emission. This is in part because past VLBI observations were sensitive only to surface brightness temperatures $T_B \gg 10^6$ K, and AGN are the only non-thermal sources able to reach for such high temperatures. Moreover, no thermal mechanism (e.g. supernova explosions) can reach such high temperatures in radio. Therefore, VLBI detections meant secure non-thermal mechanisms for the emissions, and confirmation of an AGN.

Due to recent improvements in sensitivity, the VLBI technique can now sample regimes ($T_B < 10^5$ K) were a wider range of mechanisms can account for the observed radio emission. For example, Kewley et al. 2000 observed a sample of 61 local ($z < 0.025$) *IRAS* FIR-luminous galaxies, using the Parkes-Tidbinbilla Interferometre at 2.3 GHz. They found a compact radio core in ~ 37% of objects classified as star-burst galaxies, and in ~ 80% of those classified as AGN, down to a sensitivity limit of 1 mJy. These compact cores show a bi-modal distribution, and Kewley et al. 2000 explained this dichotomy observing that compact sources with luminosity $L_{2.3\,\mathrm{GHz}} \gtrsim 1.7 \times 10^{21}$ W Hz^{-1} are real AGN, while cores with a lower radio luminosity are most likely caused by complexes of compact (1–3 pc diametre) supernova remnants (SNR) of very high ($\lesssim 10^5$ K) brightness temperature.

As a VLBI detection is no longer a definite sign of an AGN, each detection requires

Table 2.3: Summarised characteristics of the targets.

Target	S_{VLA} (μJy)	S_{VLBI} (μJy)	S_{VLBI}/S_{VLA}	r.m.s. (μJy/beam)	z	Spectral index[(d)]	K-corr. $L_{1.4\,\mathrm{GHz}}{}^{VLBI}$ ($\times 10^{23}$ W Hz^{-1})	Host type[(e)]
(1)	(2)	(3)	(4)	(5)	(6)	(7)	(8)	(9)
RL106	360.0 ± 14.7	155 ± 29	0.43 ± 0.08	17	1.06[(a)]	$-(0.52 \pm 0.09)$	6.6 ± 1.2	P
RQ851	221.5 ± 15.1	110 ± 26	0.50 ± 0.12	19	1.35[(b)]	-0.75	9.7 ± 2.3	MS
RQ76	268.5 ± 15.7	186 ± 36	0.69 ± 0.14	23	1.38[(c)]	-0.75	17.2 ± 3.3	SB
RQ26	318.3 ± 16.6	$\lesssim 157$	...	52	1.59[(c)]	$-(0.27 \pm 0.23)$	...	–
RQ174	299.8 ± 14.0	$\lesssim 125$	...	42	2.85[(a)]	$-(0.78 \pm 0.12)$	...	MS
RL728	326.2 ± 13.2	$\lesssim 109$	...	36	1.08[(c)]	$-(0.75 \pm 0.17)$	...	SB

Target	Restoring beam (mas^2)	T_B ($\times 10^4$ K)	Linear size (pc)	Max. linear size of sensitivity (kpc)	ν^{YSN} (SN yr^{-1})	ν^{SNR} (SN yr^{-1})
(1)	(10)	(11)	(12)	(13)	(14)	(15)
RL106	$\sim 67 \times 38$	2.7 ± 0.5	$\lesssim 544 \times 308$	~ 2.6	~ 126	~ 11
RQ851	$\sim 62 \times 44$	2.5 ± 0.6	$\lesssim 521 \times 370$	~ 3.2	~ 163	~ 15
RQ76	$\sim 67 \times 43$	4.0 ± 0.8	$\lesssim 564 \times 362$	~ 3.2	~ 290	~ 26

[(a)] photometric, Rafferty et al. 2011; [(b)] photometric, Taylor et al. 2009; [(c)] spectroscopic, Silverman et al. 2010; [(d)] based on 1.4 GHz data from Hales et al. (2014) and 5.5 GHz data from Huynh et al. (2012). For RQ851 and RQ76, 5.5 GHz information is lacking, and we adopted the value of -0.75 (e.g. Kukula et al. 1998) for the K-correction; [(e)] from Bonzini et al. (2015): P=Passive; MS= main sequence galaxy; SB= starburst galaxy.

further analysis to confirm its physical origin. Indeed, compact radio sources can be associated to very luminous radio supernovae (RSN), compact H II regions, compact SNRs, or AGN-driven radio emission. We consider each class of objects for our VLBI sources below.

In principle, it is possible that we observed transient SN events during our observation session. Brightness temperatures as high as 10^6 K can be expected from very luminous RSNe, like the core-collapse ones. For example, sources exceeding a brightness temperature of 10^5 K have been observed in local star-burst galaxies (e.g., Huang et al. 1994; Smith et al. 1998). The event by itself is highly improbable (to date, only ~ 50 RSNe have been detected in ~ 30 years of observations, usually as follow-up of optical events, see Lien et al. 2011). But, more important, the typical luminosity of these sources is in the range $10^{16.7}$–$10^{21.7}$ W Hz^{-1} (Lien et al., 2011). From the redshifts (see Col. 6 in Table 2.3) we can easily derive the luminosity of our detections. Our objects lie in the luminosity range 10^{23-25} W Hz^{-1} (see Col. 8 in Table 2.3), well above the expected luminosity of RSNe.

Another possibility is that our detections are compact H II regions that are dominated at radio wavelengths by thermal free-free emission. The maximum brightness temperature we expect from such regions can be expressed with (Condon et al., 1991):

$$T_B^{\mathrm{SBG,\,MAX}} \lesssim T_e \left[1 + 10 \left(\frac{\nu}{1\,\mathrm{GHz}} \right)^{0.1-\alpha_{\mathrm{NT}}} \right]$$

where T_e is the thermal electron temperature ($\sim 10^4$ K), and α_{NT} the non-thermal (NT) spectral index (~ 0.8). For the range of frequencies of our observations (from $\nu \sim 1.67$ GHz for run A, to 1.41 GHz for runs C, D and E), the maximum brightness temperature we do expect to detect from SBGs is around 10^4–10^5 K (8.00×10^4 K for run A; 8.04×10^4 K for run B; and 8.86×10^4 K for run C, D and E). Moreover, the expected size of these regions is $\ll 500$ pc. Brightness temperatures and linear sizes of our detection, in principle, are compatible with the compact H II hypothesis (see Cols. 11 and 12 in Table 2.3). However, even the most luminous among these regions (like e.g. 30 Doradus in the Large Magellanic Cloud) do not reach a radio luminosity of 10^{20} W Hz^{-1} (Hughes et al., 2007). All our sources have $L_{1.4\,\mathrm{GHz}}$ at least 3 orders of magnitude larger, ruling out the compact H II region hypothesis.

To rule out the possibility that we detected bright radio SNRs, we can estimate the supernova rate corresponding to the total radio luminosity of the sources. The non-thermal radio luminosity arising from radio-young supernovae (YSN; i.e., SNe exploded since less than 10 years), or from old supernovae remnants (typically, SNe exploded since less than $\sim 10^4$ years) can be related to the SN rates ($\nu_{\rm SN}$) through the equations (Kewley et al., 2000):

$$L_{\rm NT}^{\rm YSN}[{\rm W\,Hz^{-1}}] = 1.58 \times 10^{21} \left(\frac{\nu}{8.44\,{\rm GHz}}\right)^{-0.74} \nu_{\rm SN}$$

$$L_{\rm NT}^{\rm SNR}[{\rm W\,Hz^{-1}}] = 1.77 \times 10^{22} \left(\frac{\nu}{8.44\,{\rm GHz}}\right)^{-0.74} \nu_{\rm SN}$$

where ν is the frequency of observation. In Table 2.3 (Cols. 14 and 15) are reported the expected SN rates for the measured radio powers. These values greatly exceed the rates for even the most extreme SBGs ($\lesssim 0.4\,{\rm SN\,yr^{-1}}$; Mannucci et al. 2003), thus we suggest the VLBI sources are unlikely to be SNRs.

We conclude that, even if VLBI detection is no more unambiguous evidence of AGN, we are confident that the radio emission we detected in our targets is AGN-driven.

A VLBI non-detection of compact cores, on the other hand, does not imply the non-existence of AGN-driven radio emission in the target. It is possible that the AGN-core related radio emission is too faint for the VLBI sensitivity. Alternatively, it is possible that the AGN radio emission is extended. From the formula:

$$\vartheta_{MAX} \sim \frac{\lambda_{average}}{\text{minimum baseline} - \text{maximum dish diametre}}$$

it is possible to estimate the maximum angular size to which our observations are sensitive. These values are provided in Col. 12 of Table 2.1. In Table 2.3, Col. 13, we give the corresponding maximum physical sizes for our detections, computed at the actual redshifts of the targets. The more sensitive radio survey performed in the ECDFS so far is the one by Miller et al. (2008, 2013), with a spatial resolution of 2.8×1.6 arcsec^2, corresponding to a physical scale of ~ 13 kpc at the typical redshift of our sources. We can conclude that the missing flux, whenever strong enough to be detected with the LBA, is likely distributed on scales larger than ~ 3 kpc and smaller than ~ 13 kpc.

Whether this extended kpc-scale emission is associated to AGN (like, e.g., young or frustrated jets) or star-formation activity can not be constrained by our VLBI observations.

2.4 Summary

In this Chapter I presented the work I did to investigate the origin of radio emission in radio-quiet AGN, and which resulted in the paper *Compact radio cores in Radio-Quiet AGNs* (Maini et al., 2016a).

In Sect. 2.1 I reported a short introduction on the scientific background about this topic.

In Sect. 2.2 I reported my original work. I searched for compact radio cores within sources classified as radio-quiet following a set of criteria proposed by Bonzini et al. (2013). I selected a sub-sample of sources from the Bonzini et al. (2012) catalogue, and targeted them with the Australian LBA. Two out of four sources were detected, revealing compact radio cores which account up to $\sim 70\%$ of the total VLA arcsec-scale emission.

In Sect. 2.3 I investigated the nature of the radio emission we detected making use of the VLBI technique, excluding a star-formation-related origin, and concluding with high confidence that we are dealing with AGN-driven radio emission.

3

Further analysis of radio-quiet active galactic nuclei

In this Chapter of the Thesis I present an in-depth analysis on sources classified as RQ AGN following the criteria proposed by Bonzini et al. (2013). In my analysis I include three samples of RQ AGN: the first based on pre-existing VLBI observations by Middelberg et al. (2011a) in the CDFS field as well (Sect. 3.1); the second sample was observed by Herrera Ruiz et al. (2016) and is extracted from the COSMOS field (Sect. 3.2); finally, the third sample is based on a VLBI follow up of the *Hubble* deep field north (HDF-N; Chi et al. 2013) (Sect. 3.3). In Sect. 3.5 I analyse how the VLBI detected emission in these sources can account for most of the radio-excess within these objects, leaving only star-formation activity as origin of the residual radio emission. In Sect. 3.4 I present another compelling evidence that the emission detected with VLBI experiments is due to AGN. Finally, in Sect. 3.6 I present some work I did to search for proxies of AGN radio emission in sources classified as RQ AGN. A short conclusion summarises this Chapter (Sect. 3.7).

3.1 Radio-quiet AGN in the ECDFS field

In this Section I briefly introduce the sample originally studied by Middelberg et al. (2011a) and presented in their Paper *Wide-field VLBA observations of the Chandra deep field South*. For all the sources that were later classified as RQ AGN by Bonzini et al. (2013) (15 out of 96), here I gather multiwavelength information.

Middelberg et al. (2011a) observed at 1.4 GHz with the VLBA a sample of 96 sources in the CDFS field in 2007, targeting sources already observed with the ATCA by Norris et al. (2006). The observations, centred at $03^{h}\,32^{m}\,34.04^{s}$, $-27^{\circ}\,50'\,50.75''$ (J2000), reached an on-axis rms flux density of about $55\,\mu$Jy beam^{-1} at an angular resolution of some tens of milli-arcsec.

The main aim of the original Middelberg et al. (2011a) experiment was to demonstrate the potential of wide-field VLBI techniques which allow to follow up lower-resolution radio

Table 3.1: The full sample of RQ AGN from Middelberg et al. (2011a).

Middelberg ID	Bonzini ID	Coordinates (J2000) R.A. (hh mm ss)	Dec. (+dd mm ss)	S_{VLA} (μJy)	z	$S_{24\mu m}$ (μJy)	$q_{24,obs}$	$S_{3.6\mu m}$ (μJy)	$S_{4.5\mu m}$ (μJy)	$S_{5.8\mu m}$ (μJy)	$S_{8.0\mu m}$ (μJy)	$\mathrm{Log}\left(\frac{S_{5.8\mu m}}{S_{3.6\mu m}}\right)$	$\mathrm{Log}\left(\frac{S_{8.0\mu m}}{S_{4.5\mu m}}\right)$	$L_{2-8\,keV}$ (erg s^{-1})	QF
(1)	(2)	(3)		(4)	(5)	(6)	(7)	(8)	(9)	(10)	(11)	(12)	(13)	(14)	(15)
S360	149	03 31 39.55	−27 41 19.6	202.6 ± 14.1	2.028	1460.8 ± 12.6[a]	0.86 ± 0.03	41.1 ± 1.0[b]	56.9 ± 1.3	88.1 ± 5.3	96.9 ± 5.1	0.33 ± 0.03	0.23 ± 0.03	$< 10^{42.85}$	3
S377	216	03 31 50.79	−27 47 03.9	619.0 ± 12.0	2.259	387.3 ± 10.6[a]	−0.20 ± 0.01	18.4 ± 0.1[c]	21.1 ± 0.1	29.7 ± 0.3	30.4 ± 0.6	0.21 ± 0.01	0.16 ± 0.01	$10^{43.38}$	2
S380	225	03 31 52.13	−27 39 26.6	954.2 ± 13.6	2.296	423.9 ± 12.1[a]	−0.35 ± 0.01	21.0 ± 0.1[c]	28.4 ± 0.1	40.5 ± 0.3	39.7 ± 0.6	0.29 ± 0.01	0.15 ± 0.01	$10^{43.26}$	2
S403	319	03 32 08.56	−27 46 48.4	232.5 ± 13.8	0.310	1137.5 ± 15.0[a]	0.69 ± 0.03	310.3 ± 2.1[b]	284.1 ± 2.4	177.2 ± 6.2	480.3 ± 6.6	−0.24 ± 0.02	0.23 ± 0.01	$10^{41.03}$	2
S416	362	03 32 13.25	−27 42 41.3	88.4 ± 11.2	0.605	782.8 ± 15.1[a]	0.95 ± 0.06	143.2 ± 1.4[b]	96.2 ± 1.6	104.3 ± 5.4	109.2 ± 5.2	−0.14 ± 0.02	0.06 ± 0.02	$10^{43.21}$	3
S417	369	03 32 14.17	−27 49 10.6	121.0 ± 13.0	2.076	131.1 ± 8.3[a]	0.03 ± 0.05	8.4 ± 0.1[c]	11.4 ± 0.1	14.5 ± 0.1	11.8 ± 0.2	0.24 ± 0.01	0.02 ± 0.01	$10^{42.70}$	3
S433	439	03 32 22.61	−27 44 26.2	129.0 ± 12.2	0.738	590.2 ± 13.9[a]	0.66 ± 0.04	97.2 ± 0.1[c]	65.7 ± 0.1	67.7 ± 0.3	56.9 ± 0.2	−0.16 ± 0.01	−0.06 ± 0.01	$10^{41.72}$	2
S450	508	03 32 33.44	−27 52 28.2	141.2 ± 12.8	3.021	365.3 ± 10.2[a]	0.41 ± 0.04	3.4 ± 0.1[c]	5.6 ± 0.4	6.3 ± 0.2	12.9 ± 0.2	0.27 ± 0.02	0.36 ± 0.03	$10^{43.04}$	3
S453	542	03 32 37.74	−27 50 00.5	173.9 ± 11.9	1.619	250.9 ± 9.2[a]	0.16 ± 0.03	31.1 ± 0.1[c]	39.0 ± 0.1	35.8 ± 0.2	31.5 ± 0.2	0.06 ± 0.01	−0.09 ± 0.01	$10^{42.13}$	3
S457	553	03 32 38.93	−27 57 00.8	176.1 ± 12.9	0.297	3488.4 ± 37.2[a]	1.30 ± 0.03	277.4 ± 1.5[b]	315.3 ± 2.6	365.3 ± 5.9	954.2 ± 7.8	0.12 ± 0.01	0.48 ± 0.01	$10^{43.09}$	3
S479	625	03 32 52.56	−27 59 43.2	107.1 ± 12.5	...	200.5 ± 7.3[a]	0.27 ± 0.05	7.9 ± 0.1[c]	9.9 ± 0.1	12.7 ± 0.3	20.6 ± 0.5	0.21 ± 0.01	0.32 ± 0.01	$< 10^{42.80}$	1
S491	686	03 33 04.47	−27 38 02.0	193.7 ± 15.0	1.084	664.4 ± 8.6[a]	0.54 ± 0.03	62.5 ± 1.0[b]	52.9 ± 0.9	44.8 ± 4.5	74.9 ± 3.6	−0.15 ± 0.04	0.15 ± 0.02	$10^{42.43}$	3
S501	709	03 33 09.14	−27 58 46.6	78.5 ± 15.3	0.669	522.4 ± 6.8[a]	0.82 ± 0.08	71.6 ± 1.0[b]	50.0 ± 1.3	44.9 ± 3.6	53.5 ± 5.1	−0.20 ± 0.04	0.03 ± 0.04	$10^{42.53}$	3
S547	843	03 33 34.58	−27 47 51.2	660.0 ± 14.6	0.857	1166.0 ± 17.8[b]	0.25 ± 0.01	68.2 ± 0.6[c]	49.2 ± 0.9	42.3 ± 3.2	65.3 ± 5.8	−0.21 ± 0.03	0.12 ± 0.04	$10^{43.62}$	2
S550	851	03 33 36.44	−27 43 55.6	221.5 ± 15.1	1.345	479.7 ± 17.3[b]	0.34 ± 0.03	54.1 ± 1.1[b]	76.2 ± 1.5	97.8 ± 5.4	106.1 ± 5.2	0.26 ± 0.03	0.14 ± 0.02	$10^{43.49}$	3

[a] from Lutz et al. (2011); [b] from SWIRE DR3 (Lonsdale et al., 2003; Surace et al., 2005); [c] from SEIP. Notes [b] and [c] refer to all Columns from 8 to 11.

Table 3.2: Summarised characteristics of Middelberg et al. (2011a) detection.

Middelberg ID (1)	Bonzini ID (2)	S_{VLA} (μJy) (3)	S_{VLBI} (μJy) (4)	S_{VLBI}/S_{VLA} (5)	z_{phot} (6)	Spectral index[(a)] (7)	K-corr. $L^{VLBI}_{1.4\,GHz}$ ($\times 10^{23}$ W Hz^{-1}) (8)	ν^{YSN} (SN yr^{-1}) (9)	ν^{SNR} (SN yr^{-1}) (10)
S380	225	954.2 ± 13.6	1000 ± 240	1.05 ± 0.25	2.296	−0.55 ± 0.07	236.0 ± 56.6	~ 3953	~ 353

[(a)] based on VLA data at 1.4 and 4.9 GHz, as reported by Kellermann et al. (2008).

fields, providing high sensitivity and parsec-resolution datasets for many sources simultaneously. A new correlation technique was developed for the experiment, and the ECDFS was selected due to its extended coverage at any wavelength. In particular the Norris et al. (2006) catalogue was used as input radio catalogue.

Twenty sources were successfully detected (plus one only tentatively), confirming the technical feasibility of the new wide-field VLBI technique implemented. Most of the detected sources are mJy sources. At the time of the Middelberg et al. (2011a) experiments, 16 out of these 21 sources had a classification provided by Norris et al. (2006), and 14 of them were expected to harbour an AGN.

All the 96 sources targeted by Middelberg et al. (2011a) are also included in the VLA catalogue produced by Miller et al. (2008), and were therefore part of the sample studied by Bonzini et al. (2013) for which a source classification as SFG, RL AGN or RQ AGN was provided. Fifteen of them turn out to be classified as RQ AGN, and only one of them was detected by the VLBI experiment (source 225 of Bonzini et al. 2013, S380 of Norris et al. 2006), but its classification as RQ AGN is not certain (i.e., quality flag 2; see Sect. 2.2.1 for details). Nineteen out of 21 of the VLBI-detected sources are classified as 'secure' RL AGN, and the tentatively detected source is a nearby ($z = 0.08$) 'secure' SFG.

In Table 3.1 are reported the flux densities of the IR and X-ray counterparts of the 15 sources classified as RQ AGN. For the cross matching at 24 μm I used the published catalogue by Lutz et al. (2011) when available, or the SWIRE DR3 (Lonsdale et al., 2003; Surace et al., 2005) catalogues when not. These last catalogues have been used to find also IRAC counterparts when present, otherwise I used the on-line *Spitzer* Enhanced Imaging Products (SEIP)[10] catalogue, which reports measures for both IRAC and MIPS bands. For the X-ray band the cross matching had been already performed by Bonzini et al. (2013).

In Col. 1 the ID of the sources are listed, as reported in Middelberg et al. (2011a) and Norris et al. (2006); Col. 2 lists the IDs as reported by Bonzini et al. (2012). Cols. 3 and 4 list the VLA positions (RA and Dec) and the VLA flux densities and errors from Miller et al. (2013); Col. 5 lists the redshifts of the sources (when available) as reported by Bonzini et al. (2013); Col. 6 lists the MIPS 24 μm flux densities; Cols. 8, 9, 10, and 11 list the IRAC flux densities, while Col. 14 the X-ray luminosities as reported by Bonzini et al. (2013). Finally, Col. 15 lists the classification quality flag as provided by Bonzini et al. (2013).

[10] http://irsa.ipac.caltech.edu/cgi-bin/Gator/nph-scan?submit=Select&projshort=SPITZER; SEIP Source List Catalogue

3.2 Radio-quiet AGN in the COSMOS field

In this Section I report an extended analysis of the sample presented by Herrera Ruiz et al. (2016) in the Letter Unveiling the origin of the radio emission in Radio Quiet Quasars. *For this paper I searched for the infrared counterpart to the radio sources, and double checked the classification of the objects as radio-quiet following the same criteria exposed in Section 2.2. Overall, my contribution to the Letter was around 5%. The text in the following Section was written by myself and is based upon the work I performed for Herrera Ruiz et al. (2016).*

To advance the understanding on how AGN populate the faint radio population, Herrera Ruiz et al. (in prep.) took a statistical approach, observing $\sim$ 3000 radio sources from the Schinnerer et al. (2010) COSMOS field at 1.54 GHz. Schinnerer et al. (2010) observed the 2 deg^2 field with the VLA, producing a mosaic with 1σ sensitivity of $\sim 12\,\mu$Jy beam^{-1} in the central 50×50 arcmin^2 at an angular resolution of 2.5×2.5 arcsec^2. Herrera Ruiz et al. (in prep.) observed the field with the VLBA, reaching 1σ sensitivity of $\sim 10\,\mu$Jy beam^{-1} in the central part of the field at a milli-arcsec resolution. They detected 468 radio sources with VLBI with a S/N ratio higher than 5.5.

As side project they checked if any of the VLBA detections was actually associated with RQQs. As a first step they searched for quasars, by cross matching the Schinnerer et al. (2010) radio catalogue with the Half Million Quasars catalogue by Flesch (2015), with a matching radius of 0.5". In total 38 counterparts were identified, 24 of which confirmed as quasar by the $M_{B-\mathrm{band}} < -23$ quasar definition introduced by Schmidt & Green (1983), the others characterised by fainter B-band luminosities.

To distinguish between RL and RQ sources, Herrera Ruiz et al. (2016) used two criteria:

- The intrinsic infrared-to-radio luminosity ratio ($q_{24\,int} = \mathrm{Log}(L_{24\,\mu\mathrm{m}}/L_{1.4\,\mathrm{GHz}})$), as defined by Appleton et al. (2004). A source is considered as potentially RQ when $q_{24\,int} > 0$;
- The observed radio-to-optical ratio ($R_V = \mathrm{Log}(S_{1.4\,\mathrm{GHz}}/S_V)$), as defined by Padovani et al. (2009, 2011). A source is considered as potentially RQ when $R_V < 1.4$.

Given that the 24 μm luminosity could be contaminated by AGN emission, a source is classified as RQ only when both these criteria are satisfied. A total of 22 sources out of 38 fit this RQ classification, 18 of which confirmed as quasars (i.e. $M_{B-\mathrm{band}} < -23$). Herrera Ruiz et al. (2016) detected 3 of these sources with the VLBA, all of them confirmed quasar. To ensure that these sources are correctly classified as RQ, they extensively studied these objects at different wavelengths following several of the radio-loudness criteria discussed by Hao et al. (2014).

My personal contribution to the work was to apply the Bonzini et al. (2013) RQ AGN criteria using the process outlined in Sec. 2.2.1, as a further check on their nature.

For the *Spitzer* IRAC bands, I performed a cross matching either with the published catalogue by Richards et al. (2009) or with the on-line catalogue SEIP. For the MIPS 24 μm

Table 3.3: The full sample of RQ AGN from Herrera Ruiz et al. (2016).

COSMOS-VLBA ID	Coordinates (J2000) R.A.	Dec.	$S^{(a)}_{VLA}$	z	$S_{24\mu m}$	$q_{24,obs}$	$S_{3.6\mu m}$	$S_{4.5\mu m}$	$S_{5.8\mu m}$	$S_{8.0\mu m}$	$\mathrm{Log}\left(\frac{S_{5.8\mu m}}{S_{3.6\mu m}}\right)$	$\mathrm{Log}\left(\frac{S_{8.0\mu m}}{S_{4.5\mu m}}\right)$	$L_{2-10\,keV}$	QF
	(hh mm ss)	(+dd mm ss)	(μJy)		(μJy)		(μJy)	(μJy)	(μJy)	(μJy)			(erg s^{-1})	
(1)	(2)		(3)	(4)	(5)	(6)	(7)	(8)	(9)	(10)	(11)	(12)	(13)	(14)
C0304	9 58 29.23	+2 15 42.77	90 ± 15 ^{U}	0.946$^{(b)}$	1081.0 ± 22.0	1.08 ± 0.07	120.4 ± 0.2	114.3 ± 0.2	120.3 ± 0.7	152.1 ± 1.4	0.000 ± 0.003	0.124 ± 0.004	$10^{43.07}$ $^{(e)}$	3
C0366	9 58 35.98	+1 51 57.08	362 ± 15 ^{R}	2.939$^{(c)}$	664.0 ± 17.0	0.26 ± 0.02	120.1 ± 0.2	130.8 ± 0.3	160.9 ± 0.8	265.1 ± 1.4	0.127 ± 0.002	0.307 ± 0.003	$10^{44.01}$ $^{(e)}$	3
C1049	9 59 40.75	+2 19 38.85	430 ± 11 ^{U}	1.459$^{(b)}$	1382.0 ± 253.0	0.51 ± 0.08	138.3 ± 0.2	224.4 ± 0.3	344.5 ± 0.9	528.4 ± 1.6	0.396 ± 0.001	0.372 ± 0.001	$10^{44.75}$ $^{(e)}$	3
C1061	9 59 42.10	+2 41 3.13	101 ± 14 ^{U}	1.795$^{(b)}$	978.0 ± 224.0	0.99 ± 0.12	58.7 ± 0.1	94.3 ± 0.2	166.8 ± 0.7	251.1 ± 1.3	0.454 ± 0.002	0.425 ± 0.002	$10^{43.84}$ $^{(e)}$	3
C1080	9 59 43.42	+2 7 7.26	259 ± 17 ^{R}	2.220$^{(d)}$	1368.0 ± 15.0	0.72 ± 0.03	110.5 ± 0.2	169.7 ± 0.3	307.1 ± 0.9	520.5 ± 1.4	0.444 ± 0.001	0.487 ± 0.001	$10^{44.43}$ $^{(e)}$	3
C1107	9 59 46.02	+2 47 43.58	214 ± 20 ^{U}	1.067$^{(b)}$	3763.0 ± 24.0	1.25 ± 0.04	421.7 ± 0.5	595.0 ± 0.6	902.6 ± 1.3	1325.6 ± 2.0	0.330 ± 0.001	0.348 ± 0.001	$10^{44.57}$ $^{(f)}$	3
C1397	10 0 8.92	+2 14 40.63	293 ± 11 ^{U}	2.536$^{(d)}$	2932.0 ± 163.0	1.00 ± 0.03	152.8 ± 0.2	223.1 ± 0.3	408.1 ± 0.8	721.6 ± 1.4	0.427 ± 0.001	0.510 ± 0.001	$10^{43.47}$ $^{(e)}$	3
C1457	10 0 14.08	+2 28 38.85	146 ± 11 ^{U}	1.253$^{(b)}$	1345.0 ± 17.0	0.96 ± 0.03	140.9 ± 0.2	225.5 ± 0.3	330.8 ± 0.7	493.7 ± 1.4	0.371 ± 0.001	0.340 ± 0.001	$10^{44.05}$ $^{(e)}$	3
C1483	10 0 16.30	+1 51 4.47	79 ± 12 ^{U}	1.134$^{(b)}$	1661.0 ± 32.0	1.32 ± 0.07	123.6 ± 0.2	152.0 ± 0.3	199.6 ± 0.8	281.9 ± 1.5	0.208 ± 0.002	0.268 ± 0.002	$10^{44.21}$ $^{(e)}$	3
C1726	10 0 34.94	+2 2 34.87	59 ± 10 ^{U}	1.180$^{(b)}$	572.0 ± 18.0	0.99 ± 0.07	93.3 ± 0.2	107.7 ± 0.2	132.9 ± 0.8	174.2 ± 1.4	0.154 ± 0.003	0.209 ± 0.004	$10^{44.21}$ $^{(e)}$	3
C1756	10 0 38.01	+2 8 22.57	347 ± 12 ^{R}	1.825$^{(b)}$	1589.0 ± 115.0	0.66 ± 0.03	116.9 ± 0.2	174.8 ± 0.3	258.0 ± 0.8	354.7 ± 1.4	0.344 ± 0.002	0.307 ± 0.002	$10^{44.29}$ $^{(e)}$	3
C1856	10 0 46.80	+1 47 37.28	57 ± 16 ^{U}	1.851$^{(b)}$	605.0 ± 15.0	1.03 ± 0.12	58.4 ± 0.1	84.0 ± 0.2	125.0 ± 0.6	147.4 ± 1.3	0.330 ± 0.002	0.244 ± 0.004	$10^{43.97}$ $^{(e)}$	3
C1861	10 0 46.93	+2 0 15.97	137 ± 16 ^{U}	1.920$^{(b)}$	1100.0 ± 21.0	0.90 ± 0.05	75.0 ± 0.1	110.8 ± 0.2	187.0 ± 0.7	273.9 ± 1.3	0.397 ± 0.002	0.393 ± 0.002	$10^{44.37}$ $^{(e)}$	3
C1897	10 0 49.91	+2 5 0.01	311 ± 16 ^{R}	1.240$^{(c)}$	2983.0 ± 87.0	0.98 ± 0.03	249.8 ± 0.3	407.5 ± 0.4	638.5 ± 1.1	966.2 ± 1.6	0.408 ± 0.001	0.375 ± 0.001	$10^{44.70}$ $^{(e)}$	3
C1950	10 0 55.38	+2 34 41.55	78 ± 12 ^{U}	1.403$^{(b)}$	1392.0 ± 20.0	1.25 ± 0.07	99.7 ± 0.2	166.1 ± 0.3	254.9 ± 0.8	407.6 ± 1.7	0.408 ± 0.002	0.390 ± 0.002	$10^{44.46}$ $^{(e)}$	3
C1968	10 0 56.71	+2 17 20.71	37 ± 9 ^{U}	2.078$^{(b)}$	278.0 ± 17.0	0.88 ± 0.11	31.0 ± 0.1	41.5 ± 0.2	64.1 ± 0.7	88.5 ± 1.5	0.315 ± 0.005	0.329 ± 0.008	$10^{44.06}$ $^{(e)}$	3
C2412	10 1 30.37	+1 43 4.34	263 ± 16 ^{U}	1.571$^{(b)}$	829.0 ± 17.0	0.50 ± 0.03	47.2 ± 0.1	69.0 ± 0.2	103.6 ± 0.6	188.7 ± 1.4	0.341 ± 0.003	0.437 ± 0.003	$10^{44.16}$ $^{(e)}$	3
C2565	10 1 41.32	+2 10 31.26	95 ± 12 ^{U}	0.982$^{(b)}$	619.0 ± 44.0	0.81 ± 0.06	133.0 ± 0.2	144.3 ± 0.2	186.7 ± 0.7	223.3 ± 1.3	0.147 ± 0.002	0.190 ± 0.003	$10^{44.11}$ $^{(e)}$	3
C2701	10 1 53.29	+2 24 36.66	55 ± 11 ^{U}	0.667$^{(b)}$	1120.0 ± 74.0	1.31 ± 0.09	146.6 ± 0.2	176.6 ± 0.3	252.2 ± 0.7	321.8 ± 1.5	0.236 ± 0.001	0.261 ± 0.002	$10^{43.59}$ $^{(e)}$	3
C2749	10 1 57.56	+1 52 4.87	62 ± 11 ^{U}	1.264$^{(b)}$	445.0 ± 36.0	0.86 ± 0.08	68.2 ± 0.2	80.0 ± 0.2	86.4 ± 0.7	109.6 ± 1.5	0.103 ± 0.004	0.137 ± 0.006	$10^{44.22}$ $^{(f)}$	3
C3053	10 2 32.12	+2 35 37.10	87 ± 20 ^{U}	0.658$^{(b)}$	2163.0 ± 24.0	1.40 ± 0.10	470.2 ± 0.4	569.8 ± 0.5	736.6 ± 1.0	873.4 ± 1.6	0.195 ± 0.001	0.185 ± 0.001	$10^{44.06}$ $^{(f)}$	3
C3198	10 2 56.53	+2 11 58.65	104 ± 20 ^{U}	3.500$^{(b)}$	986.0 ± 21.0	0.98 ± 0.08	51.9 ± 0.1	66.6 ± 0.2	91.4 ± 0.7	209.6 ± 1.6	0.246 ± 0.003	0.498 ± 0.004	$10^{44.97}$ $^{(f)}$	3

$^{(a)}$ from Schinnerer et al. (2010), ^{U} = unresolved source, ^{R} = resolved source; $^{(b)}$ from Brusa et al. (2010); $^{(c)}$ from Trump et al. (2009); $^{(d)}$ from Civano et al. (2012); $^{(e)}$ from Brightman et al. (2014), the luminosity is rest-framed; $^{(f)}$ from Griffith & Stern (2010), the luminosity is not K-corrected.

Table 3.4: Summarised characteristics of Herrera Ruiz et al. (2016) detections.

Target	S_{VLA} (μJy)	S_{VLBI} (μJy)	S_{VLBI}/S_{VLA}	z_{spec}	Spectral index[(a)]	K-corr. $L_{1.4\,GHz}{}^{VLBI}$ ($\times10^{23}$ W Hz^{-1})
(1)	(2)	(3)	(4)	(5)	(6)	(7)
C0366	362 ± 15	255 ± 29	0.70 ± 0.09	2.939	−0.75	132.9 ± 15.1
C1397	293 ± 11	156 ± 24	0.53 ± 0.08	2.536	−0.75	58.5 ± 9.0
C1897	311 ± 16	236 ± 28	0.76 ± 0.10	1.240	−0.75	17.1 ± 2.0

Target	Restoring beam (mas^2)	T_B ($\times10^5$ K)	Linear scale (pc)	ν^{YSN} (SN yr^{-1})	ν^{SNR} (SN yr^{-1})
(1)	(8)	(9)	(10)	(11)	(12)
C0366	~ 15.9 × 7.0	11.8 ± 1.3	$\lesssim$ 123 × 54	~ 2388	~ 213
C1397	~ 15.8 × 7.3	7.0 ± 1.1	$\lesssim$ 127 × 59	~ 1051	~ 94
C1897	~ 17.2 × 8.6	8.2 ± 1.0	$\lesssim$ 143 × 72	~ 308	~ 27

[(a)] assumed, from Kukula et al. (1998).

band, the cross matching has been performed either with the published catalogue by Lutz et al. (2011) or with the on-line catalogue SEIP. The results obtained are always consistent, and here I refer to the published catalogues (Richards et al. 2009 and Lutz et al. 2011) for consistency with the work I did in the CDFS field (see Sect. 2.2.2.1 and 2.2.2.2).

To identify X-ray AGN counterparts, I performed the cross matching with the catalogue by Brightman et al. (2014), which provides K-corrected $L_{2-10\,keV}$. Some sources are not included in Brightman et al. (2014), thus we supplemented our search using the catalogue by Griffith & Stern (2010). This catalogue does not report K-corrected X-ray luminosities, but usually the observed luminosity in hard-X band is close to the intrinsic one (Szokoly et al., 2004), and all the sources lacking of Brightman et al. counterpart are at least two orders of magnitude brighter than the Szokoly et al. (2004) criterion used to identify AGN ($L_{2-8\,keV} > 10^{42}$ erg s^{-1}).

In Table 3.3 the flux densities of the IR and X-ray counterparts I found by cross matching the VLA sources are provided. In Col. 1 the COSMOS-VLBA IDs are listed, as reported in Herrera Ruiz et al. (in prep.); Cols. 2 and 3 list the VLA positions (RA and Dec) and the VLA flux densities and errors from Schinnerer et al. (2010) (integrated flux when the source is resolved, peak flux when unresolved); Col. 4 lists the spectroscopic redshifts; Col. 5 the MIPS 24 μm flux densities from Lutz et al. (2011); Cols. 7, 8, 9, and 10 the IRAC flux densities from Richards et al. (2009); Col. 13 the X-ray luminosities from Brightman et al. (2014) or Griffith & Stern (2010). Finally, Col. 14 lists a classification quality flag computed following the Bonzini et al. (2013) criteria.

3.3 Radio-quiet AGN in the HDF-N field

In this Section I introduce the sample studied by Chi et al. (2013) in their Paper *Deep, wide-field, global VLBI observations of the Hubble deep field north (HDF-N) and flanking fields (HFF)*. I re-analysed their sample applying the classification criteria exposed in 2.2.

Muxlow et al. (2005) performed a follow up of the radio survey by Richards (2000), reaching unprecedented sensitivity and resolution in the *Hubble* Deep Field (HDF) and in

Table 3.5: The full sample of RQ AGN from Chi et al. (2013).

Muxlow ID	Coordinates (J2000) R.A.	Dec.	S_{VLA}	z	$S_{24\mu m}$	q_{24obs}	$S_{3.6\mu m}$	$S_{4.5\mu m}$	$S_{5.8\mu m}$	$S_{8.0\mu m}$	$\mathrm{Log}\left(\frac{S_{5.8\mu m}}{S_{3.6\mu m}}\right)$	$\mathrm{Log}\left(\frac{S_{8.0\mu m}}{S_{4.5\mu m}}\right)$	L_{2-8keV}	QF
	(hh mm ss)	(+dd mm ss)	(μJy)		(μJy)		(μJy)	(μJy)	(μJy)	(μJy)			(erg s^{-1})	
(1)	(2)		(3)	(4)	(5)	(6)	(7)	(8)	(9)	(10)	(11)	(12)	(13)	(14)
J123606+620951	12 36 06.61	+62 09 51.14	196.0 ± 12.8	0.638[a]	499.0 ± 8.3	0.41 ± 0.03	127.0 ± 6.4	88.8 ± 4.4	98.5 ± 4.9	90.4 ± 4.6	−0.11 ± 0.03	0.01 ± 0.03	$> 10^{42.13}$	2
J123608+621035	12 36 08.12	+62 10 35.90	217.0 ± 13.6	0.681[a]	2300.0 ± 13.5	1.03 ± 0.03	78.0 ± 3.9	73.6 ± 3.7	129.0 ± 6.5	264.0 ± 13.2	0.22 ± 0.03	0.55 ± 0.03	$10^{42.15}$	3
J123616+621513	12 36 16.14	+62 15 13.94	53.9 ± 8.4	2.580[a]	326.0 ± 8.0	0.78 ± 0.07	12.7 ± 0.6	18.1 ± 0.9	28.5 ± 1.5	40.8 ± 2.1	0.35 ± 0.03	0.35 ± 0.03	$10^{43.06}$	3
J123618+621635	12 36 18.02	+62 16 35.27	47.1 ± 8.4	0.679[a]	656.0 ± 7.1	1.14 ± 0.08	97.5 ± 4.9	86.6 ± 4.3	86.9 ± 4.4	101.0 ± 5.1	−0.05 ± 0.03	0.07 ± 0.03	$10^{43.20}$	3
J123621+621109	12 36 21.23	+62 11 09.01	52.6 ± 8.2	1.014[a]	261.0 ± 8.6	0.70 ± 0.07	130.0 ± 6.5	96.5 ± 4.8	71.6 ± 3.6	60.4 ± 3.1	−0.26 ± 0.03	−0.20 ± 0.03	$10^{42.50}$	3
J123622+621629	12 36 22.65	+62 16 29.72	70.9 ± 8.7	2.400[a]	417.0 ± 8.2	0.77 ± 0.05	20.3 ± 1.0	27.5 ± 1.4	35.5 ± 1.8	26.6 ± 1.4	0.24 ± 0.03	−0.01 ± 0.03	$> 10^{42.38}$	3
J123629+621045	12 36 29.12	+62 10 45.98	81.4 ± 8.7	1.013[a]	730.0 ± 12.7	0.95 ± 0.05	97.0 ± 4.9	86.8 ± 4.3	76.0 ± 3.8	72.1 ± 3.6	−0.11 ± 0.03	−0.08 ± 0.03	$10^{42.53}$	3
J123630+620923	12 36 30.05	+62 09 23.90	46.3 ± 8.2	0.953[a]	223.0 ± 7.1	0.68 ± 0.08	27.2 ± 1.4	39.2 ± 2.0	59.9 ± 3.0	120.0 ± 6.0	0.34 ± 0.03	0.49 ± 0.03	$> 10^{42.18}$	3
J123632+620759	12 36 32.56	+62 07 59.85	90.6 ± 9.3	1.994[a]	820.0 ± 9.6	0.96 ± 0.04	22.8 ± 1.1	28.0 ± 1.4	48.6 ± 2.5	108.0 ± 5.4	0.33 ± 0.03	0.59 ± 0.03	$10^{42.79}$	3
J123633+621005	12 36 33.73	+62 10 05.96	46.5 ± 8.1	1.016[a]	581.0 ± 9.0	1.10 ± 0.08	74.2 ± 3.7	56.8 ± 2.8	44.9 ± 2.3	49.5 ± 2.5	−0.22 ± 0.03	−0.06 ± 0.03	$10^{42.34}$	3
J123635+621424	12 36 35.58	+62 14 24.05	87.8 ± 8.8	2.011[b]	1520.0 ± 14.4	1.24 ± 0.04	64.9 ± 3.3	97.3 ± 4.9	172.0 ± 8.6	284.0 ± 14.2	0.42 ± 0.03	0.47 ± 0.03	$10^{43.02}$	3
J123642+621331	12 36 42.09	+62 13 31.43	467.0 ± 24.6	4.424[a]	209.0 ± 5.6	-0.35 ± 0.06	7.16 ± 0.4	8.73 ± 0.4	12.3 ± 0.7	11.4 ± 0.7	0.23 ± 0.03	0.12 ± 0.03	$10^{43.14}$	3
J123642+621545	12 36 42.21	+62 15 45.52	150.0 ± 10.7	0.857[a]	866.0 ± 10.3	0.76 ± 0.03	116.0 ± 5.8	95.4 ± 4.8	108.0 ± 5.4	125.0 ± 6.3	−0.03 ± 0.03	0.12 ± 0.03	$10^{42.60}$	3
J123711+621330	12 37 11.25	+62 13 30.85	132.0 ± 10.1	1.996[c]	537.0 ± 9.3	0.61 ± 0.03	39.1 ± 2.0	44.8 ± 2.2	51.8 ± 2.6	36.3 ± 1.9	0.12 ± 0.03	−0.09 ± 0.03	$10^{42.52}$	3
J123711+621325	12 37 11.99	+62 13 25.77	53.9 ± 8.1	1.996[c]	219.0 ± 6.6	0.61 ± 0.07	9.4 ± 0.5	11.5 ± 0.6	15.7 ± 0.9	11.6 ± 0.7	0.22 ± 0.03	0.00 ± 0.03	$> 10^{42.30}$	3
J123716+621733	12 37 16.68	+62 17 33.33	346.0 ± 19.2	1.146[a]	1240.0 ± 15.5	0.55 ± 0.02	62.7 ± 3.1	81.5 ± 4.1	124.0 ± 6.2	219.0 ± 11.0	0.30 ± 0.03	0.43 ± 0.03	$10^{42.78}$	3

[a] from Richards (2000); [b] from Dawson et al. (2001); [c] from Teplitz et al. (2011);

Table 3.6: Summarised characteristics of Chi et al. (2013) detections.

Target	S_{VLA} (μJy)	S_{VLBI} (μJy)	S_{VLBI}/S_{VLA}	z_{spec}	Spectral index[(a)]	K-corr. $L^{VLBI}_{1.4\,GHz}$ ($\times10^{23}$ W Hz^{-1})	ν^{YSN} (SN yr^{-1})	ν^{SNR} (SN yr^{-1})
(1)	(2)	(3)	(4)	(5)	(6)	(7)	(8)	(9)
J123608+621035	217.0 ± 13.6	140 ± 30	0.65 ± 0.14	0.681	−0.36 ± 0.08	2.0 ± 0.4	~ 34	~ 3
J123642+621331	467.0 ± 24.6	348 ± 47	0.75 ± 0.11	4.424	−0.94 ± 0.06	612.1 ± 82.7	~ 10252	~ 915
J123642+621545	150.0 ± 10.7	343 ± 101	2.29 ± 0.36	0.857	−0.50 ± 0.07	9.0 ± 2.6	~ 150	~ 13
J123716+621733	346.0 ± 19.2	177 ± 25	0.51 ± 0.08	1.146	< −0.76	> 10.8 ± 1.5	$\gtrsim$ 180	$\gtrsim$ 16

[(a)] from Richards (2000); for J123716+621733 is reported an upper limit (< −0.76).

the *Hubble* Flanking Fields (HFF) thanks to a combination of VLA and Multi-Element Radio-Linked Interferometer Network (MERLIN). In an area centred at $12^h\,36^m\,49.4^s$, +62° 12' 58.0" (J2000), they achieved a 1σ sensitivity of about 3.3 μJy beam^{-1} at an angular resolution in the range 0.2–0.5 arcsec at 1.4 GHz. A total of 92 radio sources were detected.

In an effort to distinguish between radio emission generated by star-forming processes and AGN, Chi et al. (2013) observed this sample of 92 sources with the global VLBI array, reaching a sensitivity of 7.3 μJy beam^{-1} at an angular resolution of 4 mas in the central 0–2 arcmin part of the field. A total of 12 sources were detected at VLBI scales.

I reclassified the sources detected by Chi et al. (2013) following the Bonzini et al. (2013) criteria for RQ AGN. The cross matching in the IR was performed using the published catalogue by Teplitz et al. (2011) which reports measures for both IRAC and MIPS bands. For the X-ray band the cross matching was performed with the catalogue by Alexander et al. (2003). This catalogue does not report K-corrected X-ray luminosities, but provides spectral slopes for the sources, using which I could compute the K-correction (see Table 3.5, Col. 13).

In Table 3.5 are reported the flux densities of the IR and X-ray counterparts I found cross matching the VLA sources. In Col. 1 the IDs are listed, as reported in Muxlow et al. (2005); Cols. 2 and 3 list the VLA positions (RA and Dec) and the VLA flux densities and errors from Muxlow et al. (2005); Col. 4 lists the spectroscopic redshifts; Col. 5 the MIPS 24 μm flux densities from Teplitz et al. (2011); Cols. 7, 8, 9, and 10 the IRAC flux densities from Teplitz et al. (2011); Col. 13 the X-ray luminosities computed based on Alexander et al. (2003) flux densities and spectral slopes. Finally, Col. 14 lists a classification quality flag computed following the Bonzini et al. (2013) criteria.

RQ AGN J123642+621545 show a VLBI-measured radio flux density significantly greater than the VLA-measured one, probably due to radio variability. This very fact implies that this source is dominated by AGN-driven emission. Moreover, this behaviour makes doubtful the classification of this source as RQ, as the VLA observation could have been carried out during a quiescent phase. Nevertheless, computing the $q_{24\,obs}$ value using the $S_{1.4\,GHz}$ measured with the VLBI technique does not modify the classification of this source as RQ (from $q_{24\,obs} = 0.76 \pm 0.03$ to $q_{24\,obs} = 0.40 \pm 0.13$), but only affects the quality flag value (from 'secure' to 'reasonable'; see Sect. 2.2.1 for details).

3.4 RQ AGN and the fundamental plane of SMBH activity

Tables 3.2, 3.4, and 3.6 summarise the characteristics of the VLBI-detected sources in the three samples, respectively. The last two Columns of each table, in particular, list the expected SN rates I computed as derived from the VLBI-detected radio emission. As for the Maini et al. (2016a) sources (see Sect. 2.3), these rates greatly exceed the value expected

Table 3.7: K-corrected radio and X-ray luminosities, for the sources belonging to the samples here analysed and provided of a VLBI detection.

Source	K-corr. $L^{VLBI}_{1.4\,\mathrm{GHz}}$ ($\times 10^{23}$ W Hz^{-1})	K-corr. $L_{1.4\,\mathrm{GHz}}$ ($\times 10^{32}$ W)	K-corr. $L_{2-10\,\mathrm{keV}}$ (W)	Obscured	Separation (arcsec)	Distance from Panessa's correlation
(1)	(2)	(3)	(4)	(5)	(6)	(7)
RQ76	17.2 ± 3.3	24.25 ± 4.65	$10^{37.59\pm0.03}$	Obscured [a]	0.89	−2.02
RQ851	9.7 ± 2.3	13.68 ± 3.24	...	...	...	...
225	236.0 ± 56.6	326.39 ± 78.28	$10^{36.26}$	Obscured [b]	0.72	+0.28
C0366	132.9 ± 15.1	204.666 ± 23.254	$10^{37.01}$	Unobscured [c]	0.93	+0.43
C1397	58.5 ± 9.0	90.09 ± 13.86	$10^{36.47}$	Unobscured [c]	0.29	+0.65
C1897	17.1 ± 2.0	26.334 ± 3.08	$10^{37.70}$	Unobscured [c]	0.34	−0.66
J123608+621035	2.0 ± 0.4	2.80 ± 0.56	$10^{35.15}$	Obscured [d]	0.10 [e]	−0.62
J123642+621331	612.1 ± 82.7	856.94 ± 115.8	$10^{36.14}$	Obscured? [d]	0.22 [e]	+0.07
J123642+621545	9.0 ± 2.6	12.6 ± 3.64	$10^{35.60}$	Unobscured [d]	0.09 [e]	+0.84
J123716+621733	> 10.8 ± 1.5	> 15.12 ± 2.1	$10^{35.78}$	Obscured [d]	0.22 [e]	−0.69

[a] Treister et al. (2009) report a Hydrogen column density for this source of $\sim 10^{22.4}$ cm^{-2}, which implies a significant amount of absorption. We consider this source obscured;
[b] Vattakunnel et al. (2012) report a Hydrogen column density for this source of $\lesssim 10^{22.97}$ cm^{-2}. We consider this source obscured;
[c] All these source have been fitted by Brightman et al. (2014) with templates with Hydrogen column density of 10^{20} cm^{-2}. These sources are considered unobscured;
[d] Richards et al. (2007) provide information on the obscuration of these sources;
[e] from Richards et al. (2007).

even for the most extreme SBGs (see Sect. 2.3). Therefore, we exclude that star formation can cause the emission detected through VLBI technique within RQ sources, suggesting that it is probably related to AGN. In this Section we aim at findings further evidence that this is actually the case.

In the four samples here analysed, a total of 10 RQ AGN have been detected. As reported in Table 3.7, for 9 ot them an X-ray counterpart was found (the exception is RQ 851). This can allow us to explore if these sources lie in the so called 'fundamental plane of SMBH activity' (Merloni et al., 2003; Falcke et al., 2004a), and in particular in its $L_{\mathrm{X\text{-}ray}}$–$L_{1.4\,\mathrm{GHz}}$ projection, as reported by Panessa et al. (2007).

Panessa et al. (2007) studied a sample of local ($D_L < 100$ Mpc, $z < 0.023$) Seyfert galaxies from Panessa et al. (2006), finding an empirical correlation between nuclear radio and X-ray luminosities (corrected for galactic and intrinsic absorption), suggesting that the accretion flow and the radio emission are strongly coupled. This correlation is the same one found for RL radio galaxies, whose radio emission is well known to be due to relativistic jets (Orienti et al., 2015). This seems to point towards a common mechanism between the two populations, but the large difference in luminosity between Seyfert galaxies and radio galaxies prevents from strong statements.

The correlation found by Panessa et al. (2007) is:

$$\mathrm{Log}\ L_{2-10\,\mathrm{keV}} = (0.62 \pm 0.04) \times \mathrm{Log}\ L_{1.4\,\mathrm{GHz}} + (18.17 \pm 1.46)$$

In the following we derived the $L_{2-10\,\mathrm{keV}}$ - $L_{1.4\,\mathrm{GHz}}$ correlation for our sample of VLBI-detected RQ AGN. Removing all the sources with a luminosity measure in only one band, and applying an ordinary least squares bisector fitting, we found the correlation:

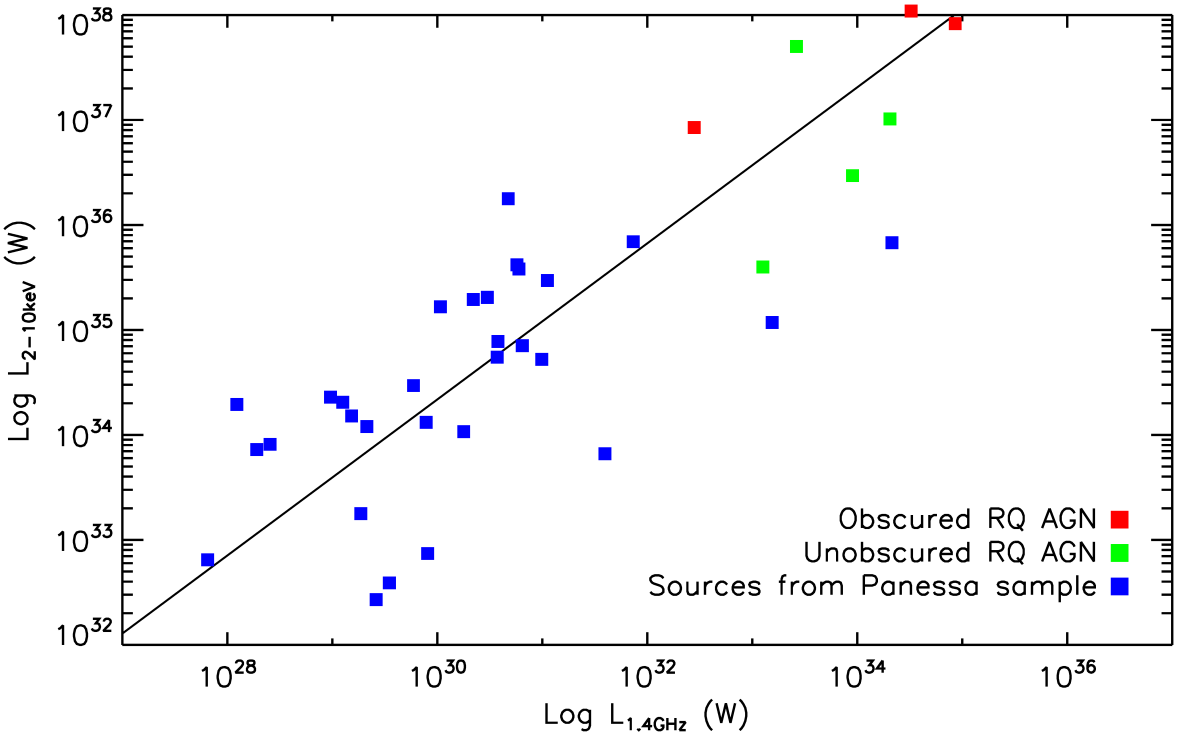

Figure 3.1: Positions of the sources with radio and X-ray detections, in the $L_{1.4\,\mathrm{GHz}}$–$L_{2-10\,\mathrm{keV}}$ plane (adapted from Panessa et al. 2007). The red squares are the obscured sources, for which a correction on the Hard-X fluxes has been applied. Green squares are the unobscured sources, for which no correction has been applied. Blue squares represent the original sources from Panessa et al. (2007).

$$\mathrm{Log}\, L_{2-10\,\mathrm{keV}} = (0.74 \pm 0.13) \times \mathrm{Log}\, L_{1.4\,\mathrm{GHz}} + (12.03 \pm 3.91)$$

with dispersions of $\sigma = 0.74$. Within the errors this correlation is fully consistent with the one of Panessa et al. (2007).

The intrinsic obscuration in the X-ray regime is related to the column density of H I content. Column densities of the order of $\sim 10^{20}\,\mathrm{cm}^{-2}$ (which is also the column density of our own Galaxy) are typical of unobscured sources (objects usually referred as 'Type 1', where we can see directly the broad-line region). The X-ray flux densities we can measure in these sources are essentially the intrinsic ones, which correction is around 0.1–0.2% (Alexander et al., 2003; Lehmer et al., 2005).

For column densities $\gtrsim 10^{22}\,\mathrm{cm}^{-2}$ sources start to present significant absorption in the X-ray, and a correction is needed to the observed X-ray flux densities. For column densities $\gtrsim 10^{25}\,\mathrm{cm}^{-2}$, the source is defined 'Compton-thick', and the only X-ray emission we can see comes from scattering and reflection from the narrow-line region and the hot corona of the central black hole. In this last case, any direct measure of the intrinsic X-ray luminosity is prevented (Panessa et al., 2006).

In general, intrinsic luminosities for heavily obscured sources can be as high as 10^2–10^3 times the measured one, depending on the amount of absorption and on the viewing angle with respect to the obscuring torus (see, e.g., Ghisellini et al. 1994; Iwasawa et al. 1997; Matt et al. 1999; Guainazzi et al. 2000). For the obscured sources, we considered a representative correction factor of 60 (see Panessa et al. 2006 for details).

The RQ sources detected with VLBI technique have slightly larger X-ray and VLBI radio luminosities than the sources analysed by Panessa et al. (2007). Our sources are at significantly higher redshift than the ones analysed by Panessa et al. (2007). This may be simply due to the well-known Malmquist bias (i.e. the observational bias which leads to preferentially detect intrinsically brighter objects at higher redshift in a flux-limited survey). Their location is nevertheless consistent with the relation found by Panessa et al. (2007) (see Figure 3.1).

In Table 3.7, Column 9, is reported the distance between the source and the fitting line. All the sources lie within 1.2σ distance from the line (except source RQ76, see below). This strengthen the conclusion that the radio emission detected with VLBI technique within these sources is due to AGN. The only source for which such a conclusion might be doubtful is RQ76, which lies almost at 3σ from the correlation line. It is perhaps worth noting that the LBA position of this latter source lies outside the X-ray positional error ellipse (see Figure 2.5), and a large offset was also found with respect to the VLA position (see discussion in Sect. 2.2.2.1).

3.5 Consistency of the detections

The confirmation of the presence of AGN-driven radio emission within some RQ AGN is relevant by itself, but it is also important to understand how much of the VLBI-missed radio emission can be ascribed to star-formation in these objects. This can help us to understand the relative importance of AGN and SF activity in sources classified as RQ AGN.

In a statistical way this work has been undertaken by Bonzini et al. (2015), who compared the star-formation rates (SFR) derived respectively from radio and IR luminosities in the ECDFS field to search for systematic radio excesses in RQ AGN that could be accounted for by an AGN. In the radio domain they made use of VLA data from Miller et al. (2008, 2013), and applied the Yun et al. (2001) relation to estimate the $\mathrm{SFR}_{radio}^{VLA}$. In the IR domain they derived IR bolometric luminosities by fitting the IR SED using data from several catalogues (e.g., Taylor et al. 2009; Cardamone et al. 2010; Damen et al. 2011) along with flux densities at 70, 100 and 160 μm from the *Herschel* PACS Evolutionary Probe programme (Lutz et al., 2011). The total IR luminosities were converted to SFR_{IR} using the Kennicutt (1998) relation. The use of the whole IR band allows more reliable estimates of the SFR_{IR} than those based on the $S_{24\,\mu\mathrm{m}}$ fluxes alone (Bonzini et al., 2013). Indeed, $S_{24\,\mu\mathrm{m}}$ flux densities can be contaminated by the presence of a torus surrounding the central BH, which results in an IR excess (Papovich et al., 2007; Daddi et al., 2007b).

Taking into account only the sources provided of *Herschel* PACS counterpart, Bonzini et al. (2015) derived best-fit radio-FIR correlations for RQ AGN and SFGs which are very close to each other:

$$\mathrm{Log\ SFR}_{FIR}^{RQ\,AGN} = (0.96 \pm 0.05) \times \mathrm{Log\ SFR}_{radio}^{RQ\,AGN} + (-0.09 \pm 0.10)$$

$$\mathrm{Log\ SFR}_{FIR}^{SFG} = (0.97 \pm 0.02) \times \mathrm{Log\ SFR}_{radio}^{SFG} + (0.02 \pm 0.04)$$

with a dispersion around the correlation slightly larger for RQ AGN ($\sigma_{\mathrm{RQ\,AGN}} = 0.24$) than for SFGs ($\sigma_{\mathrm{SFG}} = 0.21$). Including also sources without PACS counterpart (and therefore less reliable SFR_{IR} measurements), these same radio-FIR correlations become:

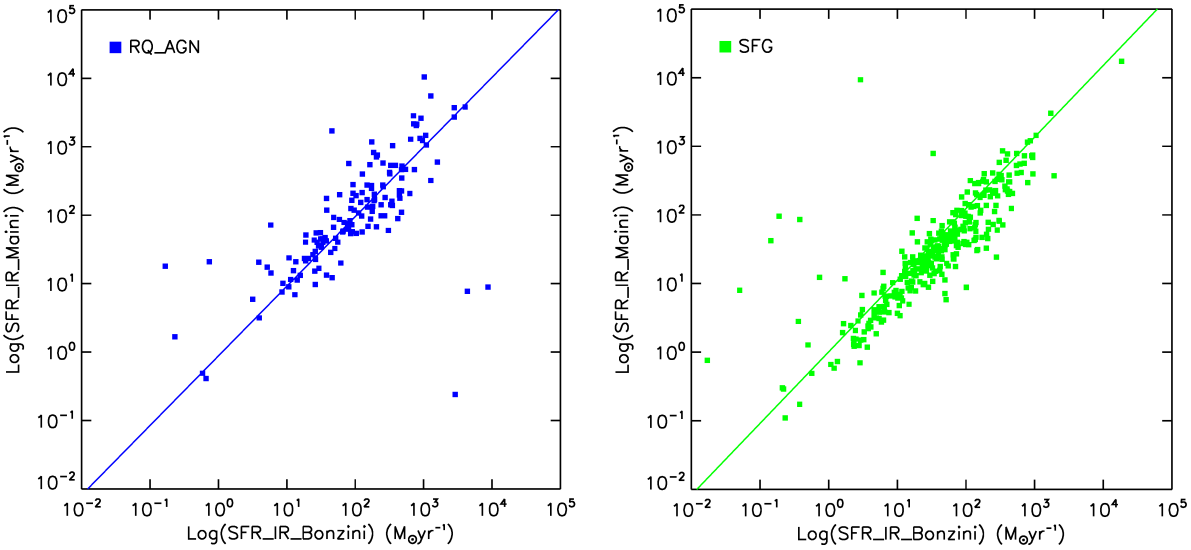

Figure 3.2: Comparison between the SFRs obtained from 24 μm flux densities and the SFRs obtained by Bonzini et al. (2015) from FIR. *Left*: RQ AGN. *Right*: SFGs. The solid lines represent the best fits.

$$\text{Log SFR}_{FIR}^{RQ\,AGN} = (1.09 \pm 0.07) \times \text{Log SFR}_{radio}^{RQ\,AGN} + (-0.55 \pm 0.17)$$

$$\text{Log SFR}_{FIR}^{SFG} = (1.00 \pm 0.04) \times \text{Log SFR}_{radio}^{SFG} + (-0.16 \pm 0.08)$$

and the dispersions increase ($\sigma_{\text{RQ AGN}} = 0.37$ and $\sigma_{\text{SFG}} = 0.33$).

This similarity suggested that the RQ AGN class is dominated by star formation activity, and that the larger dispersion might be due to contamination by AGN emission. We can test this idea by comparing the expected SFR from VLBI-missed radio luminosity and IR luminosity, by assuming all the missing radio flux is caused by star formation activity.

To perform this analysis we first re-evaluated the radio and IR SFRs using different relations with respect to the ones used by Bonzini et al. (2015). In particular we relied the IR SFR on 24 μm flux densities only, which is less reliable than the FIR-derived one. This was necessary as the information in the FIR band (from *Herschel*) was not available to us for the RQ AGN VLBI-detected sample (9 sources) under analysis (see Sects. 2.2, 3.1, 3.2, and 3.3). Given the aforementioned caveat, the following analysis has to be considered preliminary. We plan to repeat it using SED fitting procedures in the next future, including *Herschel* data.

In the radio domain, we used the Condon (1992) and Huynh (2004) relation (see Appendix A):

$$\text{SFR}_{radio}[\text{M}_\odot\,\text{yr}^{-1}] = Q \times \frac{L_{1.4\,\text{GHz}}[\text{W Hz}^{-1}]}{4.581 \times 10^{21}}$$

where $Q = 3.24$ when assuming the Chabrier initial mass function (IMF); while in the IR domain we use the Bell et al. (2005) relation:

$$\text{SFR}_{IR}[\text{M}_\odot\,\text{yr}^{-1}] = 9.8 \times 10^{-11} \times (L_{IR}^{Bol}[\text{L}_\odot] + 2.2\,L_{UV}[\text{L}_\odot])$$

Table 3.8: Radio and IR SFRs for VLBI-detected RQ AGN. The radio-based SFR has been computed using the VLBI-missing flux.

Target	$S_{VLBI}^{missing}$	K-corr. missing $L_{1.4\,GHz}$	SFR_{radio}	$S_{24\mu m}$	IR bolometric luminosity	SFR_{IR}	$\frac{SFR_{radio}}{SFR_{IR}}$
	(μJy)	($\times 10^{23}$ W Hz^{-1})	($M_\odot$ yr^{-1})	(μJy)	(10^{12} L$_\odot$)	($M_\odot$ yr^{-1})	
(1)	(2)	(3)	(4)	(5)	(6)	(7)	(8)
ECDFS samples							
RQ76	82.5 ± 39.3	7.6 ± 3.6	539 ± 257	935.3 ± 11.5	5.28 ± 0.06	549 ± 7	1.0 ± 0.5
RQ851	111.5 ± 30.1	9.8 ± 2.6	691 ± 187	479.7 ± 17.3	2.50 ± 0.09	260 ± 9	2.7 ± 0.7
225	0.0 ± 240.0	0.0 ± 56.6	0 ± 4000	423.9 ± 10.3	5.13 ± 0.12	533 ± 15	...
COSMOS sample							
C0366	107.0 ± 32.6	55.8 ± 17.0	3943 ± 1201	664.0 ± 17.0	30.17 ± 0.77	3135 ± 80	1.3 ± 0.4
C1397	137.0 ± 26.4	51.3 ± 9.9	3632 ± 700	2932.0 ± 163.0	55.27 ± 3.07	5741 ± 319	0.6 ± 0.1
C1897	75.0 ± 32.2	5.4 ± 2.3	385 ± 165	2983.0 ± 87.0	10.57 ± 0.31	1098 ± 32	0.4 ± 0.2
HDF-N sample							
J123608+621035	77.0 ± 32.9	1.1 ± 0.5	79 ± 34	2300.0 ± 13.5	1.49 ± 0.01	155 ± 1	0.5 ± 0.2
J123642+621331	119.0 ± 41.2	209.3 ± 72.5	14803 ± 5128	209.0 ± 5.6	60.05 ± 1.61	6238 ± 167	2.4 ± 0.8
J123642+621545[(a)]	...	...	...	866.0 ± 10.3	0.84 ± 0.01	88 ± 1	...
J123716+621733	169.0 ± 31.5	> 10.3 ± 1.9	727 ± 135	1240.0 ± 15.5	3.12 ± 0.04	324 ± 4	2.2 ± 0.4

[(a)] For this source we do not provide a SFR_{radio}^{VLBI} estimate due to its nature of variable radio source (see Sect. 3.3). This prevented us to properly disentangle the radio emission due to AGN and star formation activity.

where the L_{IR}^{Bol} can be approximately computed from the 24 μm fluxes (Lutz et al., 2011; Lonsdale et al., 2003; Surace et al., 2005) using the correction factors reported by Wuyts et al. (2008), under the assumption that the UV contribution can be neglected (Daddi et al., 2007b; Rees et al., 2016). Bell et al. (2005) assume a Kroupa IMF, and we rescale it to a Chabrier IMF by multiplying by a factor of 1.06.

These relations provide results that are consistent with the ones by Bonzini et al. (2015). In Figure 3.2 is reported the comparison between the SFRs derived as part of this Thesis and by Bonzini et al. (2015) for RQ AGN and SFGs (left and right, respectively). Only $\sim 6\%$ of the RQ AGN from Bonzini et al. (2015) are not classified as such when using the 24 μm-based relation, meaning that we could expect < 1 spurious classification in our VLBI-detected RQ AGN sample.

From the statistical point of view, the good match between the $SFR_{24\,\mu m}$ and the SFR_{FIR} is demostrated by the fact that the best fits are very close to be the bisector of the plane:

$$\text{Log SFR}_{Maini}^{RQ\,AGN} = (1.02 \pm 0.06) \times \text{Log SFR}_{Bonzini}^{RQ\,AGN} + (-0.06 \pm 0.14)$$

$$\text{Log SFR}_{Maini}^{SFG} = (1.04 \pm 0.04) \times \text{Log SFR}_{Bonzini}^{SFG} + (0.00 \pm 0.07)$$

with dispersions of $\sigma_{\text{RQ AGN}} = 0.45$ and $\sigma_{\text{SFG}} = 0.32$, respectively. While not relevant from a statistical point of view, the few outliers present in Fig. 3.2 are probably associated to unreliable 24 μm measurements and/or 24 μm emission being contaminated by an AGN dusty torus.

Table 3.8 reports the radio and IR SFRs obtained for the RQ AGN VLBI-detected sample under consideration (10 sources from the ECDFS, the COSMOS and the HDF fields). The radio SFRs have been computed considering only the VLBI missing flux. The derived radio-to-IR SFR ratios (last column) are typically between 0.5 and 1.5, i.e. consistent with 1, considering the associated errors. Three sources, however show values in excess of 2: RQ851 (ECDFS); J123642+621331 and J123716+621733 (HDF-North). This probably indicates that some residual AGN-related emission is present beyond the scale probed by the VLBI observations.

Two sources are excluded from this analysis: source 225 (ECDFS), with $S_{VLBI} = S_{VLA}$ (i.e., $S_{VLBI}^{missing} = 0$), and the variable source J123642+621545 (HDF-North), where $S_{VLBI} \gg S_{VLA}$. For both of them a SFR_{radio} vs. SFR_{IR} comparison is not meaningful.

These result support the idea that the radio emission in (at least some) RQ AGN may be of composite nature. Interestingly, the VLBI-detected emission often accounts for all the observed radio excess with respect to the FIR/radio correlation expected for SFGs. This seems to imply that the AGN-related emission is all confined within scales of a few hundreds of parsecs. In those cases where a residual radio excess remains after removing the VLBI core, it is likely that kpc-scale AGN jets are present, but not detected as beyond the maximum scale probed by the VLBI observations.

The results discussed here are very limited from a statistical point of view and more sensitive VLBI observations would be needed. However they are in line with the hypothesis that AGN contamination is the cause of the observed radio excess in RQ AGN (Bonzini et al., 2015). If compact AGN cores are a general property of RQ AGN does remain to be seen.

3.6 Proxies of VLBI-sized emission within RQ AGN

In our (specifically designed) experiment we targeted with LBA 4 sources classified as RQ AGN in the ECDFS, and we detected 2 of them (see Sect. 2.2). Three other RQ AGN samples have been observed with VLBI facilities so far: 15 sources have been targeted with VLBA in the ECDFS field by Middelberg et al. (2011a), 22 with VLBA in the COSMOS field by Herrera Ruiz et al. (2016), and 16 with VLA+MERLIN in the HDF-N field by Chi et al. (2013). Out of these, 1, 3, and 4 sources (respectively) have been detected by these groups (see Sect. 3.1, 3.2, and 3.3, respectively). Therefore, the total amount of RQ AGN sources observed so far with VLBI technique amount to 56, out of which 10 have been detected.

This sample of objects is too small to be of any strong statistical significance. Moreover, the 4 surveys that observed these sources are very different in purposes and designs, which makes it impossible a direct comparison between the results. Nevertheless, we decided to compare the characteristics of the targeted sources with those of the corresponding RQ AGN parent samples, to search for some common features that can help to pinpoint those RQ AGN within which we can expect to find VLBI-sized activity. This can potentially help to better design future, sub-mJy radio surveys, and/or better understand the activity ongoing within these sources.

In Figure 3.3 is shown the K-corrected VLA-based 1.4 GHz luminosity distribution of the sources belonging to all the 4 samples of RQ AGN analysed so far. The bulk of RQ AGN population typically have radio luminosities in the range 10^{23} – $10^{24.5}$ W Hz^{-1}, while the VLBI detected ones show a flatter distribution. In addition, virtually all the RQ AGN with $L_{1.4\,\mathrm{GHz}}^{K-\mathrm{corr}} > 10^{25}$ W Hz^{-1} have a detected VLBI core. This may just reflect the limited VLBI sensitivity, but may also be a hint that VLBI-detected cores in RQ AGN pinpoint an

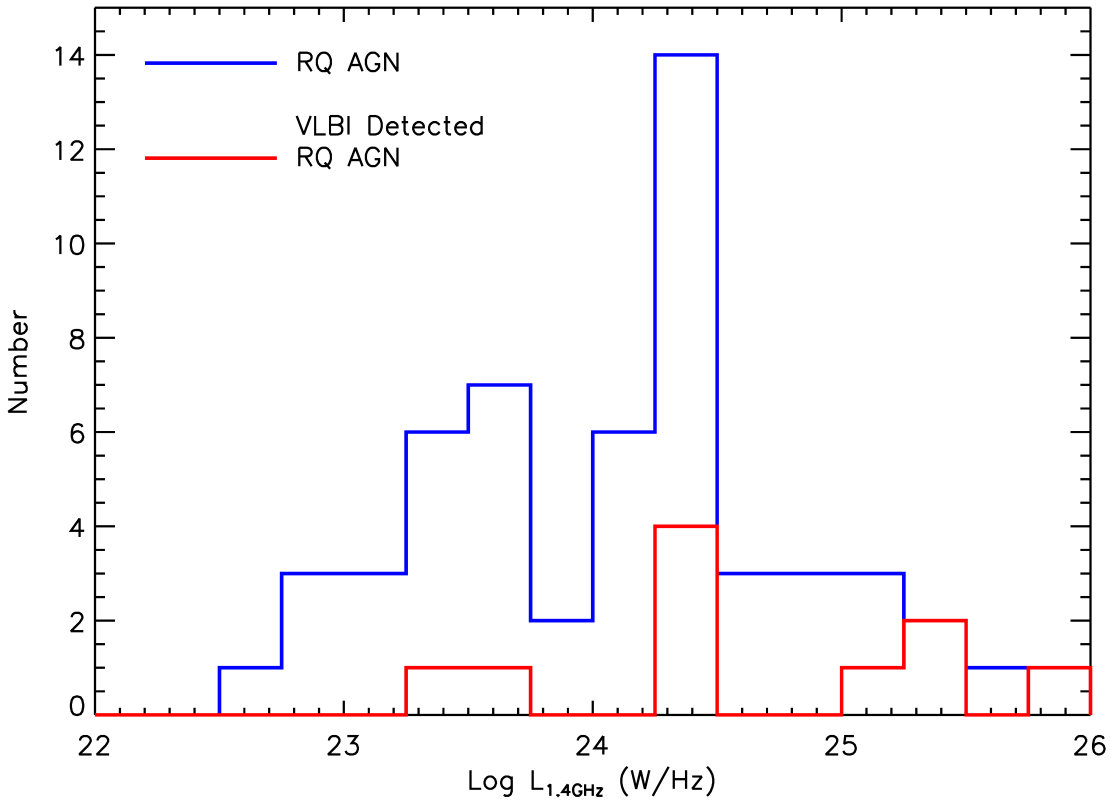

Figure 3.3: *K*-corrected VLA-based 1.4 GHz luminosity distribution of the RQ AGN belonging to all the samples analysed in this Thesis. The blue histogram represents the full sample, while the red one the sources that have been detected through VLBI technique.

intermediate class of AGN between RL and pure RQ AGN.

In Figure 3.4 is shown the redshift distribution of the sources belonging to all the 4 samples of RQ AGN reported in this Thesis. The majority of sources lie in the interval $0.5 < z < 2.5$, with VLBI detections widespread along the entire distribution. Again there is a hint towards higher redshift sources being more likely detected at VLBI scale than lower redshift ones. But this can just be a consequence of selection effects. Indeed in flux limited surveys, higher redshift sources are typically more powerful. And as shown in Figure 3.3 more powerful sources are more likely to be VLBI-detected.

For all the sources of the 4 samples (except for RQ174 in ECDS of our sample), the IR flux densities are available for all the four IRAC bands. These allow us to build the AGN wedge of the IRAC colour-colour diagram (Lacy et al., 2004; Donley et al., 2012), and explore how the VLBI-detected and VLBI-undetected RQ AGN populate it. The membership of the AGN wedge was used by Bonzini et al. (2013) only as a secondary feature to determine if a source can be classified as AGN or SFG, and to define the quality flag of the classification.

As mentioned in Sect. 1.2, the AGN wedge highlights the region within the IRAC colour-colour space where sources characterised by a rising power law in the NIR and MIR bands lie. This power law is nowadays interpreted as a strong signature of AGN presence within the galaxy: the AGN is powerful enough to heat the dust surrounding the central SMBH so that the power-law blackbody radiation which results from the heating overcomes the galaxy emission at the same wavelengths (see, e.g., Figure 1.6 and Donley et al. 2012).

The higher the redshift, however, the lower the wavelengths sampled by the IRAC bands.

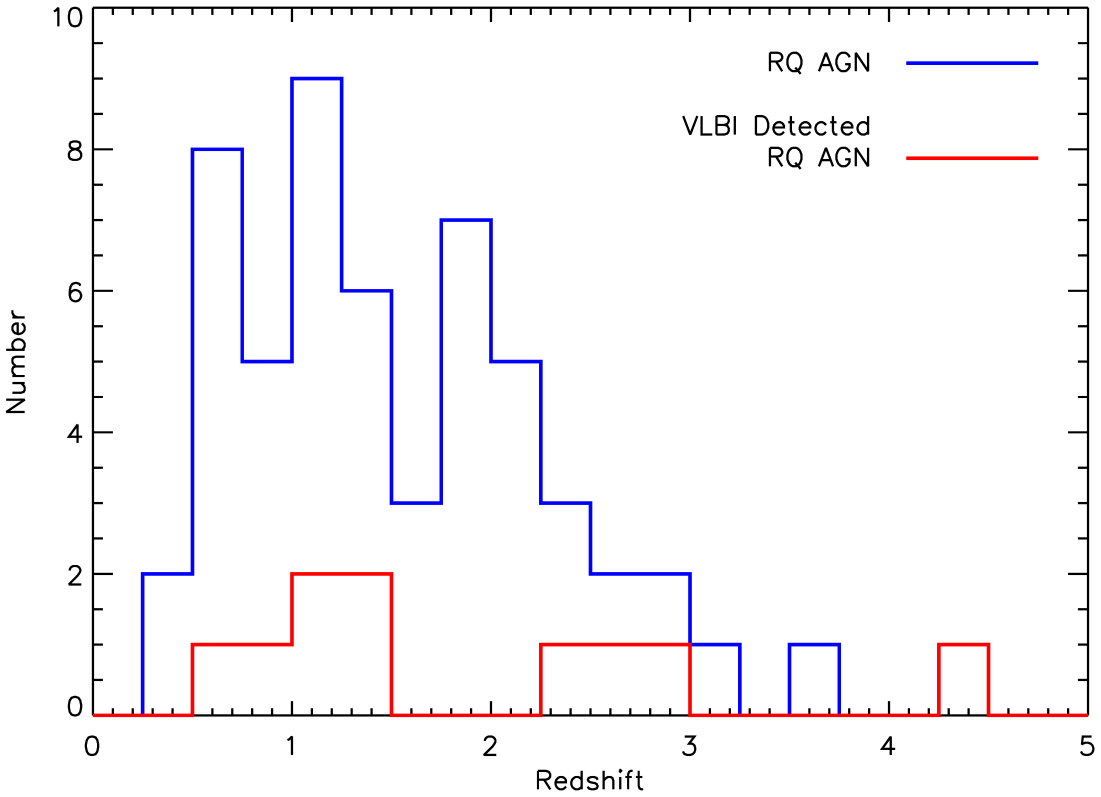

Figure 3.4: Redshift distribution of the RQ AGN belonging to all the samples analysed in this Thesis. The blue histogram represents the full sample, while the red one the sources that have been detected through VLBI technique.

This makes the AGN wedge progressively less useful to verify the presence of an AGN within the galaxy. At redshift 3, for instance, the IRAC bands sample wavelengths between 0.9 and 2.0 μm, where the light from stars dominate the SED of SFGs and composite objects (see Figure 1.6). To avoid contamination by high-redshift SFGs, therefore, the reliability of the Donley AGN wedge is limited to redshift $\lesssim 2.5$ (see, e.g., Cowley et al. 2016). As shown in Figure 3.4, the great majority of the sources belonging to the so-far available RQ AGN samples lie in fact at redshift < 2.5 (48 out of 55, for which a redshift is available), which allows to use the AGN wedge in a meaningful way.

In Figure 3.5 is reported how RQ AGN sources populate the IRAC colour-colour parameter space. Almost all the detected sources lie very close or within the conservative AGN wedge proposed by Donley et al. (2012), and all of them within the extended wedge proposed by Lacy et al. (2004), which is however more contaminated by SFGs. This is an interesting finding. All our VLBI-detected RQ AGN have robust VLBI cores (i.e. accounting for $\geq 50\%$ of the total radio emission). It seems then that in these sources the AGN dominate both in the radio and in the IR bands. On the other hand, undetected sources lying outside the wedge are consistent with their radio emission being dominated by star formation activity.

The only VLBI-detected RQ AGN lying outside the conservative AGN wedge is the HDF-N source J123642+621545. Interesting to notice, the radio emission detected for this source through the VLBI technique is greater than the one detected through the VLA (see Table 3.6), a clear indication of variability. This source should then be regarded with caution, as some variability might be present also at IR bands, and the IRAC colour-colour position may be unreliable.

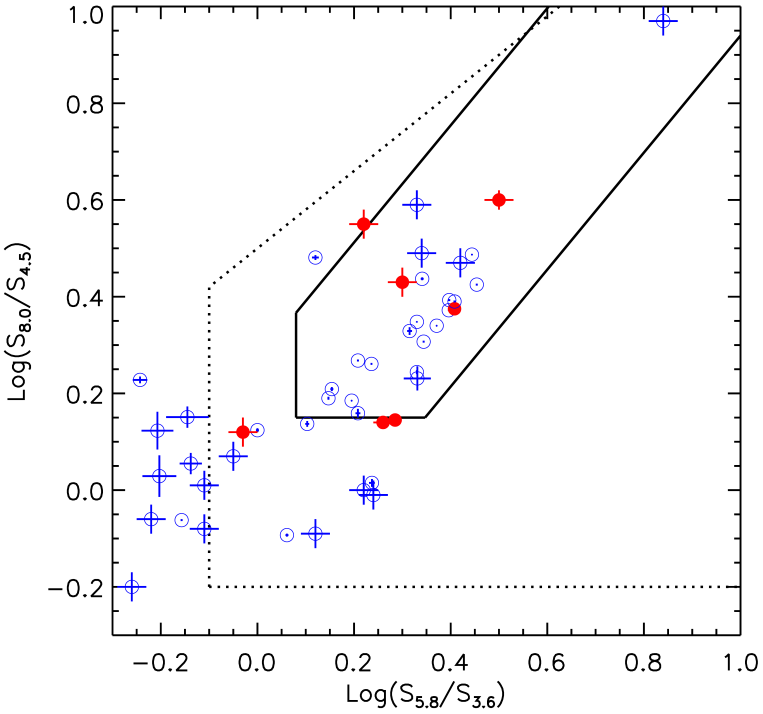

Figure 3.5: Distribution of the sources classified as RQ AGN and belonging to all the 4 samples available so far, within the IRAC colour-colour space. The dotted lines demarcate the so called 'Lacy wedge' (Lacy et al., 2004), while the solid lines demarcate the more conservative 'Donley wedge' (Donley et al., 2012). Red filled dots represent VLBI-detected RQ AGN, blue empty dots represent VLBI-undetected RQ AGN.

If the connection between a VLBI-sized detection and the positioning within the AGN wedge is confirmed, then we may use this property to pre-select targets for VLBI follow ups in future, deep radio surveys.

3.7 Conclusions

In this Chapter I presented the analysis I performed on several samples of RQ AGN.

In Sect. 3.1 is reported the new classification of the sources observed by Middelberg et al. (2011a) with the VLBI technique in the ECDS field, based on the criteria proposed by Bonzini et al. (2013). The field is the very field within which I selected the targets of my experiment (see Sect. 2.2), and a number of sources they observed are classified as RQ AGN. In particular, source 225 was already detected in their experiment.

In Sect. 3.2 it is reported the sample analysed by Herrera Ruiz et al. (2016), and the contribution I gave to their original work. I helped in the classification of 22 sources observed with VLBA as follow-up of a radio survey in the COSMOS field, confirming them as RQ following the Bonzini et al. (2013) criteria. Three of those sources were detected.

In Sect. 3.3 are reported the results of a new classification that I did following the criteria proposed by Bonzini et al. (2013) of the sources detected by Chi et al. (2013) with the VLBI technique in the GOODS-N field. I found that four of their detections (J123608+621035, J123642+621331, J123642+621545, and J123716+621733) are associated with RQ AGN according to the Bonzini et al. (2013) classification.

The VLBI observations here reported confirm that the radio emission of some sources classified as radio-quiet can be dominated by their AGN cores, rather than by star formation. The presence of AGN-driven radio emission within these objects was already clear from multi-wavelength analyses, and now it is possible to claim that at least in some of them this activity can account also for a relevant fraction of the total radio emission (up to 76% in C1897). Other papers are consistent with these results (e.g. White et al. 2015) and confirm

our conclusions using a complementary approach that did not make use of VLBI data.

In Col. 4 of Tables 2.3, 3.4, and 3.6, and Col. 5 of Table 3.2 are reported the fraction of VLA emission detected with VLBI technique. It is interesting to notice that VLBA-measured flux densities account for fractions of VLA emissions more or less consistent among the different samples (typically $\sim$ 50%–70%). The only caveat to this conclusion is that each survey has a different restoring beam size. Indeed, the LBA restoring beam in Maini et al. (2016a) is $\sim 25\times$ the VLBA beam in Herrera Ruiz et al. (2016). This actually may indicate that most of the AGN emission into RQ sources is concentrated into the very centre of the objects, i.e. within the smaller scales probed by the VLBA ($\sim$ 100 pc at the source redshifts). This may in turn imply that these sources are very young or very recently re-activated (i.e. with very small radio jets).

In Sect. 3.4 I provide some further evidence that the radio emission detected through VLBI technique is AGN-driven, while in Sect. 3.5 I perform a preliminary analysis on how the VLBI-missed radio emission is related to ongoing star formation within the host galaxy. A more complete SFR evaluation, based on the FIR SED fitting, is planned for the near future.

In Sect. 3.6 I present some early evidence that an interesting proxy to find VLBI-sized AGN-driven radio emission within sources classified as RQ AGN is the presence of a heated dusty torus around the central SMBH, which shows itself through the monotonic increases of flux densities along the four IRAC bands. The statistical significance of this conclusion is not clear with the available samples, but if confirmed this finding may be related with the accretion regime onto the central SMBH, and/or the physical mechanism responsible for the radio emission in RQ AGN.

4

Infrared-Faint Radio Sources in the SERVS deep fields: Pinpointing AGN at high redshift.

In this Chapter is reported the original work I did in the field of IFRS. This Section is an upgrade of the Paper Infrared-Faint Radio Sources in the SERVS deep fields: Pinpointing AGNs at high redshift. *(Maini et al., 2016b). Overall, my contribution to the Paper was around 90%.*

In this Chapter of the Thesis I present the work done on the Infrared-Faint Radio Sources (IFRS). After a short introduction about the relevance of this work on the topic (Sect. 4.1), and a review on the analysed samples (Sects. 4.2 and 4.3), I report my personal contribution detailing the techniques I used to analyse the radio- and IR-faint component of this population (Sect. 4.4, 4.5, 4.6, 4.7). Finally, I describe the models I built to understand the nature of these sources (Sect. 4.8) and report my conclusions (Sect. 4.9). A short conclusion summarises the current view about these sources (Sect. 4.10).

4.1 Introduction

The criteria proposed by Zinn et al. (2011) (see Sect. 1.5.3) removed the survey-dependent selection biases for the samples of IFRSs, but this came to a cost. The request for an extreme radio-to-IR ratio ($R_{3.6} > 500$) tends to exclude the radio-faintest of these sources, at a given sensitivity limit of the 3.6 μm band. The request for IR faintness ($S_{3.6\,\mu\mathrm{m}} < 30\,\mu$Jy) may limit the redshift range and area of the parameter space explored for these objects.

As a consequence, Collier et al. (2014) and Herzog et al. (2014) samples of so-called 2nd-generation IFRSs include only relatively bright radio sources ($S_{1.4\,\mathrm{GHz}} \gtrsim 9$ mJy), in addition

the coupling of the second criterion with the explicit request of an IR counterpart limits the samples to relatively bright IR sources ($S_{3.6\,\mu\mathrm{m}} \gtrsim 15\,\mu$Jy).

Therefore radio- and IR-faint IFRSs were not thoroughly explored, and their nature is still unclear. A comprehensive analysis of 1st-generation IFRSs can mitigate this limitation. From one side, due to the request of lack of any IR counterpart at the SWIRE detection limit ($3\sigma \sim 2.2\,\mu$Jy, see Sect. 1.5.1) all 1st-generation IFRSs satisfy the second criterion proposed by Zinn et al. (2011), which was since the beginning retained as a way to select sources at cosmological distances. On the other hand, many 1st-generation IFRSs lie in the sub-mJy radio regime, where radio sources can be associated with SFGs (see, e.g., Prandoni et al. 2001b; Mignano et al. 2008; Seymour et al. 2008; Smolčić et al. 2015).

With respect to the criteria proposed by Zinn et al. (2011), the search for objects lacking of any counterparts down to the SWIRE detection limit biased these samples towards radio-fainter sources, resulting in samples characterised by smaller $R_{3.6}$ ratios ($\gtrsim 100$). On the other hand, the fact that all these sources lack of an IR counterpart is a tighter criterion than the $S_{3.6\,\mu\mathrm{m}} < 30\,\mu$Jy one.

1st-generation and the 2nd-generation IFRSs studied by Collier et al. (2014) and Herzog et al. (2014) occupy two disconnected regions of the radio-IR parameter space (see Fig. 4.1). Then, a more in depth analysis is required to understand if they constitute a single population of objects, or rather a composite population, including SFGs.

To date, the most in depth analysis of the radio- and IR-faint IFRSs has been performed by Norris et al. (2011a), which investigated the IFRSs by Norris et al. (2006) in the CDFS field, and the IFRSs by Middelberg et al. (2008a) in the ELAIS-S1 field. They made use of 3.6 μm pre-release images belonging to the so far most sensitive *Spitzer* survey covering these fields, SERVS[11] (Mauduit et al., 2012).

SERVS is a deeper (5σ sensitivity $\sim 2\,\mu$Jy) follow-up of the SWIRE survey, covering a limited area ($\sim 18\,\mathrm{deg}^2$ in total) of the five SWIRE fields (CDFS, ELAIS-S1, ELAIS-N1, X-ray multi-mirror mission–large scale structure –XMM-LSS–, LH), and undertaken as part of the *Spitzer* Warm Mission. Due to the exhaustion of the *Spitzer* cryogenic coolant in May 2009, SERVS observations could only be performed in the 3.6 and 4.5 μm bands of the IRAC instrument. On the other hand, the more flexible schedule program allowed integration times ten-fold longer with respect to SWIRE. As a result, SERVS reaches a final 5σ sensitivity of 1.9 and 2.2 μJy respectively for the 3.6 and 4.5 IRAC bands (Mauduit et al., 2012).

Norris et al. (2011a) investigated faint IFRSs at 3.6 μm, stacking the 39 sources present within the SERVS mosaics. They reached a median flux density of $\widetilde{S}_{3.6\,\mu\mathrm{m}} < 0.42\,\mu$Jy, placing strong constraints on the IR properties of faint IFRSs. Moreover, Norris et al. (2011a) strengthened the link between IFRSs and HzRGs showing that no other type of object occupies the range of radio-to-IR flux density ratios of IFRS except for HzRGs (see Fig. 1.11).

Taking advantage of a new release of the SERVS images, we performed a new analysis of the radio- and IR-faintest IFRS samples.

4.2 Existing first generation IFRS samples

Out of the four samples of faint IFRSs (the ones by Norris et al. 2006; Middelberg et al. 2008a; Garn & Alexander 2008, and Banfield et al. 2011), only the one by Garn & Alexander (2008) is outside the SERVS fields. Therefore, we focused on the other samples, which belong to different radio surveys and are characterised by different sensitivities.

[11] http://irsa.ipac.caltech.edu/data/SPITZER/SERVS

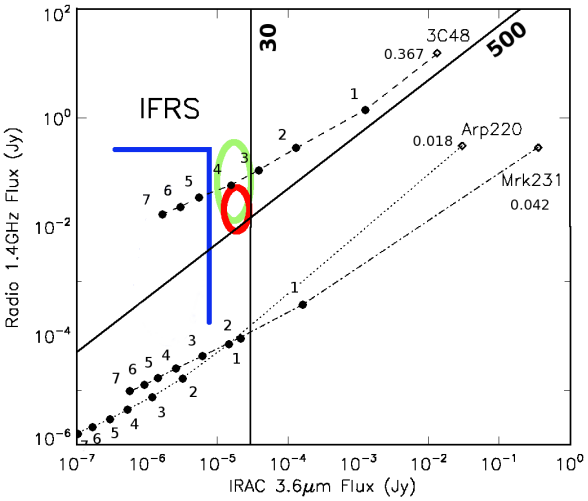

Figure 4.1: Location of some IFRS samples so far highlighted, within the 3.6 μm vs. 1.4 GHz parameter space. The two black solid lines represent the two Zinn criteria; 2nd-generation IFRSs lie in the top–left region of the plot; the green ellipse represents the sample of 1317 IFRSs by Collier et al. (2014), the red ellipse the sample of 4 IFRSs analysed by Herzog et al. (2014). The region below the blue lines ($S_{1.4\,\mathrm{GHz}} \lesssim 0.5$ Jy, $S_{3.6\,\mu\mathrm{m}} \lesssim 10\,\mu$Jy) delimit the sample we analysed. Superimposed are the flux densities expected for three sources (3C48, Arp 220, Mrk 231), obtained scaling down their actual flux densities with redshift and radio K-correction; the first point of each track reports the actual redshift of the source. Adapted from Zinn et al. (2011).

CDFS and ELAIS-S1 fields were observed with the ATCA at 1.4 GHz in the framework of the ATLAS survey (Norris et al. 2006 and Middelberg et al. 2008a). ATLAS covers about 3.5 deg^2 in each field, down to a typical rms sensitivity of 20–40 μJy, with spatial resolutions of 11×5 arcsec^2 and 10×7 arcsec^2, respectively. Since the publication of the first ATLAS data release, two further versions of the 1.4 GHz catalogues have been released (DR2 by Hales et al. 2014, and DR3 by Franzen et al. 2015). The flux densities reported in DR3 are consistent with the ones of DR1, and we decided to keep using the original flux density estimates for consistency with the previous works carried out on these samples of IFRSs.

The ELAIS-N1 field was observed at 1.4 GHz down to a rms sensitivity of 55 μJy in the framework of the DRAO *Planck* deep fields project (DRAO PDF; Taylor et al. 2007; Grant et al. 2010). The observations were carried out with the DRAO synthesis telescope (DRAO ST; Landecker et al. 2000), and combined with higher resolution VLA follow-up data (3.9×3.9 arcsec^2) and the FIRST survey (White et al. 1997, 5×5 arcsec^2) to provide better positions (Banfield et al., 2011).

As reported in Sect. 1.5.1 and summarised in Table 4.1 (Column 4), 22 and 29 IFRSs were identified in the CDFS and ELAIS-S1 fields, respectively (Norris et al., 2006; Middelberg et al., 2008a). Another 18 IFRSs were identified in the ELAIS-N1 (Banfield et al., 2011).

When searching for IR counterparts in the deeper SERVS fields some problems arise. First, SERVS mosaics cover smaller regions than the corresponding SWIRE ones. Therefore, the analysis is necessarily limited to sub-sets of the original IFRS samples, i.e. those located within the 3.6 and/or 4.5 μm SERVS fields. Moreover, SERVS approaches the confusion limited flux density regime (see Sect. 4.4.2 for more details) and some IFRSs lie in extremely crowded regions, increasing the likelihood of false cross-identifications. This forced us to reject three additional sources (one in the CDFS field and two in the ELAIS-N1 field: CS0283, DRAO6, and DRAO10). Of the original 69 1st-generation IFRSs belonging to the three aforementioned SWIRE fields, we retain in our study only 43 sources located within the SERVS 3.6 μm mosaics (see Table 4.1, Column 6). Finally, we notice that the 4.5 μm IRAC detector has a slightly shifted field of view with respect to the 3.6 μm one (Surace et al. 2005). Therefore the total number of original IFRSs within the footprint of the 4.5 μm mosaics is slightly smaller (40 instead of 43, see Table 4.4 for details).

Table 4.1: Main parameters of the radio, SWIRE and SERVS surveys, together with the number of 1st-generation IFRSs identified in each SWIRE and SERVS 3.6 μm field.

	1.4 GHz[(a)]	SWIRE[(b)]		SERVS[(c)]	
Field	Area	Area	IFRSs	Area	IFRSs
Name	(deg^2)	(deg^2)	(#)	(deg^2)	(#)
(1)	(2)	(3)	(4)	(5)	(6)
CDFS	3.7	6.58	22	4.5	21
ELAIS-S1	3.9	14.26	29	3.0	17
ELAIS-N1	15.2	8.70	18	2.0	5
Total			69		43

[(a)] The 1.4 GHz flux density limits in CDFS and ELAIS-S1 fields (ATLAS survey) are $\sim 100\,\mu$Jy, while in ELAIS-N1 (DRAO DF) is $\sim 275\,\mu$Jy.
[(b)] The SWIRE coverage refers to the IRAC instrument only. The average SWIRE 5σ flux density limits are 3.7, 5.4, 48 and 37.8 μJy in the four IRAC bands, respectively.
[(c)] the average SERVS 5σ flux density limits are 1.9 μJy at 3.6 μm band, and 2.2 μJy at 4.5 μm band.

4.3 New sample in the LH SERVS field

The LH field was observed at 1.4 GHz with the Westerbork Synthesis Radio Telescope (WSRT; Prandoni et al., submitted), covering about 6 deg^2 with a spatial resolution of 11×9 arcsec^2. This survey produced a catalogue of about 6000 radio sources down to a 5σ flux limit of 55 μJy. We searched for IFRSs in the LH field by cross-matching (searching radius of ~ 2 arcsec) this catalogue with the SERVS IR (3.6 μm) images and catalogues, which cover about 4.0 deg^2 in the region. The search for IFRSs in this field was performed following a set of *ad hoc* criteria, designed to include IFRSs as faint as for 1st-generation IFRSs, at the same time minimising the risk of contamination from normal galaxies populations, typically characterized by $R_{3.6}$ values $\lesssim 100$ (see Norris et al. 2006).

We therefore applied a looser threshold on the radio-to-IR flux ratio than the one applied by Zinn et al. (2011), which biases IFRS samples against the faintest radio sources, by retaining as IFRSs those radio sources with $R_{3.6} = S_{1.4\,\mathrm{GHz}}/S_{3.6\,\mu\mathrm{m}} \geq 200$ when they have a counterpart in the SERVS catalogue, and $S_{1.4\,\mathrm{GHz}}/(2.0\,\mu\mathrm{Jy}) \geq 200$ when they have no counterpart in the SERVS catalogue (assuming a value of 2.0 μJy as a representative SERVS 3.6 μm detection limit). Moreover we took into account only IR counterparts unresolved at the scale of the SERVS point spread function (PSF = 1.9 arcsec; see Sect. 4.4.2 for more details), which roughly correspond to intrinsic sizes $\lesssim 32$ kpc at $z \gtrsim 1$. This size criterion allows us to exclude local (extended) sources that may be intrinsically faint, together with partially overlapping interacting galaxies, for which aperture photometry flux density measurements would be unreliable. This criterion turns out to be tighter than the $S_{3.6\,\mu\mathrm{m}} < 30\,\mu$Jy constraint applied by Zinn et al. (2011), as no one of our sources has $S_{3.6\,\mu\mathrm{m}}$ greater than 10 μJy (see Table 4.4 for details).

As a final step we performed a visual inspection of the 3.6 μm images for all the candidate IFRSs, and we removed the sources in crowded regions (i.e. for which the cross-matching is doubtful), those of uncertain radio position (e.g. due to a complex radio shape), and those coinciding with catalogued radio lobes. In the end, in the LH field we retained 21 sources at

3.6 μm, 19 of which fall inside the 4.5 μm mosaic footprint.

In summary, our analysis was carried out on a total of 64 sources over four fields, 59 of which fall inside the 4.5 μm mosaic footprint (see Table 4.4 for details).

In principle the sources belonging to the 1st-generation IFRS samples and the ones we extracted, being characterised by any or very faint IR fluxes ($S_{3.6\,\mu\mathrm{m}} < 10\,\mu$Jy), are potentially farther than the ones extracted following the Zinn et al. (2011) criteria. This allow us to perform a more comprehensive analysis of the IFRS population for several ranges of $R_{3.6}$ ratio, and to explore a more extended area of the parameter space for this class of objects.

4.4 Flux density measurement at 3.6 and 4.5 μm

Flux densities at 3.6 and 4.5 μm for all the sources in the SERVS deep fields were measured on the SERVS mosaics using a standardised procedure. Our flux density measurement includes three steps: 1) Correction for systematic offsets between radio and IR catalogues; 2) Extraction of the IR image cutouts centred on the corrected radio positions; 3) Flux density measurement through the aperture photometry technique.

4.4.1 Correction for radio-IR positional offsets and extraction of image cutouts

We rely on positional offsets between the IR and radio computed by Maini (2012), which are giving in Table 4.2 and briefly described in this section.

Positional offsets were established by cross-matching the ATLAS and SERVS catalogues for the CDFS and ELAIS-S1 fields, and the WSRT and SERVS catalogues for the LH field. For the ELAIS-N1 field we used the FIRST survey (see Sect. 4.2), as the original DRAO observations have too poor spatial resolution (42×69 arcsec^2).

For each field and SERVS frequency we cross-matched the radio and SERVS source catalogues, and derived the distribution of the separation between closest matches. Selecting the nearest neighbour as IR counterpart is clearly a very simplistic criterion, but it is adequate enough as we are interested in a statistical quantification of the average systematic offsets between catalogues.

We defined the systematic offsets as the position of the peak of the Gaussians used to fit the radio-IR separation distributions. The result are shown in Table 4.2. Some offsets are larger than the SERVS positional accuracies (0.1–0.2 arcsec), but all are well below the SERVS PSF ($\sim 2 \times 2$ arcsec^2; Mauduit et al. 2012).

We then corrected the radio positions for the corresponding offsets, and we extracted from the SERVS mosaics cutouts at both 3.6 and 4.5 μm, each centred at the corrected IFRS radio position. The cutouts are 99×99 pixels (i.e. 30×30 SERVS PSFs) wide.

Table 4.2: Radio-IR positional offsets for each field, both for 3.6 and 4.5 μm catalogues.

Field	3.6 μm band		4.5 μm band	
Name	ΔRA (arcsec)	ΔDec (arcsec)	ΔRA (arcsec)	ΔDec (arcsec)
CDFS	0.03	−0.04	−0.02	−0.20
ELAIS-S1	−0.05	−0.02	−0.19	−0.11
ELAIS-N1	0.04	−0.01	−0.19	−0.14
LH	−0.01	−0.14	0.03	0.09

4.4.2 Aperture photometry at 3.6 and 4.5 μm

For each cutout, we used the `DAOPHOT` task of the *Image Reduction and Analysis Facility* software (IRAF[12]) to measure the flux density through the aperture photometry technique, either at the centre of the cutouts (when no source was visually identified) or at the nearest IR source position (when a likely IR counterpart was present). We set the aperture radius to 1.9 arcsec, which roughly corresponds to the PSF of SERVS point sources (Mauduit et al., 2012). Finally, we multiplied the measured flux densities for the IRAC aperture corrections corresponding to that radius (1.359 for the 3.6 μm band and 1.397 for the 4.5 μm band; Surace et al. 2005).

The uncertainties in the measured aperture flux densities were again estimated using the `DAOPHOT` task. We built a grid of 15 × 15 apertures for each cutout, and we computed the flux density from each aperture. For each cutout, the distribution of such flux densities was fitted by a Gaussian. Then, we iteratively rejected the $> 3\sigma$ outliers (likely contaminated by the presence of a source) until the process converged. The standard deviation of the final Gaussian distribution is a measure of the local rms of the cutout and provides an estimate of the error on the flux density measurement. In case of non-detections a (3× local rms) upper limit is provided. In Table 4.4 (Columns 11 and 12) are reported the flux densities and the associated errors for the each counterpart we found.

This procedure allowed us to look for detections below the standard 5σ threshold of the SERVS catalogues, and to approach the true hard detection limit of the survey.

From the theoretical point of view, the reliable detection of a point (or compact) source depends on two important criteria: the 'photometric criterion', following which the intensity of a source has to be well above the stochastic fluctuation amplitude of the background sky brightness; and the 'source density criterion', following which a source has to be far enough from sources of similar brightness so that they could be properly separated and individually detected. These two criteria together set the 'confusion limit': above this level compact sources can be clearly detected (see, e.g., Scheuer 1974a; Condon 1974; Dole et al. 2003).

It has also to be noted that the interpretation of the 'confusion limit' is different in an unbiased survey (i.e., when searching for all the detections above a certain limit, as when building a survey catalogue, which typically can rely on signals above 5–6σ the map noise only) and when observing an individual source that is known to exist at a certain position (i.e., when an identification is the true aim of the search, and additional information are known from other wavelengths, which allows to take into account signals at 3σ also). Moreover, in the latter case it is possible (given certain conditions) to integrate below the confusion limit

[12] http://iraf.noao.edu/

set by the whole ensemble of sources.

Basing its analysis on the density estimate for the sources (i.e. on the 'source density criterion' only) Franceschini et al. (1991) estimated that extragalactic, low-background observations in the near-IR, for a PSF around 1.9 arcsec, are limited to a confusion limit of about 0.6 μJy. Fazio et al. (2004) showed that such a noise value was within the potentialities of the IRAC camera of *Spitzer*, for both 3.6 and 4.5 μm bands and for frame-time of 100 seconds during the warm mission, and that can be even lower for longer exposure times.

As reported by Mauduit et al. (2012), the strategy adopted for SERVS observations is composed by two epochs of six 100 seconds frames each, and the resulting mean integration time per pixel of the SERVS mosaics is very close to the design depth at $\sim$ 1200 seconds. Moreover, as reported in Instrument & Teams (2015) (version 2.1.2, Sect. 2.5.1), data from In-Orbit Checkout/Science Verification phase showed that the noise keeps decreasing as $\sqrt{N}$ (where N is the number of frames) down to 0.25 μJy for both 3.6 and 4.5 μm bands.

Therefore, if 0.6 μJy was assumed as mild sensitivity limit for the SERVS data, our procedure allows us to approach the true limit of the survey, with noise down to 0.33 μJy for the source LH2633 (se Table 4.4).

We notice that some of the brightest sources are listed in the SERVS catalogues, and the flux densities we derived are consistent with those provided by those catalogues. On the other hand our flux density errors are larger, and have to be considered as more conservative. For consistency we adopted our flux density (and error) estimates for all sources, disregarding their presence (or not) in the SERVS catalogues.

4.5 Reliability of the SERVS counterparts, false detection rate, and information at other wavelengths

To extract a sample of reliable IR identifications the close-neighbour criterion alone is not enough, and we need to associate to every SERVS counterparts we found a reliability. To compute such a quantity we applied the likelihood ratio technique (see e.g. de Ruiter et al. 1977; Sutherland & Saunders 1992; Ciliegi et al. 2003) which allows to take into account the probability of finding neither a chance identification nor a peak noise closer to the radio source than the IR candidate.

A convenient way to compute the reliability is to make use of an a-dimensional radius of cross-matching. This radius is expressed in term of combined positional accuracy of the radio and IR source positions (σ_{RA} and σ_{Dec}, Columns 5 and 6, Table 4.4), and in term of physical distance between the potential counterpart and the radio source (ΔRA and ΔDec, Columns 7 and 8, Table 4.4). To compute the combined positional accuracy (which depends on the position errors of the sources in the two wavelengths) we made the simplistic assumption that the counterpart we found is characterised by the same position accuracy of the SERVS catalogued sources (0.2 arcsec).

The adimensional radius is expressed as:

$$r_{adim} = \sqrt{\left(\frac{\Delta\mathrm{RA}}{\sigma_{RA}}\right)^2 + \left(\frac{\Delta\mathrm{Dec}}{\sigma_{Dec}}\right)^2}$$

We then need to know the expected contamination (by spurious identifications) of the counterpart pool, which depends on two quantities both described by a Poisson distribution

Table 4.3: Summary of the main parameters entering the reliability and cross-matching procedures.

Field name	Band Wavelength (μm)	Surface density ($S_{IR} > 1\,\mu$Jy) (10^{-3}/arcsec^2)	Average searching radius (arcsec)	False detection rate	Representative 3σ-rejection rms (μJy)
(1)	(2)	(3)	(4)	(5)	(6)
CDFS	3.6	8.0	1.74	~6%	0.61
	4.5	7.6	1.77	~6%	0.65
ELAIS-S1	3.6	9.5	1.60	~6%	0.62
	4.5	8.9	1.65	~7%	0.66
ELAIS-N1	3.6	9.8	1.57	~8%	0.65
	4.5	9.5	1.59	~6.5%	0.67
LH	3.6	11.3	1.49	~6%	0.58
	4.5	10.5	1.54	~5%	0.69

(which expresses the discrete probability for an event to occur n times within a fixed interval of a parameter, when it is known its average occurrence rate λ and it is known that each occurrence is independent to each other in that parameter space):

$$P(n, \lambda) = \frac{\lambda^n \, e^{-\lambda}}{n!}$$

The first of these two quantities is the probability that a random source falls within the searching area, when it is not the real counterpart. This quantity depends on the background source average surface density, and can be expressed as:

$$\lambda_{bg} = A(r_{adim}) \times N(> S_{lim})$$

In this formula A is the surface of the searching ellipse ($A(r_{adim}) = \pi \, \sigma_{RA} \, \sigma_{Dec} \, r^2_{adim}$), while $N(> S_{lim})$ is the average surface density for IR sources with flux greater than a fixed flux limit (S_{lim}). We selected the value for $S_{lim} = 1\,\mu$Jy based on our approaching the hard detection limit on SERVS, and the surface density we can expect in SERVS based on this value are reported in Table 4.3, Column 3.

The second of these quantites is the probability that within the searching region falls a random fluctuation noise of amplitude greater than $S_{lim} = 1\,\mu$Jy, that can therefore misidentified as a counterpart. This type of contamination is expressed as:

$$\lambda_{np} = N_{pxl} \times P_{Gauss}(> S_{lim})$$

In this formula N_{pxl} is the number of pixels included within the searching ellipse, which can be approximated by the relation: $N_{pxl} = A(r_{adim})/(\text{Area of 1 pixel}) = (\pi \, \sigma_{RA} \, \sigma_{Dec} \, r^2_{adim})/(0.6\,\text{arcsec})^2$, where 0.6 arcsec is the SERVS pixel size (Mauduit et al., 2012), while $P_{Gauss}(> S_{lim})$ is the Gaussian probability to have noise fluctuation $> S_{lim}$, which for $S_{lim} = 3\sigma$ is $P_{Gauss}(> S_{lim}) = (1 - 0.9973)/2 = 1.35 \times 10^{-3}$.

The reliability R of each identification can therefore be expressed as the probability to have nor a background source neither a peak noise within the searching region defined by

the distance of the potential counterpart. This combined probability is the multiplication of the two separate Poisson probabilities:

$$R(r_{adim}) = P(0, \lambda_{bg}) \times P(0, \lambda_{np}) = \frac{\lambda_{bg}^0 \, e^{-\lambda_{bg}}}{0!} \times \frac{\lambda_{pn}^0 \, e^{-\lambda_{pn}}}{0!} =$$

$$= e^{-(\lambda_{bg}+\lambda_{pn})} = e^{-\pi \, \sigma_{RA} \, \sigma_{Dec} \, r_{adim}^2 \times \left[N(>S_{lim}) + \frac{P_{Gauss}(>S_{lim})}{0.36\,\mathrm{arcsec}^2}\right]}$$

The reliability was computed for both 3.6 and 4.5 μm counterparts, and typically ranges from 70% to 99% (Column 9, Table 4.4). To avoid to be contaminated by false-positive identifications, in any following analysis we only retain SERVS counterparts with reliability >90%, while we consider as undetected all IFRSs with no (or unreliable) SERVS counterparts.

In total we found 21 reliable counterparts at 3.6 and 20 at 4.5 μm, for a total of 25 distinct IFRSs out of the original 64 sources we analysed (see Sect. 4.3). When identified at both bands the reliability constraint (>90%) is satisfied at both 3.6 and 4.5 μm. In Figure 4.2 are reported the SERVS cutouts of the reliable counterparts identified in CDFS, ELAIS-S1 and ELAIS-N1. In Figure 4.3 are reported the SERVS cutouts of the reliable counterpart identified in the LH SERVS field, with superimposed the radio contours.

The reliability as computed before gives us an estime about the goodness of the cross-matching (i.e. quantifies how confident we can be about the fact that the potential counterpart we found is the real counterpart given the catalogues and the source characteristics), but cannot guarantee that the counterpart is the actual counterpart we were searching for (for instance, the real counterpart could be below the detection threshold, while the spurious source is above). For this, we need the false identification rate.

To estimate the false detection rate we searched for serendipitous detections with reliability >90%, by shifting the positions of the radio sources by an amount between 50 and 500 arcsec in 100 steps spiralling outward, and measuring the aperture photometry at each of such positions. False detection rates range from 5 to 8% (depending on the field and on the band, see Table 4.3, Column 5), so we expect that 2–3 counterparts out of the 41 (21 at 3.6 and 20 at 4.5 μm) retained as reliable IFRSs are false.

As mentioned in Sect. 4.1, the only previous attempt to search for IFRS IR counterparts using SERVS data was performed by Norris et al. (2011a) which used a pre-release of the 3.6 μm images. They detected 3 out of 39 1st-generation IFRSs in the CDFS and ELAIS-S1 SERVS fields (CS0114, with $S_{3.6\,\mu\mathrm{m}} = 2.20 \pm 0.54\,\mu$Jy; CS0173, with $S_{3.6\,\mu\mathrm{m}} = 2.14 \pm 0.65\,\mu$Jy; and CS0255, with $S_{3.6\,\mu\mathrm{m}} = 1.91 \pm 0.53\,\mu$Jy), and reported a false detection rate very similar to the one we found in these same fields ($\sim$ 6%) concluding that all detections were consistent with being chance associations caused by confusion (these three sources are detected also by us with similar flux densities, see Table 4.4).

A direct comparison between these two results is not straightforward, due to the different techniques used in the two works, but can be accomplished to some extent. The first thing to notice is that Norris et al. (2011a) used an average searching radius $\sim$ 1 arcsec. In our work and in the same two fields, our average searching radius is $\sim$ 1.69 arcsec (see Table 4.3, Column 4), which results in a cross-matching area around 2.9× greater. This should lead to an equal increase in both the number of potential counterparts and the false detection rate.

However, we applied an improved cross-matching algorithm and a standardised criterion for source extraction and characterisation, and we did non simply rely on a by-eye search for

Figure 4.2: Images of the reliable (i.e. reliability >90%) counterparts of IFRSs identified in CDFS, ELAIS-S1, and ELAIS-N1 fields. All the images are $\sim 40 \times 40$ arcsec^2 wide, North is up and East on the left. The (inverted colours) black-and-white background images are SERVS cutouts, taken from the 3.6 or the 4.5 μm mosaics (depending on which band the reliability has been computed on). Superimposed are a red cross (marking the radio peak position, always at the centre of the cutout), and a cyan circle (marking the area within which aperture photometry was derived). From Maini et al. (2016b).

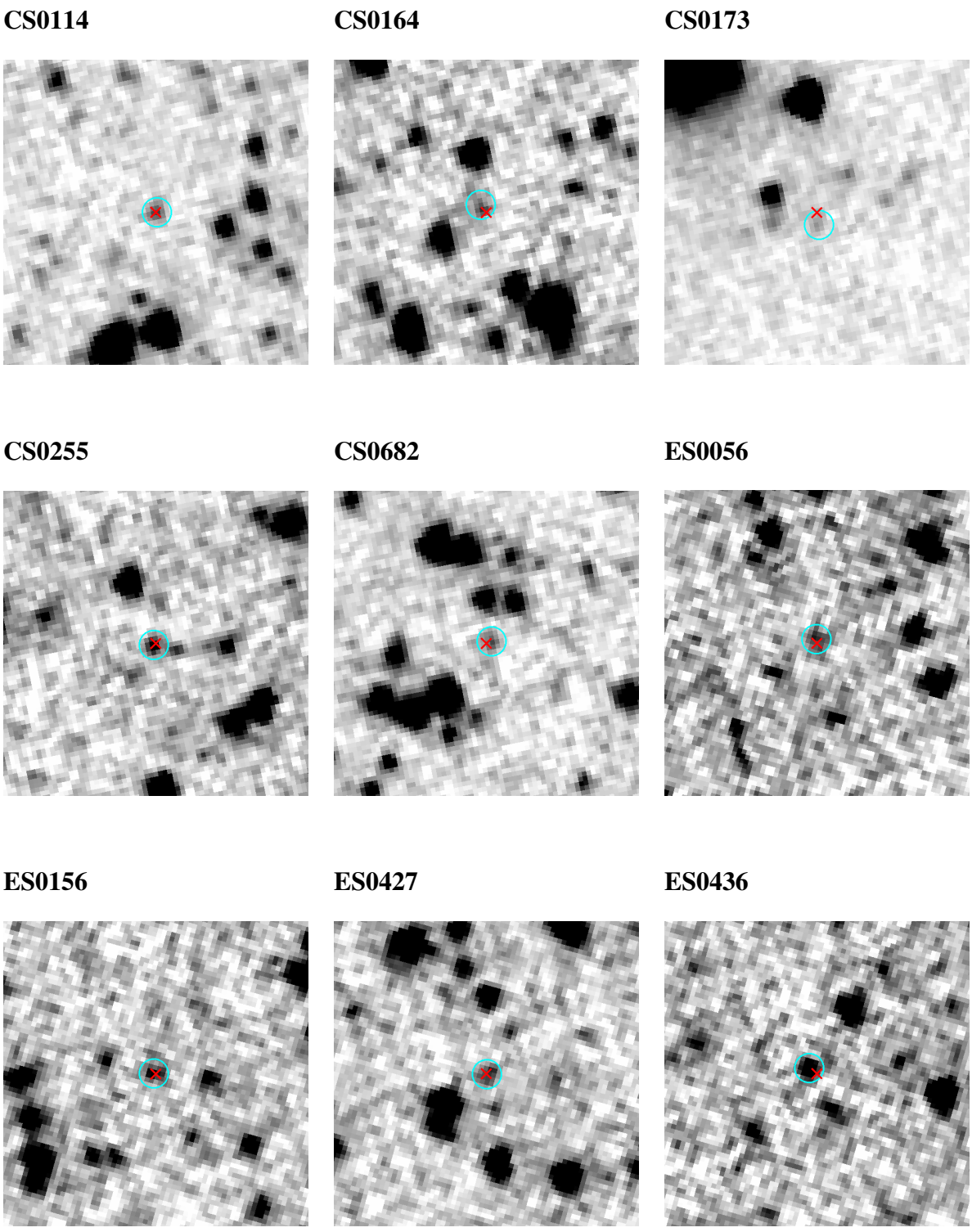

ES0593

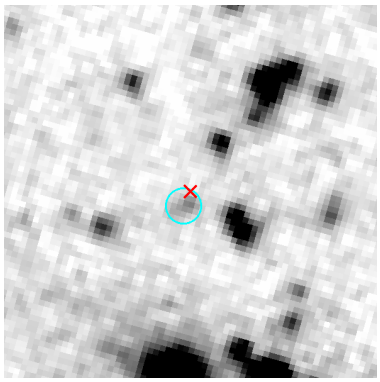

ES0696

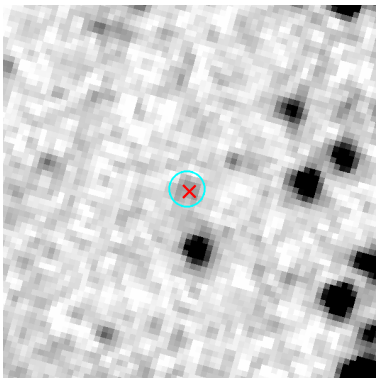

ES0913

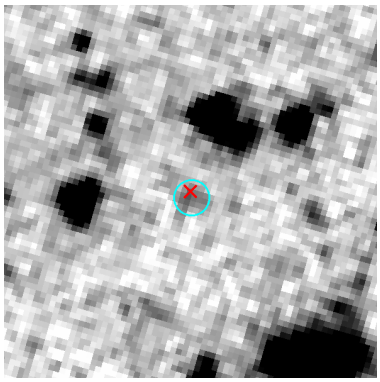

ES1154

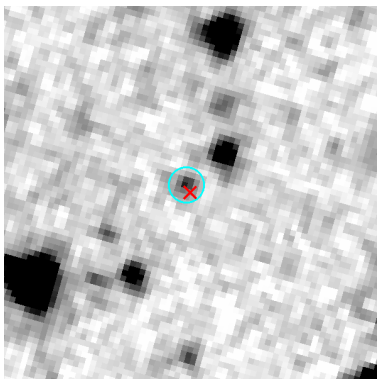

DRAO3

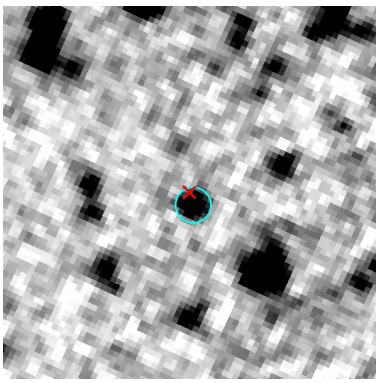

Figure 4.3: Images of the reliable (i.e. reliability >90%) counterparts of IFRSs identified in LH SERVS field. All the images are $\sim 40 \times 40\,\mathrm{arcsec}^2$ wide, North is up and East on the left. The (inverted colours) black-and-white background images are SERVS cutouts, taken from the 3.6 or the 4.5 μm mosaics (depending on which band the reliability has been computed). Superimposed are a red cross (marking the radio peak position, always at the centre of the cutout), a cyan circle (marking the area within which aperture photometry was derived), and a green square (marking the position of the optical counterparts, see Table 4.4). Also reported are the isophotes of the radio sources (magenta lines, contour levels at 10, 20, 40, 80, 160, 320, 640, and 1280σ the radio image noise). From Maini et al. (2016b).

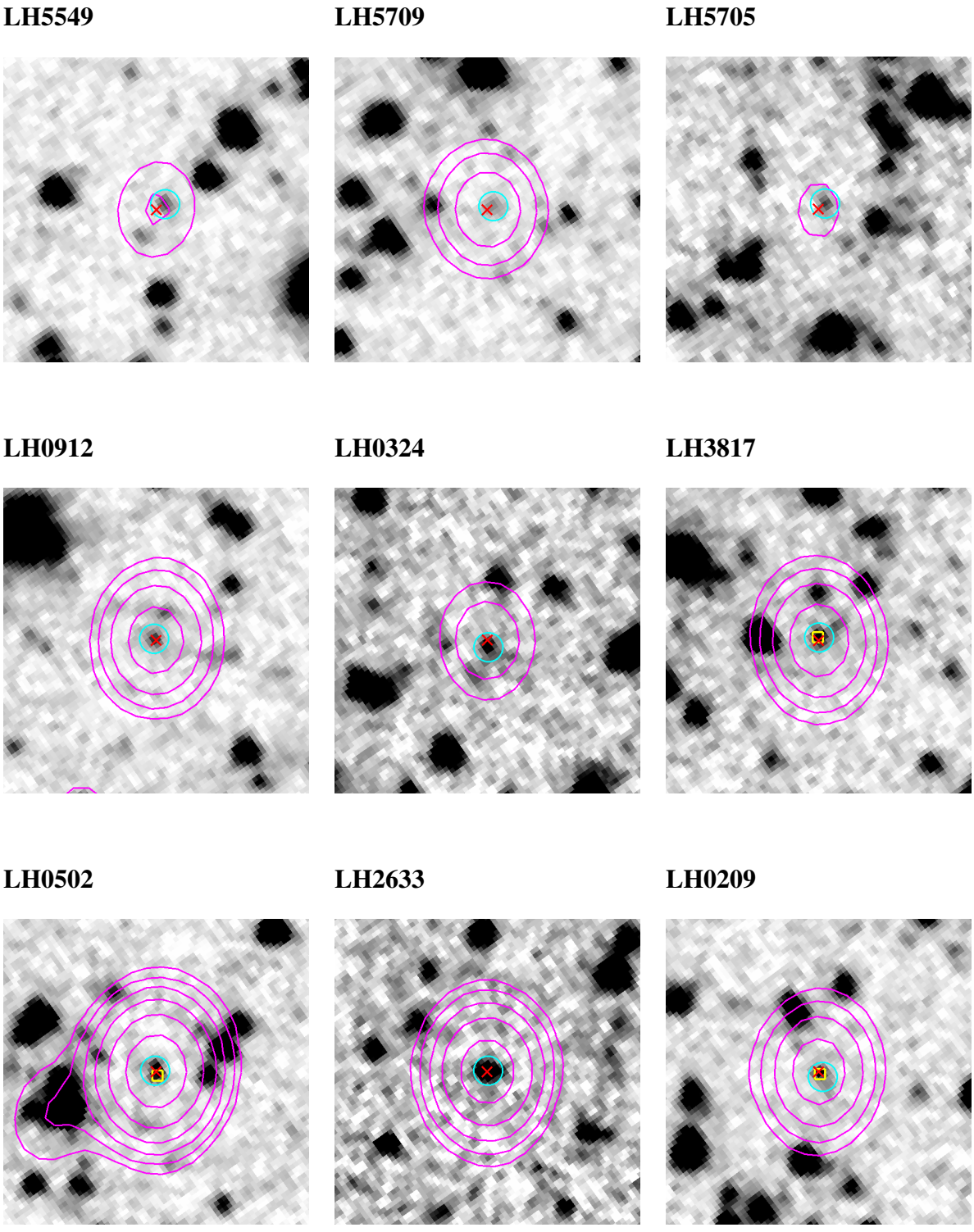

LH5785 **LH2417**

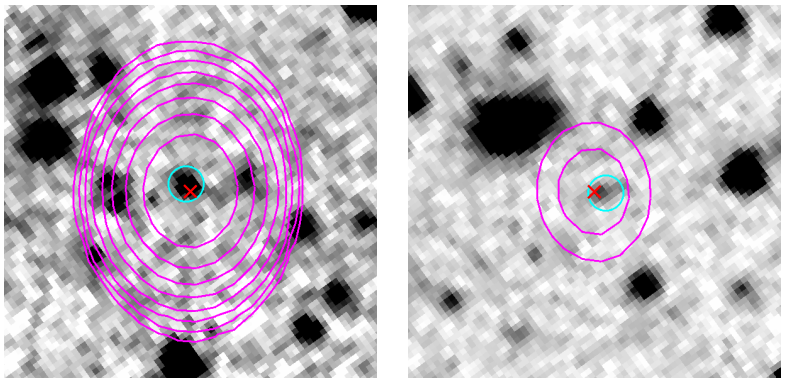

peak in intensity, which both improved the number of potential counterparts we found, and lowered the false detection rate per unit area.

In Table 4.4 we list the 3.6 and 4.5 μm aperture flux densities and errors (or the 3σ upper limits in case of no detection or unreliable SERVS identification) measured for all the sources in the SERVS fields (Columns 11 and 12). Also listed are the derived radio-to-infrared flux ratios or upper limits (Columns 13 and 14), and the 4.5-to-3.6 μm flux ratios or upper/lower limits in case of detection at only one band (Column 15). The new SERVS mosaics allowed us to get reliable IR counterparts for 21 IFRSs at 3.6 μm, for 20 at 4.5 μm, and for 16 in both bands. All detected sources have IR fluxes of a few μJy, typically with S/N $\sim$ 3–10. The three sources associated with crowded regions and discarded (see Section 4.2) are marked with '–' in all IR-related columns. The IFRSs which are located outside the 4.5 μm footprint are marked 'out' in the 4.5 μm flux density column.

For six sources we have found an optical counterpart. These counterparts have been identified by imposing a maximum search radius of 2 arcsec around the radio source position, and were found in a number of independent surveys as listed at the end of Table 4.4. With only one exception (LH3817, with K_{AB} = 20.75), the optical magnitudes of these objects are very faint (AB magnitudes $\gtrsim$ 24, see Table 4.4, Col. 17), suggesting high redshifts. None of the reliable optical counterparts has a measured redshift.

Table 4.4: Radio and infrared properties of the candidate IFRSs in SERVS fields. Column (1): field name; Column (2): source identifier; Columns (3) and (4): position of the radio source; Columns (5) and (6): uncertainties in the radio position; Column (7) and (8): distance from the claimed IR counterpart; Column (9): reliability of the identification (this value refers to the cross-matched 3.6 μm counterpart, unless the counterpart has been detected only at 4.5 μm); Column (10): 1.4 GHz flux density; Columns (11) and (12): measured 3.6 and 4.5 μm flux densities (3σ upper limits are provided in case of no detection); Columns (13) and (14): 1.4 GHz-to-3.6 μm and 1.4 GHz-to-4.5 μm flux ratios, respectively (3σ lower limits are provided in case of no detection); Column (15): 4.5 μm-to-3.6 μm flux ratio (3σ upper/lower limits are provided in case of detection at only one band); Column (16): Spectral index (from Franzen et al. 2015, except for ES0973 from Middelberg et al. 2011b); Column (17): Optical magnitude (AB system; band of reference as subscript). We notice that in case of unreliable IR identifications we provide both the measured estimates and 3σ limits (following row) for all IR or IR-derived parameters.

Field name	IFRS ID	Radio coordinates (J2000)		Combined positional accuracy (arcsec)		Distance from claimed IR 3.6/4.5 μm couterpart (arcsec)		Reliability	$S_{1.4\,\mathrm{GHz}}$	$S_{3.6\,\mu\mathrm{m}}$	$S_{4.5\,\mu\mathrm{m}}$	$S_{1.4\,\mathrm{GHz}}/S_{3.6\,\mu\mathrm{m}}$ $S_{1.4\,\mathrm{GHz}}/(3\times N_{3.6\,\mu\mathrm{m}})$	$S_{1.4\,\mathrm{GHz}}/S_{4.5\,\mu\mathrm{m}}$ $S_{1.4\,\mathrm{GHz}}/(3\times N_{4.5\,\mu\mathrm{m}})$	$S_{4.5\,\mu\mathrm{m}}/S_{3.6\,\mu\mathrm{m}}$	Spectral index	Optical magnitude
		(hh:mm:ss)	(dd:mm:ss)	σ_{RA}	σ_{Dec}	ΔRA	ΔDec	(%)	(mJy)	(μJy)	(μJy)					
(1)	(2)	(3)	(4)	(5)	(6)	(7)	(8)	(9)	(10)	(11)	(12)	(13)	(14)	(15)	(16)	(17)
CDFS	CS0114	03:27:59.89	−27:55:54.7	1.02	1.02	0.12	0.89	99	7.17 ± 1.43	2.13 ± 0.47	2.37 ± 0.47	3366 ± 1001	3025 ± 851	1.11 ± 0.33	−1.33	
	CS0122	03:28:12.99	−27:19:42.6	1.42	3.59	1.90		86	0.46 ± 0.10	1.47 ± 0.46	< 1.29	313 ± 119	> 357	< 0.88		
										< 1.38	< 1.29	> 333	> 357	…		
	CS0164	03:29:00.20	−27:37:45.7	1.02	1.26	1.21	1.06	95	1.21 ± 0.25	1.89 ± 0.50	2.51 ± 0.67	640 ± 215	482 ± 163	1.33 ± 0.50	−0.26	
	CS0173	03:29:09.66	−27:30:13.7	1.42	3.77	1.71	1.66	96	0.35 ± 0.08	1.66 ± 0.41	2.76 ± 0.48	211 ± 71	127 ± 36	1.66 ± 0.50	−0.01	
	CS0194	03:29:28.59	−28:36:18.8	1.02	1.02				6.09 ± 1.22	< 1.77	< 2.16	> 3441	> 2819	…	−0.92	
	CS0215	03:29:50.01	−27:31:52.6	1.02	1.02				1.10 ± 0.22	< 1.50	< 1.50	> 733	> 733	…	−0.71	
	CS0241	03:30:10.21	−28:26:53.0	1.02	1.54				1.28 ± 0.26	< 1.41	< 1.71	> 908	> 749	…	−1.05	
	CS0255	03:30:24.08	−27:56:58.7	1.20	3.17	0.36	0.85	99	0.55 ± 0.12	2.42 ± 0.50	3.35 ± 0.56	227 ± 68	164 ± 45	1.38 ± 0.37	0.04	
	CS0275	03:30:43.69	−28:47:55.6	1.39	1.83				0.36 ± 0.08	< 1.20	< 1.68	> 300	> 214	…		
	CS0283	03:30:48.68	−27:44:45.3	1.17	2.04	–	–	–	0.29 ± 0.07	–	–	–	–	–	–	–
	CS0415	03:32:13.07	−27:43:51.0	1.02	1.02				1.21 ± 0.25	< 1.02	< 1.20	> 1186	> 1008	…	−1.19	
	CS0446	03:32:31.54	−28:04:33.5	2.22	3.65	2.00		87	0.34 ± 0.08	1.55 ± 0.50	< 2.07	219 ± 88	> 164	< 1.34		25.55_B [a]
										< 1.50	< 2.07	> 227	> 164	…		
	CS0487	03:33:01.19	−28:47:20.7	1.02	1.60				1.12 ± 0.23	< 1.62	< 2.01	> 691	> 557	…	−0.62	
	CS0506	03:33:11.48	−28:03:19.0	1.57	2.37	2.44	2.57	83	0.17 ± 0.06	1.80 ± 0.47	2.20 ± 0.50	94 ± 41	77 ± 32	1.22 ± 0.42		26.16_B [a] 27.10_U [b] 26.15_B [b] 26.59_V [b] 26.16_R [b] 26.06_I [b] 24.38_Z [b]
										< 1.41	< 1.50	> 121	> 113	…		
	CS0538	03:33:30.20	−28:35:11.1	1.45	2.58				1.40 ± 0.28	< 2.16	< 1.95	> 648	> 718	…	−1.19	
	CS0588	03:34:04.70	−28:45:01.7	1.30	3.32				0.45 ± 0.10	< 1.41	< 1.50	> 319	> 300	…		
	CS0682	03:35:18.48	−27:57:42.2	1.20	2.88		0.73	96	0.34 ± 0.08	< 1.59	2.26 ± 0.72	> 214	150 ± 60	> 1.42		
	CS0694	03:35:25.08	−27:33:13.2	1.02	1.40				0.60 ± 0.13	< 1.98	< 2.31	> 303	> 260	…	−0.93	24.91_i [c]
	CS0696	03:35:25.25	−28:31:05.2	1.02	1.78				0.31 ± 0.07	< 1.65	< 1.71	> 188	> 181	…		
	CS0703	03:35:31.02	−27:27:02.2	1.02	1.02	3.12	3.27	70	26.08 ± 5.22	2.34 ± 0.61	1.97 ± 0.51	11145 ± 3663	13239 ± 4332	0.84 ± 0.31	−0.96	
										< 1.83	< 1.53	> 14251	> 17046	…		
	CS0706	03:35:33.22	−28:06:21.8	1.07	1.51				0.26 ± 0.07	< 1.62	< 1.95	> 160	> 133	…		
	CS0714	03:35:38.16	−27:44:00.6	1.45	2.22				0.39 ± 0.09	< 1.23	< 1.02	> 317	> 382	…		
ELAIS-S1	ES0056	00:33:46.75	−44:29:02.8	1.02	1.19		0.43	99	0.58 ± 0.12	< 1.56	2.97 ± 0.80	> 372	195 ± 66	> 1.90	−2.35	
	ES0135	00:33:30.12	−44:21:15.4	1.60	1.56				0.18 ± 0.05	< 2.28	out	> 79	…	…		
	ES0156	00:34:46.40	−44:19:26.9	1.02	1.41		0.14	99	0.37 ± 0.08	< 1.53	2.00 ± 0.44	> 242	185 ± 18	> 1.31	−0.88	
	ES0318	00:37:05.54	−44:07:33.6	1.02	1.14				1.59 ± 0.32	< 1.65	< 1.98	> 964	> 803	…	−1.42	

Field name	IFRS ID	Radio coordinates (J2000)		Combined positional accuracy (arcsec)		Distance from claimed IR 3.6/4.5 μm couterpart (arcsec)		Reliability	$S_{1.4\,\mathrm{GHz}}$	$S_{3.6\,\mu\mathrm{m}}$	$S_{4.5\,\mu\mathrm{m}}$	$S_{1.4\,\mathrm{GHz}}/S_{3.6\,\mu\mathrm{m}}$ $S_{1.4\,\mathrm{GHz}}/(3\times N_{3.6\,\mu\mathrm{m}})$	$S_{1.4\,\mathrm{GHz}}/S_{4.5\,\mu\mathrm{m}}$ $S_{1.4\,\mathrm{GHz}}/(3\times N_{4.5\,\mu\mathrm{m}})$	$S_{4.5\,\mu\mathrm{m}}/S_{3.6\,\mu\mathrm{m}}$	Spectral index	Optical magnitude
		(hh:mm:ss)	(dd:mm:ss)	σ_{RA}	σ_{Dec}	ΔRA	ΔDec	(%)	(mJy)	(μJy)	(μJy)					
(1)	(2)	(3)	(4)	(5)	(6)	(7)	(8)	(9)	(10)	(11)	(12)	(13)	(14)	(15)	(16)	(17)
ELAIS-S1	ES0427	00:34:11.59	−43:58:17.0	1.02	1.02	0.17		99	21.36 ± 4.27	1.94 ± 0.46	< 1.56	11010 ± 3415	> 13692	< 0.80	−0.95	
	ES0433	00:34:13.43	−43:58:02.4	1.02	1.02				0.25 ± 0.06	< 1.62	< 1.41	> 154	> 177	...	−1.41	
	ES0436	00:37:26.34	−43:57:33.0	1.09	1.54	1.20	1.07	93	0.19 ± 0.06	3.27 ± 0.42	4.12 ± 0.64	58 ± 20	46 ± 16	1.26 ± 0.25		
	ES0463	00:34:10.14	−43:56:25.5	1.25	1.76				0.14 ± 0.04	< 1.29	< 1.71	> 109	> 82	...		
	ES0593	00:35:10.80	−43:46:37.2	1.22	1.73	1.71	1.65	91	0.17 ± 0.05	2.98 ± 0.71	4.54 ± 0.52	57 ± 22	37 ± 12	1.52 ± 0.40		
	ES0696	00:34:02.26	−43:40:08.5	1.02	1.02	0.61		98	0.49 ± 0.11	1.33 ± 0.43	< 1.83	368 ± 145	> 268	< 1.38	0.07	
	ES0913	00:37:33.42	−43:24:53.4	1.02	1.02	0.63		98	0.68 ± 0.14	1.33 ± 0.39	< 1.47	511 ± 183	> 463	< 1.11	−1.62	
	ES0973	00:38:44.13	−43:19:20.4	1.32	1.44				9.14 ± 1.83	< 2.46	< 2.64	> 3715	> 3462	...	−1.15	
	ES1118	00:36:22.25	−43:10:15.0	1.06	1.50				0.51 ± 0.11	< 1.41	< 1.56	> 362	> 327	...		
	ES1154	00:35:46.92	−43:06:32.4	1.02	1.10	0.85	0.46	97	0.53 ± 0.11	2.11 ± 0.38	3.91 ± 0.53	251 ± 69	136 ± 34	1.85 ± 0.42	−0.56	
	ES1193	00:37:19.58	−43:02:01.4	1.07	1.52				0.23 ± 0.06	< 1.35	< 1.65	> 170	> 139	...		
	ES1259	00:38:27.17	−42:51:33.7	1.02	1.02				4.52 ± 0.90	< 2.19	out	> 2063	...	...		
	ES1260	00:38:24.94	−42:51:37.9	1.32	1.86				0.80 ± 0.16	< 1.92	out	> 417	...	...		
ELAIS-N1	DRAO3	16:05:30.48	+54:09:02.0	0.26	0.26	0.82	1.14	97	3.56 ± 0.24	5.16 ± 0.43	6.38 ± 0.74	690 ± 74	558 ± 75	1.24 ± 0.18		
	DRAO6	16:06:47.93	+54:15:10.5	0.28	0.28	–	–	–	2.23 ± 0.18	–	–	–	–	–	–	–
	DRAO7	16:08:38.74	+54:27:51.8	0.31	0.31	2.15	2.20	82	1.39 ± 0.13	2.09 ± 0.50	2.32 ± 0.50	665 ± 171	599 ± 141	...		
										< 1.50	< 1.50	> 927	> 927	...		
	DRAO8	16:09:49.75	+54:08:33.3	0.36	0.36				1.08 ± 0.13	< 1.47	< 1.17	> 735	> 923	...		
	DRAO9	16:11:12.89	+54:33:17.6	0.25	0.25				2.45 ± 0.14	< 1.32	< 1.50	> 1856	> 1633	...		
	DRAO10	16:12:12.29	+55:23:02.1	0.20	0.20	–	–	–	360.15 ± 4.20	–	–	–	–	–	–	–
	DRAO11	16:12:25.78	+54:55:03.0	0.36	0.36	2.26	2.36	80	0.84 ± 0.10	7.88 ± 0.40	12.18 ± 0.66	107 ± 14	69 ± 9	1.55 ± 0.11		
										< 1.20	< 1.98	> 700	> 424	...		
LH	LH5549	10:44:13.17	+58:48:33.3	0.27	0.30	1.32	0.90	92	3.24 ± 0.13	3.01 ± 0.37	3.67 ± 0.58	1076 ± 139	883 ± 144	1.22 ± 0.24		
	LH4124	10:44:13.77	+58:17:45.3	0.75	0.90	1.48	1.94	89	0.50 ± 0.08	1.85 ± 0.39	2.32 ± 0.56	270 ± 72	216 ± 62	1.25 ± 0.40		
										< 1.17	< 1.68	> 427	> 298	...		
	LH5709	10:44:35.75	+58:53:10.0	0.21	0.21	0.87	0.49	96	8.98 ± 0.12	2.56 ± 0.63	2.14 ± 0.58	3508 ± 865	4196 ± 1139	0.84 ± 0.31		
	LH5705	10:46:04.53	+58:53:19.0	0.36	0.41	1.05		95	0.61 ± 0.04	1.44 ± 0.44	< 1.71	424 ± 132	> 357	< 1.19		
	LH4270	10:47:11.26	+58:21:46.7	0.22	0.23				0.52 ± 0.01	< 1.32	< 1.56	> 394	> 333	...		
	LH5995	10:47:34.56	+59:07:01.2	0.34	0.39				1.47 ± 0.09	< 1.47	< 1.47	> 1000	> 1000	...		
	LH0912	10:47:59.36	+57:17:39.8	0.20	0.20	0.25	0.52	99	1.39 ± 0.01	3.08 ± 0.49	6.01 ± 0.68	451 ± 72	231 ± 26	1.95 ± 0.38		
	LH0324	10:48:06.21	+57:03:00.6	0.25	0.27	1.07	1.14	95	0.61 ± 0.02	2.53 ± 0.49	5.94 ± 0.64	241 ± 47	103 ± 12	2.35 ± 0.52		
	LH6025	10:49:04.39	+59:09:13.5	0.27	0.29				1.28 ± 0.05	< 1.14	< 1.32	> 1123	> 970	...		
	LH5512	10:49:23.18	+58:48:51.3	0.20	0.20				2.66 ± 0.01	< 1.23	< 1.50	> 2163	> 1773	...		
	LH3817	10:49:48.97	+58:12:19.6	0.20	0.20	0.27	1.04	99	1.53 ± 0.01	3.48 ± 0.44	4.06 ± 0.60	440 ± 56	377 ± 56	1.17 ± 0.23		20.75_K [d]
	LH0576	10:49:56.77	+57:10:41.2	0.21	0.22				1.15 ± 0.02	< 1.20	< 1.35	> 958	> 852	...		
	LH0502	10:51:22.09	+57:08:55.0	0.20	0.20	0.09	0.26	99	10.59 ± 0.02	4.83 ± 0.54	8.41 ± 0.58	2193 ± 245	1259 ± 87	1.74 ± 0.23		24.84_R [e]
	LH2316	10:51:30.82	+57:44:08.0	0.21	0.21				0.97 ± 0.01	< 1.77	< 1.68	> 548	> 577	...		
	LH2633	10:51:38.11	+57:49:56.8	0.20	0.20	0.10	0.12	99	2.54 ± 0.01	5.43 ± 0.33	10.00 ± 0.56	468 ± 28	254 ± 14	1.84 ± 0.15		
	LH0209	10:52:39.55	+56:58:25.6	0.20	0.20	1.00	0.68	95	2.83 ± 0.02	3.61 ± 0.50	5.37 ± 0.67	784 ± 109	527 ± 66	1.49 ± 0.28		24.41_R [e] 24.38_I [e]
	LH5785	10:53:18.14	+58:56:22.8	0.20	0.20	0.80		97	78.43 ± 0.03	4.40 ± 0.48	out	17825 ± 1945	...	...		
	LH2417	10:54:14.89	+57:45:57.7	0.23	0.25		1.20	93	0.37 ± 0.01	< 1.38	2.27 ± 0.43	> 268	163 ± 47	> 1.64		
	LH4721	10:54:57.39	+58:31:53.5	0.20	0.20				11.89 ± 0.01	< 2.19	out	> 5429	...	...		
	LH0943	10:55:48.54	+57:18:27.8	0.20	0.20				13.65 ± 0.01	< 1.32	< 1.53	> 10341	> 8922	...		
	LH1019	10:55:56.59	+57:19:59.6	0.21	0.21				0.80 ± 0.01	< 1.05	< 1.53	> 762	> 523	...		

[a] Arnouts et al. (2001), from Deep Public Survey (Mignano et al., 2007); [b] Rafferty et al. (2011), from MUSYC (Gawiser et al., 2006); [c] Mignano et al. (2007), from Deep Public Survey (Mignano et al., 2007); [d] Lawrence et al. (2007), from UKIDSS (Lawrence et al., 2007); [e] Fotopoulou et al. (2012), from IfA Deep Survey (Barris et al., 2004).

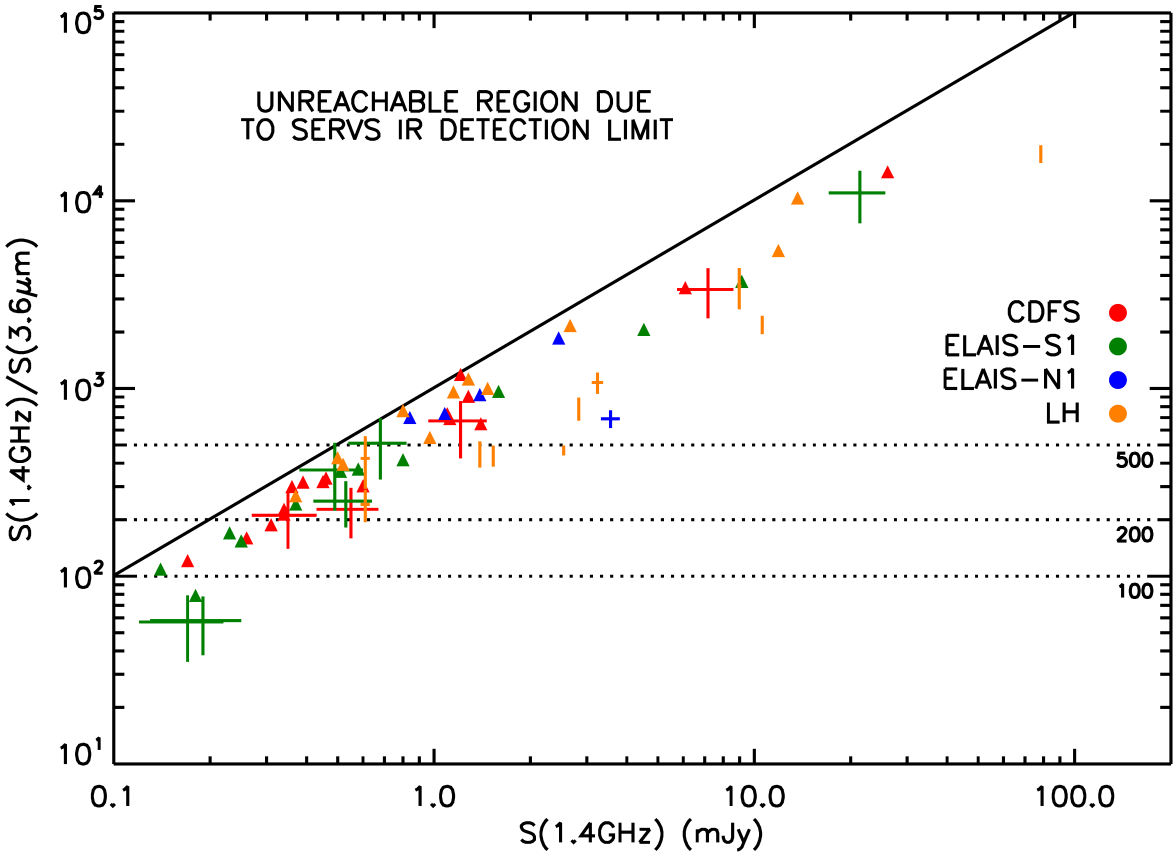

Figure 4.4: 1.4 GHz-to-3.6 μm flux density ratios versus 1.4 GHz radio flux density. The diagonal solid line marks the lowest $R_{3.6}$ values we can trace due to the combined radio and SERVS detection limits (derived assuming $S_{1.4\,\mathrm{GHz}} > 100\,\mu$Jy and $S_{3.6\,\mu\mathrm{m}} > 1\,\mu$Jy, i.e. the smallest lower limit we measure in our sample). The dotted lines indicate flux density ratios $R_{3.6} = 100$, 200 and 500. Flux ratios for reliably IR-detected IFRSs are reported as crosses (position with errors bars), while flux ratios of IR undetected/unreliable sources are indicated by triangles (lower limits). To each field corresponds a different colour, as explained in the legend. From Maini et al. (2016b).

4.6 IFRS radio-to-IR ratio distribution

Figure 4.4 shows the $R_{3.6}$ ratios (or corresponding lower limits) versus 1.4 GHz flux density for all the sources in the SERVS fields. The solid diagonal line represents the $R_{3.6}$ detection limit. It is noteworthy that sources not detected in SERVS or with unreliable identifications (triangles) span the entire range in radio flux probed by our samples. As expected more radio powerful is the source, the more extreme is the radio-to-IR ratio (but see Section 4.9 for more details).

In Table 4.5 we list the number of IFRSs found in each field (CDFS, ELAIS-S1, ELAIS-N1, LH) for different ranges of $R_{3.6}$ (< 100, 100–200, 200–500, and > 500). In case of IR undetected sources (or unreliable identifications) we assign the source to the $R_{3.6}$ range constrained by the estimated lower limit value. Sources with $R_{3.6} < 200$ cannot be found in the LH field, as we imposed a minimum threshold of 200 for our IFRS search (see Sect. 4.3). Considering that several sources have $R_{3.6}$ lower limits, at least 60% of the 55 sources with $R_{3.6} > 200$ satisfy the Zinn et al. $R_{3.6} > 500$ criterion, and most of them have $S_{1.4\,\mathrm{GHz}} > 1$ mJy. This is consistent with the fact that this criterion tends to exclude faint radio sources, as

Table 4.5: Statistics of IFRSs in the SERVS fields as a function of radio-to-infrared flux ratio ($R_{3.6}$). Columns 2, 3, 4, and 5 report the number of sources with $R_{3.6}$ in the ranges < 100, 100–200, 200–500, and > 500, respectively.

Field	radio–to–infrared flux ratio $R_{3.6}$			
	< 100	100–200	200–500	> 500
(1)	(2)	(3)	(4)	(5)
CDFS	0	3	9	9
ELAIS-S1	3	3	6	5
ELAIS-N1	0	0	0	5
LH	-	-	8	13
Total	3	6	23	32

discussed in Sect. 1.5.3. Only three sources in the ELAIS-S1 field show very low radio-to-IR ratios ($R_{3.6} < 100$) based on our new SERVS analysis, and can be explained in terms of normal galaxy populations. All these sources have $S_{1.4\,\mathrm{GHz}} < 0.2$ mJy. The rest of the sub-mJy sources ($S_{1.4\,\mathrm{GHz}} \sim 0.3$–1 mJy) typically have $R_{3.6} \sim 100$–500. They do not satisfy the stringent Zinn et al. $R_{3.6} > 500$ criterion, but display nonetheless extreme IR properties.

4.7 Average IR flux densities of undetected sources

We performed a median stacking analysis of the sources with no or unreliable counterparts at the SERVS flux limits, focusing our analysis on IFRSs with $R_{3.6} > 500$ (22 at 3.6 μm and 20 at 4.5 μm), to explore down to a fainter regime the IR properties of this extreme population. After stacking the SERVS image cutouts, 3.6 and 4.5 μm median flux densities were measured through aperture photometry, and flux errors were estimated as explained in Sect. 4.4.2, except that median stacking removes the need to reject > 3σ outliers.

No secure detection was obtained in the stacked image. At 3.6 μm we find a median flux density upper limit of $\widetilde{S}_{3.6\,\mu\mathrm{m}} < 0.46\,\mu$Jy, and for the first time we provide a median upper limit at SERVS 4.5 μm, $\widetilde{S}_{4.5\,\mu\mathrm{m}} < 0.60\,\mu$Jy (both 3$\sigma$ values). In both cases the obtained rms (0.15 and 0.20 μJy, respectively) are above the expected values for non-confusion limited images (0.13 and 0.15 μJy, respectively; see Table 4.3, Column 6). This means we reached the hard detection limit, and the stacking technique starts to fail. Nevertheless, the total lack of detection in the stacked images allows us to conclude that the counterparts' flux density distribution is probably dominated by sources whose flux densities are well below the SERVS detection limit, which in turn implies that their actual $R_{3.6}$ values are significantly larger than 500.

Norris et al. (2011a) also attempted a stacking experiment based on preliminary SERVS images of ATLAS fields, obtaining a median flux density of $\widetilde{S}_{3.6\,\mu\mathrm{m}} < 0.42\,\mu$Jy. The two 3.6 μm upper limits are remarkably similar despite Norris et al. (2011a) used 39 sources against our 22, and the fact that some of the sources stacked by Norris et al. (2011a) are detected at few μJy level by us. This again is a signal of stacking technique starting to fail. Moreover, our upper limit is slightly larger due to the fact that a smaller number of sources was stacked. The most notable differences between the sample of sources we stacked and

the one stacked by Norris et al. (2011a), is that we expanded the sample to two new fields but removed from the stacking all the sources with $R_{3.6} < 500$. Most of these sources are very faint radio sources ($S_{1.4\,\mathrm{GHz}} \lesssim 0.5\,\mathrm{mJy}$), and some have not been detected in ATLAS DR3 (Franzen et al., 2015). These sources (CS0275, CS0696, CS0706, CS0714, ES0135, ES1118, and ES1193) may be the result of unusual noise peaks or imaging artefacts.

4.8 Models of comparison

Our sample spans a much larger range in both $R_{3.6}$ ratio and radio flux density than the 'bright' Collier et al. (2014) and Herzog et al. (2014) samples. Lower flux densities and lower $R_{3.6}$ values can be explained as the result of same IR properties but lower intrinsic radio luminosities, associated with a population of less radio-loud QSOs. Alternatively it can be the result of a more diverse population and/or redshift distribution. Indeed several of our sources lie in the radio sub-mJy regime, where radio sources consist of both AGN and SFGs (see e.g. Prandoni et al. 2001b; Mignano et al. 2008; Seymour et al. 2008; Smolčić et al. 2015).

To disentangle between these different scenarios, we need to compare the radio and IR properties of our IFRSs with those of known classes of objects, including the effects of evolution and dust extinction.

To build our reference models we used the spectral energy distribution (SED) templates from the SWIRE Template Library (Polletta et al., 2007). In particular we used the templates of Arp 220 (as representative of SBGs), of Mrk 231 (as representative of composite Seyfert 1 and star-burst objects), of IRAS 19254-7245 (hereafter I19254, as representative of a composite Seyfert 2 and star-burst objects), of a 5 Gyr old Elliptical (for the hosts of elliptical radio-loud galaxies, RLG), Seyfert 1 and 2 average templates for Type 1 and 2 AGN, respectively, and QSO1 and QSO2 templates for average Type 1 and Type 2 QSOs.

For both IR and radio bands, and for all classes of objects, we assumed pure luminosity evolution (PLE), and in particular we used models accounting for a luminosity damping at high redshift ($z \gtrsim 2$). We included the effect of K-correction and intrinsic evolution (i.e. ageing).

4.8.1 K-correction

In the radio, we K-corrected the 1.4 GHz flux densities by assuming a power law spectrum ($S \propto \nu^{\alpha}$) and the formula:

$$S_{\nu,\mathrm{filter}} = S_{\nu,\mathrm{rest\text{-}frame}} \times K(z) = S_{\nu,\mathrm{rest\text{-}frame}} \times A_{\nu}(z) \times B_{\nu}(z)$$

where $A_{\nu}(z)$ is the term of bandpass enhancement, and $B_{\nu}(z)$ is the term dependents on the SED, which under the approximation of power law regime ($S_{\nu} \propto \nu^{\alpha}$) becomes very simple:

$$A_\nu(z) = \frac{\Delta\nu_{\text{filter}}}{\Delta\nu_{\text{rest-frame}}} = (1+z)$$

$$B_\nu(z) = \frac{\int_{\nu_{1,\text{filter}}}^{\nu_{2,\text{filter}}} S_{\nu,\text{filter}}\, \mathrm{d}\nu_{\text{filter}}}{\int_{\nu_{1,\text{filter}}}^{\nu_{2,\text{filter}}} S_{\nu,\text{rest-frame}}\, \mathrm{d}\nu_{\text{filter}}} = \frac{\int_{\nu_{1,\text{filter}}}^{\nu_{2,\text{filter}}} \nu_{\text{filter}}^{\alpha}\, \mathrm{d}\nu_{\text{filter}}}{\int_{\nu_{1,\text{filter}}}^{\nu_{2,\text{filter}}} \nu_{\text{rest-frame}}^{\alpha}\, \mathrm{d}\nu_{\text{filter}}} = (1+z)^{\alpha}$$

from which we have the formula:

$$S_{\nu,\text{filter}} = S_{\nu,\text{rest-frame}} \times (1+z)^{(1+\alpha)}$$

For the spectral index we assumed indicative reference values. We assumed $\alpha = -1.0$ for typically steep-spectrum sources (Arp 220, RLGs, I19254, and Type 2 AGN/QSOs), and $\alpha = 0$ for typically flat-spectrum sources (Mrk 231 and Type 1 AGN/QSOs).

In the IR, the 3.6 and 4.5 μm flux densities were K-corrected using the Hyperz software (Bolzonella et al., 2000).

4.8.2 Luminosity evolution

The intrinsic IR luminosity evolution was modelled following Stefanon & Marchesini (2013), who derived PLE models for normal galaxy populations in both rest-frame H- and J-bands, and following Assef et al. (2011), who derived PLE models for AGN in the rest-frame J-band. In particular we used the former models for Arp 220 and RLGs, and the latter for Mrk 231, I19254, AGN and QSOs. The intrinsic IR luminosity evolution for each class of objects was modelled following the evolution of the characteristic luminosity (L_*), i.e. the luminosity which marks the change from power law to exponential regime in the Schechter luminosity function.

Other models are available in the literature for a number of rest-frame IR bands (see e.g. Pozzetti et al. 2003; Babbedge et al. 2006; Saracco et al. 2006; Dai et al. 2009). For our toy models, however, subtle differences are not relevant, as we are interested only in obtaining overall reference evolutionary tracks. Our final choice was mainly dictated by: a) the wider redshift range probed by the selected models ($z < 3.5$ for Stefanon & Marchesini 2013, $z < 5$ for Assef et al. 2011), which reduces the uncertainties introduced when such models are extrapolated to higher redshifts; b) the fact that analytical forms were used to describe the evolution that take into account in a single law both positive luminosity evolution at low redshifts and luminosity damping at high redshifts ($z \gtrsim 2$).

For Type 1 and 2 AGN, Type 1 and 2 QSOs and for RLGs we assumed as reference IR luminosity ($L_0 \equiv L_*(z=0)$) the characteristic luminosity expected for these classes of objects at redshift $z = 0$, following Assef et al. (2011) and Stefanon & Marchesini (2013), respectively. For Mrk 231, Arp 220 and I10254 we assumed their own luminosity. In particular we fixed the 3.6 μm luminosity and scaled it to 4.5 μm following the templates.

We modelled the radio luminosity evolution of high-power (HP; $L \gtrsim 10^{25}$ W Hz^{-1}) AGN and composite AGN plus starburst galaxies following Dunlop & Peacock (1990). In particular we applied the PLE model derived for steep-spectrum radio sources to HP RLGs,

Type 2 AGN, Type 2 QSOs and I19254, and the flat-spectrum model to Type 1 AGN, Type 1 QSOs, and Mrk 231. Two reference radio powers ($L_0 \equiv L(z = 0)$) were assumed for RLGs, as well as for Type 1 and 2 QSOs. For RLGs, the low-power (LP) luminosity was assumed 10^{24} W Hz^{-1}, while the HP luminosity is 10^{26} W Hz^{-1}. For Type 1 and 2 QSOs the LP luminosity is higher than for RLGs (10^{25} W Hz^{-1}), while the HP luminosity is the same (10^{26} W Hz^{-1}). For Mrk 231 and IC19254 we assumed 10^{24} W Hz^{-1}, which is approximately equal to their actual radio powers.

The radio luminosity of LP ($L \lesssim 10^{24}$ W Hz^{-1}) RL AGN associated to elliptical galaxies is known to evolve less strongly, and is typically modelled with a law of the form $L(z) = L_0(1 + z)^{\beta}$ up to a given maximum redshift $z_{\rm max}$, and $L(z) = L(z_{\rm max})$ at higher redshifts. Following Hopkins (2004) we assumed $\beta = 2$, while $z_{\rm max}$ was set to 2 (this is likely a generous assumption as there are growing indications that the number density of low-power RL AGN peaks at redshift $z \lesssim 1$; see e.g. Padovani et al. 2015a).

The same evolutionary form is also used to model the radio luminosity of starburst galaxies (Arp 220-like objects). Typically β has values between 2.5 and 3.33 (see e.g. Saunders et al. 1990; Machalski & Godlowski 2000; Sadler et al. 2002; Seymour et al. 2004; Mao et al. 2012) and $z_{\rm max}$ is typically assumed to be in the range 1.5–2. We assumed $\beta = 3.3$ and $z_{\rm max} = 2$ (Hopkins et al. 1998; Hopkins 2004). This is a rough approximation, as it is known that the radio luminosity at high redshift starts to decrease, but this approximation does not significantly affects the redshift range within which such a source would be still detectable by our radio surveys. The L_0 parameter was set equal to the actual 1.4 GHz radio luminosity of Arp 220 (2×10^{23} W Hz^{-1}).

Table 4.6 summarises the reference powers and the evolutionary models applied to our templates, and the redshift range within which these models have been derived.

In panels (a), (b) and (c) of Figure 4.5 we show the IR and 1.4 GHz evolutionary tracks expected for our models, while panel (d) shows the expected $R_{3.6}$ versus redshift relation. In this case each track is truncated at the redshift at which the radio flux density drops below the typical detection limit of the radio surveys under consideration ($S_{1.4\,\rm GHz} \sim 0.1$ mJy, see Table 4.1). For AGN and QSO templates the expected radio-to-IR $R_{3.6}$ ratio tends to increase with redshift up to $z \sim 2$–3 due to the stronger positive radio evolution over the IR one. Then it starts to decrease due to the steeper decline in the radio evolution. QSOs, AGN, and HP RLGs are the only classes of objects able to reach $R_{3.6} \gtrsim 100$, further supporting previous evidences that IFRSs host an AGN. Arp 220 (dotted cyan line) keeps increasing up to the highest redshifts at which this source would be still detectable in our surveys, but never reaches the lowest $R_{3.6} \gtrsim 50$ values measured in our faint IFRS sample. The same is true for Mrk 231, LP RLGs, and I19254.

4.8.3 Dust extinction

As pointed out by Norris et al. (2011a), radio-to-IR ratios can be increased by introducing some level of reddening. The very origin of reddening in astronomical sources is the 'extinction', the phenomenon of absorption and scattering of electromagnetic radiation due to dust and gas interposed between the observer and the source of radiation.

The extinction is defined as the difference between the observed magnitude and the intrinsic, un-extincted magnitude, in a given band of observation:

$$A_{X-\rm band} = m^{\rm obs.}_{X-\rm band} - m^{\rm un\text{-}extincted}_{X-\rm band} = -2.5\,{\rm Log}\frac{L^{\rm obs.}_{X-\rm band}}{L^{\rm un\text{-}extincted}_{X-\rm band}} = -2.5\,{\rm Log}\frac{S^{\rm obs.}_{X-\rm band}}{S^{\rm un\text{-}extincted}_{X-\rm band}}$$

Table 4.6: Main modelling parameters

3.6 μm						
Class	$L_{z=0}$ [W Hz^{-1}]		Evolution	z range	Bands	References
Arp 220	3.25×10^{22}	$S_{3.6\mu m}\propto$	$10^{0.4\,[40.0\,A^{0.19}\,e^{-A}-22.388]}$	$z<1.45$	L-, K-, H-	(a)
LP/HP RLG	2.8×10^{23}		$4.758\times10^{0.4\,[37.6\,B^{0.16}\,e^{-B}-23.834]}$	$z\geq1.45$	J-, I-, R-	
			Where $A=\frac{1+z}{14.9}$ and $B=\frac{1+z}{18.5}$			
Mrk 231	1.5×10^{24}	$S_{3.6\mu m}\propto$	$10^{0.8\,z-0.2\,z^2+0.01\,z^3}$	$z<5.05$	$L\rightarrow R$	(b)
I19254	5×10^{23}					
Type 1 QSO/Type 2 QSO	2.5×10^{23}					
Type 1 AGN/Type 2 AGN	2.5×10^{23}					
4.5 μm						
Class	$L_{z=0}$ [W Hz^{-1}]		Evolution	z range	Bands	References
Arp 220	4.7×10^{22}	$S_{4.5\mu m}\propto$	$10^{0.4\,[40.0\,A^{0.19}\,e^{-A}-22.334]}$	$z<2.05$	L-, K-, H-	(a)
LP/HP RLG	1.6×10^{23}		$5.153\times10^{0.4\,[37.6\,B^{0.16}\,e^{-B}-23.896]}$	$z\geq2.05$	J-, I-, R-	
			Where $A=\frac{1+z}{14.9}$ and $B=\frac{1+z}{18.5}$			
Mrk 231	2.1×10^{24}	$S_{4.5\mu m}\propto$	$10^{0.8\,z-0.2\,z^2+0.01\,z^3}$	$z<5.05$	$L\rightarrow R$	(b)
I19254	8.4×10^{23}					
Type 1 QSO/Type 2 QSO	3.3×10^{23}					
Type 1 AGN	3.6×10^{23}					
Type 2 AGN	2.5×10^{23}					

1.4 GHz							
Class		$L_{z=0}$ [W Hz^{-1}]		Evolution	z_{MAX}	α	References
Arp 220		2×10^{23}	$S_{1.4\,GHz}\propto$	$(1+z)^{3.3}$	2	-1.0	(c) (d)
Ell RLG	LP	10^{24}	$S_{1.4\,GHz}\propto$	$(1+z)^{2.0}$	2	-1.0	(e)
	HP	10^{26}	$S_{1.4\,GHz}\propto$	$10^{(1.26\,z-0.26\,z^2)}$		-1.0	(f)
Mrk 231		10^{24}	$S_{1.4\,GHz}\propto$	$10^{(1.18\,z-0.28\,z^2)}$		0.0	(f)
Type 1 AGN		10^{25}					
Type 1 QSO	LP	10^{25}					
	HP	10^{26}					
I19254		10^{24}	$S_{1.4\,GHz}\propto$	$10^{(1.26\,z-0.26\,z^2)}$		-1.0	(f)
Type 2 AGN		10^{25}					
Type 2 QSO	LP	10^{25}					
	HP	10^{26}					

From (Polletta et al., 2007), we used a 5 Gy old Ell. template for the HP/LP RLG track, the QSO1 and QSO2 templates for QSO tracks, and the Seyfert 1 and 2 templates for AGN tracks; for Arp 220, Mrk 231, and I19254 objects we used the relative templates. (a) Stefanon & Marchesini (2013); (b) Assef et al. (2011); (c) Hopkins et al. (1998); (d) Hopkins (2004); (e) Dunlop & Peacock (1990).

The reddening arises because dust scattering and absorption act not equally at any wavelength, but are stronger at shorter wavelengths (i.e. towards the blue part of the spectrum), at least down to the middle UV regime. The differential removal of the bluer wavelengths from the spectrum of an observed source results in a greater relevance of the redder contribution to the overall emission, from which the term ‘reddening’.

The form of the extinction curve depends on the abundance and on the composition of the interposed medium, which intrinsically varies from galaxy to galaxy. This dependence, on the other hand, is stronger at the shorter wavelengths (from the blue part of the optical toward the UV, i.e. for wavelengths $\lesssim 0.35\,\mu$m; see, e.g., Gordon et al. 2003; Wang & Jiang 2014), while in the Optical/NIR regime (~ 0.35-$5\,\mu$m) the extinction curve (due to interstellar dust) can be roughly approximated by a power law in the form $A_\lambda \propto \lambda^\alpha$ (Whittet, 1988; Wang & Jiang, 2014) which has been found suitable for a number of close galaxies, beyond our Milky Way (Gordon et al., 2003).

This law has been derived for very local objects. Its validity at cosmological distances can only be assumed. Making use of the wavelength-redshift relation ($\lambda_{em} = \lambda_{obs}/(1+z)$), it is straightforward to shift from wavelength to redshift:

$$A_{\lambda_{\text{em.}}} \propto \lambda^\alpha_{\text{em.}} \propto \lambda^\alpha_{\text{obs.}}/(1+z)^\alpha$$

from which the reddening relation we applied:

$$Reddening = 10^{-0.4\times A_{\lambda_{\text{em.}}}} = 10^{-0.4\times 3.6^\alpha/(1+z)^\alpha}$$

For galactic sources, this relation would be applied directly to the observed flux densities. In our case, however, we are working with extragalactic and cosmological sources. This implies that the previous relation has to be applied to K-corrected and rejuvenated sources, from which:

$$S^{\text{obs.}}_{3.6\,\mu\text{m}} = S^{\text{un-extincted}}_{\text{em. band}} \times Reddening = S^{\text{un-extincted}}_{\text{em. band}} \times 10^{-0.4\times 3.6^\alpha/(1+z)^\alpha}$$

For the analysis of the IFRSs we explored the redshift range 0–6, but we applied a reddening only to Arp 220 $3.6\,\mu$m emission. Beyond $z \sim 3$ this source falls below the detection limit of the radio surveys we took into account. In the redshift range 0–3, the observed $3.6\,\mu$m emission is emitted at shorter and shorter wavelengths, from $3.6\,\mu$m (at $z = 0$) to $0.9\,\mu$m (at $z = 3$). These values are well inside the power law approximation limits.

The exact value of α is still matter of debate. Values in literature range between ~ -1.70 (Whittet, 1988) to ~ -2.30 (Schödel et al., 2010), but in recent years measurements closer to the steeper values are preferentially found (for further details see Stead & Hoare 2009; Wang et al. 2013; Wang & Jiang 2014). We assumed $\alpha = -2.20$. This value implies a greater amount of dust interposed between observer and source (which is what we are interested in, given that we are supposing heavily obscured SBGs; see Section 1.5.1), and is in line with the findings for the Milky Way when analysed in the direction of the galactic centre, where the amount of dust is known to be greater (see, e.g., Stead & Hoare 2009; Schödel et al. 2010; Fritz et al. 2011).

Another contribution to the reddening comes from the interposed intergalactic medium. This contribution would affect the $3.6\,\mu$m flux densities of all sources, not only of dust-rich objects like Arp 220. The more relevant results in literature (Inoue & Kamaya, 2004; Johansson & Mörtsell, 2012) found that at cosmological distances (z $\sim$ 1) the upper limit of the reddening in the B-band is smaller than $\lesssim 0.25$ mag. Under the hypothesis that the effect of the inter-galactic medium is described by a similar law to the one from inter-stellar medium (i.e., both are power law functions), this implies that in the B-band the extinction increases from ~ 5 to $\lesssim 5.25$ mag. This results in a steepening of the power law of about 4%, with α for Arp 220 changing from -2.20 to -2.29. This contribution is definitely non-relevant for the overall behaviour of $R_{3.6}$ ratios, at least as far as $z \sim 6$, and we neglected it.

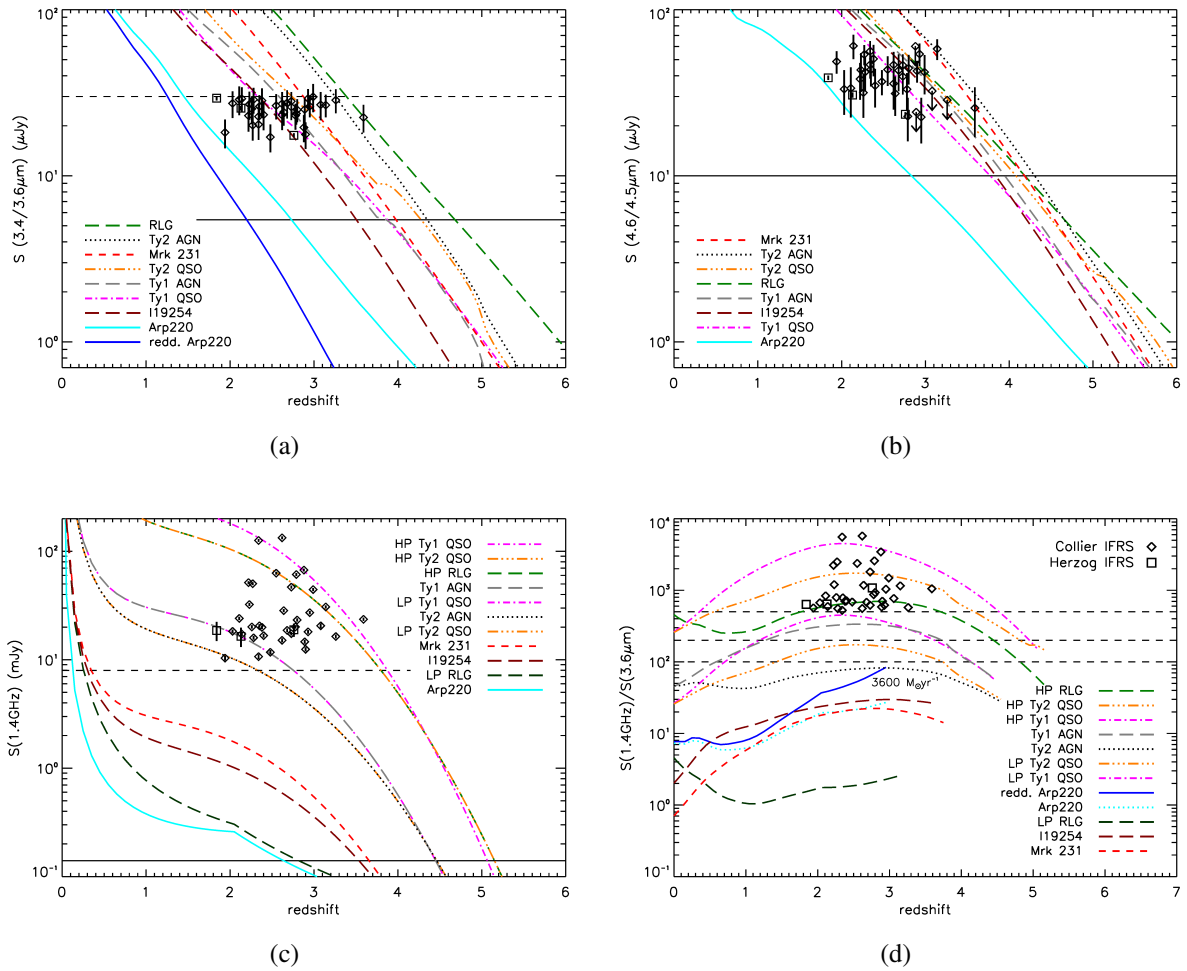

Figure 4.5: Expected flux densities and radio-to-IR flux density ratio versus redshift for our models: Type 2 and Type 1 AGN (dotted black and long-dashed grey tracks, respectively); Type 2 and Type 1 QSOs (triple dot-dashed orange and dot-dashed magenta tracks, respectively); radio galaxies (long-dashed green –for high-power– and dark green –for low-power– tracks); Arp 220, without and with reddening (dotted cyan and solid blue tracks, respectively), Mrk 231 (dashed red track), and I19254 (long-dashed brown track). Superimposed are the Collier et al. (2014) and Herzog et al. (2014) IFRSs with measured redshift (empty diamonds and empty squares, respectively). *Panel (a) – Top-left*: IR fluxes at 3.4 (WISE)/3.6 (SWIRE) μm versus redshift; the dashed horizontal line represents the 30 μJy flux density threshold used by Collier et al. (2014) and Herzog et al. (2014) to select their IFRS samples, while the solid horizontal line represents the highest flux density of a reliable detection for our sample (LH2633, $S_{3.6\,\mu\mathrm{m}} \sim 5.43\,\mu$Jy). *Panel (b) – Top-right*: IR fluxes at 4.5 (WISE)/4.6 (SWIRE) μm versus redshift; the reddened Arp 220 track follows a similar track as in panel (a), and is not shown. The solid horizontal line represents the highest flux density of a reliable detection for our sample (LH2633, $S_{4.5\,\mu\mathrm{m}} \sim 10.00\,\mu$Jy). *Panel (c) – Bottom-left*: 1.4 GHz radio flux density versus redshift; HP Type 2 QSO and RLG trends are superimposed due to the identical modelling we applied, as well as for Type 1 AGN and LP type 1 QSO, and for Type 2 AGN and LP Type 2 QSO (see Tab. 4.6). The dashed horizontal line indicates the lowest 1.4 GHz flux density measured in Collier et al. 2014 and Herzog et al. 2014 samples (7.98 mJy, see Sect. 1.5.3), while the solid horizontal line indicates the lowest 1.4 GHz flux density measured in our sample (ES0463, $S_{1.4\,\mathrm{GHz}} \sim 0.14$ mJy, see Table 4.4). *Panel (d) – Bottom-right*: $R_{3.6}$ ratio evolutionary tracks; in this plot each track is truncated at the redshift at which the radio flux density drops below the detection limit $S_{1.4\,\mathrm{GHz}} \sim 100\,\mu$Jy. The horizontal dashed lines indicate $R_{3.6}$ ratios of 100, 200 and 500. The errors associated to the measured $R_{3.6}$ ratios of the Collier et al. (2014) and Herzog et al. (2014) samples are of the same magnitude of the symbols reported in the plot, and not shown. At the end of the Arp 220 reddened track we indicate the star formation rate expected for this source if it were at redshift ~ 3, under the hypothesis that star-forming activity entirely accounts for the radio emission in this object. From Maini et al. (2016b).

In Figure 4.5 (panels (a) and (d)) the reddened track of Arp 220 is indicated by the solid blue line. At the end of this track is reported the star formation rate expected for Arp 220 at that redshift ($3600\,M_\odot\,yr^{-1}$), under the hypothesis that star formation activity entirely accounts for the radio emission in this object. This value has been obtained following Condon (1992) (see Appendix A for details). Even in this case starburst Arp 220-like galaxies hardly reach $R_{3.6} \sim 100$, but can account of the few objects in our IFRS sample with $R_{3.6} \lesssim 100$.

We notice that the evolutionary tracks shown in panels (a), (b) and (c) of Figure 4.5 are sensitive to the assumed reference luminosity and therefore should be used with caution. Panel (d), on the other hand, is more robust as it only depends on the ratio between the radio and IR flux densities.

4.8.4 Sanity checks

As a sanity check, in all panels of Figure 4.5 we also show the flux densities and/or the $R_{3.6}$ values of all Collier et al. (2014) and Herzog et al. (2014) *bright* IFRSs for which a redshift was measured (empty diamonds and empty squares, respectively). All such IFRSs are classified as broad-line Type 1 QSOs (Collier et al., 2014; Herzog, 2015; Herzog et al., 2014). The only tracks that can reproduce their IR and radio properties (see panels (a), (b) and (c)), as well as the $R_{3.6} \gtrsim 500$ selection criterion imposed for these IFRSs, are the ones of QSOs and HP RLGs.

On average, the spectral indices of the sample by Collier et al. (2014) is flat ($\widetilde{\alpha} = 0.00$), pointing towards a core-dominated Type 1 QSO population, in excellent agreement with their spectroscopic classification. The two IFRSs from Herzog et al. (2014) with redshifts, for which a spectral index was measured, show steep spectra (-0.84 for CS0212, -0.75 for CS0265), possibly indicating that these sources are RL QSO, dominated by optically thin synchrotron emission from the radio jets.

As shown by the horizontal solid lines in panels (a), (b) and (c), our sample probe much lower radio and IR flux density ranges than the Collier et al. (2014) and Herzog et al. (2014) samples, possibly associated with different source types and/or redshift distribution.

4.9 Radio/IR properties of SERVS deep field samples

We used the evolutionary tracks described in Sect. 4.8 to assess the nature of our $\gtrsim 10\times$ fainter IFRSs, spanning a larger range of $R_{3.6}$ values (i.e. $R_{3.6} \gtrsim 50$–100). In absence of redshift information, we explored the radio and IR properties of our sample in the parameter space defined by the $S_{4.5\,\mu m}/S_{3.6\,\mu m}$ flux density ratio against the 1.4 GHz radio flux. This choice has the advantage of being independent of the assumed reference IR luminosity, while different radio luminosities just produce an horizontal shift of the evolutionary tracks.

The results are shown in Figure 4.6, in which we plot only those IFRSs detected at either 3.6 or 4.5 μm, or both. Different symbols correspond to different $R_{3.6}$ ranges: $R_{3.6} > 500$ (empty triangles), $200 < R_{3.6} < 500$ (filled triangles), $R_{3.6} < 100$ (error bars only). None of the reliably identified IFRS shown in Figure 4.6 has $100 < R_{3.6} < 200$.

Superimposed are the evolutionary tracks of the classes discussed in Sect. 4.8 (following the same colour and line style convention as in Figure 4.5), that can produce $R_{3.6} > 50$ (namely Type 1 and 2 QSO, HP RLGs, Type 1 and 2 AGN, and reddened Arp 220). The redshift increases along the tracks toward the left hand side of the plot, and each unitary increment of redshift is marked with a dot of the same colour of the track. The first of these

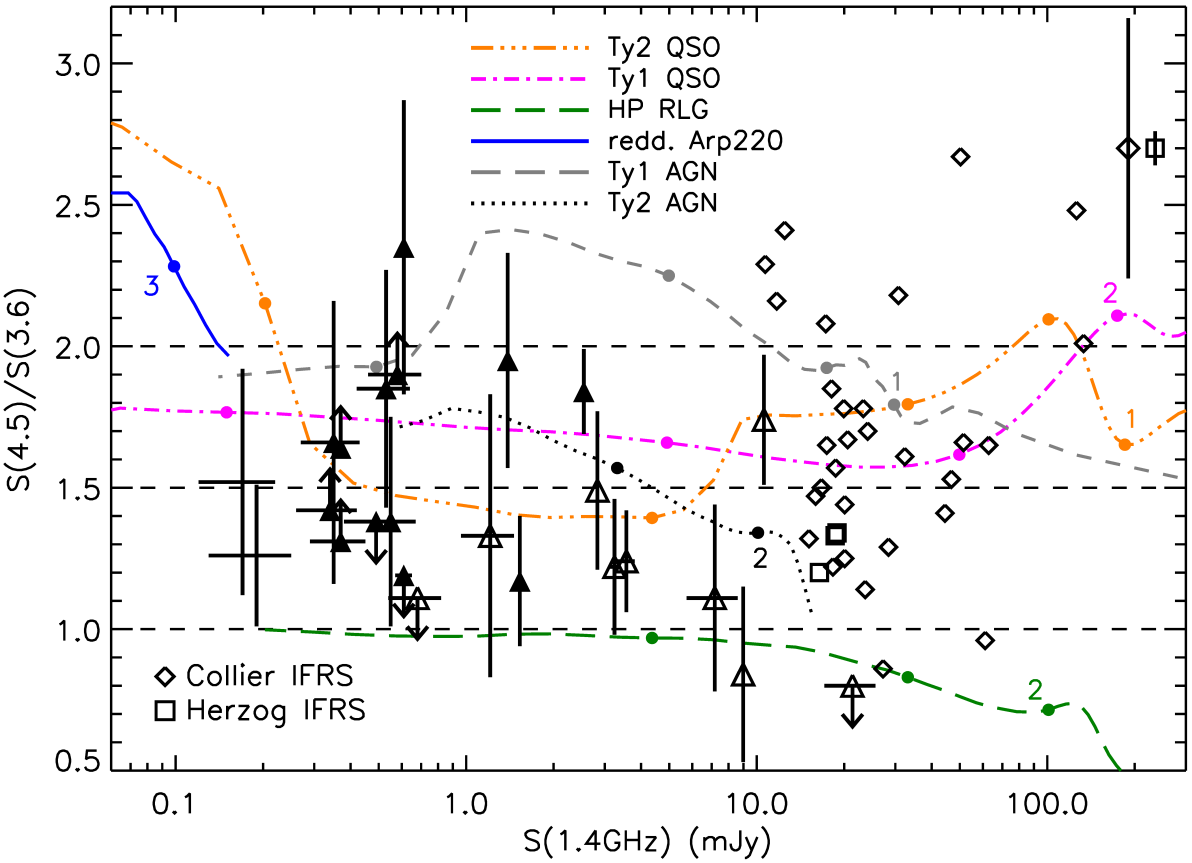

Figure 4.6: $S_{4.5\,\mu m}/S_{3.6\,\mu m}$ ratios versus 1.4 GHz flux density for IFRS sources. Sources detected only at one IR band (either 3.6 or 4.5 μm), are indicated by the corresponding upper/lower limits. The dashed horizontal lines refer to $S_{4.5\,\mu m}/S_{3.6\,\mu m}$ ratios equal to 1.0, 1.5 and 2.0 respectively. The superimposed tracks refer to HP Type 2 and 1 QSOs (triple dot-dashed orange and dot-dashed magenta respectively), HP RLGs (long-dashed green), Type 1 and 2 AGN (dashed and dotted grey, respectively) and reddened Arp 220 (solid blue). The redshift increases along the tracks toward the left hand side of the plot; unitary increments in redshift are marked by dots, starting from the value stated in figure. LP QSOs would show a similar track to HP QSOs, but slightly shifted to the left, and are not shown. All the tracks have been drawn in the redshift range within which $R_{3.6} > 50$, which is close to the smaller value we measured for our IFRSs (see Table 4.4). Empty diamonds and empty squares represent the positions of the IFRSs with redshift from Collier et al. (2014) and Herzog et al. (2014), respectively. In the top-right corner of the plot are shown the median errors for these two samples. Upward empty and filled triangles indicate IFRSs from our sample with $R_{3.6} > 500$ and between 200 and 500, respectively. The two radio-faintest sources are ES0593 and ES0436, both with $R_{3.6}$ values below 100. None of the reliably identified IFRSs shown in this plot has $R_{3.6}$ between 100 and 200. From Maini et al. (2016b).

dots reports also the first unit redshift of that track. Our IFRSs typically have $S_{4.5\,\mu m}/S_{3.6\,\mu m}$ flux ratios in the range 1–2. Due to the very large error bars ($\widetilde{\epsilon} = 0.35$ for our sample) it is difficult to say if any source has the most extreme values $S_{4.5\,\mu m}/S_{3.6\,\mu m} \geq 2$. Overall, the $S_{4.5\,\mu m}/S_{3.6\,\mu m}$ flux ratios spanned by our models cover the entire range spanned by our IFRS sample, indicating that our models can account for the whole faint IFRS population.

In Figure 4.6 we also show the brighter IFRSs from Collier et al. (2014) and Herzog et al. (2014). The median errors on their IR ratios are shown in the upper right corner of the figure ($\widetilde{\epsilon} = 0.46$ and $= 0.06$ for Collier et al. 2014 and Herzog et al. 2014, respectively). Considering

the large error bars all these IFRSs are again consistent with a QSO classification. Our fainter IFRSs are mostly consistent with being higher redshift counterparts of Collier et al. (2014) and Herzog et al. (2014) IFRSs. Sources with $R_{3.6} > 500$ would be QSOs at redshifts ($z \sim 3$–4), while IFRSs with less extreme $R_{3.6}$ ($100 < R_{3.6} < 500$) would lie at higher redshift ($z > 4$). This is consistent with the expected $R_{3.6}$ vs. redshift relation of QSOs reported in panel (d) of Figure 4.5. Only the IFRSs with lowest $S_{4.5\,\mu m}/S_{3.6\,\mu m}$ flux ratios (~ 1) are better described by the HP RLG track, and their $R_{3.6}$ values are again consistent with the expected $R_{3.6}$ vs. redshift relation.

We notice that Type 1 and 2 AGN tracks can also account for $R_{3.6} < 500$ IFRSs. Therefore, the fainter IFRS population could in principle either be associated to very high redshift QSOs or to Type 1 and 2 AGN at less extreme redshift ($2 < z < 4$), or a mixture of both.

Our faint IFRS sources have average radio spectral properties in line with Herzog et al. (2014) IFRSs. Franzen et al. (2015) reported the spectral indices computed between 1.40 and 1.71 GHz, values that are consistent with the ones computed between 1.4 GHz (from low-resolution data) and 2.3 GHz by Zinn et al. (2012), and with the ones reported by Middelberg et al. (2008a). Twenty-one of our sources in the CDFS and ELAIS-S1 have measured spectral indices (see Table 4.4, Col. 16). Thirteen of them have $R_{3.6} > 500$, and their median spectral index is very steep ($\widetilde{\alpha} = -1.05$), while 8 of them have $200 < R_{3.6} < 500$, and their median spectral index is ($\widetilde{\alpha} = -0.72$). A steep-spectrum population is more consistent with a Type 2 QSO/AGN or RLG classification.

As a final remark we notice that the faintest IFRSs in our sample ($S_{1.4\,GHz} \lesssim 200\,\mu$Jy), characterized by very low $R_{3.6}$ values (< 100), could also be associated with heavily obscured dust-enschrouded starburst galaxies at medium-high redshift ($z \sim 2$–3; blue track in Figure 4.6), even though in this case we would expect $S_{4.5\,\mu m}/S_{3.6\,\mu m} \gtrsim 2$.

4.10 Conclusions

In this Chapter I presented the work I did to better characterise the infrared-faint radio sources.

I repeated the analysis performed by Norris et al. (2011a) on the 3.6 μm SERVS images of the CDFS and ELAIS-S1 fields, using more recent and deeper 3.6 μm SERVS data, and for the first time 4.5 μm SERVS images. In addition we extended the analysis to the existing IFRS SWIRE-based sample in the ELAIS-N1 field. This study was complemented by a new IFRS sample extracted in the LH region covered by SERVS, consisting of 21 new IFRSs.

Most of our sources are characterised by 0.1 mJy $< S_{1.4\,\mathrm{GHz}} <$ 10 mJy. Thanks to the new deeper SERVS images and the use of the aperture photometry technique, we significantly increased the number of sources detected at 3.6 μm (with respect to both SWIRE and SERVS pre-release surveys; see Sect. 4.4.2). In addition we provided 4.5 μm flux density measurements for 25 objects. We identified 21 reliable counterparts at 3.6 μm and 20 at 4.5 μm, for a total of 25 distinct IFRSs. Sixteen of them have been detected in both bands. Most of the identified IFRS sources have IR fluxes of a few μJy, typically corresponding to S/N $\sim$ 3–10 in the SERVS images.

Given the different selection criteria used to identify the original IFRSs, the radio-to-IR ratio range spanned by them is rather large. From our new analysis we found that a couple of the original Norris et al. (2006) and Middelberg et al. (2008a) IFRSs have $R_{3.6} < 100$, where contamination from intermediate redshift (dust-enshrouded) SBGs is expected. In other cases, the new, fainter 3.6 μm upper limits that we derived confirmed we are dealing

with IFRSs characterized up to extremely large $R_{3.6}$ values ($\gg 500$).

We compared the observational radio and IR properties of our sample, as well as of the brighter IFRS samples extracted by Collier et al. (2014) and Herzog et al. (2014) ($S_{1.4\,\mathrm{GHz}} \sim 8.00 \rightarrow 800\,\mathrm{mJy}$ for Collier et al. 2014; $S_{1.4\,\mathrm{GHz}} \sim 7.00 \rightarrow 26.00\,\mathrm{mJy}$ for Herzog et al. 2014, 2015b), with those expected for a number of known prototypical classes of objects: Arp 220 (as SBG), HP and LP RLGs, Type 1 and 2 (i.e. obscured) QSOs and AGN, Mrk 231 (for a prototypical Seyfert 1 plus star-burst composite galaxy) and I19254 (for a prototypical Seyfert 2 plus star-burst composite galaxy). For each class we built evolutionary models taking into account K-correction and evolution, both in IR and radio bands. In the IR domain, we made the simplified assumption that these classes of sources evolve following the characteristic luminosity of the Schechter luminosity function (L_*).

In general we found that the only evolutionary tracks that can produce high $R_{3.6}$ values ($\gtrsim 100$) are those of AGN-driven sources (AGN, QSOs, and powerful RLGs). In addition we found that the predicted $R_{3.6}$ values typically show a peak at redshift $z \sim 2$–3, where $R_{3.6}$ can be larger than 500. Then the expected $R_{3.6}$ decreases to smaller values (> 100–200 at $z \sim 5$). The radio/IR properties and the redshift distribution of the bright, $R_{3.6} > 500$, IFRSs selected by Collier et al. (2014) and Herzog et al. (2014), are well reproduced by QSO evolutionary tracks, in excellent agreement with the Type 1 QSO optical classification of those with spectroscopy available.

In absence of redshift information we analysed the radio/IR properties of the fainter IFRSs in the SERVS deep fields in the parameter space defined by the (luminosity independent) $S_{4.5\,\mu\mathrm{m}}/S_{3.6\,\mu\mathrm{m}}$ flux density ratio against the 1.4 GHz radio flux. We found that most of our sources are also consistent with being QSO. Their steep radio spectral indices seem more consistent with Type 2 QSO. Only those IFRSs characterized by low $S_{4.5\,\mu\mathrm{m}}/S_{3.6\,\mu\mathrm{m}}$ values (~ 1) are better reproduced by powerful RLG evolutionary tracks (also characterized by steep spectra). Overall the $R_{3.6}$ values of our IFRSs are in good agreement with the redshift distribution predicted by the QSO and HP RLG evolutionary tracks, supporting the hypothesis that fainter and less extreme ($R_{3.6} \sim 200$) IFRS sources could be higher redshift ($z \sim 3$–5) counterparts of the Collier et al. (2014) and Herzog et al. (2014) bright IFRS samples.

Nevertheless, we cannot exclude that the two faintest ($S_{1.4\,\mathrm{GHz}} \lesssim 0.2\,\mathrm{mJy}$) sources, both with $R_{3.6} < 100$, could be associated with heavily obscured dust-enshrouded SBGs, even though in this case larger $S_{4.5\,\mu\mathrm{m}}/S_{3.6\,\mu\mathrm{m}}$ values than those observed are predicted (> 2). Under this hypothesis, these two sources would lie at redshift ~ 2.4, have a radio power $L \sim 9 \times 10^{24}\,\mathrm{W\,Hz^{-1}}$, and a SFR $\gtrsim 4 \times 10^3\,\mathrm{M_\odot\,yr^{-1}}$. These values are high, but observed in HyLIRG and/or Sub-Millimetre Galaxies (SMG) (see e.g. Ivison et al. 1998; Alonso-Herrero 2013; Barger et al. 2014). We also speculated that faint IFRSs could be (at least in part) associated to extremely low (IR) luminosity AGN at less extreme redshifts, rather than to more standard bright $z > 4$ QSO and/or RLG populations. While this is unlikely to explain the whole of the faint IFRSs, only spectroscopic follow-ups can disentangle between these two alternative scenarios.

As suggested by Norris et al. (2011a) and Herzog et al. (2014), a $S_{3.6\,\mu\mathrm{m}}$ versus z relation seems to exist for IFRSs selected following Zinn et al. (2011) criteria, and the radio/IR properties of our fainter sample support that conclusion. Coupled with the radio-to-IR ratio ($R_{3.6}$) criterion, these relations can provide efficient criteria to pinpoint very high redshift RL QSOs and/or RLGs. Since the radio evolution of such sources seems to be stronger than the IR one, imposing a threshold of $R_{3.6} > 500$ to select IFRSs would result in rejecting the highest-redshift tail of these sources (i.e., IFRSs at redshift $z \gtrsim 4$). On the

other hand, at 1.4 GHz flux densities below 200 μJy, some contamination from intermediate-redshift ($z \sim 2$–3) dust-enshrouded SBGs is expected. To minimize such contamination only sources with $R_{3.6} > 100$–150 should be retained as high-redshift IFRS candidates.

Understanding nature and properties of the IFRS population is an exercise which goes beyond the simple scientific curiosity. First of all, it is increasingly clear that they represent a well defined class or evolutionary phase of objects, more than a peculiar and exceptional phenomenon. Moreover, due to their relatively high spatial density ($\sim$ 3–7 IFRS deg^{-2}), it is expected that future deep and sensitive radio surveys (such as EMU; Norris et al. 2011b), combined with IR observations, will discover IFRSs in the thousands. If confirmed as high and very high redshift sources, IFRSs could play an important role in the characterisation of the early Universe.

Only a few $z > 5$ radio sources have been found so far (the highest redshift radio galaxy being at $z \sim 5.19$; van Breugel et al. 1999), and a number of techniques to efficiently pre-select high-redshift candidates are being used (see e.g. Falcke et al. 2004b). We found that the first of the two criteria proposed by Zinn et al. (2011) ($R_{3.6} > 500$) is not suitable to pinpoint this class of objects at wathever redshift. Beyond $z \sim 4$–4.5, it is expected that radio-to-IR ratio of Type 1 and 2 QSOs drop down to $\sim$ 200.

5 Conclusion

For long time, the limited sensitivity of extragalactic radio surveys forced the field to run as an 'independent' branch in Astrophysics, disclosing only the most radio-powerful counterparts of the IR and optical surveys. In the last ten years this situation has totally changed. The increased survey sensitivity has finally led extragalactic radio astronomy to reach for the luminosity range in which it is expected they will routinely find the counterparts of the other wavelength deep-sky surveys (see Figure 1.2). Extragalactic radio surveys sensitivity has so much improved in the last years that deep radio surveys are now sampling galaxies in the same cosmic volume studied in IR, Optical and X-rays surveys (Padovani et al., 2015b,a; Padovani, 2016).

In the next few years the revolution will be complete, and the new generation of radio arrays (e.g., ASKAP, SKA) will compete with the greatest volumes sampled by IR, Optical and X-rays surveys (see Figure 5.1, where the theoretical performance of several facilities are reported). Thanks to these new facilities, planned or just started deep-sky surveys will finally reach for the threshold of the μJy or even the sub-μJy regimes. EMU, for instance, is aiming at a final 5σ sensitivity of about $50\,\mu$Jy (Norris et al., 2011b), but already SKA 1 All-Sky continuum Survey will reach the $10\,\mu$Jy (Norris et al., 2015)), while SKA 1 Wide and SKA 1 Deep will reach, respectively, 5 and $1\,\mu$Jy (Prandoni & Seymour, 2015). SKA Ultra-Deep survey, eventually, will go beyond the threshold, aiming for 5σ sensitivities around $0.25\,\mu$Jy (Prandoni & Seymour, 2015).

As a consequence, radio surveys are becoming increasingly important in the context of cosmology and galaxy evolution, providing a powerful instrument to pinpoint both AGN and SF activity (in a way which is unbiased by dust obscuration and gas), and to separate their relative contribution (thanks to the high angular resolution that can be reached by the interferometric technique).

5.1 The sub-mJy radio sky

It is now well assessed that there are three primary processes which contribute to the extragalactic continuum radio emission at 1.4 GHz. The most powerful one is the synchrotron

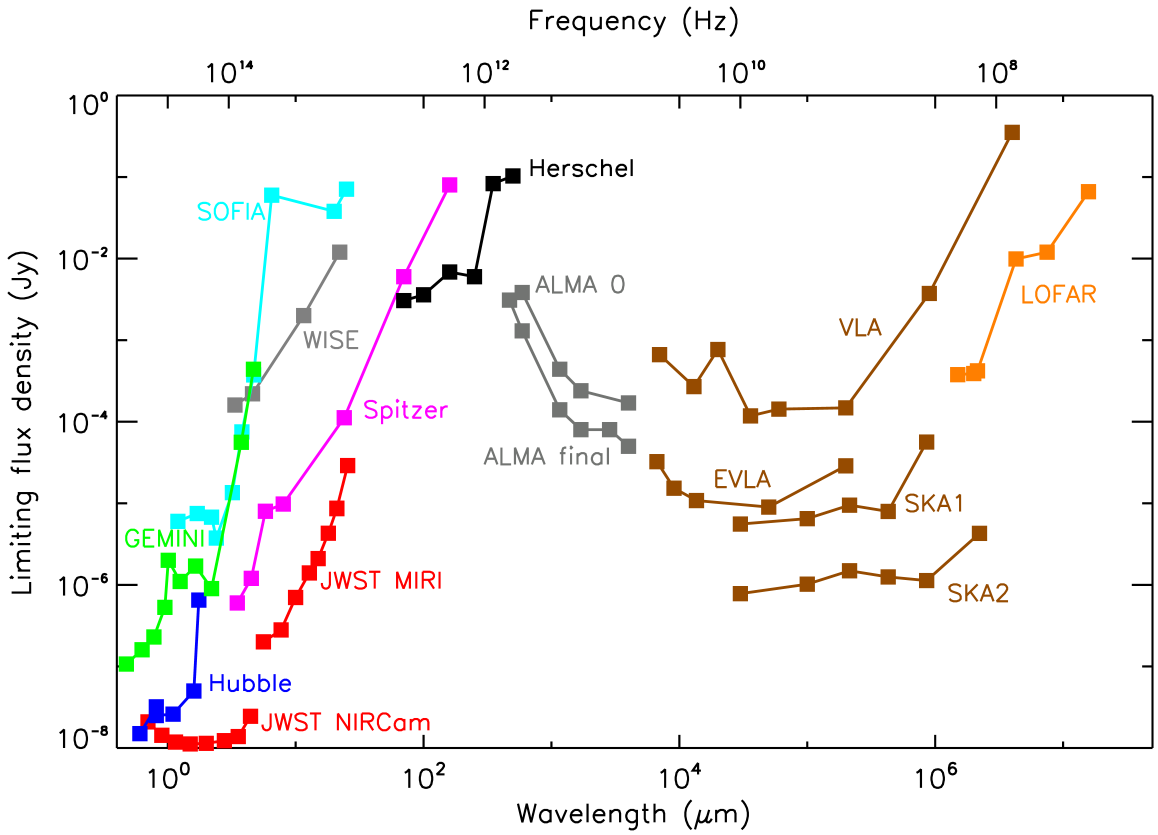

Figure 5.1: Point-source sensitivity for several existing and planned astronomical facilities, computed for a signal-to-noise ratio of 10, with 10^4 seconds of observation. From left to right: green points are *Gemini* detection limits for the *Gemini* multi-object spectrographs (GMOS)[a] and near infrared imager and spectrometer (NIRI)[b] instruments. Blue points are the *Hubble* Space Telescope detection limits for wide field camera 3 (WFC3), advanced camera for surveys (ACS), and near infrared camera and multi-object spectrometer (NICMOS; from left to right, respectively). Red points are the required sensitivity limits for James Webb space telescope (JWST) near infrared camera (NIRCam; left) and mid-infrared instrument (MIRI; right) instruments. Cyan points are the detection limits for the Stratospheric Observatory for Infrared Astronomy (SOFIA), as predicted for the First Light Infrared TEst CAMera (FLITECAM)[c] and Faint Object infraRed CAmera for the SOFIA Telescope (FORCAST)[d] instruments. Grey points on the left are the detection limits for WISE mission (Wright et al., 2010). Purple points are the *Spitzer* detection limits for IRAC and MIPS instruments (Dole et al., 2003; Fazio et al., 2004). Black points are the *Herschel* detection limits for PACS and SPIRE instruments[e]. Grey points on the right refer to the Atacama large millimeter/submillimeter array (ALMA) detection limits for two configurations (Cycle 0 array in the top and final values in the bottom curve). Top brown points refer to the VLA and eVLA detection limits (Ulvestad et al., 2009). Bottom brown points refer to the planned SKA configuration of phase 1 (SKA1) and 2 (SKA2), and have been computed on data based on Schilizzi et al. (2007). Orange points refer to LOFAR (Röttgering et al., 2006). Image adapted from the JWST website; see the website for details [e].

[a] http://www.gemini.edu/sciops/instruments/gmos/itc-sensitivity-and-overheads?q=node/10436
[b] http://www.gemini.edu/sciops/instruments/niri/itc-sensitivity-and-overheads?q=node/10088
[c] https://www.sofia.usra.edu/science/instruments/flitecam
[d] https://www.sofia.usra.edu/science/instruments/forcast
[e] https://jwst.stsci.edu/science-planning/performance-and-simulation-tools/sensitivity-overview

emission associated with relativistic electrons powered by AGN; the second one is the synchrotron emission from relativistic cosmic-ray electrons accelerated by shocks from supernovae; and the third one is the free-free bremsstrahlung emission from H II regions heated by

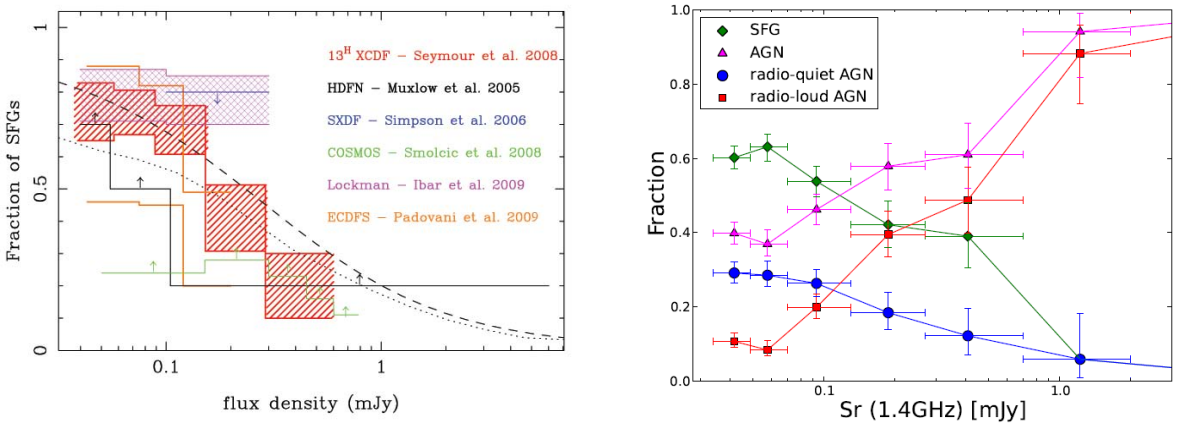

Figure 5.2: Relative contribution to the sub-mJy radio population of several classes of objects. (*Left*) SFG contribution to the overall population; from Norris et al. (2011b). (*Right*) Fractional contribution of SFGs, RQ AGN, and RL AGN (and the sum of this two classes, AGN) to the overall sub-mJy population; from Bonzini et al. (2013).

massive stars ($M_\star \gtrsim 5\,M_\odot$). In essence, while the first of these mechanisms is a tracer of ongoing accretion onto the SMBH in galactic centres, the later two are tracers of star-forming activity within the galaxies.

The bright radio sky ($L_{1.4\,\mathrm{GHz}} \gg 1$ mJy) is virtually missing of SFGs, and the source counts are dominated by the classical powerful radio galaxies and quasars, which emission is driven by RL AGN. The relative importance of SFGs increases dramatically below mJy flux levels (Richards et al. 1999; see Figure 5.2, left), while the contribution from classical powerful radio sources is expected to rapidly disappear below the mJy level (Jackson, 2004; Padovani, 2011). Current models of deep-sky surveys outcomes for telescope like SKA predict normal and SF galaxies accounting for up to 90% of the detections around 1 μJy (e.g. Wilman et al. 2008b).

Therefore, for long time it was accepted that the forthcoming deep radio surveys would have detected mainly SFGs and more quiescent galaxies. However, after many years of work on deep radio fields, it has finally been recognised that AGN still contribute significantly at μJy flux densities. The fraction of AGN at those flux density regimes is still important ($\sim 40\%$ at flux denisties $< 100\,\mu$Jy; see Figure 5.2 right). This thanks to recently established criteria able to separate radio-selected RQ AGN from RL AGN and SFGs.

Planned deep radio surveys are therefore expected to sample AGN in the millions. Several methods have been developed to idenitfy RL AGN in deep radio fields.

One of the most widely used is the ratio between the mid- and far-IR and the radio luminosities (van der Kruit, 1971, 1973; Dickey & Salpeter, 1984; Bell, 2003). In particular, 24 μm and 70 μm flux densities are widespread used (e.g., Appleton et al. 2004; Boyle et al. 2007; Sargent et al. 2010; Mao et al. 2011, and Section 1.5.1). Indeed SFGs show a very tight correlation between these two emissions from one side and radio emission from the other side, a correlation that holds for several order of magnitudes in luminosity and for a large span of redshifts (Condon, 1992; Ibar et al., 2008; Bonzini et al., 2015). The mechanisms at the root of these correlations are, from the IR side, the thermal re-processing of (newborn) stars emission from dusty H II regions, and, from the 1.4 GHz side, the synchrotron radiation from relativistic electrons accelerated in SNRs from the same population of massive stars that heat and ionize the H II regions (Harwit & Pacini, 1975; de Jong et al., 1985).

A further ingredient has to be added to RL AGN and SFGs. Recent works have revealed

the presence of a third population of radio sources in the sub-mJy radio sky, the RQ AGN (e.g., Padovani et al. 2009; Bonzini et al. 2012). The unexpected radio detection of large numbers of RQ AGN (which account up to ∼ 30% of the total detections below 0.1 mJy; see Figure 5.2, right), traditionally studied at optical or X-ray wavelengths and usually studied in radio only in the local Universe, opens new exciting perspectives for deep radio surveys. Indeed, for the first time it appears possible to study all main extragalactic populations (galaxies and AGN) with only one survey and one selection function, in the radio band.

However, the unexpected detection of this component implies that the separation of RL AGN from SFGs is not the only challenge that deep radio surveys have to face. It became relevant also to confidently separate RL from RQ AGN (Bonzini et al., 2013), especially considering that the emission mechanism in RQ AGN is still matter of debate.

5.1.1 Nuclear activity within radio-quiet AGN

A lot of work has been done in the attempt to solve the RL/RQ dichotomy in the local ($z \lesssim 1$) Universe. Thanks to multiwavelength surveys and extensive analyses it is now clear that local RQ quasars contain both AGN and star-forming activity, in proportion variable within the object (e.g., Condon et al. 1991). At high redshift the dichotomy is more vicious, biased by unresolved detections and limited sensitivity of the current radio surveys. Only designed observations can address this question, and the current results are obviously of reduced statistical meaning.

In the local Universe, where RQ AGN can be resolved by high-resolution facilities (like VLBI arrays), these sources often display compact radio cores and weak jet-like structures which classifies them as AGN; but those objects within which these features could not be detected lie on the same far–IR-to-radio correlation as the SFGs (Roy et al., 1998), or can be classified as SFGs due to the emission–line-to-radio–luminosity ratio diagnostics (Baum & Heckman, 1989; Rawlings & Saunders, 1991), or the 4000 Å break strength (Poggianti & Barbaro, 1997; Heckman & Best, 2014), suggesting that the bulk of their radio emission is actually powered by star formation (Bonzini et al., 2015). Nevertheless these sources are classified as AGN due to several others diagnostics, like the emission-line diagrams (Kewley et al., 2001) or the colour-colour IRAC diagrams (Lacy et al., 2004; Donley et al., 2012).

This discrimination has become one of the main challenge for the proper interpretation of deep radio surveys, and current analyses are mainly done on a statistical basis (e.g. Bonzini et al. 2013, 2015; and Section 2.2.1). This challenge will be even more relevant with the future, deep radio surveys, where objects belonging to these three classes are expected to be detected in the millions (Norris et al., 2011b).

Until now, radio surveys traditionally probed RL AGN, which however represents only about 10% of the overall AGN population. The work reported here confirms that the radio emission of some sources classified as RQ can be dominated by AGN, rather than by star formation (up to around 100% of the total radio emission in source 225 by Middelberg et al. 2011a). Moreover, other authors are findings similar results using complementary approaches that does not make use of VLBI observations (White et al., 2015).

The emerging scenario is that at redshifts $z \gtrsim 1$ there exists a class of hybrid objects where AGN and SF activity coexist in the host galaxies, with radio outputs similar to each other. It is already known that many RL AGN are hosted by galaxies with strong star formation (Alexander et al., 2005b; Norris et al., 2007a; Alexander, 2008), and these star-forming RL AGN dominate the most radio-luminous AGN at high redshift (Rees et al., 2016). Our

observations (see Sect. 2.2) and our re-analysis (see Chap. 3) of recent data show that AGN-driven radio emission can be a relevant contribution also within sources characterised by intermediate and low radio emission, and lying at intermediate and high redshifts. The radio emission from these sources seems to be highly concentrated in the centre of the galaxy.

With the next generation of radio telescopes, radio surveys will routinely reach the μJy-level sensitivities and in the same cases (e.g. SKA-MID) at sub-kpc scale spatial resolutions. This will compete with the current VLBI observations, and the overall AGN population will be studied with a single selection function. The intermediate redshift ($z \gtrsim 1$) RL/RQ dichotomy will finally be addressed in a statistical way. The first, relevant outcome will be the derivation of unbiased radio luminosity function for each type of activity (AGN and SF activity) to provide a reliable census of the bolometric luminosity associated to the two phenomena over cosmic time. In turn, this will finally help to fully understand the interplay between them, and to hopefully solve the problem of AGN triggering mechanism and duty cycle.

In Sect. 3.6 I presented some early evidence that a potential proxy to find VLBI-sized AGN-driven radio emission within sources classified as RQ AGN is the positioning within the AGN wedge of the IRAC colour-colour diagram proposed by Donley et al. (2012). This wedge has been built to highlight the monotonic increase of flux densities along the four IRAC bands, which is interpreted as signature of an heated dusty torus around the central SMBH. From the physical point of view, the low and very compact radio-emission level of these sources and the presence of a dusty torus around the central SMBH both point towards an interpretation of these objects as very young or recently reactivated AGN sources.

If this evidence is confirmed, we expect that a combination of the statistical criteria proposed by Bonzini et al. (2012, 2013) and the IRAC colour-colour space positioning can constitute a powerful proxy to explore the faint-end tail of the AGN-driven radio emission at intermediate/high redshift. This faint-end population is particularly relevant in the attempt to solve the riddle of the RL/RQ dichotomy, and a robust pre-selection of candidates for higher resolution follow ups is critical to build significant samples of these objects.

5.1.2 Infrared-faint radio sources

The search for high and very high redshift RL AGN is a task of paramount relevance to understand the evolution of galaxies, and to understand formation and accretion history of SMBHs. To date, only a handful of radio sources have been found at $z > 5$ (the farthest of which lies at $z \sim 5.19$; van Breugel et al. 1999), and a number of techniques to efficiently pre-select high-redshift candidates are being used (see e.g. Falcke et al. 2004b). Deep radio surveys offer also a natural way to select faint sources associated to very high-redshift powerful RL AGN.

In the past decade a new class of RL AGN has been found, the so-called infrared-faint radio sources (IFRS). These objects start to appear above 1 mJy, but extend to the sub-mJy regime. The main observational feature of these sources is their extreme radio-to-IR ratio, which makes them very easy to highlight in multiwavelength surveys, and to follow down to intermediate and high redshifts. Current studies, mainly relying on bright ($\gg 1$ mJy) samples (Collier et al., 2014; Herzog et al., 2014), suggest that these sources are associated to broad line Type 1 AGN, at redshift $2 < z < 3$, with typical radio luminosities of RL QSOs.

IFRSs, besides constituting a well defined class of radio sources by themselves, are therefore a promising beacon to explore the depths of the Universe, especially if pushing their search to sub-mJy radio flux densities.

The work presented here contributed casting light on the radio- and IR-faintest samples of these sources, highlighting how these samples are probably of the same nature of bright IFRSs (RL QSOs), but lie at a higher redshift. More important, it has been found that the first of the two criteria recently adopted in literature to spot these sources ($R_{3.6} > 500$; Zinn et al. 2011) is not suitable to track them to high redshift. Beyond $z \sim 4$–4.5, it is expected that radio-to-IR ratio of Type 1 and 2 QSOs drop down to ~ 200, requiring a relaxation of the selection criteria.

Given their inferred high spatial density ($\sigma_{IFRS} \sim 10^1$–10^2 deg^{-2}), future deep radio surveys are expected to discover these objects in the million. If their high redshift nature will be confirmed, IFRSs will finally help to trace the BH accretion history with meaningful statistical samples.

A

Star formation rate from radio luminosity

The relation that links the radio luminosity and the star formation rate has been derived by Condon (1992). At 1.4 GHz two are the main mechanisms of radio emission in normal galaxies.

The first mechanism is related to the non-thermal (synchrotron) radio emission from relativistic cosmic-ray electrons accelerated by shocks from supernovae. The conversion to star-formation rate is obtained by assuming that all stars more massive than $8\,M_\odot$ end as radio supernovae, and using the empirical relation between radio luminosity and supernova rate observed in the Milky Way. This contribution has the form:

$$\frac{L_{\text{non-thermal}}}{\text{W Hz}^{-1}} \sim 5.3 \times 10^{21} \left(\frac{\nu}{\text{GHz}}\right)^{\alpha_{\text{NT}}} \frac{\text{SFR}(\text{M} \gtrsim 5\,\text{M}_\odot)}{\text{M}_\odot\,\text{yr}^{-1}}$$

where $\alpha_{\text{NT}} = -0.8$ is the non-thermal spectral index.

The second mechanism is related to the thermal radio emission from free-free bremsstrahlung from H II regions heated by massive ($M_{star} \gtrsim 5\,M_\odot$) stars, and the conversion is obtained assuming dust absorption of Lyman photons as negligible. This contribution is:

$$\frac{L_{\text{thermal}}}{\text{W Hz}^{-1}} \sim 5.5 \times 10^{20} \left(\frac{\nu}{\text{GHz}}\right)^{-0.1} \frac{\text{SFR}(\text{M} \gtrsim 5\,\text{M}_\odot)}{\text{M}_\odot\,\text{yr}^{-1}}$$

Therefore the expected relation is:

$$\frac{\text{SFR}_{radio}}{\text{M}_\odot\,\text{yr}^{-1}} = \frac{\text{SFR}^{\text{non-thermal}}_{radio}}{\text{M}_\odot\,\text{yr}^{-1}} + \frac{\text{SFR}^{\text{thermal}}_{radio}}{\text{M}_\odot\,\text{yr}^{-1}} =$$

$$= Q \times \frac{(L_{1.4\,\text{GHz}}/\text{W Hz}^{-1})}{5.3 \times 10^{21}\,(\nu/\text{GHz})^{-0.8} + 5.5 \times 10^{20}\,(\nu/\text{GHz})^{-0.1}}$$

The factor Q takes into account the fact that Condon (1992) derived the formula considering the SFR only for stars more massive than $5\,M_\odot$ (Huynh, 2004). The generalisation is derived with the formula:

$$Q = \frac{\int_{0.1\,M_\odot}^{120\,M_\odot} M\,\psi(M)\,dM}{\int_{5\,M_\odot}^{120\,M_\odot} M\,\psi(M)\,dM}$$

where $\psi(M) \propto M^{-x}$ is the IMF.

In Chap. 3 (Sect. 3.5), we made explicit use of this formula to compute the SFR expected for the residual (i.e., not detected by VLBI-based experiments) radio emission at 1.4 GHz, and compared this value with the one obtained from the IR bolometric luminosity for the same source. This procedure has been applied by Bonzini et al. (2015) on a statistical base, and they made use of formulae based on Chabrier (2003) initial mass function.

The factor Q for the Chabrier (2003) IMF can be computed as:

$$Q_{Chabrier} = \frac{\int_{0.1\,M_\odot}^{120\,M_\odot} M\,\psi(M)\,dM}{\int_{5\,M_\odot}^{120\,M_\odot} M\,\psi(M)\,dM} = 3.24$$

from which the values reported in Sect. 3.5.

In Chap. 4 (Sect. 4.8 and Fig. 4.5 (d)), we reported the expected SFR for an Arp 220-like SBG at redshift $z \sim 3$, under the hypothesis that SF activity accounts for all the radio emission. The value reported ($3600\,M_\odot\,yr^{-1}$) has been obtained with this very formula.

The value we used for Q is the value we expect for the actual Arp 220. The SFR of this galaxy at its real redshift ($z = 0.018126 \pm 0.000023$; de Vaucouleurs et al. 1991) is known, via IR proxy, to be of the order SFR $\sim 10^2\,M_\odot\,yr^{-1}$ (Martín, 2011; Scoville, 2013). Also known are its radio flux at 1.4 GHz ($S_{1.4\,GHz} \sim 300 \pm 40$ mJy; Condon et al. 1983), and from the VLA data at 1.4 GHz and 4.8 GHz (Parra et al., 2010) it is possible to compute the spectral index of the source ($\alpha = -0.468$). Therefore, the intrinsic luminosity of Arp 220 is quick to compute ($L_{1.4\,GHz} = 2.19 \times 10^{23}\,W\,Hz^{-1}$).

It is also recognised that there is no significant AGN in the centre of Arp 220, so it is possible to assume that all the current radio luminosity at 1.4 GHz is due purely to SF activity. Inverting the formula by Condon (1992) it is then possible to derive the current value for the factor Q:

$$Q = SFR \times \frac{4.581 \times 10^{21}\,W\,Hz^{-1}}{L_{1.4\,GHz}} = 2.08$$

Under the simple hypotheses that this value is constant with cosmic time (at least as far as $z \sim 3$), assuming that AGN has always been unimportant inside Arp 220, and using the evolutionaty model we applied for SBG, it is then straightforward to compute the SFR expected for Arp 220 (and Arp 220-like SBGs) at redshift ~ 3:

$$SFR_{Arp\,220}(z \sim 3) = 3.6 \times 10^3\,M_\odot\,yr^{-1}$$

References

Afonso, J., Bizzocchi, L., Ibar, E., et al. 2011, Ultra Steep Spectrum Radio Sources in the Lockman Hole: SERVS Identifications and Redshift Distribution at the Faintest Radio Fluxes, Vol. 743, ApJ, 743, 122

Ahn, C. P., Alexandroff, R., Allende Prieto, C., et al. 2014, *The Tenth Data Release of the Sloan Digital Sky Survey: First Spectroscopic Data from the SDSS-III Apache Point Observatory Galactic Evolution Experiment*, Vol. 211, ApJS, 211, 17

Ahn, C. P., Alexandroff, R., Allende Prieto, C., et al. 2012, *The Ninth Data Release of the Sloan Digital Sky Survey: First Spectroscopic Data from the SDSS-III Baryon Oscillation Spectroscopic Survey*, Vol. 203, ApJS, 203, 21

Aird, J., Nandra, K., Laird, E. S., et al. 2010, *The evolution of the hard X-ray luminosity function of AGN*, Vol. 401, MNRAS, 401, 2531

Alexander, D. M. 2008, *The X-ray-infrared/submillimetre connection and the legacy era of cosmology*, Vol. 329, Astronomische Nachrichten, 329, 127

Alexander, D. M., Bauer, F. E., Brandt, W. N., et al. 2003, *The Chandra Deep Field North Survey. XIII. 2 Ms Point-Source Catalogs*, Vol. 126, AJ, 126, 539

Alexander, D. M., Bauer, F. E., Chapman, S. C., et al. 2005a, *The X-Ray Spectral Properties of SCUBA Galaxies*, Vol. 632, ApJ, 632, 736

Alexander, D. M., Smail, I., Bauer, F. E., et al. 2005b, *Rapid growth of black holes in massive star-forming galaxies*, Vol. 434, Nature, 434, 738

Aller, M. C. & Richstone, D. 2002, *The Cosmic Density of Massive Black Holes from Galaxy Velocity Dispersions*, Vol. 124, AJ, 124, 3035

Alonso-Herrero, A. 2013, *AGN and star formation activity in local luminous and ultraluminous infrared galaxies*, ArXiv e-prints

Antonucci, R. 1993, *Unified models for active galactic nuclei and quasars*, Vol. 31, ARA&A, 31, 473

Appleton, P. N., Fadda, D. T., Marleau, F. R., et al. 2004, *The Far- and Mid-Infrared/Radio Correlations in the Spitzer Extragalactic First Look Survey*, Vol. 154, ApJS, 154, 147

Arnouts, S., Vandame, B., Benoist, C., et al. 2001, *ESO imaging survey. Deep public survey: Multi-color optical data for the Chandra Deep Field South*, Vol. 379, A&A, 379, 740

Assef, R. J., Kochanek, C. S., Ashby, M. L. N., et al. 2011, *The Mid-IR- and X-ray-Selected QSO Luminosity Function*, Vol. 728, ApJ, 728, 56

Babbedge, T. S. R., Rowan-Robinson, M., Vaccari, M., et al. 2006, *Luminosity functions for galaxies and quasars in the Spitzer Wide-area Infrared Extragalactic Legacy Survey*, Vol. 370, MNRAS, 370, 1159

Baldry, I. K., Glazebrook, K., Brinkmann, J., et al. 2004, *Quantifying the Bimodal Color-Magnitude Distribution of Galaxies*, Vol. 600, ApJ, 600, 681

Baloković, M., Smolčić, V., Ivezić, Ž., et al. 2012, *Disclosing the Radio Loudness Distribution Dichotomy in Quasars: An Unbiased Monte Carlo Approach Applied to the SDSS-FIRST Quasar Sample*, Vol. 759, ApJ, 759, 30

Banfield, J. K., George, S. J., Taylor, A. R., et al. 2011, *Polarized Radio Sources: A Study of Luminosity, Redshift, and Infrared Colors*, Vol. 733, ApJ, 733, 69

Barger, A. J., Cowie, L. L., Chen, C.-C., et al. 2014, *Is There a Maximum Star Formation Rate in High-redshift Galaxies?*, Vol. 784, ApJ, 784, 9

Barris, B. J., Tonry, J. L., Blondin, S., et al. 2004, *Twenty-Three High-Redshift Supernovae from the Institute for Astronomy Deep Survey: Doubling the Supernova Sample at $z \gtrsim 0.7$*, Vol. 602, ApJ, 602, 571

Baum, S. A. & Heckman, T. 1989, *Extended optical line emitting gas in powerful radio galaxies - What is the radio emission-line connection?*, Vol. 336, ApJ, 336, 702

Begelman, M. C. 2012, *Radiatively inefficient accretion: breezes, winds and hyperaccretion*, Vol. 420, MNRAS, 420, 2912

Behroozi, P. S., Wechsler, R. H., & Conroy, C. 2013, *The Average Star Formation Histories of Galaxies in Dark Matter Halos from z = 0-8*, Vol. 770, ApJ, 770, 57

Bell, E. F. 2003, *Estimating Star Formation Rates from Infrared and Radio Luminosities: The Origin of the Radio-Infrared Correlation*, Vol. 586, ApJ, 586, 794

Bell, E. F., Papovich, C., Wolf, C., et al. 2005, *Toward an Understanding of the Rapid Decline of the Cosmic Star Formation Rate*, Vol. 625, ApJ, 625, 23

Bernardi, G., Greenhill, L. J., Mitchell, D. A., et al. 2013, *A 189 MHz, 2400 deg^2 Polarization Survey with the Murchison Widefield Array 32-element Prototype*, Vol. 771, ApJ, 771, 105

Blandford, R. D. & Begelman, M. C. 1999, *On the fate of gas accreting at a low rate on to a black hole*, Vol. 303, MNRAS, 303, L1

Blundell, K. M. & Beasley, A. J. 1998, *The central engines of radio-quiet quasars*, Vol. 299, MNRAS, 299, 165

Bock, D. C.-J., Large, M. I., & Sadler, E. M. 1999, *SUMSS: A Wide-Field Radio Imaging Survey of the Southern Sky. I. Science Goals, Survey Design, and Instrumentation*, Vol. 117, AJ, 117, 1578

Bolzonella, M., Miralles, J.-M., & Pelló, R. 2000, *Photometric redshifts based on standard SED fitting procedures*, Vol. 363, A&A, 363, 476

Bonzini, M., Mainieri, V., Padovani, P., et al. 2015, *Star formation properties of sub-mJy radio sources*, Vol. 453, MNRAS, 453, 1079

Bonzini, M., Mainieri, V., Padovani, P., et al. 2012, *The Sub-mJy Radio Population of the E-CDFS: Optical and Infrared Counterpart Identification*, Vol. 203, ApJS, 203, 15

Bonzini, M., Padovani, P., Mainieri, V., et al. 2013, *The sub-mJy radio sky in the Extended Chandra Deep Field-South: source population*, Vol. 436, MNRAS, 436, 3759

Boyle, B. J., Cornwell, T. J., Middelberg, E., et al. 2007, *Extending the infrared radio correlation*, Vol. 376, MNRAS, 376, 1182

Brightman, M., Nandra, K., Salvato, M., et al. 2014, *Compton thick active galactic nuclei in Chandra surveys*, Vol. 443, MNRAS, 443, 1999

Brinchmann, J., Charlot, S., White, S. D. M., et al. 2004, *The physical properties of star-forming galaxies in the low-redshift Universe*, Vol. 351, MNRAS, 351, 1151

Brusa, M., Civano, F., Comastri, A., et al. 2010, *The XMM-Newton Wide-field Survey in the Cosmos Field (XMM-COSMOS): Demography and Multiwavelength Properties of Obscured and Unobscured Luminous Active Galactic Nuclei*, Vol. 716, ApJ, 716, 348

Burbidge, G. 1967, *Quasi-stellar objects*

Cameron, A. D., Keith, M., Hobbs, G., et al. 2011, *Are the infrared-faint radio sources pulsars?*, Vol. 415, MNRAS, 415, 845

Canalizo, G. & Stockton, A. 2001, *Quasi-Stellar Objects, Ultraluminous Infrared Galaxies, and Mergers*, Vol. 555, ApJ, 555, 719

Cardamone, C. N., van Dokkum, P. G., Urry, C. M., et al. 2010, *The Multiwavelength Survey by Yale-Chile (MUSYC): Deep Medium-band Optical Imaging and High-quality 32-band Photometric Redshifts in the ECDF-S*, Vol. 189, ApJS, 189, 270

Cattaneo, A., Faber, S. M., Binney, J., et al. 2009, *The role of black holes in galaxy formation and evolution*, Vol. 460, Nature, 460, 213

Chabrier, G. 2003, *Galactic Stellar and Substellar Initial Mass Function*, Vol. 115, PASP, 115, 763

Chi, S., Barthel, P. D., & Garrett, M. A. 2013, *Deep, wide-field, global VLBI observations of the Hubble deep field north (HDF-N) and flanking fields (HFF)*, Vol. 550, A&A, 550, A68

Chiu, H.-Y. 1964, *Gravitational Collapse*, Vol. 17, Physics Today, 17, 5

Ciliegi, P., Zamorani, G., Hasinger, G., et al. 2003, *A deep VLA survey at 6 cm in the Lockman Hole*, Vol. 398, A&A, 398, 901

Cirasuolo, M., Celotti, A., Magliocchetti, M., & Danese, L. 2003, *Is there a dichotomy in the radio loudness distribution of quasars?*, Vol. 346, MNRAS, 346, 447

Civano, F., Elvis, M., Brusa, M., et al. 2012, *The Chandra COSMOS Survey. III. Optical and Infrared Identification of X-Ray Point Sources*, Vol. 201, ApJS, 201, 30

Cohen, A. S., Lane, W. M., Cotton, W. D., et al. 2007, *The VLA Low-Frequency Sky Survey*, Vol. 134, AJ, 134, 1245

Collier, J. D., Banfield, J. K., Norris, R. P., et al. 2014, *Infrared-faint radio sources: a new population of high-redshift radio galaxies*, MNRAS

Condon, J. J. 1974, *Confusion and Flux-Density Error Distributions*, Vol. 188, ApJ, 188, 279

Condon, J. J. 1987, *A 1.49 GHz atlas of spiral galaxies with B(T) = +12 or less and delta = -45 deg or greater*, Vol. 65, ApJS, 65, 485

Condon, J. J. 1992, *Radio emission from normal galaxies*, Vol. 30, ARA&A, 30, 575

Condon, J. J., Condon, M. A., Broderick, J. J., & Davis, M. M. 1983, *Optical identifications of flat-spectrum radio sources*, Vol. 88, AJ, 88, 20

Condon, J. J., Cotton, W. D., Greisen, E. W., et al. 1998, *The NRAO VLA Sky Survey*, Vol. 115, AJ, 115, 1693

Condon, J. J., Cotton, W. D., Yin, Q. F., et al. 2003, *The SIRTF First-Look Survey. I. VLA Image and Source Catalog*, Vol. 125, AJ, 125, 2411

Condon, J. J., Huang, Z.-P., Yin, Q. F., & Thuan, T. X. 1991, *Compact starbursts in ultraluminous infrared galaxies*, Vol. 378, ApJ, 378, 65

Cowley, M. J., Spitler, L. R., Tran, K.-V. H., et al. 2016, *ZFOURGE catalogue of AGN candidates: an enhancement of 160-μm-derived star formation rates in active galaxies to z = 3.2*, Vol. 457, MNRAS, 457, 629

Croston, J. H., Hardcastle, M. J., Mingo, B., et al. 2011, *A Large-scale Shock Surrounding a Powerful Radio Galaxy?*, Vol. 734, ApJ, 734, L28

Croton, D. J., Springel, V., White, S. D. M., et al. 2006, *The many lives of active galactic nuclei: cooling flows, black holes and the luminosities and colours of galaxies*, Vol. 365, MNRAS, 365, 11

Daddi, E., Alexander, D. M., Dickinson, M., et al. 2007a, *Multiwavelength Study of Massive Galaxies at z˜2. II. Widespread Compton-thick Active Galactic Nuclei and the Concurrent Growth of Black Holes and Bulges*, Vol. 670, ApJ, 670, 173

Daddi, E., Dickinson, M., Morrison, G., et al. 2007b, *Multiwavelength Study of Massive Galaxies at z˜2. I. Star Formation and Galaxy Growth*, Vol. 670, ApJ, 670, 156

Dai, X., Assef, R. J., Kochanek, C. S., et al. 2009, *Mid-Infrared Galaxy Luminosity Functions from the AGN and Galaxy Evolution Survey*, Vol. 697, ApJ, 697, 506

Damen, M., Labbé, I., van Dokkum, P. G., et al. 2011, *The SIMPLE Survey: Observations, Reduction, and Catalog*, Vol. 727, ApJ, 727, 1

Dawson, S., Stern, D., Bunker, A. J., Spinrad, H., & Dey, A. 2001, *Serendipitously Detected Galaxies in the Hubble Deep Field*, Vol. 122, AJ, 122, 598

De Breuck, C., Seymour, N., Stern, D., et al. 2010, *The Spitzer High-redshift Radio Galaxy Survey*, Vol. 725, ApJ, 725, 36

de Jong, T., Klein, U., Wielebinski, R., & Wunderlich, E. 1985, *Radio continuum and far-infrared emission from spiral galaxies - A close correlation*, Vol. 147, A&A, 147, L6

de Ruiter, H. R., Willis, A. G., & Arp, H. C. 1977, *A Westerbork 1415 MHz survey of background radio sources. II - Optical identifications with deep IIIA-J plates*, Vol. 28, A&AS, 28, 211

de Vaucouleurs, G., de Vaucouleurs, A., Corwin, Jr., H. G., et al. 1991, *Third Reference Catalogue of Bright Galaxies. Volume I: Explanations and references. Volume II: Data for galaxies between 0^h and 12^h. Volume III: Data for galaxies between 12^h and 24^h.*

Dekel, A., Sari, R., & Ceverino, D. 2009, *Formation of Massive Galaxies at High Redshift: Cold Streams, Clumpy Disks, and Compact Spheroids*, Vol. 703, ApJ, 703, 785

Del Moro, A., Alexander, D. M., Mullaney, J. R., et al. 2013, *GOODS-Herschel: radio-excess signature of hidden AGN activity in distant star-forming galaxies*, Vol. 549, A&A, 549, A59

Deng, X.-F. 2013, *A tool for the morphological classification of galaxies: the concentration index*, Vol. 13, Research in Astronomy and Astrophysics, 13, 651

Dewdney, P., Hall, P., Schillizzi, R., & Lazio, J. 1999, *The square kilometre array*, Vol. 97, Proc. Inst. of Electrical and Electronics Engineers, 97, 1482

Dickey, J. M. & Salpeter, E. E. 1984, *1.4 GHz continuum sources in the Hercules cluster*, Vol. 284, ApJ, 284, 461

Dole, H., Lagache, G., & Puget, J.-L. 2003, *Predictions for Cosmological Infrared Surveys from Space with the Multiband Imaging Photometer for SIRTF*, Vol. 585, ApJ, 585, 617

Donley, J. L., Koekemoer, A. M., Brusa, M., et al. 2012, *Identifying Luminous Active Galactic Nuclei in Deep Surveys: Revised IRAC Selection Criteria*, Vol. 748, ApJ, 748, 142

Dunlop, J. S., McLure, R. J., Kukula, M. J., et al. 2003, *Quasars, their host galaxies and their central black holes*, Vol. 340, MNRAS, 340, 1095

Dunlop, J. S. & Peacock, J. A. 1990, *The Redshift Cut-Off in the Luminosity Function of Radio Galaxies and Quasars*, Vol. 247, MNRAS, 247, 19

Edge, D. O., Shakeshaft, J. R., McAdam, W. B., Baldwin, J. E., & Archer, S. 1959, *A survey of radio sources at a frequency of 159 Mc/s*, Vol. 68, MmRAS, 68, 37

Elmouttie, M., Haynes, R. F., Jones, K. L., Sadler, E. M., & Ehle, M. 1998, *Radio continuum evidence for nuclear outflow in the Circinus galaxy*, Vol. 297, MNRAS, 297, 1202

Elvis, M., Wilkes, B. J., McDowell, J. C., et al. 1994, *Atlas of quasar energy distributions*, Vol. 95, ApJS, 95, 1

Fabian, A. C. 1999, *X-ray studies of black holes in AGN*, in Highlights in X-ray Astronomy, ed. B. Aschenbach & M. J. Freyberg, Vol. 272, 127

Falcke, H., Körding, E., & Markoff, S. 2004a, *A scheme to unify low-power accreting black holes. Jet-dominated accretion flows and the radio/X-ray correlation*, Vol. 414, A&A, 414, 895

Falcke, H., Körding, E., & Nagar, N. M. 2004b, *Compact radio cores: from the first black holes to the last*, Vol. 48, New A Rev., 48, 1157

Fanaroff, B. L. & Riley, J. M. 1974, *The morphology of extragalactic radio sources of high and low luminosity*, Vol. 167, MNRAS, 167, 31P

Fazio, G. G., Hora, J. L., Allen, L. E., et al. 2004, *The Infrared Array Camera (IRAC) for the Spitzer Space Telescope*, Vol. 154, ApJS, 154, 10

Ferrarese, L. & Merritt, D. 2000, *A Fundamental Relation between Supermassive Black Holes and Their Host Galaxies*, Vol. 539, ApJ, 539, L9

Flesch, E. W. 2015, *The Half Million Quasars (HMQ) Catalogue*, Vol. 32, PASA, 32, e010

Fotopoulou, S., Salvato, M., Hasinger, G., et al. 2012, *Photometry and Photometric Redshift Catalogs for the Lockman Hole Deep Field*, Vol. 198, ApJS, 198, 1

Franceschini, A., Toffolatti, L., Mazzei, P., Danese, L., & de Zotti, G. 1991, *Galaxy counts and contributions to the background radiation from 1 micron to 1000 microns*, Vol. 89, A&AS, 89, 285

Franzen, T. M. O., Banfield, J. K., Hales, C. A., et al. 2015, *ATLAS - I. Third release of 1.4 GHz mosaics and component catalogues*, Vol. 453, MNRAS, 453, 4020

Franzen, T. M. O., Sadler, E. M., Chhetri, R., et al. 2014, *Deep 20-GHz survey of the Chandra Deep Field South and SDSS Stripe 82: source catalogue and spectral properties*, Vol. 439, MNRAS, 439, 1212

Fritz, T. K., Gillessen, S., Dodds-Eden, K., et al. 2011, *Line Derived Infrared Extinction toward the Galactic Center*, Vol. 737, ApJ, 737, 73

Gaibler, V., Khochfar, S., Krause, M., & Silk, J. 2012, *Jet-induced star formation in gas-rich galaxies*, Vol. 425, MNRAS, 425, 438

Gallimore, J. F., Baum, S. A., & O'Dea, C. P. 2004, *The Parsec-Scale Radio Structure of NGC 1068 and the Nature of the Nuclear Radio Source*, Vol. 613, ApJ, 613, 794

Garn, T. & Alexander, P. 2008, *Deep 610-MHz Giant Metrewave Radio Telescope observations of the Spitzer extragalactic First Look Survey field - III. The radio properties of infrared-faint radio sources*, Vol. 391, MNRAS, 391, 1000

Garn, T., Green, D. A., Hales, S. E. G., Riley, J. M., & Alexander, P. 2007, *Deep 610-MHz Giant Metrewave Radio Telescope observations of the Spitzer extragalactic First Look Survey field - I. Observations, data analysis and source catalogue*, Vol. 376, MNRAS, 376, 1251

Gastaldello, F., Buote, D. A., Temi, P., et al. 2009, *X-Ray Cavities, Filaments, and Cold Fronts in the Core of the Galaxy Group NGC 5044*, Vol. 693, ApJ, 693, 43

Gawiser, E., van Dokkum, P. G., Herrera, D., et al. 2006, *The Multiwavelength Survey by Yale-Chile (MUSYC): Survey Design and Deep Public UBVRIz' Images and Catalogs of the Extended Hubble Deep Field-South*, Vol. 162, ApJS, 162, 1

Gebhardt, K., Bender, R., Bower, G., et al. 2000, *A Relationship between Nuclear Black Hole Mass and Galaxy Velocity Dispersion*, Vol. 539, ApJ, 539, L13

Genzel, R., Eckart, A., Ott, T., & Eisenhauer, F. 1997, *On the nature of the dark mass in the centre of the Milky Way*, Vol. 291, MNRAS, 291, 219

Ghisellini, G., Haardt, F., & Matt, G. 1994, *The Contribution of the Obscuring Torus to the X-Ray Spectrum of Seyfert Galaxies - a Test for the Unification Model*, Vol. 267, MNRAS, 267, 743

Ghisellini, G., Haardt, F., & Matt, G. 2004, *Aborted jets and the X-ray emission of radio-quiet AGNs*, Vol. 413, A&A, 413, 535

Giavalisco, M., Ferguson, H. C., Koekemoer, A. M., et al. 2004, *The Great Observatories Origins Deep Survey: Initial Results from Optical and Near-Infrared Imaging*, Vol. 600, ApJ, 600, L93

Giroletti, M. & Panessa, F. 2009, *The Faintest Seyfert Radio Cores Revealed by VLBI*, Vol. 706, ApJ, 706, L260

Goldschmidt, P., Kukula, M. J., Miller, L., & Dunlop, J. S. 1999, *A Comparison of the Optical Properties of Radio-loud and Radio-quiet Quasars*, Vol. 511, ApJ, 511, 612

Gonzalez-Martin, O., Masegosa, J., Marquez, I., et al. 2015, *On the LINER nuclear obscuration, Compton-thickness and the existence of the dusty torus; Clues from Spitzer/IRS spectra*, ArXiv e-prints

Gordon, K. D., Clayton, G. C., Misselt, K. A., Landolt, A. U., & Wolff, M. J. 2003, *A Quantitative Comparison of the Small Magellanic Cloud, Large Magellanic Cloud, and Milky Way Ultraviolet to Near-Infrared Extinction Curves*, Vol. 594, ApJ, 594, 279

Grant, J. K., Taylor, A. R., Stil, J. M., et al. 2010, *The DRAO Planck Deep Fields: The Polarization Properties of Radio Galaxies at 1.4 GHz*, Vol. 714, ApJ, 714, 1689

Griffin, M. J., Abergel, A., Abreu, A., et al. 2010, *The Herschel-SPIRE instrument and its in-flight performance*, Vol. 518, A&A, 518, L3

Griffith, R. L. & Stern, D. 2010, *Morphologies of Radio-, X-ray-, and Mid-infrared-selected Active Galactic Nuclei*, Vol. 140, AJ, 140, 533

Grogin, N. A., Kocevski, D. D., Faber, S. M., et al. 2011, *CANDELS: The Cosmic Assembly Near-infrared Deep Extragalactic Legacy Survey*, Vol. 197, ApJS, 197, 35

Gruppioni, C., Pozzi, F., Zamorani, G., & Vignali, C. 2011, *Modelling galaxy and AGN evolution in the infrared: black hole accretion versus star formation activity*, Vol. 416, MNRAS, 416, 70

Guainazzi, M., Matt, G., Brandt, W. N., et al. 2000, *A broad-band X-ray view of NGC 4945*, Vol. 356, A&A, 356, 463

Haardt, F. & Maraschi, L. 1991, *A two-phase model for the X-ray emission from Seyfert galaxies*, Vol. 380, ApJ, 380, L51

Haardt, F., Maraschi, L., & Ghisellini, G. 1994, *A model for the X-ray and ultraviolet emission from Seyfert galaxies and galactic black holes*, Vol. 432, ApJ, 432, L95

Haas, M., Klaas, U., Müller, S. A. H., et al. 2003, *The ISO view of Palomar-Green quasars*, Vol. 402, A&A, 402, 87

Hales, C. A., Norris, R. P., Gaensler, B. M., et al. 2014, *ATLAS 1.4 GHz Data Release 2 - I. Observations of the CDF-S and ELAIS-S1 fields and methods for constructing differential number counts*, Vol. 441, MNRAS, 441, 2555

Hao, H., Sargent, M. T., Elvis, M., et al. 2014, *Inter-comparison of Radio-Loudness Criteria for Type 1 AGNs in the XMM-COSMOS Survey*, ArXiv e-prints

Harris, D. E. & Krawczynski, H. 2006, *X-Ray Emission from Extragalactic Jets*, Vol. 44, ARA&A, 44, 463

Harrison, C. official web page, http://astro.dur.ac.uk/ cpnc25/research.html

Harwit, M. & Pacini, F. 1975, *Infrared galaxies - Evolutionary stages of massive star formation*, Vol. 200, ApJ, 200, L127

Heckman, T. M. 1980, *An optical and radio survey of the nuclei of bright galaxies - Activity in normal galactic nuclei*, Vol. 87, A&A, 87, 152

Heckman, T. M. & Best, P. N. 2014, *The Coevolution of Galaxies and Supermassive Black Holes: Insights from Surveys of the Contemporary Universe*, Vol. 52, ARA&A, 52, 589

Herrera Ruiz, N., Middelberg, E., Norris, R. P., & Maini, A. 2016, *Unveiling the origin of the radio emission in Radio Quiet Quasars*, Vol. in prep., A&A, in prep.

Herzog, A. 2015, *Infrared-Faint Radio Sources*, PhD thesis, Macquarie University (Sydney – Australia); Ruhr-Universitaet Bochum (Bochum – Germany)

Herzog, A., Middelberg, E., Norris, R. P., et al. 2014, *Infrared-faint radio sources are at high redshifts. Spectroscopic redshift determination of infrared-faint radio sources using the Very Large Telescope*, Vol. 567, A&A, 567, A104

Herzog, A., Middelberg, E., Norris, R. P., et al. 2015a, *Active galactic nuclei cores in infrared-faint radio sources. Very long baseline interferometry observations using the Very Long Baseline Array*, Vol. 578, A&A, 578, A67

Herzog, A., Norris, R. P., Middelberg, E., et al. 2016, *The radio spectral energy distribution of infrared-faint radio sources*, ArXiv e-prints

Herzog, A., Norris, R. P., Middelberg, E., et al. 2015b, *Infrared-faint radio sources remain undetected at far-infrared wavelengths. Deep photometric observations using the Herschel Space Observatory*, Vol. 580, A&A, 580, A7

Higdon, J. L., Higdon, S. J. U., Weedman, D. W., et al. 2005, *Spitzer Observations of Optically "Invisible" Radio and X-Ray Sources: High-Redshift Active Galactic Nuclei*, Vol. 626, ApJ, 626, 58

Higdon, J. L., Higdon, S. J. U., Willner, S. P., et al. 2008, *Radio and Infrared Selected Optically Invisible Sources in the Boötes NDWFS*, Vol. 688, ApJ, 688, 885

Ho, L. C. 2008, *Nuclear Activity in Nearby Galaxies*, Vol. 46, ARA&A, 46, 475

Hooper, E. J., Impey, C. D., Foltz, C. B., & Hewett, P. C. 1995, *Radio properties of optically selected quasars*, Vol. 445, ApJ, 445, 62

Hooper, E. J., Impey, C. D., Foltz, C. B., & Hewett, P. C. 1996, *The Radio Properties of Optically Selected Quasars. III. Comparison between Optical and X-Ray Selected Samples*, Vol. 473, ApJ, 473, 746

Hopkins, A. M. 2004, *On the Evolution of Star-forming Galaxies*, Vol. 615, ApJ, 615, 209

Hopkins, A. M., Mobasher, B., Cram, L., & Rowan-Robinson, M. 1998, *The PHOENIX Deep Survey: 1.4-GHz source counts*, Vol. 296, MNRAS, 296, 839

Hotan, A. W., Bunton, J. D., Harvey-Smith, L., et al. 2014, *The Australian Square Kilometre Array Pathfinder: System Architecture and Specifications of the Boolardy Engineering Test Array*, Vol. 31, PASA, 31, e041

Huang, Z. P., Thuan, T. X., Chevalier, R. A., Condon, J. J., & Yin, Q. F. 1994, *Compact radio sources in the starburst galaxy M82 and the Sigma-D relation for supernova remnants*, Vol. 424, ApJ, 424, 114

Hughes, A., Staveley-Smith, L., Kim, S., Wolleben, M., & Filipović, M. 2007, *An Australia Telescope Compact Array 20-cm radio continuum study of the Large Magellanic Cloud*, Vol. 382, MNRAS, 382, 543

Hummel, E., van der Hulst, J. M., & Keel, W. C. 1987, *Circumnuclear star formation in the central region of the barred spiral galaxy NGC 1097*, Vol. 172, A&A, 172, 32

Huynh, M. T. 2004, *Constraining the star formation history of the Universe with deep radio data*, PhD thesis, Research School of Astronomy and Astrophysics – Australian National University (Canberra – Australia)

Huynh, M. T., Hopkins, A. M., Lenc, E., et al. 2012, *The ATLAS 5.5 GHz survey of the extended Chandra Deep Field South: catalogue, source counts and spectral indices*, Vol. 426, MNRAS, 426, 2342

Huynh, M. T., Norris, R. P., Siana, B., & Middelberg, E. 2010, *Evidence for Infrared-faint Radio Sources as $z \gtrsim 1$ Radio-loud Active Galactic Nuclei*, Vol. 710, ApJ, 710, 698

Ibar, E., Cirasuolo, M., Ivison, R., et al. 2008, *Exploring the infrared/radio correlation at high redshift*, Vol. 386, MNRAS, 386, 953

Inoue, A. K. & Kamaya, H. 2004, *Amount of intergalactic dust: constraints from distant supernovae and the thermal history of the intergalactic medium*, Vol. 350, MNRAS, 350, 729

Instrument, I. & Teams, I. S. 2015, *IRAC Instrument Handbook*

Ivezić, Ž., Menou, K., Knapp, G. R., et al. 2002, *Optical and Radio Properties of Extragalactic Sources Observed by the FIRST Survey and the Sloan Digital Sky Survey*, Vol. 124, AJ, 124, 2364

Ivezić, Z., Richards, G., Hall, P., et al. 2004, *Quasar Radio Dichotomy: Two Peaks, or not Two Peaks, that is the Question*, in Astronomical Society of the Pacific Conference Series, Vol. 311, "AGN Physics with the Sloan Digital Sky Survey", ed. G. T. Richards & P. B. Hall, 347

Ivison, R. J., Smail, I., Le Borgne, J.-F., et al. 1998, *A hyperluminous galaxy at z=2.8 found in a deep submillimetre survey*, Vol. 298, MNRAS, 298, 583

Iwasawa, K., Fabian, A. C., & Matt, G. 1997, *The iron K line complex in NGC1068: implications for X-ray reflection in the nucleus*, Vol. 289, MNRAS, 289, 443

Jackson, C. A. 2004, *Deep radio continuum studies with the SKA: evolution of radio AGN populations*, Vol. 48, New A Rev., 48, 1187

Jannuzi, B. T. & Dey, A. 1999, *The NOAO Deep Wide-Field Survey*, in Astronomical Society of the Pacific Conference Series, Vol. 191, Photometric Redshifts and the Detection of High Redshift Galaxies, ed. R. Weymann, L. Storrie-Lombardi, M. Sawicki, & R. Brunner, 111

Jarvis, M. J. 2012, *Multi-wavelength Extragalactic Surveys and the Role of MeerKAT and SALT*, Vol. 16, African Skies, 16, 44

Jarvis, M. J. & Rawlings, S. 2004, *The accretion history of the universe with the SKA*, Vol. 48, New A Rev., 48, 1173

Johansson, J. & Mörtsell, E. 2012, *Combined constraints on intergalactic dust from quasar colours and the soft X-ray background*, Vol. 426, MNRAS, 426, 3360

Kapinska, A. D., Hardcastle, M., Jackson, C., et al. 2015, *Unravelling lifecycles and physics of radio-loud AGN in the SKA Era*, Advancing Astrophysics with the Square Kilometre Array (AASKA14), 173

Karouzos, M., Im, M., Trichas, M., et al. 2014, *A Tale of Two Feedbacks: Star Formation in the Host Galaxies of Radio AGNs*, Vol. 784, ApJ, 784, 137

Kauffmann, G., Heckman, T. M., White, S. D. M., et al. 2003, *The dependence of star formation history and internal structure on stellar mass for 10^5 low-redshift galaxies*, Vol. 341, MNRAS, 341, 54

Kawaguchi, T., Shimura, T., & Mineshige, S. 2001, *Broadband Spectral Energy Distributions of Active Galactic Nuclei from an Accretion Disk with Advective Coronal Flow*, Vol. 546, ApJ, 546, 966

Kellermann, K. I., Condon, J. J., Kimball, A. E., Perley, R. A., & Ivezic, Z. 2016, *Radio Loud and Radio Quiet Quasars*, ArXiv e-prints

Kellermann, K. I., Fomalont, E. B., Mainieri, V., et al. 2008, *The VLA Survey of the Chandra Deep Field-South. I. Overview and the Radio Data*, Vol. 179, ApJS, 179, 71

Kellermann, K. I., Sramek, R., Schmidt, M., Shaffer, D. B., & Green, R. 1989, *VLA observations of objects in the Palomar Bright Quasar Survey*, Vol. 98, AJ, 98, 1195

Kennicutt, Jr., R. C. 1998, *Star Formation in Galaxies Along the Hubble Sequence*, Vol. 36, ARA&A, 36, 189

Kewley, L. J., Dopita, M. A., Sutherland, R. S., Heisler, C. A., & Trevena, J. 2001, *Theoretical Modeling of Starburst Galaxies*, Vol. 556, ApJ, 556, 121

Kewley, L. J., Heisler, C. A., Dopita, M. A., et al. 2000, *Compact Radio Emission from Warm Infrared Galaxies*, Vol. 530, ApJ, 530, 704

Kimball, A. E. & Ivezić, Ž. 2008, *A Unified Catalog of Radio Objects Detected by NVSS, First, WENSS, GB6, and SDSS*, Vol. 136, AJ, 136, 684

Kimball, A. E., Kellermann, K. I., Condon, J. J., Ivezić, Ž., & Perley, R. A. 2011, *The Two-component Radio Luminosity Function of Quasi-stellar Objects: Star Formation and Active Galactic Nucleus*, Vol. 739, ApJ, 739, L29

Klamer, I. J., Ekers, R. D., Sadler, E. M., & Hunstead, R. W. 2004, *Molecular Gas at High Redshift: Jet-induced Star Formation?*, Vol. 612, ApJ, 612, L97

Komatsu, E., Smith, K. M., Dunkley, J., et al. 2011, *Seven-year Wilkinson Microwave Anisotropy Probe (WMAP) Observations: Cosmological Interpretation*, Vol. 192, ApJS, 192, 18

Kormendy, J. & Ho, L. C. 2013, *Coevolution (Or Not) of Supermassive Black Holes and Host Galaxies*, Vol. 51, ARA&A, 51, 511

Kormendy, J. & Richstone, D. 1995, *Inward Bound—The Search For Supermassive Black Holes In Galactic Nuclei*, Vol. 33, ARA&A, 33, 581

Kukula, M. J., Dunlop, J. S., Hughes, D. H., & Rawlings, S. 1998, *The radio properties of radio-quiet quasars*, Vol. 297, MNRAS, 297, 366

Lacy, M., Baum, S. A., Chandler, C. J., et al. 2016, *The VLA Sky Survey (VLASS): Description and Science Goals*, in American Astronomical Society Meeting Abstracts, Vol. 227, American Astronomical Society Meeting Abstracts, 324.09

Lacy, M., Laurent-Muehleisen, S. A., Ridgway, S. E., Becker, R. H., & White, R. L. 2001, *The Radio Luminosity-Black Hole Mass Correlation for Quasars from the FIRST Bright Quasar Survey and a "Unification Scheme" for Radio-loud and Radio-quiet Quasars*, Vol. 551, ApJ, 551, L17

Lacy, M., Storrie-Lombardi, L. J., Sajina, A., et al. 2004, *Obscured and Unobscured Active Galactic Nuclei in the Spitzer Space Telescope First Look Survey*, Vol. 154, ApJS, 154, 166

Lacy, M., Wilson, G., Masci, F., et al. 2005, *The Infrared Array Camera Component of the Spitzer Space Telescope Extragalactic First Look Survey*, Vol. 161, ApJS, 161, 41

Laing, R. A., Jenkins, C. R., Wall, J. V., & Unger, S. W. 1994, *Spectrophotometry of a Complete Sample of 3CR Radio Sources: Implications for Unified Models*, in Astronomical Society of the Pacific Conference Series, Vol. 54, The Physics of Active Galaxies, ed. G. V. Bicknell, M. A. Dopita, & P. J. Quinn, 201

Landecker, T. L., Dewdney, P. E., Burgess, T. A., et al. 2000, *The synthesis telescope at the Dominion Radio Astrophysical Observatory*, Vol. 145, A&AS, 145, 509

Lawrence, A., Warren, S. J., Almaini, O., et al. 2007, *The UKIRT Infrared Deep Sky Survey (UKIDSS)*, Vol. 379, MNRAS, 379, 1599

Lehmer, B. D., Brandt, W. N., Alexander, D. M., et al. 2005, *The Extended Chandra Deep Field-South Survey: Chandra Point-Source Catalogs*, Vol. 161, ApJS, 161, 21

Leslie, S. K., Kewley, L. J., Sanders, D. B., & Lee, N. 2016, *Quenching star formation: insights from the local main sequence*, Vol. 455, MNRAS, 455, L82

Lien, A., Chakraborty, N., Fields, B. D., & Kemball, A. 2011, *Radio Supernovae in the Great Survey Era*, Vol. 740, ApJ, 740, 23

Lilly, S. J., Carollo, C. M., Pipino, A., Renzini, A., & Peng, Y. 2013, *Gas Regulation of Galaxies: The Evolution of the Cosmic Specific Star Formation Rate, the Metallicity-Mass-Star-formation Rate Relation, and the Stellar Content of Halos*, Vol. 772, ApJ, 772, 119

Lonsdale, C. J., Smith, H. E., Rowan-Robinson, M., et al. 2003, *SWIRE: The SIRTF Wide-Area Infrared Extragalactic Survey*, Vol. 115, PASP, 115, 897

Luo, B., Bauer, F. E., Brandt, W. N., et al. 2008, *The Chandra Deep Field-South Survey: 2 Ms Source Catalogs*, Vol. 179, ApJS, 179, 19

Lutz, D., Poglitsch, A., Altieri, B., et al. 2011, *PACS Evolutionary Probe (PEP) - A Herschel key program*, Vol. 532, A&A, 532, A90

Lynden-Bell, D. 1969, *Galactic Nuclei as Collapsed Old Quasars*, Vol. 223, Nature, 223, 690

Machalski, J. & Godlowski, W. 2000, *1.4 GHz luminosity function of galaxies in the Las Campanas redshift survey and its evolution*, Vol. 360, A&A, 360, 463

Magnelli, B., Popesso, P., Berta, S., et al. 2013, *The deepest Herschel-PACS far-infrared survey: number counts and infrared luminosity functions from combined PEP/GOODS-H observations*, Vol. 553, A&A, 553, A132

Magorrian, J., Tremaine, S., Richstone, D., et al. 1998, *The Demography of Massive Dark Objects in Galaxy Centers*, Vol. 115, AJ, 115, 2285

Maini, A. 2012, *Searching for Infrared-Faint Radio Sources in the SERVS deep fields: a class of high-z obscured radio-loud AGNs?*, PhD thesis, Alma Mater Studiorum Università di Bologna

Maini, A., Prandoni, I., Norris, R. P., Giovannini, G., & Spitler, L. R. 2016a, *Compact radio cores in radio-quiet active galactic nuclei*, Vol. 589, A&A, 589, L3

Maini, A., Prandoni, I., Norris, R. P., et al. 2016b, *Infrared-Faint Radio Sources in the SERVS deep fields: Pinpointing AGNs at high redshift*, A&A

Mainieri, V., Hasinger, G., Cappelluti, N., et al. 2007, *The XMM-Newton Wide-Field Survey in the COSMOS Field. IV. X-Ray Spectral Properties of Active Galactic Nuclei*, Vol. 172, ApJS, 172, 368

Maiolino, R., Gallerani, S., Neri, R., et al. 2012, *Evidence of strong quasar feedback in the early Universe*, Vol. 425, MNRAS, 425, L66

Manchester, R. N., Hobbs, G. B., Teoh, A., & Hobbs, M. 2005, *The Australia Telescope National Facility Pulsar Catalogue*, Vol. 129, AJ, 129, 1993

Mancuso, C., Lapi, A., Cai, Z. Y., et al. 2015, *Radio Observations of Star Forming Galaxies in the SKA era*, Advancing Astrophysics with the Square Kilometre Array (AASKA14), 82

Mannucci, F. 2007, *The Star Formation Density at $z \sim 7$*, in Astronomical Society of the Pacific Conference Series, Vol. 380, Deepest Astronomical Surveys, ed. J. Afonso, H. C. Ferguson, B. Mobasher, & R. Norris, 87

Mannucci, F., Maiolino, R., Cresci, G., et al. 2003, *The infrared supernova rate in starburst galaxies*, Vol. 401, A&A, 401, 519

Mao, M. Y., Huynh, M. T., Norris, R. P., et al. 2011, *No Evidence for Evolution in the Far-infrared-Radio Correlation out to z ˜ 2 in the Extended Chandra Deep Field South*, Vol. 731, ApJ, 731, 79

Mao, M. Y., Sharp, R., Norris, R. P., et al. 2012, *The Australia Telescope Large Area Survey: spectroscopic catalogue and radio luminosity functions*, Vol. 426, MNRAS, 426, 3334

Maoz, D., Nagar, N. M., Falcke, H., & Wilson, A. S. 2005, *The Murmur of the Sleeping Black Hole: Detection of Nuclear Ultraviolet Variability in LINER Galaxies*, Vol. 625, ApJ, 625, 699

Martín, S. 2011, *Extragalactic Line Surveys*, in IAU Symposium, Vol. 280, The Molecular Universe, ed. J. Cernicharo & R. Bachiller, 351–360

Matt, G., Guainazzi, M., Maiolino, R., et al. 1999, *One more surprise from the Circinus Galaxy: BeppoSAX discovery of a transmission component in hard X-rays*, Vol. 341, A&A, 341, L39

Mauch, T., Murphy, T., Buttery, H. J., et al. 2003, *SUMSS: a wide-field radio imaging survey of the southern sky - II. The source catalogue*, Vol. 342, MNRAS, 342, 1117

Mauduit, J.-C., Lacy, M., Farrah, D., et al. 2012, *The Spitzer Extragalactic Representative Volume Survey (SERVS): Survey Definition and Goals*, Vol. 124, PASP, 124, 714

McAlary, C. W. & Rieke, G. H. 1988, *A near-infrared and optical study of X-ray selected Seyfert galaxies. II - Models and interpretation*, Vol. 333, ApJ, 333, 1

McNamara, B. R. & Nulsen, P. E. J. 2007, *Heating Hot Atmospheres with Active Galactic Nuclei*, Vol. 45, ARA&A, 45, 117

McNamara, B. R., Wise, M., Nulsen, P. E. J., et al. 2000, *Chandra X-Ray Observations of the Hydra A Cluster: An Interaction between the Radio Source and the X-Ray-emitting Gas*, Vol. 534, ApJ, 534, L135

Merloni, A., Heinz, S., & di Matteo, T. 2003, *A Fundamental Plane of black hole activity*, Vol. 345, MNRAS, 345, 1057

Middelberg, E., Deller, A., Morgan, J., et al. 2011a, *Wide-field VLBA observations of the Chandra deep field South*, Vol. 526, A&A, 526, A74

Middelberg, E., Norris, R. P., Cornwell, T. J., et al. 2008a, *Deep Australia Telescope Large Area Survey Radio Observations of the European Large Area ISO Survey S1/Spitzer Wide-Area Infrared Extragalactic Field*, Vol. 135, AJ, 135, 1276

Middelberg, E., Norris, R. P., Hales, C. A., et al. 2011b, *The radio properties of infrared-faint radio sources*, Vol. 526, A&A, 526, A8

Middelberg, E., Norris, R. P., Tingay, S., et al. 2008b, *The first VLBI image of an infrared-faint radio source*, Vol. 491, A&A, 491, 435

Mignano, A., Miralles, J.-M., da Costa, L., et al. 2007, *ESO imaging survey: optical deep public survey*, Vol. 462, A&A, 462, 553

Mignano, A., Prandoni, I., Gregorini, L., et al. 2008, *The ATESP 5 GHz radio survey. II. Physical properties of the faint radio population*, Vol. 477, A&A, 477, 459

Miller, L., Peacock, J. A., & Mead, A. R. G. 1990, *The bimodal radio luminosity function of quasars*, Vol. 244, MNRAS, 244, 207

Miller, N. A., Bonzini, M., Fomalont, E. B., et al. 2013, *The Very Large Array 1.4 GHz Survey of the Extended Chandra Deep Field South: Second Data Release*, Vol. 205, ApJS, 205, 13

Miller, N. A., Fomalont, E. B., Kellermann, K. I., et al. 2008, *The VLA 1.4 GHz Survey of the Extended Chandra Deep Field-South: First Data Release*, Vol. 179, ApJS, 179, 114

Mills, B. Y. 1981, *The Molonglo Observatory synthesis telescope*, Vol. 4, Proceedings of the Astronomical Society of Australia, 4, 156

Muxlow, T. W. B., Richards, A. M. S., Garrington, S. T., et al. 2005, *High-resolution studies of radio sources in the Hubble Deep and Flanking Fields*, Vol. 358, MNRAS, 358, 1159

Nagar, N. M., Falcke, H., Wilson, A. S., & Ulvestad, J. S. 2002, *Radio sources in low-luminosity active galactic nuclei. III. "AGNs" in a distance-limited sample of "LLAGNs"*, Vol. 392, A&A, 392, 53

Narayan, R. & Yi, I. 1994, *Advection-dominated accretion: A self-similar solution*, Vol. 428, ApJ, 428, L13

Netzer, H. 2015, *Revisiting the Unified Model of Active Galactic Nuclei*, Vol. 53, ARA&A, 53, 365

Netzer, H., Lutz, D., Schweitzer, M., et al. 2007, *Spitzer Quasar and ULIRG Evolution Study (QUEST). II. The Spectral Energy Distributions of Palomar-Green Quasars*, Vol. 666, ApJ, 666, 806

Neugebauer, G., Oke, J. B., Becklin, E. E., & Matthews, K. 1979, *Absolute spectral energy distribution of quasi-stellar objects from 0.3 to 10 microns*, Vol. 230, ApJ, 230, 79

Norris, R., Basu, K., Brown, M., et al. 2015, *The SKA Mid-frequency All-sky Continuum Survey: Discovering the unexpected and transforming radio-astronomy*, Advancing Astrophysics with the Square Kilometre Array (AASKA14), 86

Norris, R. P., Afonso, J., Appleton, P. N., et al. 2006, *Deep ATLAS Radio Observations of the Chandra Deep Field-South/Spitzer Wide-Area Infrared Extragalactic Field*, Vol. 132, AJ, 132, 2409

Norris, R. P., Afonso, J., Bacon, D., et al. 2013, *Radio Continuum Surveys with Square Kilometre Array Pathfinders*, Vol. 30, PASA, 30, e020

Norris, R. P., Afonso, J., Cava, A., et al. 2011a, *Deep Spitzer Observations of Infrared-faint Radio Sources: High-redshift Radio-loud Active Galactic Nuclei?*, Vol. 736, ApJ, 736, 55

Norris, R. P., Hopkins, A. M., Afonso, J., et al. 2011b, *EMU: Evolutionary Map of the Universe*, Vol. 28, PASA, 28, 215

Norris, R. P., Middelberg, E., & Boyle, B. J. 2007a, *ATLAS: Deep Radio Observations of Six Square Degrees*, in Astronomical Society of the Pacific Conference Series, Vol. 380, "Deepest Astronomical Surveys", ed. J. Afonso, H. C. Ferguson, B. Mobasher, & R. Norris, 229

Norris, R. P., Tingay, S., Phillips, C., et al. 2007b, *Very long baseline interferometry detection of an Infrared-Faint Radio Source*, Vol. 378, MNRAS, 378, 1434

O'Dea, C. P. 1998, *The Compact Steep-Spectrum and Gigahertz Peaked-Spectrum Radio Sources*, Vol. 110, PASP, 110, 493

Oliver, S. J., Bock, J., Altieri, B., et al. 2012, *The Herschel Multi-tiered Extragalactic Survey: HerMES*, Vol. 424, MNRAS, 424, 1614

Orienti, M., D'Ammando, F., Giroletti, M., Giovannini, G., & Panessa, F. 2015, *The physics of the radio emission in the quiet side of the AGN population with the SKA*, Advancing Astrophysics with the Square Kilometre Array (AASKA14), 87

Orienti, M. & Prieto, M. A. 2010, *Radio structures of the nuclei of nearby Seyfert galaxies and the nature of the missing diffuse emission*, Vol. 401, MNRAS, 401, 2599

Padovani, P. 2011, *The microjansky and nanojansky radio sky: source population and multiwavelength properties*, Vol. 411, MNRAS, 411, 1547

Padovani, P. 2016, The faint radio sky: radio astronomy becomes mainstream, ArXiv e-prints

Padovani, P., Bonzini, M., Kellermann, K. I., et al. 2015a, *Radio-faint AGN: a tale of two populations*, Vol. 452, MNRAS, 452, 1263

Padovani, P., Bonzini, M., Kellermann, K. I., et al. 2015b, "Back at the Edge of the Universe" Conference

Padovani, P., Mainieri, V., Tozzi, P., et al. 2009, *The Very Large Array Survey of the Chandra Deep Field South. IV. Source Population*, Vol. 694, ApJ, 694, 235

Padovani, P., Miller, N., Kellermann, K. I., et al. 2011, *The VLA Survey of Chandra Deep Field South. V. Evolution and Luminosity Functions of Sub-millijansky Radio Sources and the Issue of Radio Emission in Radio-quiet Active Galactic Nuclei*, Vol. 740, ApJ, 740, 20

Panessa, F., Barcons, X., Bassani, L., et al. 2007, *The X-ray and radio connection in low-luminosity active nuclei*, Vol. 467, A&A, 467, 519

Panessa, F., Bassani, L., Cappi, M., et al. 2006, *On the X-ray, optical emission line and black hole mass properties of local Seyfert galaxies*, Vol. 455, A&A, 455, 173

Papovich, C., Rudnick, G., Le Floc'h, E., et al. 2007, *Spitzer Mid- to Far-Infrared Flux Densities of Distant Galaxies*, Vol. 668, ApJ, 668, 45

Parra, R., Conway, J. E., Aalto, S., et al. 2010, *COLA. III. Radio Detection of Active Galactic Nucleus in Compact Moderate Luminosity Infrared Galaxies*, Vol. 720, ApJ, 720, 555

Peterson, B. M. 1997, *An Introduction to Active Galactic Nuclei*

Pilkington, J. D. H. & Scott, J. F. 1965, *A survey of radio sources between declinations 20° and 40°*, Vol. 69, MmRAS, 69, 183

Poggianti, B. M. & Barbaro, G. 1997, *Indicators of star formation: 4000 Å break and Balmer lines.*, Vol. 325, A&A, 325, 1025

Poglitsch, A., Waelkens, C., Geis, N., et al. 2010, *The Photodetector Array Camera and Spectrometer (PACS) on the Herschel Space Observatory*, Vol. 518, A&A, 518, L2

Polletta, M., Tajer, M., Maraschi, L., et al. 2007, *Spectral Energy Distributions of Hard X-Ray Selected Active Galactic Nuclei in the XMM-Newton Medium Deep Survey*, Vol. 663, ApJ, 663, 81

Pounds, K. A., Nandra, K., Stewart, G. C., George, I. M., & Fabian, A. C. 1990, *X-ray reflection from cold matter in the nuclei of active galaxies*, Vol. 344, Nature, 344, 132

Pozzetti, L., Cimatti, A., Zamorani, G., et al. 2003, *The K20 survey. V. The evolution of the near-IR Luminosity Function*, Vol. 402, A&A, 402, 837

Prandoni, I., de Ruiter, H. R., Ricci, R., et al. 2010, *The ATESP 5 GHz radio survey. III. 4.8, 8.6 and 19 GHz follow-up observations of radio galaxies*, Vol. 510, A&A, 510, A42

Prandoni, I., Gregorini, L., Parma, P., et al. 2001a, *The ATESP radio survey. III. Source counts*, Vol. 365, A&A, 365, 392

Prandoni, I., Gregorini, L., Parma, P., et al. 2001b, *The ATESP radio survey. IV. Optical identifications and spectroscopy in the EIS-A region*, Vol. 369, A&A, 369, 787

Prandoni, I. & Seymour, N. 2015, *Revealing the Physics and Evolution of Galaxies and Galaxy Clusters with SKA Continuum Surveys*, Advancing Astrophysics with the Square Kilometre Array (AASKA14), 67

Rafferty, D. A., Brandt, W. N., Alexander, D. M., et al. 2011, *Supermassive Black Hole Growth in Starburst Galaxies over Cosmic Time: Constraints from the Deepest Chandra Fields*, Vol. 742, ApJ, 742, 3

Rawlings, S. & Saunders, R. 1991, *Evidence for a common central-engine mechanism in all extragalactic radio sources*, Vol. 349, Nature, 349, 138

Readhead, A. C. S., Taylor, G. B., Xu, W., et al. 1996, *The Statistics and Ages of Compact Symmetric Objects*, Vol. 460, ApJ, 460, 612

Rees, G. A., Spitler, L. R., Norris, R. P., et al. 2016, *Radio galaxies in ZFOURGE/NMBS: no difference in the properties of massive galaxies with and without radio-AGN out to z = 2.25*, Vol. 455, MNRAS, 455, 2731

Rengelink, R. B., Tang, Y., de Bruyn, A. G., et al. 1997, *The Westerbork Northern Sky Survey (WENSS), I. A 570 square degree Mini-Survey around the North Ecliptic Pole*, Vol. 124, A&AS, 124

Richards, A. M. S., Muxlow, T. W. B., Beswick, R., et al. 2007, *Using VO tools to investigate distant radio starbursts hosting obscured AGN in the HDF(N) region*, Vol. 472, A&A, 472, 805

Richards, E. A. 2000, *The Nature of Radio Emission from Distant Galaxies: The 1.4 GHZ Observations*, Vol. 533, ApJ, 533, 611

Richards, E. A., Fomalont, E. B., Kellermann, K. I., et al. 1999, *Optically Faint Microjansky Radio Sources*, Vol. 526, ApJ, 526, L73

Richards, G. T., Deo, R. P., Lacy, M., et al. 2009, *Eight-Dimensional Mid-Infrared/Optical Bayesian Quasar Selection*, Vol. 137, AJ, 137, 3884

Richards, G. T., Lacy, M., Storrie-Lombardi, L. J., et al. 2006, *Spectral Energy Distributions and Multiwavelength Selection of Type 1 Quasars*, Vol. 166, ApJS, 166, 470

Rieke, G. H., Alonso-Herrero, A., Weiner, B. J., et al. 2009, *Determining Star Formation Rates for Infrared Galaxies*, Vol. 692, ApJ, 692, 556

Rix, H.-W., Barden, M., Beckwith, S. V. W., et al. 2004, *GEMS: Galaxy Evolution from Morphologies and SEDs*, Vol. 152, ApJS, 152, 163

Robertson, J. G. 1991, *The Most and Other Radio Telescopes*, Vol. 44, Australian Journal of Physics, 44, 729

Röttgering, H., Afonso, J., Barthel, P., et al. 2011, *LOFAR and APERTIF Surveys of the Radio Sky: Probing Shocks and Magnetic Fields in Galaxy Clusters*, Vol. 32, Journal of Astrophysics and Astronomy, 32, 557

Röttgering, H. J. A., Braun, R., Barthel, P. D., et al. 2006, *LOFAR - Opening up a new window on the Universe*, ArXiv Astrophysics e-prints

Röttgering, H. J. A., van Weeren, R., Miley, G., et al. 2010, *LOFAR and the low frequency universe. Probing the formation and evolution of massive galaxies, AGN and clusters*, in ISKAF2010 Science Meeting

Roy, A. L., Norris, R. P., Kesteven, M. J., Troup, E. R., & Reynolds, J. E. 1998, *Seyfert galaxies and the radio-far-infrared correlation*, Vol. 301, MNRAS, 301, 1019

Ryle, M., Smith, F. G., & Elsmore, B. 1950, *A preliminary survey of the radio stars in the Northern Hemisphere*, Vol. 110, MNRAS, 110, 508

Sadler, E. M., Jackson, C. A., Cannon, R. D., et al. 2002, *Radio sources in the 2dF Galaxy Redshift Survey - II. Local radio luminosity functions for AGN and star-forming galaxies at 1.4 GHz*, Vol. 329, MNRAS, 329, 227

Sandage, A. 1965, *The Existence of a Major New Constituent of the Universe: the Quasistellar Galaxies*, Vol. 141, ApJ, 141, 1560

Sanders, D. B., Phinney, E. S., Neugebauer, G., Soifer, B. T., & Matthews, K. 1989, *Continuum energy distribution of quasars - Shapes and origins*, Vol. 347, ApJ, 347, 29

Saracco, P., Fiano, A., Chincarini, G., et al. 2006, *Probing the evolution of the near-infrared luminosity function of galaxies to z 3 in the Hubble Deep Field-South*, Vol. 367, MNRAS, 367, 349

Sargent, M. T., Schinnerer, E., Murphy, E., et al. 2010, *The VLA-COSMOS Perspective on the Infrared-Radio Relation. I. New Constraints on Selection Biases and the Non-Evolution of the Infrared/Radio Properties of Star-Forming and Active Galactic Nucleus Galaxies at Intermediate and High Redshift*, Vol. 186, ApJS, 186, 341

Saunders, W., Rowan-Robinson, M., Lawrence, A., et al. 1990, *The 60-micron and far-infrared luminosity functions of IRAS galaxies*, Vol. 242, MNRAS, 242, 318

Scheuer, P. A. G. 1974a, *Fluctuations in the X-ray background*, Vol. 166, MNRAS, 166, 329

Scheuer, P. A. G. 1974b, *Models of extragalactic radio sources with a continuous energy supply from a central object*, Vol. 166, MNRAS, 166, 513

Schilizzi, R. T., Alexander, P., Cordes, J. M., et al. 2007, *SKA Memo 100: Preliminary Specifications for the Square Kilometre Array*

Schiminovich, D., Wyder, T. K., Martin, D. C., et al. 2007, *The UV-Optical Color Magnitude Diagram. II. Physical Properties and Morphological Evolution On and Off of a Star-forming Sequence*, Vol. 173, ApJS, 173, 315

Schinnerer, E., Sargent, M. T., Bondi, M., et al. 2010, *The VLA-COSMOS Survey. IV. Deep Data and Joint Catalog*, Vol. 188, ApJS, 188, 384

Schmidt, M. & Green, R. F. 1983, *Quasar evolution derived from the Palomar bright quasar survey and other complete quasar surveys*, Vol. 269, ApJ, 269, 352

Schödel, R., Najarro, F., Muzic, K., & Eckart, A. 2010, *Peering through the veil: near-infrared photometry and extinction for the Galactic nuclear star cluster. Accurate near infrared H, Ks, and L' photometry and the near-infrared extinction-law toward the central parsec of the Galaxy*, Vol. 511, A&A, 511, A18

Scoville, N. Z. 2013, *Evolution of star formation and gas*, ed. J. Falcón-Barroso & J. H. Knapen, 491

Seymour, N., Dwelly, T., Moss, D., et al. 2008, *The star formation history of the Universe as revealed by deep radio observations*, Vol. 386, MNRAS, 386, 1695

Seymour, N., Huynh, M., Dwelly, T., et al. 2009, *Investigating the far-IR/radio correlation of star-forming Galaxies to z = 3*, Vol. 398, MNRAS, 398, 1573

Seymour, N., McHardy, I. M., & Gunn, K. F. 2004, *Radio observations of the 13^{h}XMM-Newton/ROSAT Deep X-ray Survey Area*, Vol. 352, MNRAS, 352, 131

Seymour, N., Stern, D., De Breuck, C., et al. 2007, *The Massive Hosts of Radio Galaxies across Cosmic Time*, Vol. 171, ApJS, 171, 353

Shakeshaft, J. R., Ryle, M., Baldwin, J. E., Elsmore, B., & Thomson, J. H. 1955, *A survey of radio sources between declinations −38° and +83°*, Vol. 67, MmRAS, 67, 106

Shang, Z., Brotherton, M. S., Green, R. F., et al. 2005, *Quasars and the Big Blue Bump*, Vol. 619, ApJ, 619, 41

Shang, Z., Brotherton, M. S., Wills, B. J., et al. 2011, *The Next Generation Atlas of Quasar Spectral Energy Distributions from Radio to X-Rays*, Vol. 196, ApJS, 196, 2

Shankar, F., Weinberg, D. H., & Miralda-Escudé, J. 2009, *Self-Consistent Models of the AGN and Black Hole Populations: Duty Cycles, Accretion Rates, and the Mean Radiative Efficiency*, Vol. 690, ApJ, 690, 20

Shields, G. A. 1978, *Thermal continuum from acretion disks in quasars*, Vol. 272, Nature, 272, 706

Silva, L., Granato, G. L., Bressan, A., & Danese, L. 1998, *Modeling the Effects of Dust on Galactic Spectral Energy Distributions from the Ultraviolet to the Millimeter Band*, Vol. 509, ApJ, 509, 103

Silverman, J. D., Green, P. J., Barkhouse, W. A., et al. 2008, *The Luminosity Function of X-Ray-selected Active Galactic Nuclei: Evolution of Supermassive Black Holes at High Redshift*, Vol. 679, ApJ, 679, 118

Silverman, J. D., Lamareille, F., Maier, C., et al. 2009, *Ongoing and Co-Evolving Star Formation in zCOSMOS Galaxies Hosting Active Galactic Nuclei*, Vol. 696, ApJ, 696, 396

Silverman, J. D., Mainieri, V., Salvato, M., et al. 2010, *The Extended Chandra Deep Field-South Survey: Optical Spectroscopy of Faint X-ray Sources with the VLT and Keck*, Vol. 191, ApJS, 191, 124

Smith, H. E., Lonsdale, C. J., Lonsdale, C. J., & Diamond, P. J. 1998, *A Starburst Revealed—Luminous Radio Supernovae in the Nuclei of ARP 220*, Vol. 493, ApJ, 493, L17

Smolčić, V., Padovani, P., Delhaize, J., et al. 2015, *Exploring AGN Activity over Cosmic Time with the SKA*, Advancing Astrophysics with the Square Kilometre Array (AASKA14), 69

Smolčić, V., Schinnerer, E., Scodeggio, M., et al. 2008, *A New Method to Separate Star-forming from AGN Galaxies at Intermediate Redshift: The Submillijansky Radio Population in the VLA-COSMOS Survey*, Vol. 177, ApJS, 177, 14

Stead, J. J. & Hoare, M. G. 2009, *The slope of the near-infrared extinction law*, Vol. 400, MNRAS, 400, 731

Stefanon, M. & Marchesini, D. 2013, *The evolution of the rest-frame J- and H-band luminosity function of galaxies to z=3.5*, Vol. 429, MNRAS, 429, 881

Strittmatter, P. A., Hill, P., Pauliny-Toth, I. I. K., Steppe, H., & Witzel, A. 1980, *Radio observations of optically selected quasars*, Vol. 88, A&A, 88, L12

Sturm, E., González-Alfonso, E., Veilleux, S., et al. 2011, *Massive Molecular Outflows and Negative Feedback in ULIRGs Observed by Herschel-PACS*, Vol. 733, ApJ, 733, L16

Surace, J. A., Shupe, D. L., Fang, F., et al. 2005, *Data Processing and Validation of the SWIRE Survey*, Vol. SWIRE Data Delivery Document, NASA-IPAC, SWIRE Data Delivery Document, NASA-IPAC

Sutherland, W. & Saunders, W. 1992, *On the likelihood ratio for source identification*, Vol. 259, MNRAS, 259, 413

Szokoly, G. P., Bergeron, J., Hasinger, G., et al. 2004, *The Chandra Deep Field-South: Optical Spectroscopy. I*, Vol. 155, ApJS, 155, 271

Taylor, A. R., Stil, J. M., Grant, J. K., et al. 2007, *Radio Polarimetry of the ELAIS N1 Field: Polarized Compact Sources*, Vol. 666, ApJ, 666, 201

Taylor, E. N., Franx, M., van Dokkum, P. G., et al. 2009, *A Public, K-Selected, Optical-to-Near-Infrared Catalog of the Extended Chandra Deep Field South (ECDFS) from the Multiwavelength Survey by Yale-Chile (MUSYC)*, Vol. 183, ApJS, 183, 295

Telfer, R. C., Zheng, W., Kriss, G. A., & Davidsen, A. F. 2002, *The Rest-Frame Extreme-Ultraviolet Spectral Properties of Quasi-stellar Objects*, Vol. 565, ApJ, 565, 773

Teplitz, H. I., Chary, R., Elbaz, D., et al. 2011, *Spitzer Infrared Spectrometer 16 μm Observations of the Goods Fields*, Vol. 141, AJ, 141, 1

Terashima, Y. & Wilson, A. S. 2003, *Chandra Snapshot Observations of Low-Luminosity Active Galactic Nuclei with a Compact Radio Source*, Vol. 583, ApJ, 583, 145

Terlevich, R., Tenorio-Tagle, G., Franco, J., & Melnick, J. 1992, *The starburst model for active galactic nuclei - The broad-line region as supernova remnants evolving in a high-density medium*, Vol. 255, MNRAS, 255, 713

Treister, E., Virani, S., Gawiser, E., et al. 2009, *Optical Spectroscopy of X-Ray Sources in the Extended Chandra Deep Field South*, Vol. 693, ApJ, 693, 1713

Trump, J. R., Impey, C. D., Elvis, M., et al. 2009, *The COSMOS Active Galactic Nucleus Spectroscopic Survey. I. XMM-Newton Counterparts*, Vol. 696, ApJ, 696, 1195

Ulvestad, J. S., Antonucci, R. R. J., & Barvainis, R. 2005, *VLBA Imaging of Central Engines in Radio-Quiet Quasars*, Vol. 621, ApJ, 621, 123

Ulvestad, J. S., Perley, R. A., & Chandler, C. J. 2009, *The Very Large Array Observational status summary*

Urry, C. M. & Padovani, P. 1995, *Unified Schemes for Radio-Loud Active Galactic Nuclei*, Vol. 107, PASP, 107, 803

van Breugel, W., De Breuck, C., Stanford, S. A., et al. 1999, *A Radio Galaxy at z = 5.19*, Vol. 518, ApJ, 518, L61

van der Kruit, P. C. 1971, *Observations of core sources in Seyfert and normal galaxies with the Westerbork synthesis radio telescope at 1415 MHz.*, Vol. 15, A&A, 15, 110

van der Kruit, P. C. 1973, *High-resolution Radio Continuum Observations of Bright Spiral Galaxies at 1415 MHz: A General Discussion*, Vol. 29, A&A, 29, 263

van Haarlem, M. P., Wise, M. W., Gunst, A. W., et al. 2013, *LOFAR: The LOw-Frequency ARray*, Vol. 556, A&A, 556, A2

Vanden Berk, D. E., Richards, G. T., Bauer, A., et al. 2001, *Composite Quasar Spectra from the Sloan Digital Sky Survey*, Vol. 122, AJ, 122, 549

Vattakunnel, S., Tozzi, P., Matteucci, F., et al. 2012, *The radio-X-ray relation as a star formation indicator: results from the Very Large Array-Extended Chandra Deep Field-South*, Vol. 420, MNRAS, 420, 2190

Wang, S., Gao, J., Jiang, B. W., Li, A., & Chen, Y. 2013, *The Mid-infrared Extinction Law and its Variation in the Coalsack Nebula*, Vol. 773, ApJ, 773, 30

Wang, S. & Jiang, B. W. 2014, *Universality of the Near-Infrared Extinction Law Based on the APOGEE Survey*, ArXiv e-prints

Wang, T.-G., Zhou, H.-Y., Wang, J.-X., Lu, Y.-J., & Lu, Y. 2006, *Evidence for a Population of Beamed Radio-intermediate Quasars*, Vol. 645, ApJ, 645, 856

Whitaker, K. E., van Dokkum, P. G., Brammer, G., & Franx, M. 2012, *The Star Formation Mass Sequence Out to $z = 2.5$*, Vol. 754, ApJ, 754, L29

White, R. L., Becker, R. H., Gregg, M. D., et al. 2000, *The FIRST Bright Quasar Survey. II. 60 Nights and 1200 Spectra Later*, Vol. 126, ApJS, 126, 133

White, R. L., Becker, R. H., Helfand, D. J., & Gregg, M. D. 1997, *A Catalog of 1.4 GHz Radio Sources from the FIRST Survey*, Vol. 475, ApJ, 475, 479

White, S. V., Jarvis, M. J., Häußler, B., & Maddox, N. 2015, *Radio-quiet quasars in the VIDEO survey: evidence for AGN-powered radio emission at $S_{1.4\,GHz} < 1$ mJy*, Vol. 448, MNRAS, 448, 2665

Whittet, D. C. B. 1988, *The observed properties of interstellar dust in the infrared*, in Dust in the Universe, ed. M. E. Bailey & D. A. Williams, 25–53

Wilkes, B. J. & Elvis, M. 1987, *Quasar energy distributions. I - Soft X-ray spectra of quasars*, Vol. 323, ApJ, 323, 243

Wilman, R. J., Miller, L., Jarvis, M. J., et al. 2008a, *A semi-empirical simulation of the extragalactic radio continuum sky for next generation radio telescopes*, Vol. 388, MNRAS, 388, 1335

Wilman, R. J., Miller, L., Jarvis, M. J., et al. 2008b, *A semi-empirical simulation of the extragalactic radio continuum sky for next generation radio telescopes*, Vol. 388, MNRAS, 388, 1335

Wright, E. L. 2006, *A Cosmology Calculator for the World Wide Web*, Vol. 118, PASP, 118, 1711

Wright, E. L., Eisenhardt, P. R. M., Mainzer, A. K., et al. 2010, *The Wide-field Infrared Survey Explorer (WISE): Mission Description and Initial On-orbit Performance*, Vol. 140, AJ, 140, 1868

Wuyts, S., Labbé, I., Schreiber, N. M. F., et al. 2008, *FIREWORKS U_{38}-to-24 μm Photometry of the GOODS Chandra Deep Field-South: Multiwavelength Catalog and Total Infrared Properties of Distant K_s-selected Galaxies*, Vol. 682, ApJ, 682, 985

Xue, Y. Q., Luo, B., Brandt, W. N., et al. 2011, *The Chandra Deep Field-South Survey: 4 Ms Source Catalogs*, Vol. 195, ApJS, 195, 10

York, D. G., Adelman, J., Anderson, Jr., J. E., et al. 2000, *The Sloan Digital Sky Survey: Technical Summary*, Vol. 120, AJ, 120, 1579

Yu, Q. & Tremaine, S. 2002, *Observational constraints on growth of massive black holes*, Vol. 335, MNRAS, 335, 965

Yun, M. S., Reddy, N. A., & Condon, J. J. 2001, *Radio Properties of Infrared-selected Galaxies in the IRAS 2 Jy Sample*, Vol. 554, ApJ, 554, 803

Zamfir, S., Sulentic, J. W., & Marziani, P. 2008, *New insights on the QSO radio-loud/radio-quiet dichotomy: SDSS spectra in the context of the 4D eigenvector1 parameter space*, Vol. 387, MNRAS, 387, 856

Zheng, W., Kriss, G. A., Telfer, R. C., Grimes, J. P., & Davidsen, A. F. 1997, *A Composite HST Spectrum of Quasars*, Vol. 475, ApJ, 475, 469

Zinn, P.-C., Middelberg, E., & Ibar, E. 2011, *Infrared-faint radio sources: a cosmological view. AGN number counts, the cosmic X-ray background and SMBH formation*, Vol. 531, A&A, 531, A14

Zinn, P.-C., Middelberg, E., Norris, R. P., & Dettmar, R.-J. 2013, *AGN feedback works both ways*, ArXiv e-prints

Zinn, P.-C., Middelberg, E., Norris, R. P., et al. 2012, *The Australia Telescope Large Area Survey: 2.3 GHz observations of ELAIS-S1 and CDF-S. Spectral index properties of the faint radio sky*, Vol. 544, A&A, 544, A38

Zubovas, K. & King, A. R. 2012, *AGN Winds and the Black-Hole - Galaxy Connection*, in Astronomical Society of the Pacific Conference Series, Vol. 460, AGN Winds in Charleston, ed. G. Chartas, F. Hamann, & K. M. Leighly, 235